RICE UNIVERSITY

By

Jordan L. Shivers

A THESIS SUBMITTED
IN PARTIAL FULFILLMENT OF THE
REQUIREMENTS FOR THE DEGREE

Doctor of Philosophy

APPROVED, THESIS COMMITTEE

Frederick MacKintosh
Frederick MacKintosh (Feb 24, 2022 16:41 CST)

Fred C. MacKintosh

Paul A Janmey
Paul A Janmey (Feb 24, 2022 20:05 EST)

Paul Janmey

Matteo Pasquali

Oleg Igoshin

HOUSTON, TEXAS

February 2022

RICE UNIVERSITY

Phase transitions in the rheology of biopolymer networks

by

Jordan L. Shivers

A Thesis Submitted
in Partial Fulfillment of the
Requirements for the Degree

Doctor of Philosophy

Committee:
Prof. Fred C. MacKintosh, Chair
Prof. Matteo Pasquali
Prof. Paul A. Janmey
Prof. Oleg Igoshin

Houston, TX
Feb. 2022

Abstract

Most biological materials are stabilized internally by disordered networks of long, thin protein assemblies known as biopolymers. These networks occupy a negligible fraction of the space inside cells and tissues, yet are largely responsible for their extraordinary mechanical properties and exceptional resilience against unpredictable physiological loads. An essential contributor to this resilience is their highly strain-dependent stiffness; they easily deform to accommodate small strains, yet resist damage by stiffening significantly in response to larger strains. Recent work has suggested that the phenomenon of strain-induced stiffening in stiff or athermal biopolymer networks, like the collagen-rich extracellular matrix, constitutes a phase transition between distinct mechanical regimes, analogous to connectivity-controlled rigidity transitions observed in networks and other amorphous materials. Simulations have shown that this transition is heralded by classic signatures of continuous phase transitions, including power law scaling of relevant observables and a diverging correlation length.

In this thesis, we develop theoretical and computational models to describe the mechanics and dynamics of disordered elastic networks near the onset of rigidity. We develop a real space renormalization-based scaling theory that establishes relationships between the various critical exponents describing the scaling of the elastic moduli and fluctuations in networks near both the strain-controlled and connectivity-controlled rigidity transitions, which we validate using simulations of coarse-grained elastic networks. We then describe the rheology of fluid-immersed networks near the strain-induced stiffening transition and demonstrate that a coupling between diverging strain fluctuations and time-dependent energy dissipation leads to emergent power law rheology at a critical prestrain. Next, we explore the effects of criticality on a phenomenon in biopolymer networks known as the nonlinear Poisson effect, which describes their tendency to shrink dramatically and strongly align when stretched, a behavior with potentially major consequences for matrix-embedded cells. We show that this effect coincides with an analogous extension-controlled rigidity transition and describe the influence of this transition on network rearrangement and the scaling of the apparent Young's modulus. We further propose a physical mechanism for the unusual compression-driven stiffening effect observed in tissues. Considering a simplified model tissue consisting of a disordered network with embedded stiff particles, we construct a phase diagram describing a unique regime of compression-driven, tension-dominated mechanical stability that arises in these systems before conventional jamming, which we validate in simulations.

Preface

Portions of this thesis have been adapted from research articles written during my dissertation period, all of which are listed below.

- **Jordan L. Shivers**, Jingchen Feng, Abhinav Sharma, and Fred C. MacKintosh. Normal stress anisotropy and marginal stability in athermal elastic networks. ***Soft Matter***, 15 (7): 1666–1675, 2019.

- **Jordan L. Shivers**, Sadjad Arzash, Abhinav Sharma, and Fred C. MacKintosh. Scaling Theory for Mechanical Critical Behavior in Fiber Networks. ***Physical Review Letters***, 122 (18): 188003, 2019.

- Sadjad Arzash, **Jordan L. Shivers**, Albert J. Licup, Abhinav Sharma, and Fred C. MacKintosh. Stress-stabilized subisostatic fiber networks in a ropelike limit. ***Physical Review E***, 99 (4): 042412, 2019.

- **Jordan L. Shivers**, Sadjad Arzash, and Fred C. MacKintosh. Nonlinear Poisson Effect Governed by a Mechanical Critical Transition. ***Physical Review Letters***, 124 (3): 038002, 2020.

- Sadjad Arzash, **Jordan L. Shivers**, and Fred C. MacKintosh. Finite size effects in critical fiber networks. ***Soft Matter***, 16 (29): 6784–6793, 2020.

- **Jordan L. Shivers**, Jingchen Feng, Anne S. G. van Oosten, Herbert Levine, Paul A. Janmey, and Fred C. MacKintosh. Compression stiffening of fibrous networks with stiff inclusions. ***Proceedings of the National Academy of Sciences***, 117 (35): 21037–21044, 2020.

- Sadjad Arzash, **Jordan L. Shivers**, and Fred C. MacKintosh. Shear-induced phase transition and critical exponents in three-dimensional fiber networks. ***Physical Review E***, 104 (2): L022402, 2021.

- Dawei Song, **Jordan L. Shivers**, Fred C. MacKintosh, Alison E. Patteson, and Paul A. Janmey. Cell-induced confinement effects in soft tissue mechanics. ***Journal of Applied Physics***, 129 (14): 140901, 2021.

- Katarzyna Pogoda, Fitzroy J. Byfield, Piotr Deptuła, Mateusz Cieśluk, Łukasz Suprewicz, Karol Skłodowski, **Jordan L. Shivers**, Anne S. G. van Oosten, Katrina Cruz, Ekaterina Tarasovetc, Ekaterina L. Grishchuk, Fred C. MacKintosh, Robert Bucki, Alison E. Patteson, and Paul A. Janmey. Unique role

of vimentin networks in compression stiffening of cells and protection of nuclei from compressive stress. *under review*, 2022.

- **Jordan L. Shivers**, Abhinav Sharma, and Fred C. MacKintosh. Non-affinity controls critical slowing down and rheology near the onset of rigidity. arxiv:2203.04891, 2022.

Acknowledgments

I thank my advisor, Fred MacKintosh, for encouraging me to come to Rice and for being a truly phenomenal mentor and research guide.

I thank our collaborators, Abhinav Sharma, Paul Janmey, Gijsje Koenderink, Herbert Levine, Alison Patteson, and Michael Rubinstein, for their support and endless patience.

I thank the members of my committee, Matteo Pasquali, Oleg Igoshin, and Paul Janmey, for taking the time to review and provide feedback on this thesis.

I thank the current and former members of the MacKintosh group for providing a warm and welcoming environment: Jingchen, Tomer, Anupama, Lucas, Prathamesh, Sadjad, and Sihan.

I thank Cliff Brangwynne and Sravanti Uppaluri for introducing me to soft matter, guiding my undergraduate thesis research, and teaching me how to properly write a scientific paper.

I am indebted to all of the people in my life who have led me toward a career in science. I owe special thanks to Mrs. Randolph, my middle school science teacher, whose encouragement and generosity set me on this path in the first place.

I am thankful to family and friends for providing constant support and keeping me sane. Thank you to my brothers, Jeffery, Jacob, and Justin, and to my friends from home and from college. Thank you also to all of the members of the Nguyen family for welcoming me in more than a decade ago.

I owe everything to my best friend and partner, Taylor. Thank you for always believing in me and for being such an incredible parent to Stanley.

Finally, I am grateful to the funding sources that have made this work possible, including the Riki Kobayashi Fellowship in Chemical Engineering, the Lodieska Stockbridge Vaughn Fellowship, the Sunit Patel '85 Endowed Fellowship, the Texas Space Grant Consortium Graduate Fellowship, the Ken Kennedy Institute Oil and Gas HPC Conference Fellowship, and the NSF Center for Theoretical Biological Physics (PHY-2019745) and Division of Materials Research (DMR-1826623).

Contents

List of Figures

Chapter 1

Introduction

1.1 Semiflexible polymers in living materials

Billions of years of evolution have produced an incredible diversity of biological materials. Cells, the simplest unit of life, are soft machines comprising a flexible outer membrane enclosing a densely crowded, constantly rearranging suspension of subcellular components that vary tremendously in function and form, such as organelles, cytoskeletal filaments, and motor proteins [1–3]. These components coordinate to carry out the chemical and mechanical actions responsible for crucial cellular processes such as motility, self-replication, and differentiation. Cells, in turn, interact mechanically with the surrounding extracellular matrix to produce important tissue-level phenomena such as wound healing, coordinated force generation in muscles, and morphogenesis in development [4]. Interpreting how these components interact to give rise to these essential biological phenomena, and understanding how and why problems arise in disease, requires a quantitative description of cells and tissues as materials.

In spite of this diversity, one finds that basic underlying structures are repeated in many different biological contexts. Perhaps the most important of these, from a mechanical perspective, are the many varieties of *semiflexible biopolymers*, filamentous

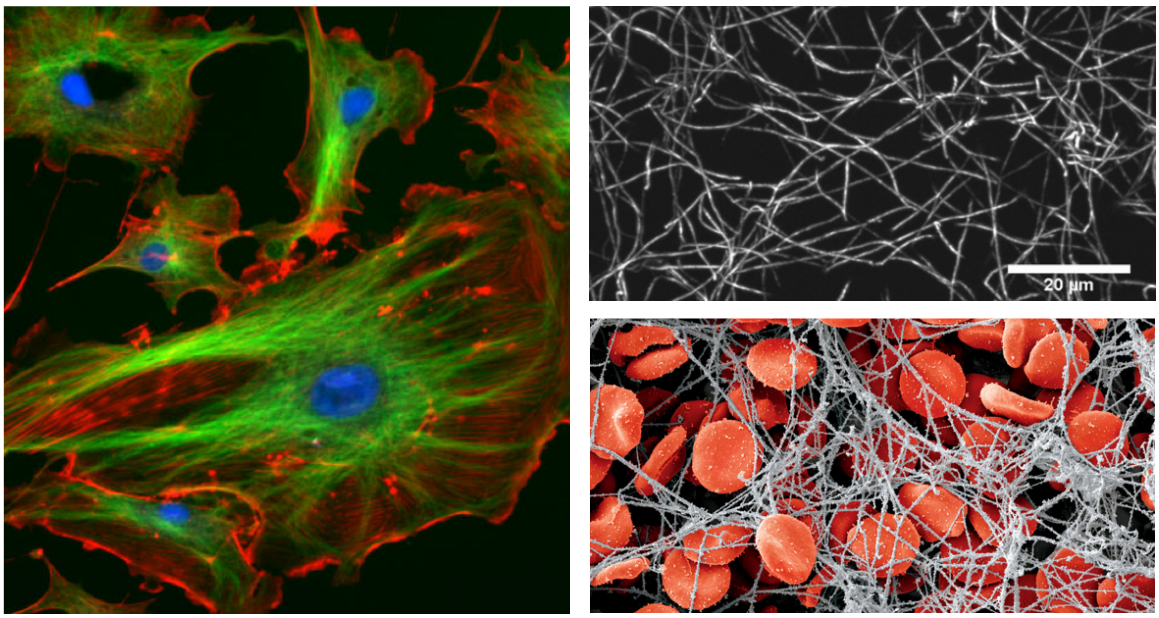

Figure 1.1: Left: Mammalian cells with fluorescently labeled microtubules (green), actin filaments (red), and DNA (blue), from http://rsb.info.nih.gov/ij/images/. Top right: Confocal micrograph of a reconstituted network of collagen type-1, adapted from Ref. [5]. Bottom right: Artificially colored electron micrograph of a blood clot showing fibrin (grey) and red blood cells (red), from http://www.ikelos.info/electronmicroscopy/.

assemblies of proteins that assemble into mechanical scaffolding for cells, tissues, and beyond [3, 6, 7]. Despite occupying a negligible fraction of the total volume, disordered biopolymer networks are essential for the mechanical integrity of living materials, especially given the large stresses and strains to which living things are generally subjected in normal operation. For example, the biopolymer actin forms networks on and around the cell membrane, as shown in Fig. 1.1a, and is essential for cell motility [8], and the intermediate filament vimentin plays an essential role in protecting the cell nucleus from large deformations [9]. Collagen (Fig. 1.1b) is the most abundant protein in the extracellular matrix and is an essential contributor to the stability of connective tissue under physiological stresses [10, 11]. The biopolymer fibrin (see Fig. 1.1c) plays an essential role in wound healing as the predominant structural element of blood clots [12–14]; in the body, clots that form after an injury must sustain an intact protective seal during a damaged vessel's continued operation, often involving

large shear, tensile or compressive forces, in order to effectively prevent blood loss and provide stable mechanical scaffolding for the formation of replacement tissue [14, 15]. Fibrous networks are also produced in many contexts by plants, fungi and animals for uses beyond internal tissue structure: for example, gels are produced by fish and amphibians as external protective enclosures for eggs [16], hagfish produce a remarkable fibrous gel to deter predators [17], and spiders construct webs and egg cases from silk [18].

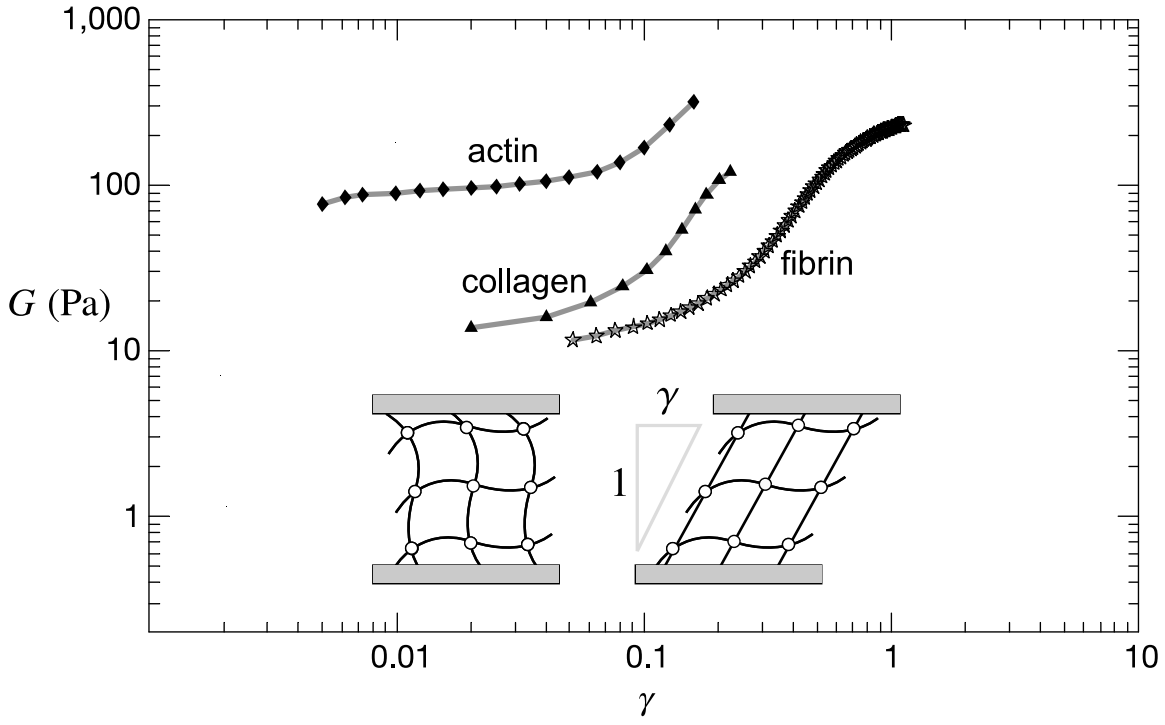

Figure 1.2: Measurements of the strain-dependent apparent shear modulus G in reconstituted biopolymer gels, adapted from Ref. [19].

While fibrous networks generally occupy relatively small volume and mass fractions, they provide biological materials with remarkable structural stability and tunable mechanical behaviors that differentiate them from typical synthetic materials [20]. One such behavior is their tendency to stiffen significantly when stretched or sheared. Fig. 1.2, adapted in part from Ref. [19], shows experimental measurements of the strain-dependent stiffness of reconstituted actin, collagen and fibrin gels. In these

materials, the stiffness (the apparent shear modulus, in this case) increases by nearly an order of magnitude or more in response to strains of less than 100%. Another striking feature of filament networks is the manner in which they deform in response to tensile stress, depicted in Figure 1.3. When such a network is uniaxially stretched enough to stiffen, it responds with dramatic internal rearrangements and changes in its macroscopic shape, coincident with similarly dramatic changes in its mechanical properties; fibers become highly aligned along the extension axis, in tandem with a significant increase in local density due to contraction along the transverse axes [21–24]. This alignment and contraction is a consequence of a fibrous material's tendency to stiffen significantly under low levels of applied extensional stress or strain, coupled with its typically very small volume fraction and relatively weak resistance to applied compression [25–28], as we discuss in Chapter 6. This behavior is especially evident in the strain observed in a region between two contractile inclusions, e.g. cells [29–31] or clusters of cells [23]. If the biopolymer of interest is fluorescently tagged, fluorescence microscopy reveals an increased network density via the increased brightness in the strained regions between cells (see Fig. 1.3d and e) [32]. This alignment effect plays an important role in cell-cell mechanosensing in the extracellular matrix [29, 31, 32], as it enables the transmission of forces over longer distances than would be possible in a conventional linear elastic medium [31].

Semiflexible polymers are distinguished from flexible polymers by their larger *persistence length* ℓ_p, a temperature-dependent quantity that describes the typical length scale over which the local orientation of a filament remains correlated in the presence of thermal fluctuations [34, 35]. While entropy drives flexible polymers into crumpled, random conformations, the increased bending resistance of semiflexible polymers prevents this crumpling while still, in many cases, remaining small enough for entropic effects to contribute significantly to their elastic properties. Many biopolymers are semiflexible, with persistence lengths that are typically significantly larger than

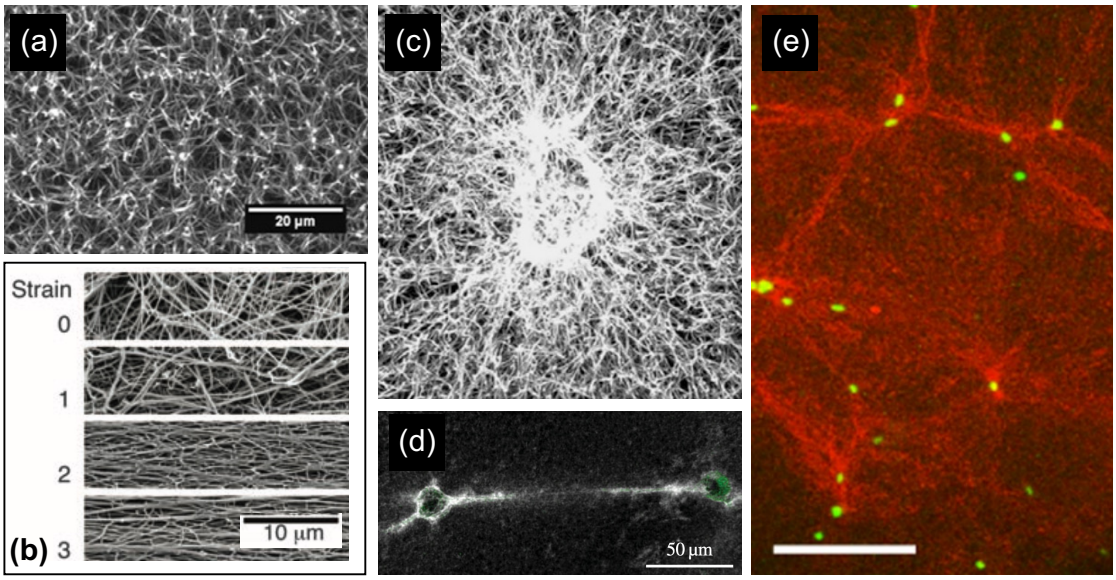

Figure 1.3: (a) An isotropic reconstituted fibrin network, from Ref. [33]. (b) Alignment of fibers along the (horizontal) axis of applied uniaxial extension in a fibrin network under strains of up to 300%, from Ref. [24]. (c) Densification and reorientation of a fibrin network, with the same concentration as in (a), by an embedded contractile cell, from Ref. [33]. Scale bar is the same as in (a). (d) Between two contractile cells (green) in a fibrin network (white), a dense and aligned "tether" of fibers forms. Image from Ref. [32]. (e) Similar strain-driven alignment and densification is seen when contractile cells (green) are embedded in collagen (red) networks. Image from Ref. [23], scale bar 200 μm.

the length scale of a single subunit (molecule or protein) and instead on the order of, or larger than, the distance between entanglements or crosslinks [36]. Even when thermal effects are negligible (as is the case for stiffer filaments, like collagen fibers [11]), thin elastic filaments necessarily exist in an intermediate regime between flexible polymers and rigid rods. With or without entropic effects, the essential behavior that these filaments share is a tendency to provide a soft bending-dominated response to small deformations that transitions to a dramatically more stiff stretching-dominated response as an applied extension straightens and elongates the filament.

Networks of semiflexible polymers display unique and materially useful mechanical behaviors including, for example, strain-stiffening [37], compression softening [38], and negative normal stress [39]. There is thus significant interest in improving our understanding of how the properties of the individual filaments and crosslinking

proteins, the network topology, and external passive and active influences such as cells and molecular motors can change both the macroscopic and microscopic viscoelastic properties of these networks. Continued work in this area will deepen our understanding of biopolymer networks and inform the design of new functional materials.

1.1.1 Theory

Most biopolymers are classified as semiflexible, meaning that their persistence length ℓ_p is long enough relative to the relevant contour length ℓ_c (for example, the typical length between crosslinks) to avoid collapsing into a random coil, yet short enough to ensure that thermally induced bending remains relevant. Thus, semiflexible polymers constitute an intermediate between flexible polymers ($\ell_p \ll \ell_c$) and rigid rods ($\ell_p \gg \ell_c$), and in contrast to both, they exhibit a nonlinear force-extension relation [20].

The standard model for semiflexible polymers is the extensible worm-like chain, which treats a polymer as a homogeneous cylindrical elastic rod of radius r with Young's modulus E. The stretching rigidity of such a rod, with units of force, is the product of its Young's modulus and cross-sectional area, $\mu = E\pi r^2$, while its bending rigidity is $\kappa = EI = E\pi r^4/4$, in which $I = \pi r^4/4$ is the cross-sectional moment of inertia of a homogeneous cylindrical rod with radius r [36]. We can write the Hamiltonian of a single filament as the sum of two integrals

$$\mathcal{H}_f = \frac{\mu}{2}\int ds \left(\frac{d\ell}{ds}\right)^2 + \frac{\kappa}{2}\int ds \left|\frac{\partial \vec{t}}{\partial s}\right|^2 \tag{1.1}$$

in which s is the arc length coordinate, $d\ell/ds$ is the relative elongational strain at coordinate s, $\vec{t}$ is the tangent vector along the fiber, and the integrals are taken over the full fiber length. This Hamiltonian describes the energy of a semiflexible polymer as a function of its conformation, allowing for the evaluation of a polymer's

force-extension relation if the Young's modulus E and filament radius r are known. Here, the (temperature-dependent) persistence length is related to the bending energy as $\ell_p = \kappa/(k_B T)$, in which k_B is Boltzmann's constant and T is the temperature.

As we are interested in the mechanics of spatially complex interconnected networks of these filaments, computer simulations are necessary. Thus, we consider discrete extensible worm-like chains [40], for which the Hamiltonian for each filament is

$$\mathcal{H}_f = \frac{\mu}{2} \sum_{ij} \frac{(\ell_{ij} - \ell_{ij,0})^2}{\ell_{ij,0}} + \frac{\kappa}{2} \sum_{ijk} \frac{(\theta_{ijk} - \theta_{ijk,0})^2}{\ell_{ijk,0}} \tag{1.2}$$

in which the sums are taken over all consecutive pairs ij and triplets ijk of nodes along the fiber length, ℓ_{ij} and $\ell_{ij,0}$ are the length and rest length between nodes i and j, θ_{ijk} and $\theta_{ijk,0}$ are the angle and rest angle between bonds ij and jk, and $\ell_{ijk,0} = (\ell_{ij,0} + \ell_{jk,0})/2$. For a network of many interconnected filaments, the full network Hamiltonian is simply the sum over all filaments, $\mathcal{H} = \sum_f \mathcal{H}_f$.

1.2 Rigidity transitions

This thesis is largely concerned with the factors that control changes in *stiffness*, a word that can refer to any of a wide variety of measures of a material's resistance to deformation. For most of the work in this thesis, we will focus on a system's resistance to shear, so the relevant stiffness is the shear modulus, G. If we apply simple shear strain γ to a material sample, as sketched in Fig. 1.2, we will generally find that it opposes this applied deformation with resistance in the form of shear stress, σ, with units of force per area. The shear modulus, plotted for various reconstituted biopolymer gels in Fig. 1.2, is simply the ratio of stress to strain, $G = \sigma/\gamma$, sharing the same units as the stress.

A conceptually simple way to adjust a substance's rigidity is to change its underlying structure. This could include, for example, changing the volume fraction of particles

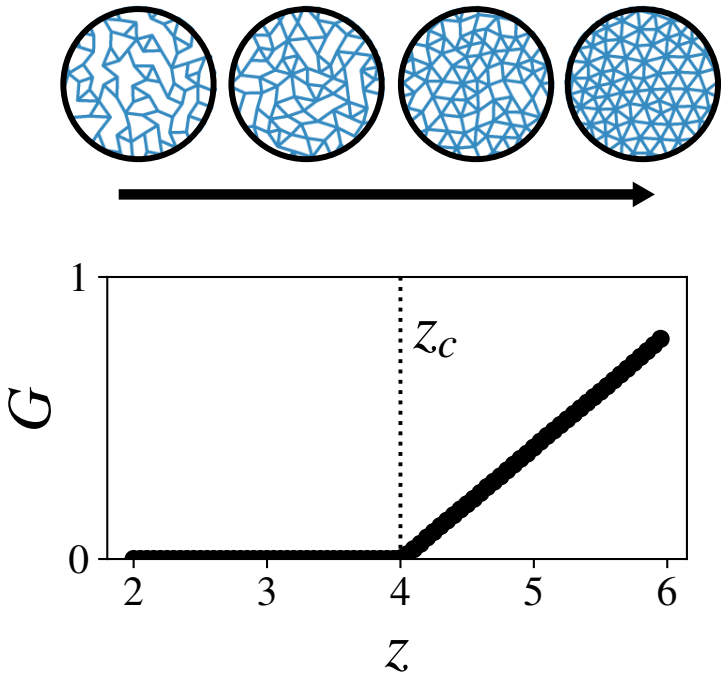

Figure 1.4: The linear shear modulus G for packing-derived spring networks with dimensionality $d = 2$ becomes nonzero when the average connectivity z exceeds the isostatic point $z_c = 2d$.

[41, 42] in granular media and colloidal suspensions, changing the volume fraction of air bubbles in a foam [43], or changing the number of springs in a random spring network [44, 45]. This sort of structural rigidity transition can be understood in view of a balance between a system's number of degrees of freedom and number of constraints (e.g. contacts between pairs of particles, connections between network nodes), as pointed out initially by Maxwell [46]. He noted that a d-dimensional frame with N nodes and average coordination number z is rigid if the N_c constraints satisfy $N_c \geq dN - d(d+1)/2$ [46]. Writing this in terms of the average number of constraints per node $z = 2N_c/N$ and letting $N \to \infty$ results in a simple rigidity criterion, $z \geq 2d$. The precise connectivity at which such a structure becomes rigid is referred to as the *isostatic point*, $z_c = 2d$. In Fig. 1.4, we plot the linear shear modulus $G = \lim_{\gamma \to 0} \sigma/\gamma$ for random spring networks as a function of the average connectivity z; networks with $z < z_c$ are referred to as *floppy*, with $G = 0$. More specifically, a floppy material is one

that can rearrange in some manner without paying an energy penalty. The small-strain mechanical properties of systems near the isostatic point become quite unusual, with power law scaling of the elastic moduli and large nonaffine fluctuations (deviation from a macroscopically homogeneous strain) that signal a diverging correlation length. In other words, in amorphous materials, the isostatic point corresponds to a phase transition between macroscopically floppy (zero stiffness) and rigid (finite stiffness) regimes. See, for example, prior work on jammed packings [47], foams [43], and random spring networks [48]. While biopolymer networks are generally structurally "subisostatic," they have nonzero shear moduli because of the additional constraints imposed by the bending rigidity of the filaments.

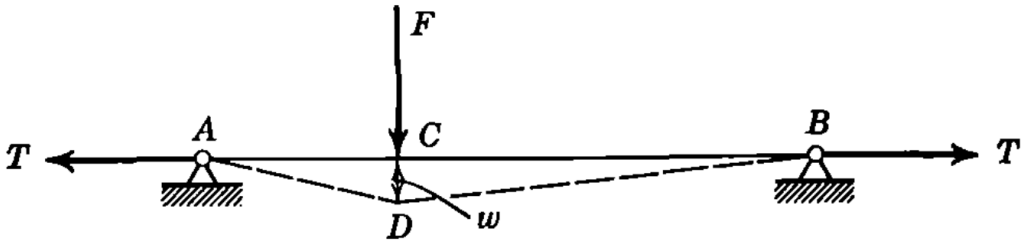

Figure 1.5: From Ref. [49]: An illustration of a string under tension T subjected to perpendicular deflection. The apparent rigidity of the string is highly sensitive to the tension exerted on its ends.

However, changes in structure are not the only way for a system to attain rigidity. Maurice Biot begins the first chapter of *Mechanics of Incremental Deformation* [49] with the statement

> *It is well known that a state of initial stress in a deformable medium induces mechanical properties which depend mainly on the magnitude of the stress and are quite distinct from those associated with the rigidity of the material itself.*

pointing out the very simple example of a string under tension, sketched in Fig. 1.5. The apparent rigidity of the string, as measured by the force F required to induce a

deflection w, is extremely sensitive to magnitude of the tension T exerted on its ends. If the tension is removed and the ends of the spring are brought together closer than the at-rest length of the string, the string appears to have no resistance to deflection. Yet, when T is finite, the string resists deflection and thus appears to have a finite stiffness.

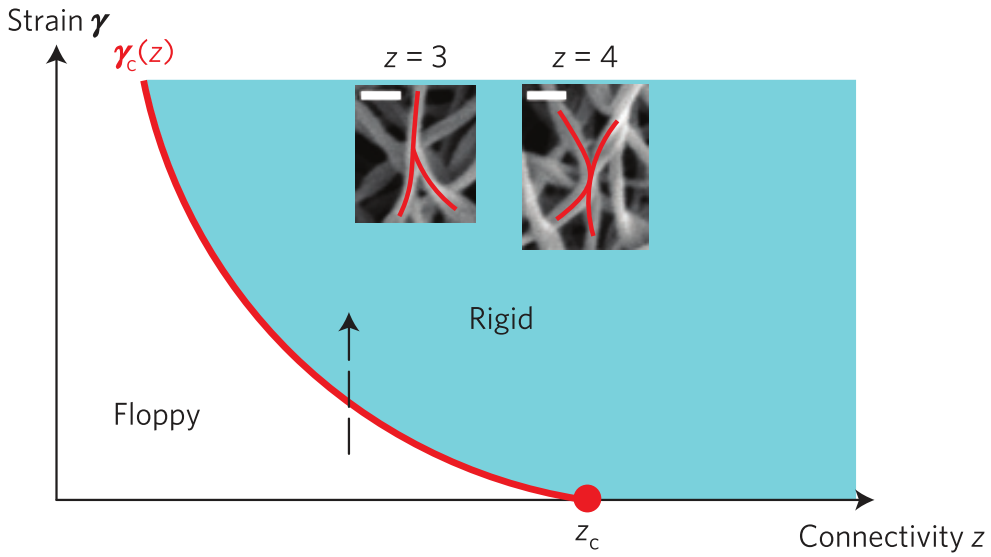

Figure 1.6: Schematic phase diagram for the strain-controlled rigidity transition, adapted from Ref. [50].

Likewise, for the random spring networks sketched in Fig. 1.4, one finds that a floppy network with $G = 0$ (i.e. $z < z_c$) can develop rigidity under an applied stress or strain. For example, as the authors of Ref. [50] depicted in the phase diagram reproduced in Fig. 1.6, so-called "subisostatic' networks develop rigidity at a critical shear strain γ_c that depends on the network's connectivity. This critical strain marks a strain-controlled transition between floppy and rigid regimes, and one observes the same sort of unusual criticality-associated properties as those observed in the isostatic case (e.g. diverging strain fluctuations and power law scaling of the elastic moduli) [50–52]. In elastic networks with stretching and bending interactions, e.g. biopolymer gels, this strain-driven rigidification corresponds to a smooth crossover between a soft,

bending-dominated regime and a stiff, stretching-dominated regime. That said, the effect is still substantial even for nonzero bending rigidity; for example, the data in Fig. 1.2 show that shearing a fibrin gel to $\gamma \approx 1$ leads to a roughly 20-fold increase in G.

1.3 Rheology

Rheology is the study of the deformation and flow of matter [53]. In general, the term refers to methods for characterizing a material's viscoelastic response to an applied deformation. This is especially important for biopolymer gels, for which the apparent viscoelastic properties can vary tremendously depending on the type and magnitude of the applied deformation as well as the time and length scales involved. Methods for measuring a material's rheological properties fall into two broad categories: *microrheology* [54–56], in which material properties are deduced from the behavior of one or more microscopic probes that are either passively observed or actively subjected to external forces induced by e.g. optical tweezers [57] or magnetic fields [58], and *macrorheology*, in which one measures a macroscopic sample's response to a stress or strain applied by a device called a rheometer. This thesis primarily discusses simulations that are analogous to macrorheology; in general, we apply macroscopic strains to a simulated bulk sample and measure the resulting stress. Two common torsional rheometer geometries, sketched in Fig. 1.7, are the cone-plate rheometer, which enables the application of a uniform simple shear strain, and the parallel plate rheometer, which applies a non-uniform shear strain but has the advantage of allowing the measurement of a sample's response to shear as a function of applied uniaxial compression or extension [53, 59, 60].

In a torsional rheometer, we apply some time-dependent shear strain $\gamma(t)$ to a sample and measure (or, stated more accurately, compute from the torque) the

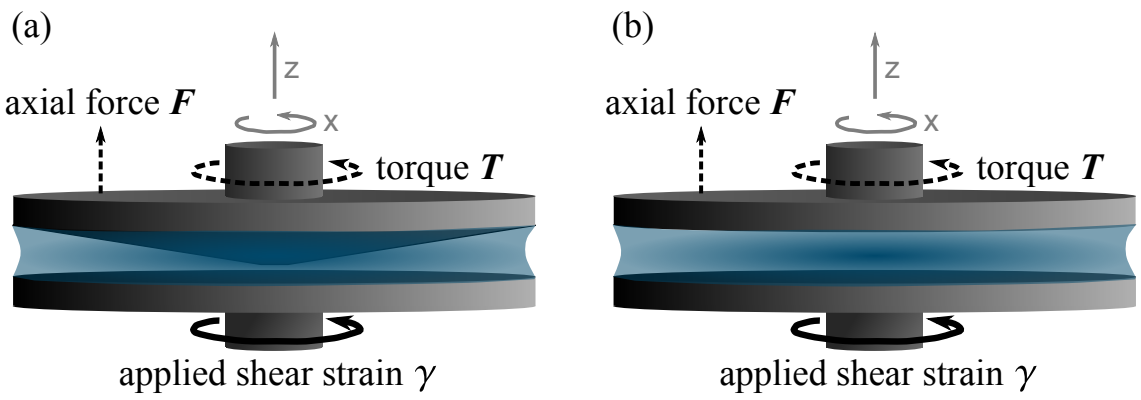

Figure 1.7: Schematic representation of (a) a cone-plate rheometer, in which the applied shear strain is uniform across the sample, and (b) a parallel plate rheometer, which applies non-uniform shear strain. Shear strain is applied by rotating the bottom plate and the corresponding axial force and torque on the top plate are measured and used for computing the normal and shear stresses.

resulting shear stress $\sigma(t)$, or vice-versa. A commonly used method for measuring a material's linear viscoelasticity is *small amplitude oscillatory shear*, in which, for a strain-controlled protocol, we apply an oscillatory strain with amplitude γ_0 and frequency ω,

$$\gamma(t) = \gamma_0 e^{i\omega t} \tag{1.3}$$

and measure the resulting shear stress,

$$\sigma(t) = \sigma_0 e^{i\omega t} = \gamma_0 G^*(\omega) e^{i\omega t} \tag{1.4}$$

Here, $G^*(\omega) = G'(\omega) + iG''(\omega)$ is the complex modulus. The real term, $G'(\omega)$, is the storage modulus, which essentially measures a material's elastic character; in the zero-frequency limit, it is equivalent to the linear shear modulus. The imaginary term, $G''(\omega)$, is the loss modulus, which describes a material's viscous or dissipative character.

To probe a material's response to larger strains, a strategy that has proven successful is the application of superimposed small amplitude oscillatory strain to pre-strained or

pre-stressed samples [37]. The principle is the same, however. For a strain-controlled protocol, we subject the sample to a prestrain γ_0, about which we apply an oscillatory change in strain

$$\delta\gamma(t) = \delta\gamma_0 e^{i\omega t} \tag{1.5}$$

and we measure the resulting change in stress,

$$\delta\sigma(t) = \delta\sigma_0 e^{i\omega t} = \delta\gamma_0 K^*(\omega) e^{i\omega t} \tag{1.6}$$

In this case, the complex differential modulus $K^*(\omega) = K'(\omega) + iK''(\omega)$ is a function of the applied prestrain. In the low-frequency limit, we recover the static differential modulus $K = \lim_{\omega\to 0} K'(\omega) = \partial\sigma/\partial\gamma$.

1.4 Outline of this thesis

This dissertation is motivated by the ubiquity of fibrous network structures and the importance of their unique properties in living systems, and focuses on three major areas of the rheology of biopolymer networks and their composites: (1) rheological phase transitions, (2) normal stresses and the nonlinear Poisson effect, and (3) compression stiffening in cells and tissues. We will utilize theoretical and computational models to explore these behaviors and learn lessons for the design of new materials with responsive, tunable properties.

Chapter 2 describes quantitative models for semiflexible polymer networks that are used elsewhere in this thesis. We first describe an analytical calculation of a gel's strain-dependent stress tensor that relies on the assumption of affine deformation. Then, we consider numerical models for disordered networks that properly account for nonaffine deformation. After describing the construction of these systems, we outline the manner in which we subject them to macroscopic strain and discuss methods for

computing the resulting stress tensor.

Chapter 3 focuses on our efforts to understand nonlinear phenomena controlled by normal stresses in biopolymer networks, extending prior work aimed at understanding the phenomenon of "negative normal stress" [39, 61]. We focus on the behavior of shear-driven normal stresses near the strain stiffening transition and explore how these are controlled by network structure, filament properties and proximity to an underlying point of marginal stability. We further describe the unusually broad force distributions that develop in these networks at the onset of rigidity.

Chapter 4 describes a theoretical and computational study of the scaling behavior of disordered networks near the onset of rigidity. We use real space renormalization in tandem with coarse-grained network simulations to characterize the strain-controlled and connectivity-controlled rigidity transitions; specifically, we develop and test relationships between the critical exponents governing the scaling of the apparent stiffness and nonaffine strain fluctuations with the distance to the critical strain. We investigate these scaling relationships further in later work (see Refs. [62] and [63]).

Chapter 5 discusses a study of the dynamics of semiflexible polymer networks embedded in a viscous medium. We find that stress relaxation in prestressed or prestrained networks in the vicinity the strain stiffening transition reflects a diverging characteristic timescale controlled by proximity to the transition. We then demonstrate that this critical slowing down is a direct consequence of the coupling between divergent nonaffine fluctuations and the dissipative interactions between the network and solvent, and we describe a simple linear relationship between the nonaffinity and effective viscosity.

Chapter 6 discusses the nonlinear Poisson effect, a surprising consequence of normal stresses that develop in disordered networks under applied extensional strain. We demonstrate that this unusual effect, which corresponds to dramatic contraction that occurs upon extension-driven stiffening, is associated with a mechanical phase

transition and, consequently, coincides with large nonaffine fluctuations and power law scaling of the various mechanical quantities, just as we observed earlier in previous chapters in systems under applied shear. We then characterize how these effects are suppressed by bending interactions and controlled by network connectivity in a variety of network structures.

Chapter 7 discusses an investigation of the cause of the unusual compression stiffening effect observed in many living tissues. We describe a physical mechanism for this effect that involves the emergence of a compression-driven, tension-stabilized regime – a cooperative effect that reflects both the strain stiffening properties of the interstitial network and the volume fraction-controlled steric interactions between the embedded particles. Using a minimal model of interconnected repulsive particles, we develop a predictive phase diagram that describes the dependence of this effect on the volume fraction of particles and the network's critical strain, which we test using simulations.

Chapter 2

Modeling fiber networks

This chapter briefly discusses the quantitative models used throughout the rest of this thesis. We first describe an analytical calculation of the stress tensor for an idealized material that is initially isotropic and that undergoes strictly affine deformation. Then, we describe methods for contructing and simulating the rheology of disordered networks with various underlying structures.

2.1 Affine isotropic network model

We first consider a simple isotropic "network" model that captures the response of a single filament to an applied deformation, averaging over all possible initial filament orientations. This model captures the mechanics of a system in which the deformation is *affine* and thus described on all scales by the deformation gradient tensor $\mathbf{\Lambda}$. This model has been used in prior work to compute the stress-strain response of an affinely-deforming isotropic network of semiflexible filaments with a proper nonlinear force-extension relation [19, 35]. For simplicity, we will consider a simple Hookean force-extension relation here. This will provide a baseline expectation for the behavior we should expect from a disordered network in an affine (e.g. very highly z or high κ) limit.

Consider a filament segment with initial orientation $\hat{\mathbf{n}}$ subjected to deformation gradient tensor $\mathbf{\Lambda}(\gamma)$. The deformation changes the filament's length and orientation, resulting in a tension $\boldsymbol{\tau}$ directed along its new orientation. Treating the filament

as a linear elastic element with stretching stiffness μ and initial length $\ell_0 = 1$, we can write the tension vector as $\boldsymbol{\tau} = \tau \boldsymbol{\Lambda}\hat{\mathbf{n}}/\left|\boldsymbol{\Lambda}\hat{\mathbf{n}}\right|$, with $\tau = \mu(|\boldsymbol{\Lambda}\hat{\mathbf{n}}| - 1)$. Taking the average, over all initial filament orientations, of the product of the i component of the tension, $\tau\Lambda_{il}n_l/\left|\boldsymbol{\Lambda}\hat{\mathbf{n}}\right|$, and the line density of filaments crossing the j plane after the deformation, $\frac{\rho}{\det\boldsymbol{\Lambda}}\Lambda_{jk}n_k$, yields the stress tensor [19, 64],

$$\sigma_{ij} = \frac{\rho}{\det\boldsymbol{\Lambda}}\left\langle \tau \frac{\Lambda_{il}n_l\Lambda_{jk}n_k}{|\boldsymbol{\Lambda}\hat{\mathbf{n}}|} \right\rangle. \tag{2.1}$$

We will consider a system under volume-preserving simple shear,

$$\boldsymbol{\Lambda}(\gamma) = \begin{pmatrix} 1 & 0 & \gamma \\ 0 & 1 & 0 \\ 0 & 0 & 1 \end{pmatrix} \tag{2.2}$$

for which $\det\boldsymbol{\Lambda} = 1$ and the transformed orientation vector is

$$\boldsymbol{\Lambda}\hat{\mathbf{n}} = \begin{pmatrix} \sin\theta\cos\varphi + \gamma\cos\theta \\ \sin\theta\sin\varphi \\ \cos\theta \end{pmatrix}. \tag{2.3}$$

Thus, for filaments in 3D with initial polar angle θ and azimuthal angle φ, the stress tensor is

$$\sigma_{ij} = \frac{\rho}{4\pi}\int_\varphi\int_\theta d\theta d\varphi \sin\theta \left[\tau\frac{\Lambda_{il}n_l\Lambda_{jk}n_k}{|\boldsymbol{\Lambda}\hat{\mathbf{n}}|}\right], \tag{2.4}$$

We compute the xz, xx, and zz components of the stress tensor for the 3D case as follows:

$$\sigma_{xz} = \frac{\rho}{4\pi}\int_\varphi\int_\theta d\theta d\varphi \sin\theta \left[\tau\frac{(\sin\theta\cos\varphi + \gamma\cos\theta)\cos\theta}{|\boldsymbol{\Lambda}\hat{\mathbf{n}}|}\right] \tag{2.5}$$

$$\sigma_{xx} = \frac{\rho}{4\pi}\int_\varphi\int_\theta d\theta d\varphi \sin\theta \left[\tau\frac{(\sin\theta\cos\varphi + \gamma\cos\theta)^2}{|\boldsymbol{\Lambda}\hat{\mathbf{n}}|}\right] \tag{2.6}$$

$$\sigma_{zz} = \frac{\rho}{4\pi} \int_{\varphi} \int_{\theta} d\theta d\varphi \sin\theta \left[\tau \frac{\cos^2\theta}{|\mathbf{\Lambda}\hat{\mathbf{n}}|} \right] \tag{2.7}$$

The integrals are taken over the ranges $0 \leq \theta \leq 2\pi$ and $0 \leq \varphi \leq \pi$.

We repeat the same process for the 2D case, in which the deformation tensor for simple shear is

$$\mathbf{\Lambda}(\gamma) = \begin{pmatrix} 1 & \gamma \\ 0 & 1 \end{pmatrix} \tag{2.8}$$

and the transformed orientation vector is

$$\mathbf{\Lambda}\hat{\mathbf{n}} = \begin{pmatrix} \cos\theta + \gamma \sin\theta \\ \sin\theta \end{pmatrix}. \tag{2.9}$$

The resulting components of the 2D stress tensor are calculated as follows:

$$\sigma_{xz} = \frac{\rho}{2\pi} \int_{\theta} d\theta \left[\tau \frac{(\cos\theta + \gamma \sin\theta)\sin\theta}{|\mathbf{\Lambda}\hat{\mathbf{n}}|} \right] \tag{2.10}$$

$$\sigma_{xx} = \frac{\rho}{2\pi} \int_{\theta} d\theta \left[\tau \frac{(\cos\theta + \gamma \sin\theta)^2}{|\mathbf{\Lambda}\hat{\mathbf{n}}|} \right] \tag{2.11}$$

$$\sigma_{zz} = \frac{\rho}{2\pi} \int_{\theta} d\theta \left[\tau \frac{\sin^2\theta}{|\mathbf{\Lambda}\hat{\mathbf{n}}|} \right] \tag{2.12}$$

The components of the stress tensors for the 2D and 3D cases are shown in Fig. 2.1a. At low strains, $\sigma_{xz} \sim \gamma$ and $\sigma_{xx} \sim \sigma_{zz} \sim \gamma^2$. At larger strains (above $\gamma \approx 1$), σ_{zz} approaches a constant value, while σ_{xz} and σ_{xx} both "stiffen" due to filament reorientation before again growing as $\sigma_{xz} \sim \gamma$ and $\sigma_{xx} \sim \gamma^2$. The effect of this reorientation in stiffening the network is more apparent in the differential shear modulus, $K = \partial\sigma_{xz}/\partial\gamma$, shown in Fig. 2.1b. The large upper limit of γ in Fig. 2.1 is used simply to highlight the scaling of the stress tensor components at large strains.

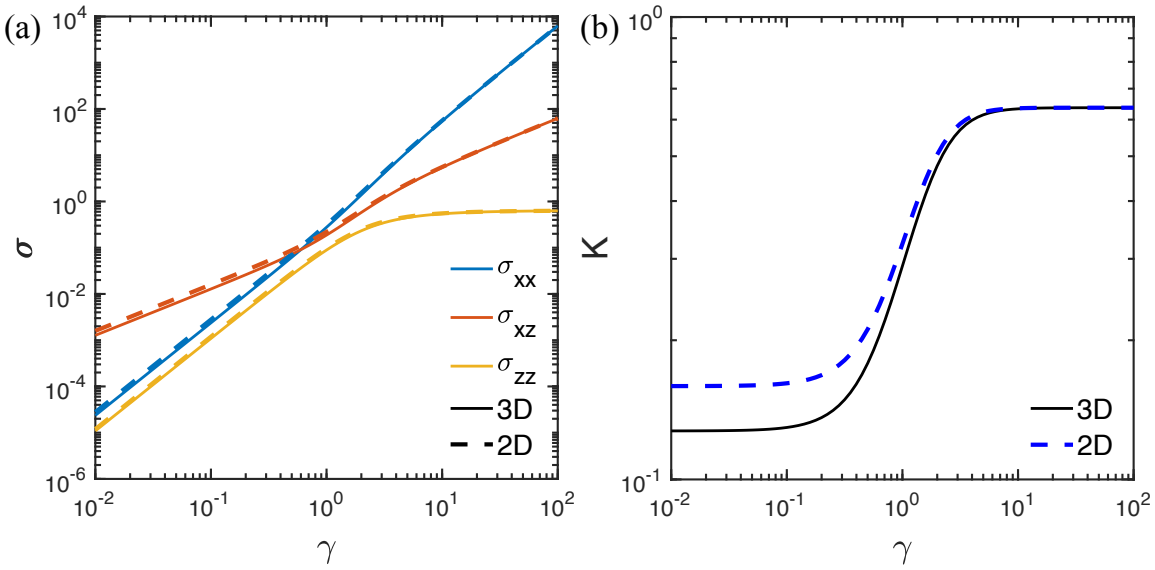

Figure 2.1: (a) Selected components of the stress tensor $\boldsymbol{\sigma}$ for the 2D and 3D isotropic network models. For this data, the line density is the inverse of the area (volume) of a circle (sphere) of diameter $\ell_0 = 1$, $\rho_{2D} = 4/\pi$ and $\rho_{3D} = 6/\pi$. (b) The differential shear modulus K stiffens due to reorientation of the initially isotropically distributed springs.

2.2 Disordered network models

While the affine isotropic network model is a useful limit to consider, it ignores the obviously important contributions of orientational disorder and nonaffine rearrangement. To more accurately capture the mechanics of actual semiflexible polymer networks, we turn to simulations of disordered networks.

2.2.1 Lattice-based networks

The mechanical properties of disordered elastic networks have long been studied via lattice-based models [65, 66], including the two-dimensional square [67], triangular [48, 65], Kagome [68, 69], and honeycomb [51] lattices, as well as the three-dimensional diamond [70, 71], face-centered cubic [48, 50], and 3D-kagome [72] lattices. Some of these have strange, singular mechanical properties originating from their regular structure; for example, the square, cubic and regular honeycomb lattices exhibit a differential shear modulus with quadratic dependence on the strain, $K \sim \gamma^2$, in the low-

strain limit and thus have no linear modulus G without the addition of bond-bending interactions.

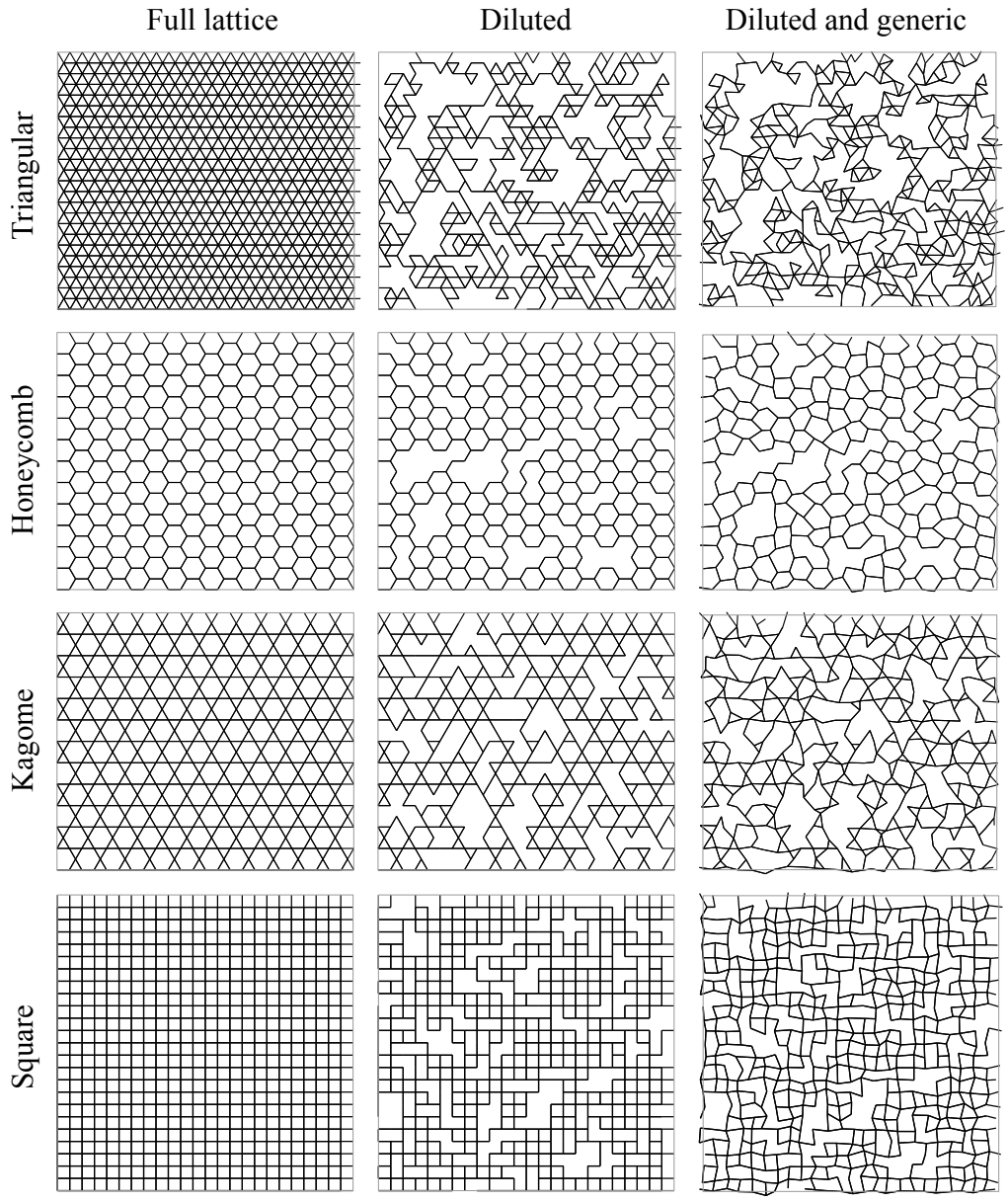

Figure 2.2: (a) Examples of various periodic lattice structures. We begin with regular lattices (left column), from which we generate disordered *diluted* networks (center column) by randomly cutting bonds until the desired coordination number z is reached ($z = 3.3$ here for the diluted triangular, Kagome and square networks, and $z = 2.8$ for the diluted honeycomb network). We can further introduce disorder and mitigate lattice effects by displacing each node from its initial location on the lattice – in this case, we do so by a random distance $d \in [0, \delta_{\max}/2]$ in a random direction – resulting in a so-called generic diluted network (right column) [44]. The networks shown in the right column have $\delta_{\max} = 0.7$. For all diluted networks shown here, dangling ends and dangling clusters have been removed.

We construct triangular networks by first placing system-spanning fibers on a periodic triangular lattice and then adding a freely-rotating crosslink at each intersection. Where fibers cross the boundaries, they reconnect with themselves. After the crosslinks are added, each node in the network has a connectivity of 6, and the inter-crosslink distance is the same as the lattice spacing, l_0. To ensure that no fiber is system-spanning, we then cut a single randomly chosen bond on each fiber. Since the macroscopic coordination number $z = 6$ of the initial triangular lattice is greater than the two-dimensional isostatic coordination $z_c = 4$, generating subisostatic networks requires removing additional bonds in a process known as dilution, in which we randomly cut bonds until the desired z is reached. Alternatively, we can reduce the local coordination number of the triangular lattice to $z = 4$ by turning it into a "phantom" triangular lattice [48, 73], which involves instead adding a crosslink only between two of the three fibers, chosen randomly, at each intersection.

The honeycomb lattice is a sublattice of the triangular lattice with maximum connectivity $z = 3$. As we mentioned before, the regular honeycomb lattice is anomalous, in that without bending interactions it has no linear shear modulus. However, with bending interactions it is a reasonable model for branched networks; moreover, the undiluted lattice can be made to behave as a diluted lattice, with a tunable critical strain, by randomly distorting the node locations [51]. The face-centered cubic (FCC) and phantom FCC lattices are generated using the same method as the triangular and phantom triangular lattices, in 3D, as in prior work [36]. The essential differences are that the undiluted FCC lattice has local connectivity of $z = 12$, whereas the isostatic connectivity in 3D is $z_c = 6$. Phantom FCC lattice generation requires randomly crosslinking 3 pairs of fibers at each intersection, resulting in a connectivity of $z = 4$.

Upon straining an undistorted network (one with long fibers that are perfectly straight at zero strain), one will typically observe an initial low-strain softening of

the shear modulus K [74] associated with the buckling of the long fibers. This effect becomes quite significant in networks with high mean connectivity. In order to mitigate this effect, after generating each network we can distort each node by a random distance of magnitude $\delta_{max}/2$ in a random direction, resulting in a *generic* network [44], and subsequently redefine the network's rest lengths and rest angles. Figure 2.3 shows the buckling-related softening effect and its mitigation in triangular networks.

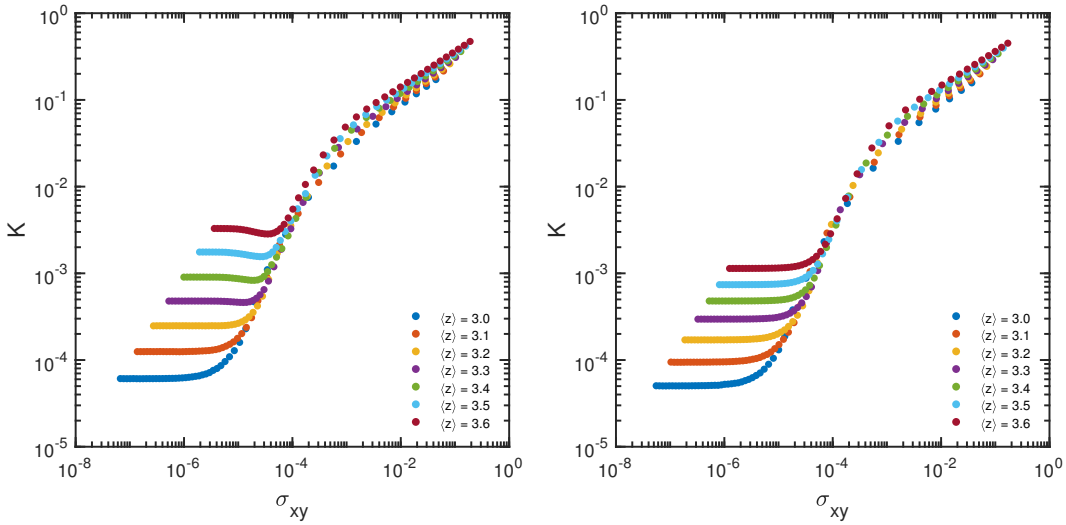

Figure 2.3: Left: K vs. σ_{xy} for undistorted phantom triangular networks at various connectivities with $\kappa = 10^{-4}$ and network size $W = 60$. The dip in K due to buckling is apparent for networks with higher $\langle z \rangle$, and hence longer fibers. Right: K vs. σ_{xy} for the same networks with $\delta_{max} = 0.6$.

Lattice-based networks are more simple to implement computationally than off-lattice network structures and, due to the uniform lattice spacing l_0, are quite numerically stable. This means that the energy landscape is relatively easy to traverse during energy minimization, in comparison to networks with significant bond-length heterogeneity. However, an important disadvantage of lattice-based networks is that even with the addition of topological and/or positional disorder, they by definition do not have isotropic angular distributions. For example, the regular triangular lattice only has bonds oriented at 0°, 60°, and 120° with respect to the horizontal. Particularly at low strains, these biased angular distributions can lead to unusual behavior of the normal stresses, as we will see in Chapter 3.

2.2.2 Mikado networks

The Mikado network is a conceptually simple, orientationally isotropic (in the limit of large systems) disordered network model that has been used extensively to study the mechanical behavior of semiflexible polymer networks [40, 52, 75–77]. The model's name derives from the game *Mikado*, also known as pick-up sticks, for which the setup involves randomly dropping sticks onto the ground to form a disordered pile. Generation of a Mikado network involves essentially the same process: rods of length ℓ_r are placed with a random orientation in a random location within periodic box of side length L. Where two rods intersect, a crosslink is added. Bending interactions are considered along the fibers and stretching interactions are considered between pairs of crosslinks. The relevant length scales in these networks are the average inter-crosslink distance l_c and the box size L.

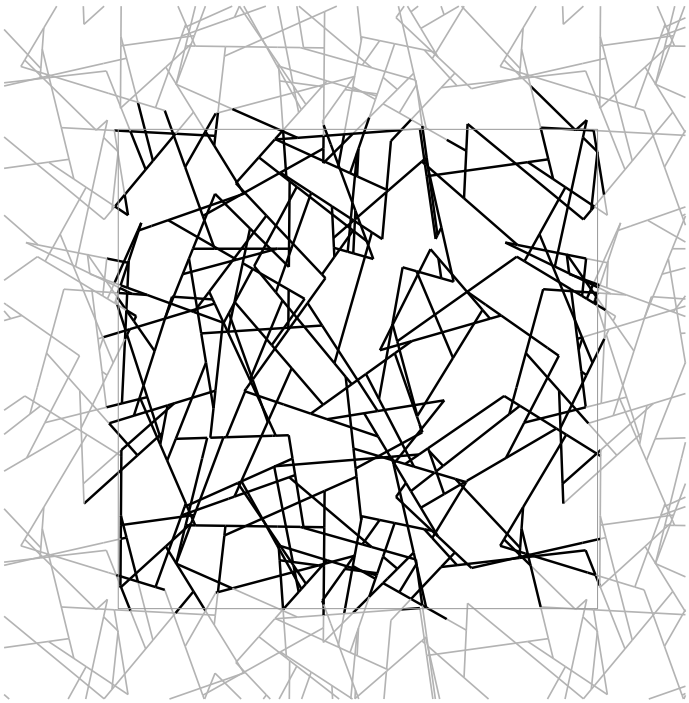

Figure 2.4: A small Mikado network with dangling ends removed.

Benefits of Mikado networks include the approximate angular isotropy (in the limit of large systems) and the convenient fact that they are always subisostatic,

since the average connectivity is necessarily always less than $z_c = 4$. However, a major computational disadvantage of Mikado networks is that small inter-crosslink distances, which occur often due to the random nature of the fiber deposition, can make simulating large Mikado networks with bending interactions very difficult due to slow energy minimization.

2.2.3 Jammed packing-derived networks

Structures derived from jammed disk or sphere packings are a useful alternative to Mikado networks and have been used quite extensively in the study of disordered elastic networks [78–80]. These avoid the numerical instability caused by short segments and maintain angular isotropy in the large-system limit. To generate jammed packings of soft disks, we first specify $N = L^2$ positions, in a box of side length L, that will correspond to the centers of the soft disks. Half of the disks have radius r_0 and half have radius $r_0 f$, in which f is some ratio specified to avoid crystallization associated with monodisperse radii (see Fig. 2.5b). A commonly used value is $f = 1.4$ [81, 82], which produces a packing with no macroscopic order (see Fig. 2.5a). After seeding initial locations, the radii of the disks are incrementally increased from $r_0 = 0$ in small steps. Overlapping disks interact via a simple one-sided (repulsive) spring potential, such that the energy between disks i and j, with radii r_i and r_j, respectively, is

$$U_{ij} = \begin{cases} \frac{\mu_d}{2}\left(r_i + r_j - r_{ij}\right)^2 & \text{if } r_{ij} \leq r_i + r_j \\ 0 & \text{if } r_{ij} > r_i + r_j \end{cases} \tag{2.13}$$

in which μ_d is the disk spring constant and r_{ij} is the distance between disks i and j. The total energy of the system is simply the sum of all inter-disk interaction potentials, $U_{tot} = \frac{1}{2}\sum_i \sum_{j \neq i} U_{ij}$, where the factor of $1/2$ accounts for double-counting. The energy is relaxed after each growth step using the FIRE algorithm [83], until the

contact network (the network of overlapping spheres) of the mechanically equilibrated structure has the desired connectivity. A few resulting structures are shown in Fig. 2.5.

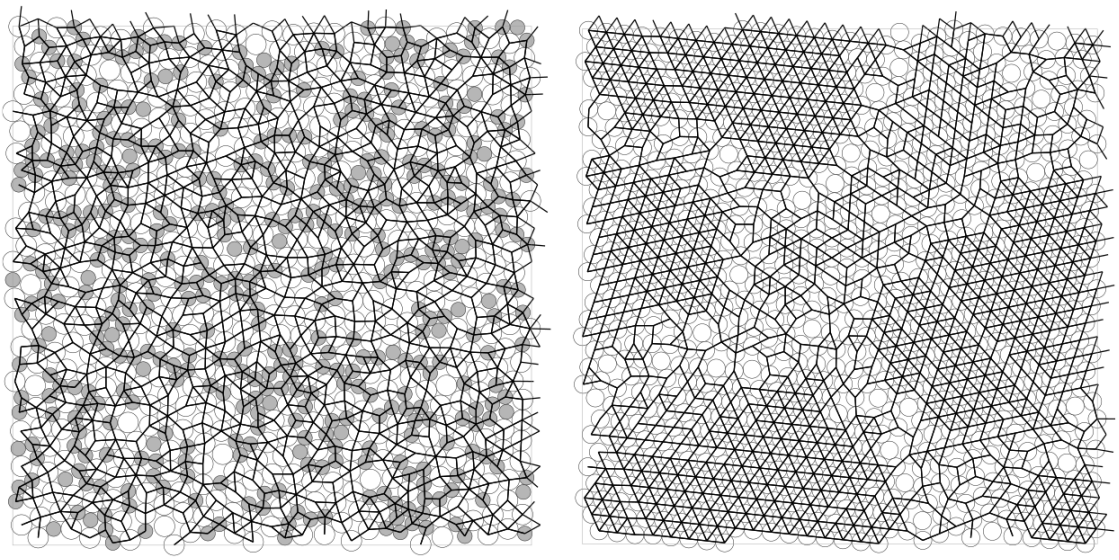

Figure 2.5: Jammed packings of 900 soft disks with $z \approx 4$ generated using the compression protocol. Packings of bidisperse disks with ratio of radii $1{:}\,1.4$ (left) yield a highly disordered contact network (shown by the black lines, and excluding rattlers), whereas radially monodisperse packings (right) exhibits large subsections with crystalline order.

After generating an initial isostatic or superisostatic contact network, we dilute the network to a subisostatic connectivity by randomly removing bonds. We also remove dangling ends and dangling clusters during the dilution process (see Fig. 2.7), so that all bonds contributing to the reported connectivity of the final network contribute to its mechanical response under applied strain. We include stretching interactions between network nodes, as well as bond-bending interactions between each bond and all of its nearest neighbors. Note that the contact network is drawn only between intersecting disks, such that "rattlers," disks that move freely and do not contribute to the packing's finite energy, are not included.

These networks constitute a simple alternative to lattice-based networks that is positionally disordered, numerically stable and easily extended to three dimensions (see Fig. 2.6). We make use of three-dimensional packing-derived networks in Chapters

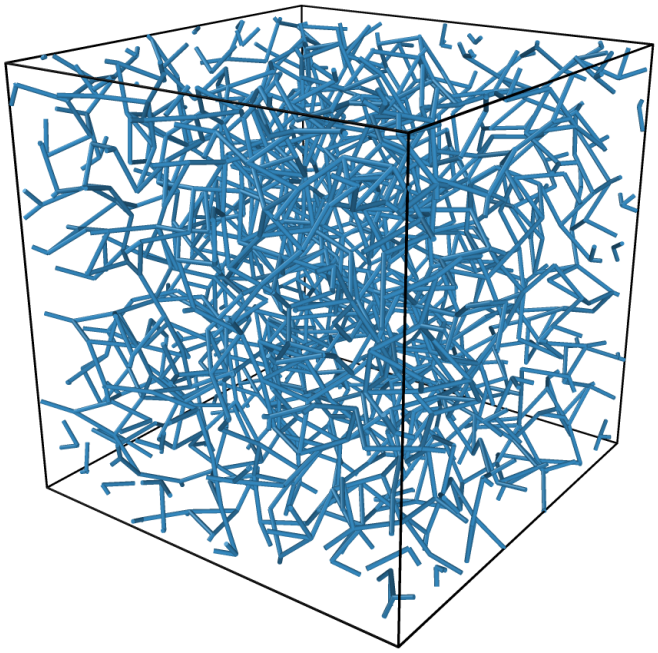

Figure 2.6: A small three-dimensional packing-derived network with average connectivity $z = 3$.

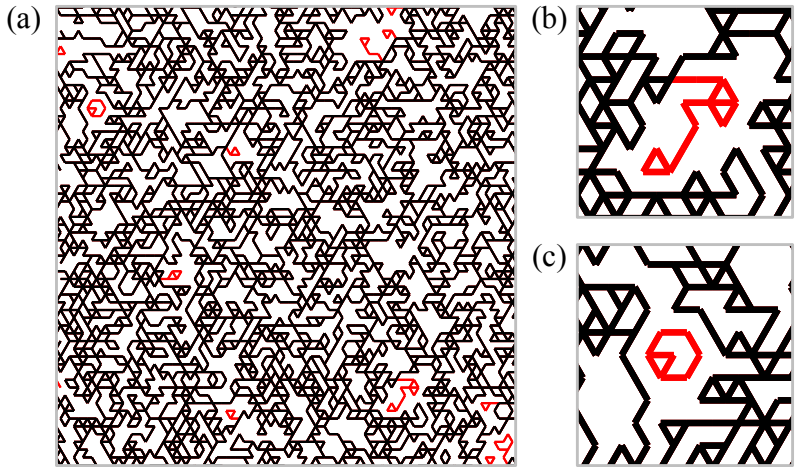

Figure 2.7: (a) Image of a network with dangling and disconnected clusters shown in red. (b) A dangling cluster (red) is defined as a cluster of bonds connected to the rest of the network by only one bond. These are detected and removed by removing "bridges," bonds which, if cut, disconnect the graph. Bridges are identified as biconnected components containing only one bond. (c) We remove disconnected clusters (red) by identifying all independent connected components and retaining only the largest one. The Boost graph library [84] is utilized for identification of connected and biconnected components.

3, 6, 5 and 7.

2.2.4 Generalized Lees-Edwards boundary conditions

A typical rheological simulation involves applying a macroscopic strain and measuring the resulting macroscopic stresses. In an experiment, this would be done by placing a sample of the substance of interest in a rheometer and imposing macroscopic strain by moving one or more of the sample boundaries (with the details depending on the geometry of the rheometer). In order to measure bulk properties of the material, the experimental geometry must be large enough safely ignore edge effects. In simulations, achieving this limit can be difficult due to computational limitations, so periodic boundary conditions are often used. Since periodic boundary conditions remove edges, macroscopic strain cannot be applied the conventional way, i.e. by applying a stress along one of the edges. Instead, we apply macroscopic strain by transforming the lattice vectors that define the spatial relationships between adjacent images of the periodic network. The resulting modified boundary conditions are known as Lees-Edwards boundary conditions [85] (usually used in the application of simple shear), which allow us to apply an arbitrary deformation gradient tensor to a periodic system.

With typical Lees-Edwards boundary conditions, and assuming for the sake of simplicity that the periodic box is an unrotated rectangle, the locations of all the periodic images of each node are defined by multiples of two orthogonal vectors, $\vec{u}$ and $\vec{v}$. Let $\vec{u}$ be the vector connecting a node to its image on the right, such that $-\vec{u}$ connects it to its image on the left, and $\vec{v}$ and $-\vec{v}$ connect it to its upper and lower images (the actual orientation of the rectangle relative to the horizontal depends on the initial rotation of the system). For typical, unrotated systems with stationary boundary conditions, $\vec{u}$ and $\vec{v}$ simply correspond to the horizontal and vertical dimensions of the system. With Lees-Edwards boundary conditions, macroscopic strain is applied by transforming the boundary vectors according to the deformation gradient tensor.

Let the initial boundary vectors be $\vec{u}_0$ and $\vec{v}_0$. To apply strain to a system that

has been rotated by angle θ, we apply the same rotation by θ to the boundary vectors using the rotation matrix,

$$R = \begin{pmatrix} \cos\theta & -\sin\theta \\ \sin\theta & \cos\theta \end{pmatrix} \tag{2.14}$$

Applying the deformation gradient tensor Λ then involves just changing the boundary vectors, $\vec{u} = \Lambda R\vec{u}_0$ and $\vec{v} = \Lambda R\vec{v}_0$. For simple shear γ with $\theta = 0$, we have the typical Lees-Edwards boundary conditions, i.e. $\vec{u} = (L_x + L_y\gamma)\hat{x} + 0\hat{y}$ and $\vec{v} = 0\hat{x} + L_y\hat{y}$.

To probe a system under quasistatic strain, we apply an incremental affine (homogeneous) shear strain step to all of the nodes, after which the system's energy is relaxed with the generalized Lees-Edwards boundary conditions enforced. After this relaxation, the properties of the energy-minimized system (e.g. its stress tensor) are computed.

2.2.5 Computing the stress tensor

Here, we will discuss two equivalent methods for computing the stress tensor for a system under quasistatic conditions: calculation using the principle of virtual work and calculation of the virial stress tensor. According to the principle of virtual work, the variation in the system's energy $\delta\mathcal{H}$ due to an infinitesimal applied strain $\delta\gamma$ can be expressed as $\delta\mathcal{H} = V\sigma_{xz}\delta\gamma$, such that we can express the shear stress as

$$\sigma_{xz}(\gamma) = \frac{1}{V}\frac{\partial\mathcal{H}(\gamma)}{\partial\gamma} = \lim_{\delta\gamma\to 0}\frac{1}{V}\frac{\mathcal{H}(\gamma+\delta\gamma) - \mathcal{H}(\gamma)}{\delta\gamma} \tag{2.15}$$

Thus, for a system at shear strain γ, we can apply a small shear strain increment $\delta\gamma$ and measure the change in energy of the system $\delta\mathcal{H} = \mathcal{H}(\gamma+\delta\gamma)$ to estimate $\sigma_{xz}(\gamma)$ numerically. It is important to note that $\mathcal{H}(\gamma)$ is the energy of the system *after energy minimization* at the imposed strain γ. In practice, we can apply incremental shear strain steps to the system over some strain range, relaxing the energy at each strain

in order to determine $\mathcal{H}(\gamma)$, and subsequently compute the numerical derivative of the $\partial\mathcal{H}(\gamma)/\partial\gamma$ curve to determine $\sigma_{xz}(\gamma)$. We can likewise apply the virtual work principle to determine the normal stresses as a function of shear strain. After relaxing the system at some shear strain γ, we apply small uniaxial strains $\delta\varepsilon_x$ and $\delta\varepsilon_z$ in order to determine the normal stresses σ_{xx} and σ_{zz}:

$$\sigma_{xx}(\gamma) = \frac{1}{V}\frac{\partial\mathcal{H}(\gamma)}{\partial\varepsilon_x} = \lim_{\delta\varepsilon_x\to 0}\frac{1}{V}\frac{\mathcal{H}(\gamma,\delta\varepsilon_x)-\mathcal{H}(\gamma,0)}{\delta\varepsilon_x} \tag{2.16}$$

$$\sigma_{zz}(\gamma) = \frac{1}{V}\frac{\partial\mathcal{H}(\gamma)}{\partial\varepsilon_z} = \lim_{\delta\varepsilon_z\to 0}\frac{1}{V}\frac{\mathcal{H}(\gamma,\delta\varepsilon_z)-\mathcal{H}(\gamma,0)}{\delta\varepsilon_z} \tag{2.17}$$

Note that, when using this method, the applied strain increment must be small enough to yield an accurate numerical derivative but large enough to avoid errors due to the tolerance used in the energy minimization. The main disadvantage of the virtual work method is that it requires a numerical derivative of $\mathcal{H}$ in order to calculate any of the stresses. Even worse, computing $K = \partial\sigma_{xz}/\partial\gamma$ requires two numerical derivatives. As a result, this method can lead to a significant noise in the calculation of K.

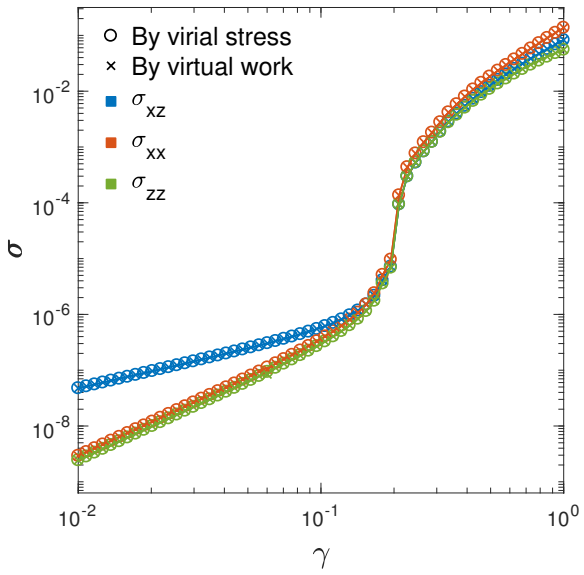

Figure 2.8: The various components of the 2D stress tensor computed via the virtual work method and the virial stress tensor calculation are equivalent These data correspond to a triangular lattice-based network with $W = 40$, $z = 3.4$, and $\kappa = 10^{-6}$.

We can instead compute the *virial stress tensor* to avoid taking a numerical derivative. Here we briefly derive the expression for the virial stress tensor following the argument of Doi and Edwards in Ref. [86]. Considering an arbitrary plane intersecting the network at position h perpendicular to the β-axis, the $\alpha\beta$-stress component on this plane, $\sigma_{\alpha\beta}(h)$, is defined as the α component of the force $F_\alpha(h)$ exerted by the network above the plane onto the network below the plane, normalized by area A of the network intersected by the plane. Thus, we can compute the macroscopic stress component $\sigma_{\alpha,\beta}$ by averaging $\sigma_{\alpha,\beta}(h)$ over the full length of the network along the β-axis, which we denote L:

$$\sigma_{\alpha,\beta} = \langle \sigma_{\alpha,\beta}(h) \rangle_h = \langle F_\alpha(h) \rangle_h / A \tag{2.18}$$

$$\sigma_{\alpha\beta} = \frac{1}{AL} \int_0^L dh F_\alpha(h) \tag{2.19}$$

Noting that $V = AL$,

$$\sigma_{\alpha\beta} = \frac{1}{V} \int_0^L dh F_\alpha(h) \tag{2.20}$$

Ignoring solvent effects, we can define $F_\alpha(h)$ in terms of the α component of the force $\vec{f_{ij}}$ exerted by node j on node i, yielding

$$F_\alpha(h) = \sum_{i,j} f_{ij\alpha} \Gamma(h - r_{i\beta}) \Gamma(r_{j\beta} - h) \tag{2.21}$$

in which

$$\Gamma(\eta) = \begin{cases} 1 & \text{for } \eta > 0 \\ 0 & \text{for } \eta < 0 \end{cases} \tag{2.22}$$

and $r_{k\beta}$ is the β component of the position vector of node k, $\vec{r}_k$. Inserting the definition

for $F_\alpha(h)$ into Eq. 2.20, we find

$$\sigma_{\alpha\beta} = \frac{1}{V}\sum_{i,j} f_{ij\alpha}\int_0^L dh\Gamma(h - r_{i\beta})\Gamma(r_{j\beta} - h) \tag{2.23}$$

$$\sigma_{\alpha\beta} = \frac{1}{V}\sum_{i,j} f_{ij\alpha}(r_{j\beta} - r_{i\beta})\Gamma(r_{j\beta} - r_{i\beta}) \tag{2.24}$$

$$\sigma_{\alpha\beta} = \frac{1}{V}\left(-\frac{1}{2}\sum_{i,j} f_{ij\alpha}(r_{i\beta} - r_{j\beta})\right) \tag{2.25}$$

$$\sigma_{\alpha\beta} = \frac{1}{2V}\sum_{ij} f_{ij\alpha}\left(r_{j\beta} - r_{i\beta}\right) \tag{2.26}$$

This yields the viral stress tensor,

$$\sigma_{\alpha\beta} = \frac{1}{2V}\sum_{ij} f_{ij\alpha} r_{ij\beta} \tag{2.27}$$

Here, $\vec{r}_{ij} = \vec{r}_j - \vec{r}_i$ is the vector between nodes i and j, and $\vec{f}_{ij}$ is the force acting on node i due to its interaction with node j. Note that the factor of $1/2$ is included to correct for double counting in the summation. Using this expression, we can compute all components of the stress tensor using only the node locations and forces between nodes as inputs. While this method offers a computationally cheaper and slightly more accurate alternative to the virtual work method, we find that both are suitable for our simple simulations (see Fig. 2.8).

Chapter 3

Normal stress anisotropy and marginal stability in athermal elastic networks

This chapter is adapted from Ref. [87]:

> **Jordan L. Shivers**, Jingchen Feng, Abhinav Sharma, and Fred C. MacKintosh. Normal stress anisotropy and marginal stability in athermal elastic networks. ***Soft Matter***, 15 (7): 1666–1675, 2019.

3.1 Abstract

Hydrogels of semiflexible biopolymers such as collagen have been shown to contract axially under shear strain, in contrast to the axial dilation observed for most elastic materials. Recent work has shown that this behavior can be understood in terms of the porous, two-component nature and consequent time-dependent compressibility of hydrogels. The apparent normal stress measured by a torsional rheometer reflects only the tensile contribution of the axial component σ_{zz} on long (compressible) timescales, crossing over to the first normal stress difference, $N_1 = \sigma_{xx} - \sigma_{zz}$ at short (incompressible) times. While the behavior of N_1 is well understood for isotropic viscoelastic materials undergoing affine shear deformation, biopolymer networks are often anisotropic and deform nonaffinely. Here, we numerically study the normal stresses that arise under shear in subisostatic, athermal semiflexible polymer networks. We show that such systems exhibit strong deviations from affine behavior and that

these anomalies are controlled by a rigidity transition as a function of strain.

3.2 Introduction

Normal solids and liquids exhibit shear stress under imposed shear deformation. With the exception of simple Newtonian liquids, most materials also develop so-called normal stresses in response to shear. Unlike shear stress, however, these stresses are directed perpendicular to surface on which they act and appear as diagonal terms in the stress tensor. In the case of elastic solids, a common manifestation of normal stress is the Poynting effect, in which a solid tends to elongate in response to torsional strain. In a classic series of experiments, Poynting observed such elongation for a variety of systems, ranging from simple metal wires to rubber [88, 89]. By symmetry, this elongation should not depend on the sign or direction of the applied torsion, leading to lowest-order response that is expected to be quadratic in the the strain. This makes the Poynting effect a fundamentally nonlinear phenomenon. This is one reason why normal stresses are typically less apparent than the shear stress, which varies linearly with strain. Nevertheless, normal stresses have very dramatic consequences, including both rod climbing and tubeless siphoning, as well as die swell [90]. These phenomena, as well as the Poynting effect, correspond to positive normal stress.

In a cone-plate rheometer, shown schematically in Fig. 3.1a, the measured axial force F in torsion depends not only on the tensile axial stress component σ_{zz}, but also on the azimuthal component σ_{xx}, which acts as a hoop stress. For incompressible materials, this hoop stress generates a radial pressure gradient that contributes vertical thrust that counteracts σ_{zz}. In this case, the sign of the first normal stress difference, $N_1 = \sigma_{xx} - \sigma_{zz}$ determines the sign of the measured axial force for sheared incompressible materials, according to $F = N_1 \pi R^2/2$. The first normal stress difference, N_1, is fundamental to the nonlinear viscoelastic response of materials and is almost

universally positive, particularly for solids. For typical polymer networks, positive N_1 results from the fact that polymer extension in the azimuthal direction tends to be greater than in the axial direction [91]. It was thus surprising when biopolymer gels, such as fibrin and collagen, were recently identified as apparent exceptions to this, with an inverted or negative Poynting effect [39, 92]. Theory and simulation studies [39, 76, 92–97] have shown that this observed negative normal stress is a generic feature of semiflexible networks, playing a significant role in the onset of the nonlinear strain-stiffening response characteristic of biopolymer networks [95, 97, 98]. However, as recently demonstrated [61, 99], this anomaly for gels can be understood to arise from their porous, two-component nature. This porosity renders the gels effectively compressible on long enough time scales, over which the radial pressure gradient relaxes as the solvent flows from the sample boundaries, such that only the negative contribution from σ_{zz} is measured, with $F = -\sigma_{zz}\pi R^2$ [61, 99]. Consistent with this interpretation, these networks showed a normal (positive) Poynting effect on short enough time scales, in which the gels become effectively incompressible, indicating that the normal stress difference N_1 remains positive.

For isotropic viscoelastic materials undergoing affine (homogeneous) simple shear deformation, the Lodge-Meissner relation relates N_1 to the shear stress σ_{xz} as $N_1 = \sigma_{xz}\gamma$ [91]. This relation, first identified by Rivlin for elastic solids [100], holds for any material in which the principal strain axes and principal stress axes remain parallel throughout the applied deformation, which is satisfied as long as the material is initially isotropic and deforms affinely [101]. Prior work has shown that networks of athermal fibers, of which collagen is a prime example, undergo highly nonaffine deformation under imposed shear strain. In such networks, it was recently shown that the degree of nonaffinity depends on the system's proximity to a strain-controlled transition that occurs along a critical line in the γ-z plane, where γ is the applied shear strain and z is the connectivity, or average number of connections to each network junction [50].

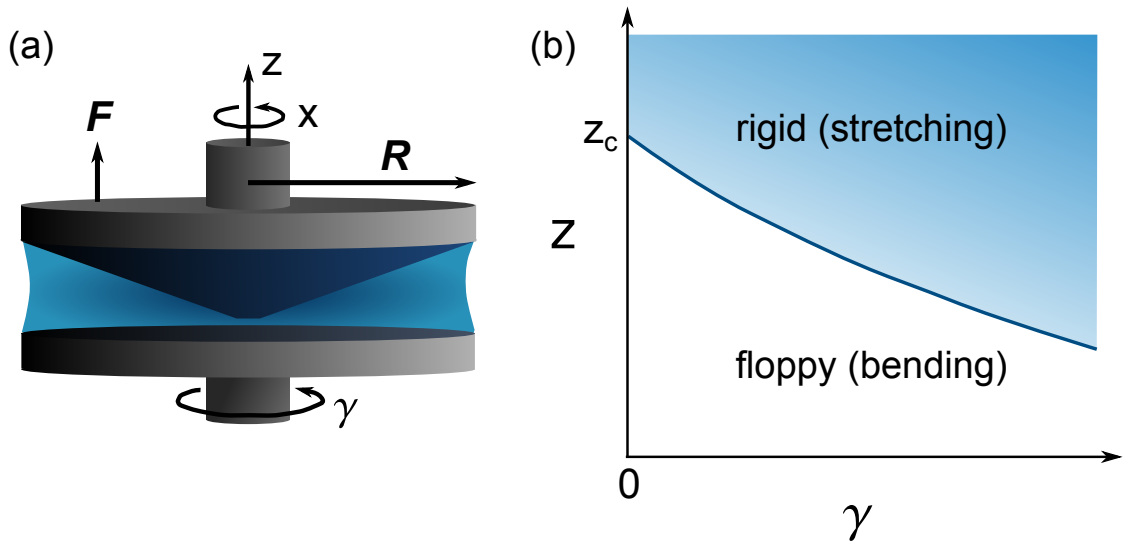

Figure 3.1: (a) Schematic of a hydrogel sample in a cone-plate rheometer of radius R, with coordinates defined such that the x-axis and z-axis are oriented along the azimuthal (shear) and axial (gradient) directions, respectively. Positive axial force F corresponds to the sample pushing up against the cone. (b) Applying sufficient shear strain γ to a subisostatic ($z < z_c$) network invokes a transition from a bending-dominated regime (floppy in the absence of bending interactions) below γ_c to a stretching-dominated regime above γ_c. The details of the phase boundary $\gamma_c(z)$ (blue line) depend on the network structure.

Strictly speaking, this transition occurs at finite strain for central-force networks below their isostatic point of (linear) marginal stability, as sketched in Fig. 3.1b. For fibers with finite bending rigidity, this line of marginal stability is manifest in a crossover from a soft, bending-dominated regime to a stiff, stretching-dominated regime. This nonlinear stiffening transition coincides with the development of a highly heterogeneous and anisotropic network of tensile force chains aligned primarily along the tension axis, similar to the marginally stable networks of compressive force chains that develop at the jamming transition in sheared granular packings [102, 103] and frictional force chains in shear-thickening suspensions [104, 105], both of which align instead along the compression axis. While force chains have been observed in fibrous networks [106–109], the properties of force chain networks that develop during macroscopic strain stiffening, and their effects on the normal stresses, have not been extensively studied. In shear-thickening suspensions, the formation of such force networks are

typically associated with anomalous, and sometimes negative, values of N_1 [110–112]. Given the similarity of the force chains in sheared semiflexible fiber networks to those observed in packings/suspensions, as well as the significant nonaffinity observed near the strain-stiffening transition, it is not obvious that the Lodge-Meissner relation should apply, or even that N_1 should be positive for these networks. While some prior theory and simulation [76, 107] studies have suggested that semiflexible networks may generally satisfy the Lodge-Meissner relation, a systematic study of the effects of network structure and nonaffinity on N_1 has been lacking.

Here, we investigate the behavior of the various normal stress components in athermal subisostatic fiber networks near the strain-stiffening transition, using numerical models of disordered semiflexible fiber networks in two and three dimensions. We show that the general scaling of the normal stresses with shear strain below, near, and above the rigidity transition remains consistent irrespective of the underlying network structure. However, we demonstrate that such networks can exhibit anomalous behavior in N_1 that is highly sensitive to the network structure, and that this anomaly is most pronounced near the point of marginal stability as a function of strain, i.e., along the phase boundary in Fig. 3.1b that corresponds to nonlinear strain-stiffening. This anomaly at the stiffening transition results from the formation of a highly heterogeneous, anisotropic, system-spanning network of strong tensile force chains, whose spatial structure and force distribution determines the relative values of each normal stress component and thus N_1. Our results suggest that any underlying anisotropy in the network structure can result in anomalous behavior in N_1 that is maximized at the critical strain, suggesting that the sign and magnitude of N_1 can, in principle, be tuned by selectively modifying the network structure. Interestingly, our results suggest that in the limit of very large and nearly isotropic systems, such as large off-lattice network models or experimental gels, the Lodge-Meissner relation should be satisfied at any strain, in spite of the significant nonaffine deformations and

heterogeneous force network associated with the critical strain.

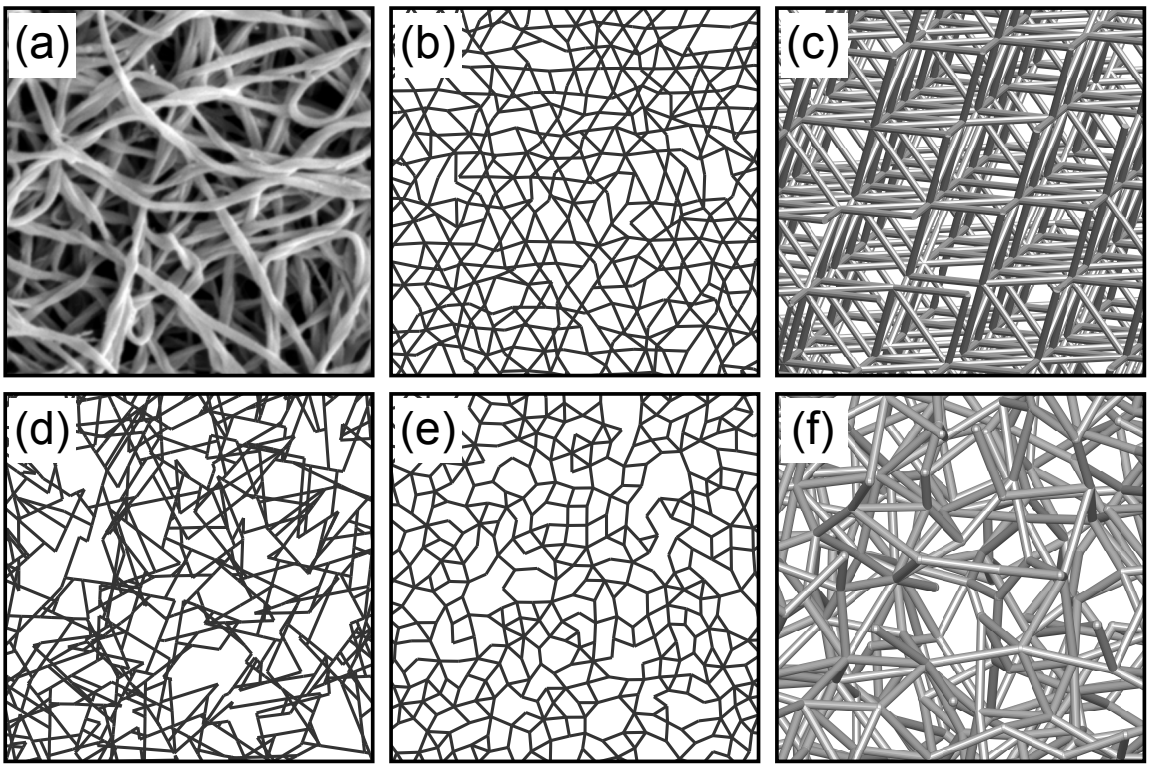

Figure 3.2: (A) Sample of a reconstituted collagen network exhibiting clear connective and geometric disorder, adapted from Ref. [50]. We investigate the mechanics of bond-diluted athermal semiflexible fiber networks including (b) phantom 2D triangular networks with added positional disorder, (c) phantom FCC lattice-based networks, (d) random fiber (Mikado) networks, (e) 2D bidisperse disk packing-derived networks and (f) 3D bidisperse sphere packing-derived networks.

3.3 Numerical models

We consider discrete models of semiflexible polymer networks in 2 and 3 dimensions, including both lattice-based and off-lattice network structures, with filament-bending (i.e. freely hinging crosslinks between fibers) and bond-bending interactions. For lattice-based models, we consider two-dimensional (triangular) and three-dimensional (face-centered cubic) lattice-based networks, and for off-lattice networks we consider two-dimensional Mikado and bidisperse disk packing-derived networks as well as three-dimensional bidisperse sphere packing-derived networks. Examples of these are shown

in Figure 3.2.

We construct disordered lattice-based networks in 2D beginning with fibers arranged on a periodic triangular lattice with lattice spacing $l_0 = 1$ and sides of W lattice units [66, 113], which we then *phantomize* by disconnecting one of three intersecting fibers at each node, in order to reduce the average network connectivity $\langle z \rangle$ to 4 [73]. Prior work has shown that, in 2D networks, the buckling of long, straight fibers leads to unrealistic mechanical effects including a dip in the differential shear modulus $K = \partial \sigma_{xz} / \partial \gamma$ [97]. We avoid this by introducing geometric distortion to the unstrained lattice network by moving each node a random distance in the range $[0, \delta_{\max}]$ in a random direction, with $\delta_{\max} \leq 0.5$ in order to avoid overlapping nodes [44, 51, 114], and subsequently redefining the rest lengths $l_{ij,0}$ between pairs of nodes and rest angles $\theta_{ijk,0}$ between connected triplets of nodes so that the geometrically disordered network exhibits zero stress in the unstrained state. In order to avoid system-spanning (or nearly system-spanning) fibers, which introduce unrealistic contributions to the macroscopic mechanics [48, 95], we remove every qth bond along each fiber, beginning with a randomly chosen bond, prior to dilution. For phantomized triangular networks, we use $W = 120$ and $q = 20$. Similarly, the process for generating 3D face-centered cubic (FCC) lattice-based networks (as shown in Figure 3.2c) begins with fibers arranged on a periodic FCC lattice [65] with sides of W lattice units with lattice spacing $l_0 = 1$. We phantomize these as well [115], yielding an average $z = 4$, and cut a single randomly chosen bond on each fiber prior to dilution. We use 3D FCC networks with $W = 25$.

Mikado networks are constructed by placing straight segments of length L with random positions and orientations into a 2D periodic box of side length W, adding crosslinks at the intersections between segments [40, 116]. Fibers are deposited randomly until the desired average crosslink density L/l_c is reached, where l_c is the average bond length. Even in the infinite crosslink density limit, Mikado networks yield $z < 4$. We generate networks with $W = 10L$ and $L/l_c \approx 12$, yielding an initial

connectivity of $z \approx 3.6$ prior to dilution.

We prepare 2D packing-derived (PD) networks by first randomly placing $N = W^2$ radially bidisperse disks with harmonic repulsive interactions within a periodic square unit cell of side length W, where half of the disks are assigned a radius $r = r_0$ and half $r = \phi r_0$, with $\phi = 1.4$ chosen to avoid long-range order [82]. We incrementally increase r_0 from 0 until the system jams, exhibiting a finite bulk modulus. From this disordered packing, we generate a contact network by connecting the centers of the overlapping disks (excluding rattlers) with springs at their rest lengths [47, 81, 117]. The same procedure is followed in 3D, using $N = W^3$ radially bidisperse harmonic repulsive spheres, also with $\phi = 1.4$, in a periodic cubic unit cell of side length W. With sufficiently large systems, this procedure generates contact networks with $z \approx 2d$, where d is the dimensionality. Unless otherwise stated, we study 2D packing-derived networks with $W = 100$ ($N = 10000$ nodes) and 3D packing-derived networks with $W = 20$ ($N = 8000$ nodes).

After generating the underlying network structure, we repeatedly remove randomly chosen bonds and any consequent dangling ends until the network reaches the desired average network connectivity z. We model the lattice-based and Mikado networks as filamentous networks with freely-hinging crosslinks, in which bending interactions are accounted for only along each fiber [40, 50], whereas the packing-derived networks are modeled instead as bond-bending networks [118] with bending interactions between all pairs of nearest-neighbor bonds. Given that the precise mechanics of the connections between fibers in real collagen and fibrin networks, which can include both branching points and crosslinks, are not well characterized, using two different crosslink models enables us to study whether the behavior of the normal stresses is independent of the detailed form of the bending interactions. Prior work has shown that these models exhibit similar linear mechanics [48, 119] and strain-driven critical behavior [50–52]. Energetically, we treat individual bonds as Hookean springs with stretching modulus

μ and pairs of bending-associated bonds with bending modulus κ. The Hamiltonian $\mathcal{H}$ of the full network is

$$\mathcal{H} = \frac{1}{V}\left[\frac{\mu}{2}\sum_{\langle ij\rangle}\frac{\left(l_{ij}-l_{ij,0}\right)^2}{l_{ij,0}} + \frac{\kappa}{2}\sum_{\langle ijk\rangle}\frac{\left(\theta_{ijk}-\theta_{ijk,0}\right)^2}{l_{ijk,0}}\right], \tag{3.1}$$

in which the sums are taken over pairs $\langle ij\rangle$ and triplets $\langle ijk\rangle$ of connected nodes, and $l_{ijk,0} = (l_{ij} + l_{jk})/2$. For networks with freely hinging crosslinks, the second sum is taken only for adjacent pairs of bonds along fibers. Here, $V = v_0 W^d$, where $v_0 = \sqrt{3}/2$ for triangular lattice-based networks, $v_0 = \sqrt{2}/2$ for FCC lattice-based networks, $v_0 = 1$ otherwise, and d is the dimensionality. As in prior work, we set $\mu = 1$ and define a dimensionless bending rigidity $\tilde{\kappa} = \kappa/\mu l_c^2$. Bond-diluted network models such as these have been shown to quite effectively describe the shear elasticity of reconstituted collagen networks [50, 98], which have a typical average value of $z \approx 3.4$ [120].

We perform simulations of networks under simple shear by incrementally increasing the shear strain γ from 10^{-2} to 1 in exponentially spaced steps, using generalized Lees-Edwards periodic boundary conditions [85]. For simplicity of notation when comparing 2D and 3D simulations, we denote x and z the directions of shear and gradient, respectively, in both cases. At each strain value, the network energy is minimized using the FIRE algorithm [83], and each component of the stress tensor $\boldsymbol{\sigma}$ is computed as

$$\sigma_{\alpha\beta} = \frac{1}{2V}\sum_{\langle ij\rangle} f_{ij,\alpha} u_{ij,\beta} \tag{3.2}$$

in which $\mathbf{u}_{ij} = \mathbf{u}_j - \mathbf{u}_i$ is the vector between nodes i and j and $\mathbf{f}_{ij}$ is the force acting on node i due to node j [86]. To symmetrize the normal stresses in the linear regime, we average the response of each network sample under positive and negative shear strain. Unless otherwise stated, the reported stress is averaged over at least 10 samples.

For comparison, we also consider the limit of an isotropic medium composed of

filaments of length $l_0 = 1$ with uniformly distributed initial orientations, which are assumed to deform affinely under simple shear. We compute the resulting stress tensor as a function of strain for this system with two complementary force extension relations: simple linear Hookean springs, which support both compression and tension, and "rope"-like springs that support only tension (see Appendix, section 3.8). For the remainder of the paper we refer to the first isotropic model as the spring model and the second as the rope model. Both analytical models satisfy the Lodge-Meissner relation under any applied strain.

3.4 Normal stresses and strain-stiffening

Without bending interactions, spring networks exhibit a finite linear shear modulus $G = \lim_{\gamma \to 0} K > 0$ only when their connectivity z, defined as the average number of connections at each node, reaches a critical isostatic connectivity z_c [48]. While the precise value of z_c is sensitive to the heterogeneity of the network structure, typical values are close to the constraint-counting value $z_{iso} = 2d$ introduced by Maxwell [46]. Under shear strain, spring networks that are subisostatic, with $z < z_c$, develop finite $K \approx \mu$ at a critical strain γ_c that depends on the network's connectivity and geometry, with $\gamma_c \to 0$ as $z \to z_c$ from below. At the critical strain, such networks develop a system-spanning branched network of primarily tensile force chains, oriented predominantly along the principal extension axis, in order to support finite stress. Associated with the development of this force chain network are characteristic signatures of criticality including diverging nonaffine fluctuations [50]. In networks with finite $\tilde{\kappa}$, K is finite and proportional to $\tilde{\kappa}$ below the critical strain, and subisostatic semiflexible polymer networks therefore undergo a transition from a bending-dominated regime to a stretching-dominated regime at the critical strain [50]. In Fig. 3.3, we show K vs. γ for several values of z, demonstrating that γ_c increases with decreasing z. For constant

z, γ_c is very weakly dependent on $\tilde{\kappa}$ in the limit of $\tilde{\kappa} \to 0$, and the networks exhibit a clear transition from a bending dominated regime ($K \propto \tilde{\kappa}$) for $\gamma < \gamma_c$ to a stretching dominated regime ($K \propto \mu$) for $\gamma > \gamma_c$ (Fig. 3.3a inset). This behavior is also clear from the proportion of the total energy arising from bending interactions, $\mathcal{H}_b/\mathcal{H}$, as we show in Fig. 3.3c: as $\tilde{\kappa}$ is decreased, the transition from the bending-dominated to stretching-dominated regime at γ_c sharpens. One can map the critical strain as a function of z to yield a phase diagram for the mechanical behavior of subisostatic networks as a function of strain and connectivity, as shown schematically in Fig 3.3b [50]. The details of the phase boundary depends on the underlying network geometry.

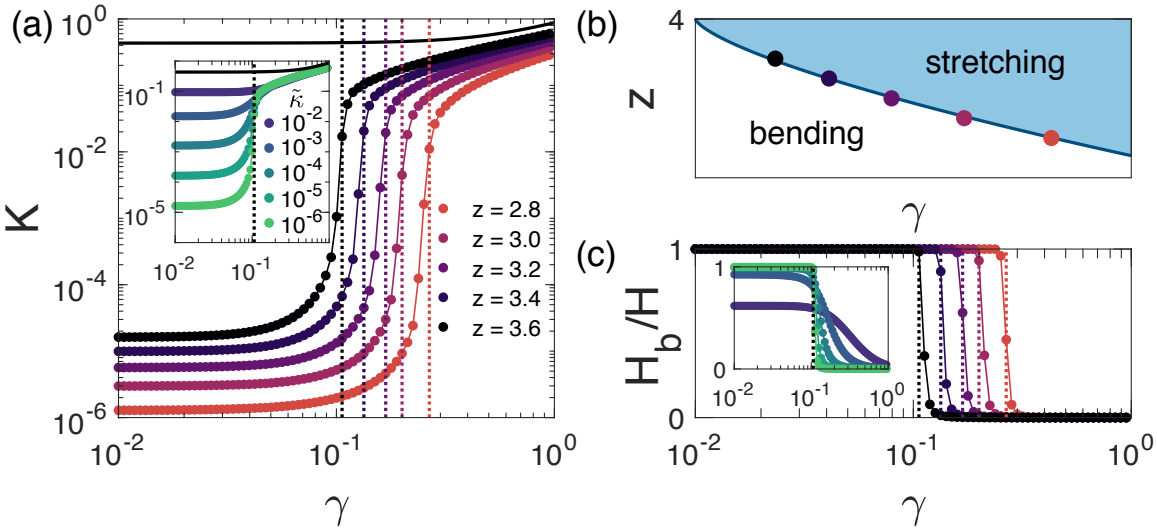

Figure 3.3: (a) Differential shear modulus K vs. strain γ for phantomized triangular networks with $\tilde{\kappa} = 10^{-6}$, $W = 120$, $\delta_{\max} = 0.4$, and varying connectivity z. The vertical dotted line for each z value indicates the critical strain γ_c, determined as the strain corresponding to the onset of finite K in the low-$\tilde{\kappa}$ limit. These curves illustrate that the critical strain increases with decreasing z. The solid black line shows the computed K for the affine isotropic network model with line density $\rho = 2\sqrt{3}$. Inset: K vs. γ for constant $z = 3.6$ and varying $\tilde{\kappa}$. (b) Schematic mechanical phase diagram indicating the increase in γ_c with decreasing z below $z_c = 2d$. (c) For the same networks, the ratio of bending energy $\mathcal{H}_b$ to total energy $\mathcal{H}$ illustrates the bending-to-stretching transition that occurs at the critical strain and (inset) sharpens with decreasing $\tilde{\kappa}$. Colors in both the main panel and inset correspond to those in panel (a). Lines between points are intended to serve as guides to the eye.

The normal stress components σ_{ii} (where $i = x, z$) both exhibit the same bending-dominated to stretching-dominated transition at the z-dependent critical strain, with

$\sigma_{ii} \propto \tilde{\kappa}$ for $\gamma < \gamma_c$ and $\sigma_{ii} \propto \mu$ for $\gamma > \gamma_c$, as shown in Fig. 3.4a for phantom triangular networks. As we show in Fig. 3.5, we observe essentially the same behavior in all subisostatic network models studied here, supporting the idea that the details of the network structure [50] and bending energy type [51] have only minor effects on the general strain-stiffening behavior of semiflexible fiber networks. Instead, the governing variables are z and γ. In Appendix, section 3.8, we show that phantomized triangular networks exhibit the same mechanical behavior with freely-hinging crosslinks as with bond-bending interactions, with the only difference being that bond-bending interactions leads to a higher apparent κ due to the additional angle constrains. We also observe that the ratio of the axial normal stress component σ_{zz} to the shear stress σ_{xz} becomes maximal, and typically greater than 1, at γ_c, as we show in Fig. 3.4b. This peak reflects the sharp transition from the bending-dominated regime, in which $\sigma_{zz} \propto \gamma^2$ and $\sigma_{xz} \propto \gamma$ for small γ, yielding $\sigma_{zz}/\sigma_{xz} \propto \gamma$, to the stretching-dominated regime, in which σ_{xz} grows as a power-law with respect to $\Delta\gamma$ and rapidly begins to dominate σ_{zz}. Preliminary observations of this phenomenon were made in prior work using Mikado networks [94] and in experiments on fibrin [92]. We observe, in all network models discussed here, that the peak follows the critical strain as z is varied and grows to a z-dependent asymptotic value as $\tilde{\kappa}$ decreases. A maximum in this ratio actually does occur in the affine isotropic spring network limit due to the gradual reorientation of fibers under increasing shear strain, but the maximal value is smaller (~ 0.4) and the peak strain much larger ($\gamma \sim 1$) than we observe for our semiflexible network models. The isotropic rope network model, in contrast, exhibits a maximum with $\sigma_{zz}/\sigma_{xz} > 1$ at zero strain. In semiflexible networks with small $\tilde{\kappa}$, it appears that the critical strain marks a transition from the linear, bending-dominated regime in which $\sigma_{zz}/\sigma_{xz} \propto \gamma$ to a rope-like regime. This results from the fact that, at and above the critical strain, tension forces vastly outweigh compressional forces in networks with low $\tilde{\kappa}$. In Fig. 3.4b, we show that systems with low $\tilde{\kappa}$ exhibit a

ratio σ_{zz}/σ_{xz} which, above γ_c, is quite close to the rope network limit, whereas for higher $\tilde{\kappa}$ networks the ratio approaches the spring network limit. The latter trend is expected, as increasing $\tilde{\kappa}$ increases the degree to which the network's fibers can support compression. Interestingly, we observe that, near the critical strain, σ_{zz}/σ_{xz} exceeds even the rope values predicted for the affine isotropic rope network limit, possibly due to the highly heterogeneous nature of the stress-bearing network at the critical strain. Nevertheless, it is apparent that a large ratio of the axial normal stress to the shear stress is a signature of the development of a rope-like stress-bearing structure at the critical strain. This is further supported by prior experimental evidence that fibrin networks with stiffer filaments exhibit a smaller peak in σ_{zz}/σ_{xz} than more flexible ones at the critical strain [92].

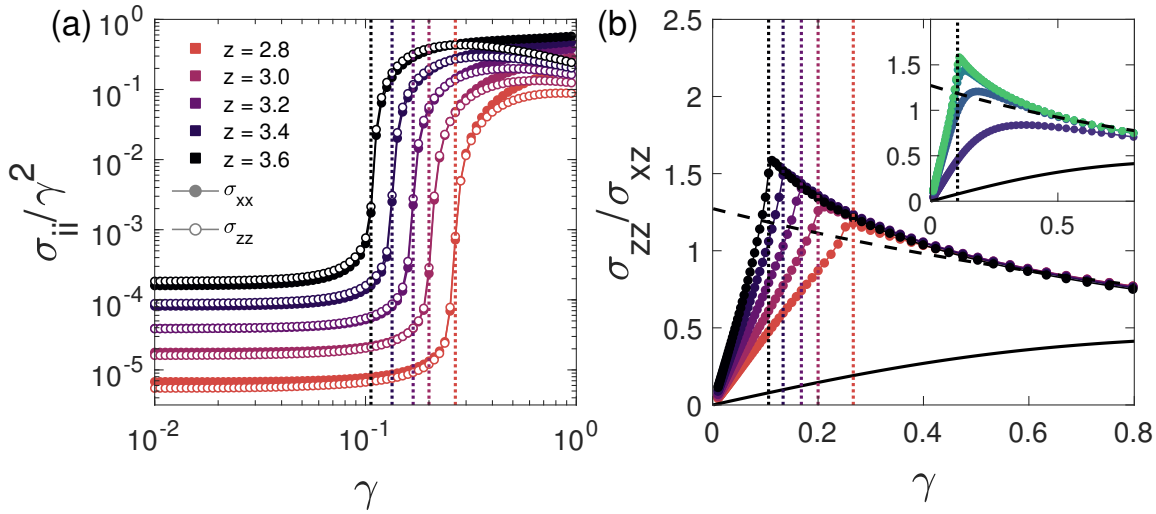

Figure 3.4: Normal stress components σ_{xx} (closed symbols) and σ_{zz} (open symbols) normalized by γ^2, for the same phantom triangular networks as in Fig. 3.3, with $\tilde{\kappa} = 10^{-6}$ and varying z. Dotted lines indicate $\gamma_c(z)$. (b) The corresponding ratio of the axial normal stress σ_{zz} to the shear stress σ_{xz} shows a peak at the critical strain for each z value that (inset) sharpens with decreasing $\tilde{\kappa}$. Colors correspond to those in Fig. 3.3. The thick solid line corresponds to the affine isotropic spring network model, and the dashed solid line corresponds to the affine isotropic rope network model.

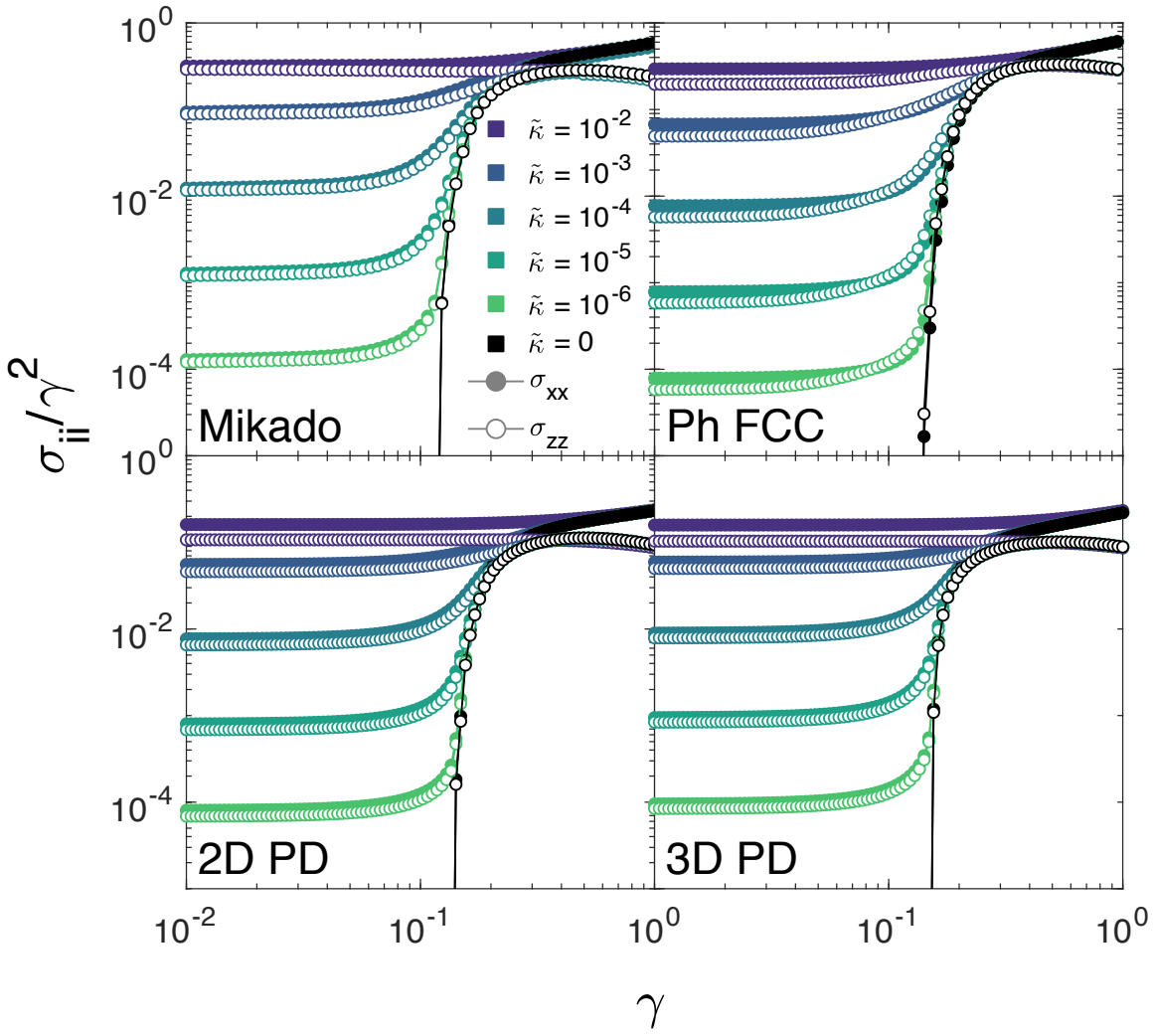

Figure 3.5: Normal stress components σ_{xx} (closed symbols) and σ_{zz} (open symbols) normalized by γ^2 for (top left) Mikado networks with $z = 3.3$, (top right) phantom FCC networks with $z = 3.4$, (bottom left) 2D packing-derived networks with $z = 3.3$, and (bottom right) 3D packing-derived networks with $z = 4.8$, all with varying $\tilde{\kappa}$.

3.5 Stress anisotropy

For typical isotropic elastic materials, the first normal stress difference $N_1 = \sigma_{xx} - \sigma_{zz}$ is positive, and for affinely deforming isotropic elastic materials like rubber it is typically well approximated by the Lodge-Meissner relation $N_1 = \sigma_{xz}\gamma$. Negative values of N_1 are unusual, but have been observed in certain materials including shear-thickening suspensions [111]. However, negative N_1 has not to date been observed in a real elastic solid. While the normal stresses we observe for all networks (Figs. 3.4

and 3.5) are similar in magnitude at and below the critical strain, we observe that the behavior of the first normal stress difference N_1 depends strongly on the underlying network structure.

Under applied strain γ, the periodic images of each node in the network transform affinely according to the simple shear deformation gradient $\Lambda(\gamma)$. This deformation gradient results in maximal elongation along its principal extension axis with orientation θ_P, with maximal compression along the perpendicular axis, as shown schematically in Fig. 3.6c for a small strain. We determine the principal strains and principal strain axes, which rotate with applied strain, as a function of γ in Appendix, section 3.8. For $\gamma = 0$, the principal extension axis is oriented $\theta_P = \pi/4$ radians above the x-axis in the x-z plane. For isotropic and affinely deforming networks with only axial forces, such as the rope and spring model, the principal stress axes exactly follow the principal strain axes under any applied γ, such that the Lodge-Meissner relation is always satisfied. That the principal stress axes follow the principal strain axes is not guaranteed in disordered networks, as they deform nonaffinely and are not perfectly isotropic.

In particular, lattice-based networks such as triangular and FCC models exhibit significant angular anisotropy; in the unstrained state, their bonds lie only along vectors corresponding to the lattice directions, and imposed local geometric disorder does little to mitigate this long-range anisotropy. We can explore the effects of this anisotropy by applying an initial rotation of ϕ radians, relative to the x-axis in the x-z plane, to the lattice prior to applying shear strain. Arbitrarily, we define the unrotated ($\phi = 0$) phantom triangular lattice as having bonds initially oriented at angles $\theta_{b,0} \in [0, \pi/3, 2\pi/3]$ relative to the x-axis. Even with significant random local geometric distortion $\delta_{max} = 0.4$, the fibers remain *on average* oriented along these initial lattice vectors. In general, tensile force chains develop in randomly diluted spring networks at the critical strain and tend to be oriented along the principal extension axis. As bonds in a phantom triangular network do not have a uniform

initial angular distribution and are instead oriented primarily along the initial lattice bond orientations for a given ϕ, the tensile force chains develop along the (slightly rotated) initial lattice bond orientation that is most stretched at γ_c, i.e. whichever is closest to the principal extension axis.

For initially unrotated ($\phi = 0$) triangular lattice networks, the dominant tensile force chains develop primarily along the bonds that are initially oriented along the $\theta_{b,0} = \pi/3$ direction, as shown in Fig. 3.6d, with softer branches oriented along the other directions. As a result, the maximum principal stress is oriented close to the $\theta_{b,0} = \pi/3$ direction, not parallel to the principal extension axis. The initial lattice orientation determines which of the (rotated) initial lattice bond orientation the tensile force chains propagate along at γ_c, thus determining the relative orientation of the maximal principal stress axis to the principal extension axis. When the initial lattice is rotated by $\phi = \pi/6$, such that the initial undistorted lattice bond vectors are oriented along $\theta_{b,0} \in [\pi/6, \pi/2, 5\pi/6]$, the dominant force chains instead propagate along the rotated lattice vector corresponding to $\theta_{b,0} = \pi/6$, as shown in Fig. 3.6e.

But how does this affect N_1? In the $\tilde{\kappa} = 0$ limit, in which forces only occur parallel to bonds, the value of N_1 is entirely determined by the individual bond orientations, with $N_1 \propto \sum_b f_b l_b \cos(2\theta_b)$ where f_b is the tension, l_b is the length, and $\theta_b \in [-\pi/4, 3\pi/4]$ is the angle of bond b relative to the x-axis in the x-z plane. This range for θ_b is convenient, as bonds under tension with $\theta_b > \pi/4$ exhibit negative N_1, whereas bonds under tension with $\theta_b < \pi/4$ exhibit positive N_1. A similar expression was used in Ref. [112] to describe relative contributions to N_1 based on force networks in non-Brownian suspensions. With finite $\tilde{\kappa}$, forces also occur perpendicular to bonds, leading to a more complicated dependence of N_1 on the network configuration. Since the tensile force networks dominate for relatively low-$\tilde{\kappa}$ networks at and above the critical strain, it is reasonable to estimate N_1 for such networks in this regime only in terms of stretching forces, i.e. as a simple function of the bond orientations.

In our disordered network models, which deform nonaffinely and always possess some anisotropy, normalizing the measured value of N_1 by the Lodge-Meissner value $(\sigma_{xz}\gamma)$ yields a quantitative measure of the degree to which the network behaves as an affinely deforming isotropic material. Since $\sigma_{xz}\gamma$ is always positive, this quantity also indicates when N_1 is negative. For the remainder of this work, we report the normalized quantity $N_1/(\sigma_{xz}\gamma)$. For unrotated ($\phi = 0$) phantom triangular lattice networks, the dominant force chains at γ_c are tensile and oriented with $\theta > \pi/4$ for small γ_c, predicting that N_1 will be negative in the limit of low $\tilde{\kappa}$. With increasing γ_c, i.e. decreasing z, the force chains should develop with orientations closer to the principal strain axis, so decreasing z should bring N_1 closer to the Lodge-Meissner value. In Fig. 3.7a, we plot $N_1/(\sigma_{xz}\gamma)$ as a function of strain for phantom triangular lattice-based networks with $\phi = 0$, small $\tilde{\kappa}$, and varying z, demonstrating that these exhibit a negative peak in N_1 at the z-dependent critical strain, corresponding to the highly anisotropic force chains with $\theta > \pi/4$ shown in Fig. 3.6d. As predicted, the magnitude of this peak decreases as z decreases and γ_c increases, as the applied strain causes the principal stress axis to approach the principal strain axis. Nevertheless, even relatively high γ_c values yield an anomalous downward peak in γ_c, indicating that these networks become maximally anisotropic at the critical strain. At large strains, of order 1 or greater, $N_1 \approx \sigma_{xz}\gamma$ for all networks, as the deformation becomes increasingly affine above the critical strain and the principal stress axis approaches the principal strain axis.

We further demonstrate in Fig. 3.7b that the peak is related to the critical strain-stiffening transition by showing that, in unrotated phantom triangular networks with constant z and varying $\tilde{\kappa}$, the peak becomes sharper in the $\tilde{\kappa} \to 0$ limit. With increasing $\tilde{\kappa}$, the deformation becomes increasingly affine, so the peak disappears and N_1 grows increasingly positive. With $\tilde{\kappa} \to \infty$, the disordered network's response approaches that of the corresponding affinely deforming *undiluted* triangular lattice,

which actually yields $N_1/(\sigma_{xz}\gamma) > 1$ for $\phi = 0$ due to its inherent angular anisotropy. Given the rotational symmetry of the triangular lattice for rotations of $n\pi/3$, we expect that, beyond small differences due to random dilution, any angular anisotropy-related mechanical behavior of the lattice should be similar for initial rotations $\phi = n\pi/6$ where n is even, whereas the opposite behavior should occur for odd n. For intermediate angles, we should observe a transition between these two cases. In Fig. 3.6a, we show the response for the full undiluted triangular lattice, as well as that of diluted phantom triangular networks with varying $\tilde{\kappa}$, with $\phi = 0$, in comparison to the corresponding curves for the "opposite" initial orientation $\phi = \pi/6$. We see that, for the full and diluted networks, $N_1/(\sigma_{xz}\gamma)$ essentially flips about the Lodge-Meissner value of 1 when the initial lattice is rotated by $\pi/6$. That the peak for the low-$\tilde{\kappa}$ case flips in sign is supportive of the idea that the orientation of the dominant force chains, shown in Fig. 3.6d-e, controls the sign and magnitude of N_1 relative to $\sigma_{xz}\gamma$. In Fig. 3.6b, we show $N_1/(\sigma_{xz}\gamma)$ for the full range of ϕ in the low-$\tilde{\kappa}$ case, demonstrating the smooth transition between the aforementioned extremes for rotations of $n\pi/6$. If an angular average is taken, the Lodge-Meissner relation is satisfied. It is interesting to note that, even for the phantom diluted triangular lattice, certain intermediate rotations should approximately satisfy the Lodge-Meissner relation at the critical strain as long as the dominant force chains, and thus the principal stress axis, are parallel to the principal extension axis. Phantom FCC networks, which also exhibit angular anisotropy, show qualitatively similar behavior, with a downward peak in $N_1/(\sigma_{xz}\gamma)$ for $\phi = 0$.

For off-lattice networks with no long-range order, including Mikado and 2D/3D PD networks, the force chains that develop at the critical strain still occur with a directional bias towards the principal extension axis, but the lack of an underlying lattice structure means that they exhibit no orientational bias above or below the principal extension axis. Nevertheless, the highly heterogeneous and branched nature of these networks means that even for relatively large system sizes, some samples do

exhibit deviation from the Lodge-Meissner relation at the critical strain. In Fig. 3.8a, we show that $N_1/(\sigma_{xz}\gamma)$ exhibits anomalous behavior with a peak at the critical strain for certain samples for small ($W = 50$, $N = 2500$ nodes) 2D packing-derived networks, indicating that this effect can occur in off-lattice networks. Averaging over an ensemble of initial network structures, the Lodge-Meissner relation is approximately satisfied. We show in Fig. 3.8b, that larger networks ($W = 140$, $N = 19600$ nodes) still exhibit anomalous peaks at the critical strain, but that these are typically lower in magnitude than those observed in smaller systems. The deviation from the LM relation in the bending-dominated regime appears to decrease with increasing system size as well. For a given network, the dominant force chains arise along the network's "shortest paths" [107] consisting of connected bonds oriented close to the principal extension axis at a given strain, which have some excess length for $\gamma < \gamma_c$. The critical strain corresponds to the strain at which, in the $\tilde{\kappa} = 0$ limit, one or more of these shortest paths can no longer rearrange without the stretching of their constituent bonds. Thus, the structure of the force chain network and the resulting value of $N_1/(\sigma_{xz}\gamma)$, is determined at the critical strain by the orientations of these (initially randomly oriented) paths.

While we do observe that individual samples typically closely approximate the Lodge-Meissner relation, it is unsurprising that finite-sized systems occasionally show anomalous behavior at the critical strain, as a consequence of the finite chance of some angular bias of the force chain network away from the principal extension axis. In the thermodynamic limit, the Lodge-Meissner relation should be satisfied even at the critical strain for individual networks, as increasing the system size should increase the likelihood that the system can "find" shortest paths close to the principal strain axis. In other words, deviation from the Lodge-Meissner relation requires a preferential orientation of the principal stress axis above (or below) the principal extension axis, which can only occur due to some underlying bond orientation bias in the initial network structure. For off-lattice models like packing-derived networks with

no long-ranged structural anisotropy, such a preferential orientation is not possible in the limit of large system sizes, so the Lodge-Meissner relation is satisfied. We observe the same behavior for 3D PD networks and Mikado networks as in 2D PD networks. It is worth noting that in off-lattice networks, like in the lattice-based networks, one can cause $N_1/(\sigma_{xz}\gamma)$ to flip about the Lodge-Meissner value by appropriately rotating the initial structure, and averaging over all possible initial orientations removes any deviation from Lodge-Meissner.

To emphasize the dependence of the value of N_1 on the highly heterogeneous force chain network structure at the critical strain, we show examples of force chains for Mikado, 2D PD, and unrotated phantom triangular networks with $\tilde{\kappa} = 0$ at the critical strain in Fig. 3.9. Mikado and PD networks show randomly branched force chains with a directional bias towards the principal extension axis, whereas the unrotated phantom triangular network shows the expected force chains oriented above the principal extension axis (and above $\theta_b = \pi/4$). Additionally, we compute the distribution of contributions to N_1 due to bonds oriented with angle $\theta = \theta_b - \pi/4$, normalized by $\sigma_{xz}\gamma$, for each network structure as a function of $\Delta\gamma = \gamma - \gamma_c$, also shown in Fig. 3.9. Integrating these distributions over θ yields $N_1/(\sigma_{xz}\gamma)$ as a function of strain. At large strains, the networks all show very similar behavior, with primarily positive contributions to N_1 coming from primarily tensile bonds oriented close to the principal extension axis, below $\theta_b = \pi/4$, and with the total contribution satisfying the Lodge-Meissner relation.

At the critical strain, however, the value of $N_1/(\sigma_{xz}\gamma)$ is determined by the balance of very large positive and negative contributions from bonds oriented above and below $\theta_b = \pi/4$. For the Mikado and PD networks shown, these positive and negative contributions are similar in magnitude at γ_c, but for the unrotated phantom triangular lattice, the negative contribution at γ_c significantly outweighs the positive contribution, yielding the observed negative peak in $N_1/(\sigma_{xz}\gamma)$ vs. γ. The signficant heterogeneity

of the force chain network is evident in noisy nature of these distributions at γ_c. We additionally plot, as insets in Fig. 3.9, the corresponding bond force distributions $P(f/\langle f\rangle)$ at γ_c, where $f > 0$ corresponds to tension and the average $\langle f\rangle$ is taken only over bonds under tension. Similar to observations of compressive force distributions in granular packings [121–123], frictional forces in shear-thickening suspensions [104], and tensile forces in polymer crazes [124], we observe that the large ($f > \langle f\rangle$) tensile forces in our networks are, at the point of marginal stability i.e. γ_c, approximately exponentially distributed. To emphasize this, we show that the large forces can be approximated by the distribution $P(f/\langle f\rangle) \propto \exp(-\beta(f/\langle f\rangle - 1))$. We find $\beta = 0.5$ appears to reasonably describe the distributions for the networks shown here. We also note that the compressive forces appear to exhibit an exponential tail as well, although they decay faster than the tensile forces. In a network of rope-like bonds or bucklable individual bonds with $\tilde{\kappa} = 0$, there would be no compressive forces. These distributions emphasize that tensile forces dominate at the critical strain.

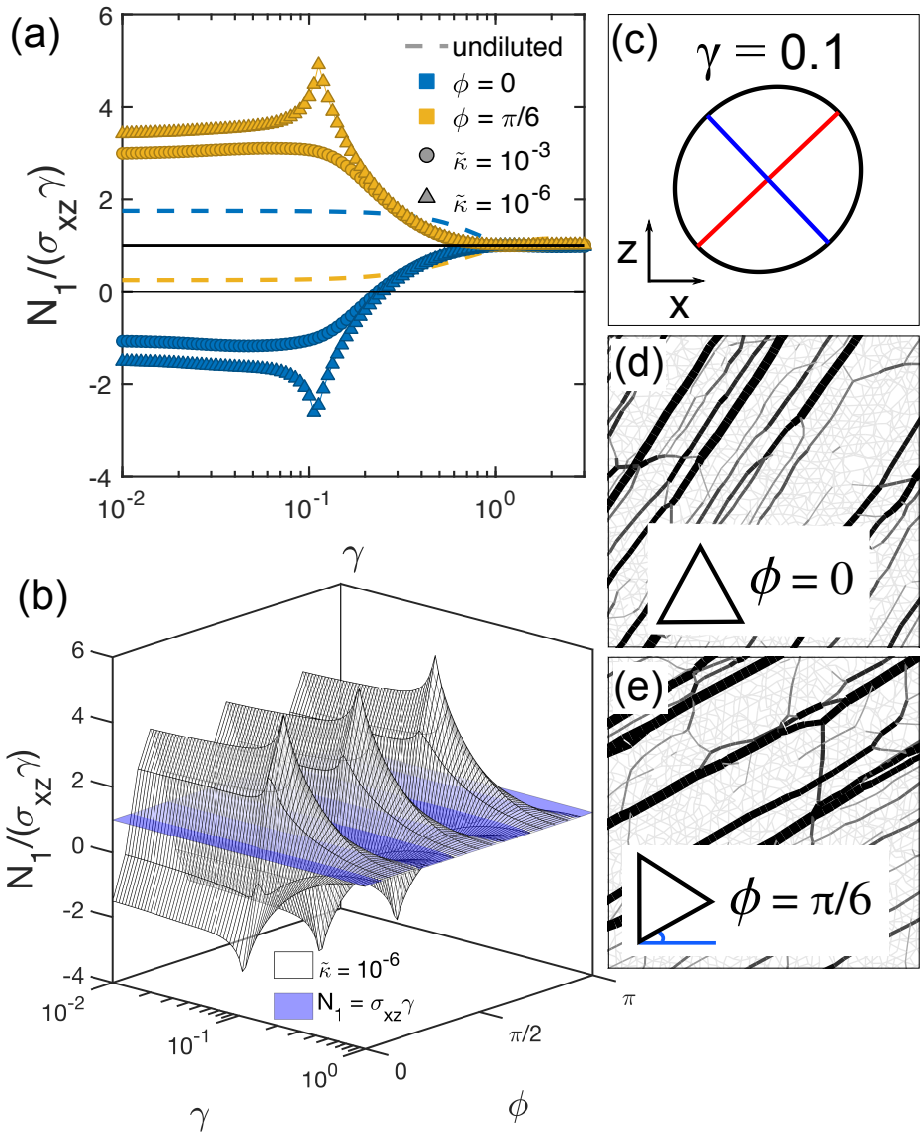

Figure 3.6: (a) N_1 normalized by the Lodge-Meissner relation $N_1 = \sigma_{xz}\gamma$ for undiluted triangular lattices (dashed lines) and phantomized triangular networks with $z = 3.6$, and $W = 120$, and varying $\tilde{\kappa}$, in which the lattice is initially rotated by angle $\phi = 0$ and $\phi = \pi/6$. In the subisostatic lattice case, the peak at the critical strain γ_c changes sign when the lattice is rotated by $\phi = n\pi/6$ with odd n, as shown in (b) for $\tilde{\kappa} = 10^{-6}$ over the full range of θ. In lattice-based networks such as these with long fibers along specific lattice vectors, force chains preferentially develop at the critical strain along whichever lattice vector is closest to the principal extension direction for a given applied strain γ (see Appendix, section 3.8). (c) The principal extension axis for the simple shear deformation gradient $\Lambda(\gamma = 0.1)$ is shown in red, with the (perpendicular) principal compression axis shown in blue. In black, we show the corresponding strain ellipsoid, projected onto the x-z plane. d) The angular orientation of the dominant force chains relative to $\theta = \pi/4$ determines the sign of N_1. For unrotated networks ($\phi = 0$) with the same parameters as in (b), the most elongated fibers at the critical strain $\gamma_c \approx 0.1$ are oriented with $\theta_b > \pi/4$, resulting in negative N_1. (e) When these networks are rotated initially by $\phi = \pi/6$, the most elongated fibers at the critical strain are instead oriented with $\theta_b < \pi/4$, resulting in positive N_1.

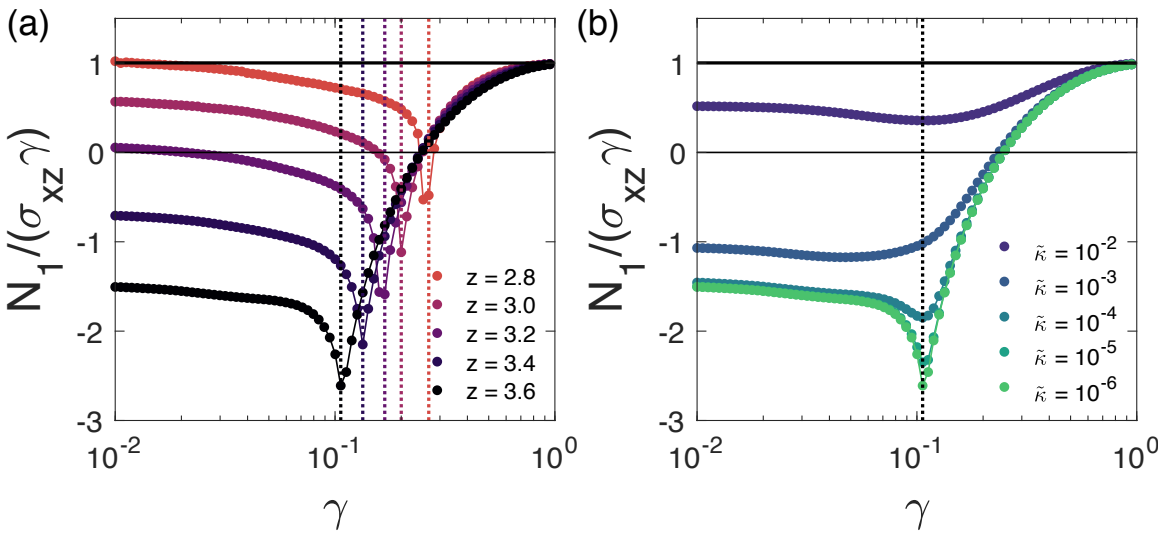

Figure 3.7: First normal stress difference $N_1 \equiv \sigma_{xx} - \sigma_{zz}$ normalized by the Lodge-Meissner relation ($N_1 = \sigma_{xz}\gamma$) in unrotated 2D distorted phantomized triangular networks ($\phi = 0$, $\delta_{\max} = 0.4$) as a function of γ for (a) $\tilde{\kappa} = 10^{-6}$ and varied $\langle z \rangle$ and (b) $\langle z \rangle = 3.6$ and varied $\tilde{\kappa}$, with the Lodge-Meissner result ($N_1/(\sigma_{xz}\gamma) = 1$) shown as a thick solid line. Deviation from the Lodge-Meissner relation increases with $\langle z \rangle$, and the ratio exhibits a downward peak and maximal anomaly at the critical strain γ_c, which grows with decreasing $\tilde{\kappa}$ and shifts with γ_c for varying $\langle z \rangle$. At high strain, ratios for all networks (irrespective of $\langle z \rangle$ and $\tilde{\kappa}$) converge to the affine result.

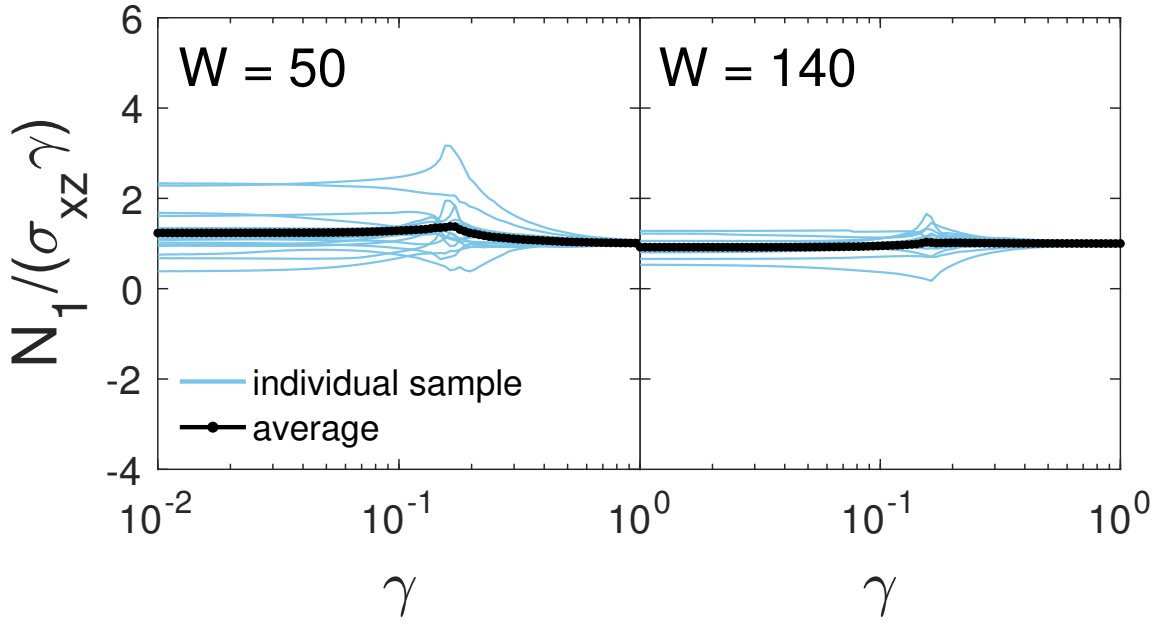

Figure 3.8: Off-lattice networks show signatures of anisotropy in N_1 at the critical strain, but these deviations appear to average out in the limit of large system sizes or when averaged over many samples. For 2D packing-derived networks with $z = 3.3$ and $\tilde{\kappa} = 10^{-6}$, we observe a decrease in the magnitude of the deviations of N_1 from the Lodge-Meissner relation with increasing system size.

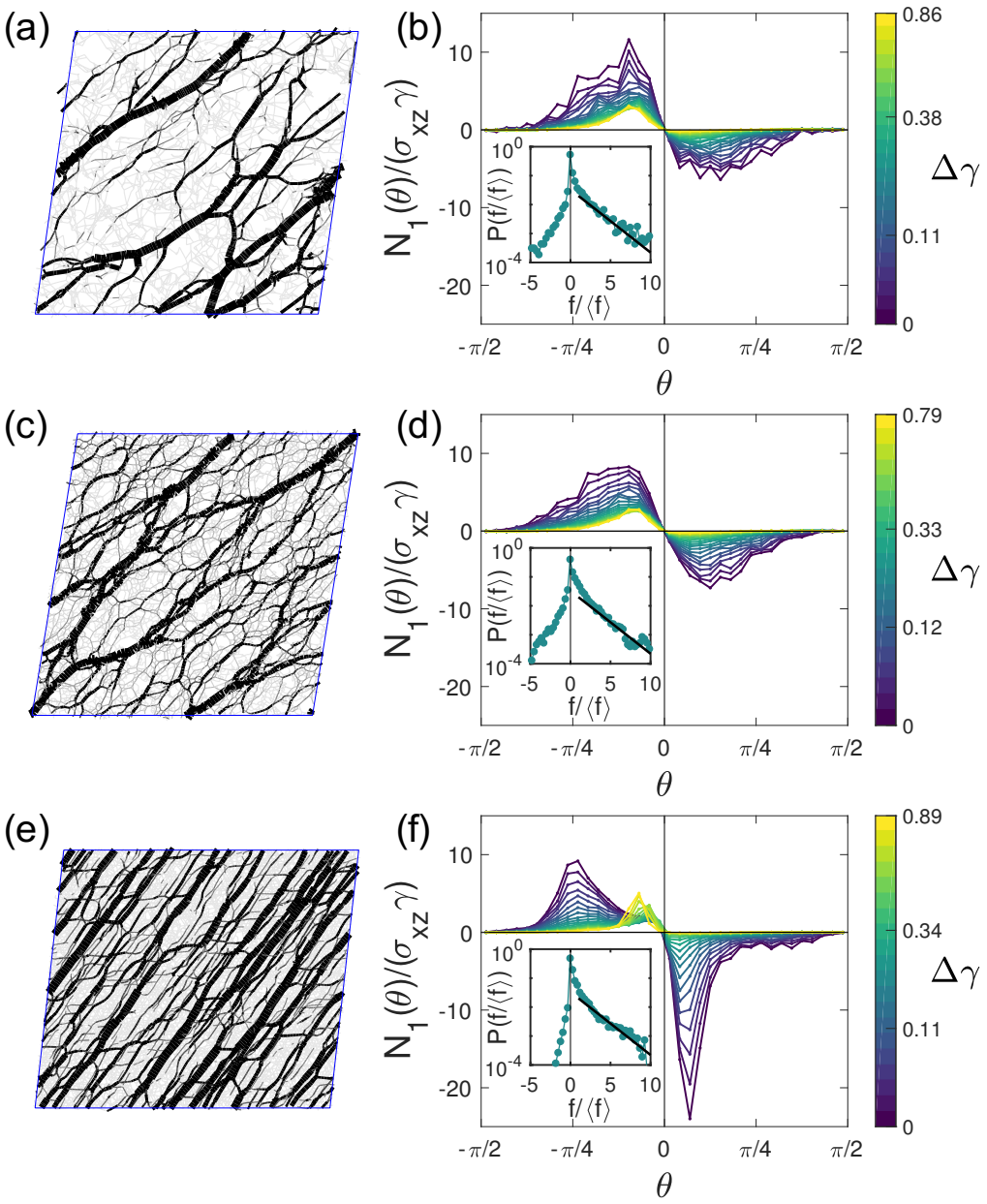

Figure 3.9: At the critical strain in the limit of $\tilde{\kappa} = 0$, a system-spanning network of force chains develops that enables the network to bear finite stress. The angular orientation of this force network's constitutent bonds determines the sign of N_1. Here, we show representative force chains for central force ($\tilde{\kappa} = 0$) networks at the critical strain for (a) a Mikado network with $z = 3.3$, (b) a packing-derived network with $W = 100$ and $z = 3.4$, and (e) a phantomized triangular network with $z = 3.6$. We also show the corresponding distributions of $N_1(\theta)$, the contribution to N_1 from bonds oriented with a given angle θ relative to $\pi/4$, normalized by $\sigma_{xz}\gamma$ for varying $\Delta\gamma = \gamma - \gamma_c$. The integral of $N_1(\theta)$ over $\theta \in [-\pi/2, \pi/2]$ yields N_1. Hence, the relative areas of the positive and negative portions of the curve for a given γ indicates the sign of N_1. The dominant contributions to N_1 are from bonds under tension. Insets: At the critical strain, the probability distribution of bond tension f, where $f_{ij} = \mu(l_{ij}/l_{ij,0} - 1)$, normalized by the mean tensile force $\langle f\rangle = \mathrm{mean}(f(f > 0))$, exhibits an exponential tail. The black solid lines corresponds to $P(f/\langle f\rangle) \propto \exp(-\beta(f/\langle f\rangle - 1))$, with $\beta = 0.5$.

3.6 Summary and discussion

In this work, we have shown the general scaling behavior of the normal stresses in the vicinity of the strain-driven stiffening transition for athermal semiflexible polymer networks, demonstrating that both the axial component σ_{zz} and azimuthal component σ_{xx} are quadratic in strain and proportional to the polymer bending rigidity $\tilde{\kappa}$ for $\gamma < \gamma_c$ but increase dramatically at the critical strain, such that both become proportional to the polymer stretching modulus μ for $\gamma > \gamma_c$. Additionally, we note that the critical strain coincides with the development of a heterogeneous network of primarily tensile force chains, similar to the compressive force chains observed in granular packings and frictional force chains observed in shear thickening suspensions. Along with the development of this force chain network, we observe a peak in the ratio of the axial normal stress to the shear stress (previously observed in prior work [92, 94]), which we show is a signature of the critical strain that becomes sharper with decreasing $\tilde{\kappa}$. For networks with low $\tilde{\kappa}$, we observe that this ratio appears to behave like the corresponding ratio for the affine rope network model, highlighting the primarily tensile nature of the stress-bearing force chain network. These observations possibly explain prior evidence that more flexible fibrin networks exhibit a sharper peak in σ_{zz}/σ_{xz} than stiffer fibrin networks [92].

Further, we observe that the highly anisotropic and heterogeneous structure of the force chain network that develops at the critical strain results in deviation of the first normal stress difference $N_1 = \sigma_{xx} - \sigma_{zz}$ from the Lodge-Meissner relation $N_1 = \sigma_{xz}\gamma$, particularly for networks with significant angular anisotropy (i.e. lattice-based models). This deviation from the Lodge-Meissner relation results from a difference in orientation of the principal stress axis from the principal extension axis, which in lattice-based models results from force chains at γ_c developing primarily along whichever of the transformed initial lattice vector directions is closest to the principal strain axis. For lattice orientations in which the principal stress and strain axes do not align, we

observe a peak in $N_1/(\sigma_{xz}\gamma)$ at the critical strain, consistent with the observation that these force chains are most anisotropic at the critical strain, and we show that appropriately rotating the lattice changes the sign of the peak. These results suggest that one can control the sign and magnitude of N_1 by modifying the network structure, similar to recent work showing that networks can be made auxetic by selectively pruning bonds [125]. We observe that similar but typically smaller peaks in $N_1/(\sigma_{xz}\gamma)$ at γ_c can also occur in off-lattice models, which lack long-range order and develop more random, branched force chain networks than lattice-based networks. While the force chain networks in off-lattice models are, on average, oriented along the principal strain axis, deviation from Lodge-Meissner is observed for finite systems at the critical strain and results from small imbalances between contributions to N_1 from bonds oriented on either side of the principal extension axis. Our results suggest that, in the thermodynamic limit, semiflexible networks with no long-range angular anisotropy (e.g. off-lattice models with $W \to \infty$) should satisfy the Lodge-Meissner relation, even at the critical strain.

This suggests that any observed deviation from the Lodge-Meissner relation in experimental measurements could serve as an indication of anisotropy in the network structure. For relatively isotropic biopolymer gels in which the sample size is much larger than the mesh size, we expect $N_1 = \sigma_{xz}\gamma$, meaning that N_1, i.e. the measured normal stress on short timescales, can be expected to be positive. This is in agreement with experimental measurements of N_1 measured for fibrin gels at high frequencies [61]. We note that prior dynamic studies of spring networks have shown that viscous damping reduces nonaffinity at high frequencies [126, 127], which we expect to further reduce deviation from the Lodge-Meissner relation in this limit.

Finally, we report force probability distributions for networks at the critical strain in the limit of $\tilde{\kappa} = 0$, showing that the dominant forces at γ_c are tensile, with additional evidence of an exponential tail in the large force probability distribution. Similar force

probability distributions have been measured for other fragile or marginally stable systems, including compressive force networks in granular packings at the jamming point [121–123], transient frictional force networks in sheared granular suspensions [104], and force networks in polymer crazes [124]. Future work will be necessary to characterize these force networks and their implications in the strain-driven stiffening transition.

3.7 Acknowledgments

This work was supported in part by the National Science Foundation Division of Materials Research (Grant DMR-1826623) and the National Science Foundation Center for Theoretical Biological Physics (Grant PHY-1427654).

3.8 Appendix

3.8.1 Affinely deforming isotropic network models

Consider a filament segment with initial orientation $\hat{\mathbf{n}}$, undergoing deformation described by the tensor $\mathbf{\Lambda}(\gamma)$. The deformation changes the filament's length and orientation, resulting in a tension $\boldsymbol{\tau}$ directed along its new orientation. Treating the filament as a linear elastic element with stretching modulus μ and initial length $l_0 = 1$, the tension vector is $\boldsymbol{\tau} = \tau \mathbf{\Lambda}\hat{\mathbf{n}}/\left|\mathbf{\Lambda}\hat{\mathbf{n}}\right|$. For the spring model, we utilize a linear Hookean force-extension relation in which the filaments support both tension and compression: $\tau = \tau_s$ where $\tau_s = \mu(|\mathbf{\Lambda}\hat{\mathbf{n}}| - 1)$. For the rope model, we instead use a one-sided force-extension relation that is only finite under tension: $\tau = \tau_r$, with

$$\tau_r = \begin{cases} \mu(|\mathbf{\Lambda}\hat{\mathbf{n}}| - 1) & (|\mathbf{\Lambda}\hat{\mathbf{n}}| > 1) \\ 0 & (|\mathbf{\Lambda}\hat{\mathbf{n}}| \leq 1) \end{cases}. \tag{3.3}$$

Taking the average, over all initial filament orientations, of the product of the i component of the tension, $\tau\Lambda_{il}n_l/\left|\mathbf{\Lambda}\hat{\mathbf{n}}\right|$, and the line density of filaments crossing the j plane after the deformation, $\frac{\rho}{\det\mathbf{\Lambda}}\Lambda_{jk}n_k$, yields the stress tensor [19, 64],

$$\sigma_{ij} = \frac{\rho}{\det\mathbf{\Lambda}}\left\langle \tau\frac{\Lambda_{il}n_l\Lambda_{jk}n_k}{\left|\mathbf{\Lambda}\hat{\mathbf{n}}\right|}\right\rangle. \tag{3.4}$$

Since we consider only volume-conserving simple shear, $\det\mathbf{\Lambda} = 1$. Thus, for filaments in 3D with initial polar angle θ and azimuthal angle φ, the stress tensor is

$$\sigma_{ij} = \frac{\rho}{4\pi}\int_\varphi\int_\theta d\theta d\varphi\sin\theta\left[\tau\frac{\Lambda_{il}n_l\Lambda_{jk}n_k}{\left|\mathbf{\Lambda}\hat{\mathbf{n}}\right|}\right], \tag{3.5}$$

in which the deformation tensor for simple shear in 3D is

$$\mathbf{\Lambda}(\gamma) = \begin{pmatrix} 1 & 0 & \gamma \\ 0 & 1 & 0 \\ 0 & 0 & 1 \end{pmatrix} \tag{3.6}$$

and the transformed orientation vector is

$$\mathbf{\Lambda}\hat{\mathbf{n}} = \begin{pmatrix} \sin\theta\cos\varphi + \gamma\cos\theta \\ \sin\theta\sin\varphi \\ \cos\theta \end{pmatrix}. \tag{3.7}$$

We compute the xz, xx, and zz components of the stress tensor for the 3D case as follows:

$$\sigma_{xz} = \frac{\rho}{4\pi}\int_\varphi\int_\theta d\theta d\varphi\sin\theta\left[\tau\frac{(\sin\theta\cos\varphi + \gamma\cos\theta)\cos\theta}{\left|\mathbf{\Lambda}\hat{\mathbf{n}}\right|}\right] \tag{3.8}$$

$$\sigma_{xx} = \frac{\rho}{4\pi}\int_\varphi\int_\theta d\theta d\varphi\sin\theta\left[\tau\frac{(\sin\theta\cos\varphi + \gamma\cos\theta)^2}{\left|\mathbf{\Lambda}\hat{\mathbf{n}}\right|}\right] \tag{3.9}$$

$$\sigma_{zz} = \frac{\rho}{4\pi}\int_\varphi\int_\theta d\theta d\varphi\sin\theta\left[\tau\frac{\cos^2\theta}{\left|\mathbf{\Lambda}\hat{\mathbf{n}}\right|}\right] \tag{3.10}$$

The integrals are taken over the ranges $0 \leq \theta \leq 2\pi$ and $0 \leq \varphi \leq \pi$. To compare with our results for the 3D FCC network, we use $\mu = 1$ and initial line density $\rho = \frac{12}{\sqrt{2}}$, corresponding to the fully-connected FCC lattice with $l_0 = 1$ [97].

We repeat the same process for the 2D case, in which the deformation tensor for simple shear is

$$\mathbf{\Lambda}(\gamma) = \begin{pmatrix} 1 & \gamma \\ 0 & 1 \end{pmatrix} \tag{3.11}$$

and the transformed orientation vector is

$$\mathbf{\Lambda}\hat{\mathbf{n}} = \begin{pmatrix} \cos\theta + \gamma \sin\theta \\ \sin\theta \end{pmatrix}. \tag{3.12}$$

The resulting components of the 2D stress tensor are calculated as follows:

$$\sigma_{xz} = \frac{\rho}{2\pi} \int_\theta d\theta \left[\tau \frac{(\cos\theta + \gamma \sin\theta)\sin\theta}{|\mathbf{\Lambda}\hat{\mathbf{n}}|} \right] \tag{3.13}$$

$$\sigma_{xx} = \frac{\rho}{2\pi} \int_\theta d\theta \left[\tau \frac{(\cos\theta + \gamma \sin\theta)^2}{|\mathbf{\Lambda}\hat{\mathbf{n}}|} \right] \tag{3.14}$$

$$\sigma_{zz} = \frac{\rho}{2\pi} \int_\theta d\theta \left[\tau \frac{\sin^2\theta}{|\mathbf{\Lambda}\hat{\mathbf{n}}|} \right] \tag{3.15}$$

Here, the integrals are taken over the range $0 \leq \theta \leq 2\pi$.

3.8.2 Principal strain axes for simple shear

For simple shear with deformation gradient tensor

$$\mathbf{\Lambda}(\gamma) = \begin{pmatrix} 1 & 0 & \gamma \\ 0 & 1 & 0 \\ 0 & 0 & 1 \end{pmatrix}, \tag{3.16}$$

we can decompose $\boldsymbol{\Lambda}$ into a combination of a pure stretch $\boldsymbol{U}$ and a rigid body rotation $\boldsymbol{R}$, satisfying $\boldsymbol{\Lambda} = \boldsymbol{RU}$. From the right Cauchy-Green tensor $\boldsymbol{C} = \boldsymbol{U}^2 = \boldsymbol{\Lambda}^T\boldsymbol{\Lambda}$, we determine

$$\boldsymbol{U} = \frac{1}{\sqrt{4+\gamma^2}} \begin{pmatrix} 2 & 0 & \gamma \\ 0 & \sqrt{4+\gamma^2} & 0 \\ \gamma & 0 & 2+\gamma^2 \end{pmatrix}. \tag{3.17}$$

The eigenvalues of $\boldsymbol{U}$ are

$$\lambda_1 = \frac{\gamma + \sqrt{\gamma^2+4}}{2}, \quad \lambda_2 = \frac{-\gamma + \sqrt{\gamma^2+4}}{2}, \quad \lambda_3 = 1 \tag{3.18}$$

with corresponding eigenvectors

$$\boldsymbol{v}_1 = \left(\frac{1}{2}\left(-\gamma + \sqrt{4+\gamma^2}\right), 0, 1\right)$$

$$\boldsymbol{v}_2 = \left(\frac{1}{2}\left(-\gamma - \sqrt{4+\gamma^2}\right), 0, 1\right)$$

$$\boldsymbol{v}_3 = (0, 1, 0)$$

λ_1 and λ_2 correspond to the elongation l/l_0 along the axes of maximum extension and compression, respectively.

The rotation matrix $\boldsymbol{R}$ is determined as $\boldsymbol{R} = \boldsymbol{\Lambda}\boldsymbol{U}^{-1}$,

$$\boldsymbol{R} = \frac{1}{\sqrt{4+\gamma^2}} \begin{pmatrix} 2 & 0 & \gamma \\ 0 & \sqrt{4+\gamma^2} & 0 \\ -\gamma & 0 & 2 \end{pmatrix} \tag{3.19}$$

The maximum stretch direction then corresponds to $\boldsymbol{v}_1' = \boldsymbol{R}\boldsymbol{v}_1$. In the limit of small strains, $\boldsymbol{v}_1'$ is oriented at $\theta = \pi/4$ above the x-axis, in the x-z plane.

3.8.3 Bending interaction models

Prior work has shown that network models with bond-bending interactions (angle constraints between all nearest-neighbor bonds) exhibit the same strain-driven critical behavior as networks with freely-hinging crosslinks (angle constraints between only initially collinear nearest-neighbor bonds) [50, 51]. To emphasize that the details of the bending interactions do not influence our conclusions with regard to the normal stresses, we consider the mechanics of phantomized triangular networks with $z = 3.4$ and either freely-hinging crosslinks (bending along initially collinear fibers) or bond-bending interactions, both with $\tilde{\kappa} = 10^{-5}$. In Fig. 3.10, we show both K and the normal stresses σ_{ii}/γ^2 for each bending interaction type. We observe that the networks show qualitatively similar behavior in both cases, with $K \propto \tilde{\kappa}$ and $\sigma_{ii} \propto \tilde{\kappa}\gamma^2$ below the critical strain. The only apparent difference is that the magnitudes of K and the normal stresses are slightly higher for bond-bending networks than for networks with freely-hinging crosslinks in the bending-dominated regime. This is due to the additional angle constraints imposed by bond-bending interactions.

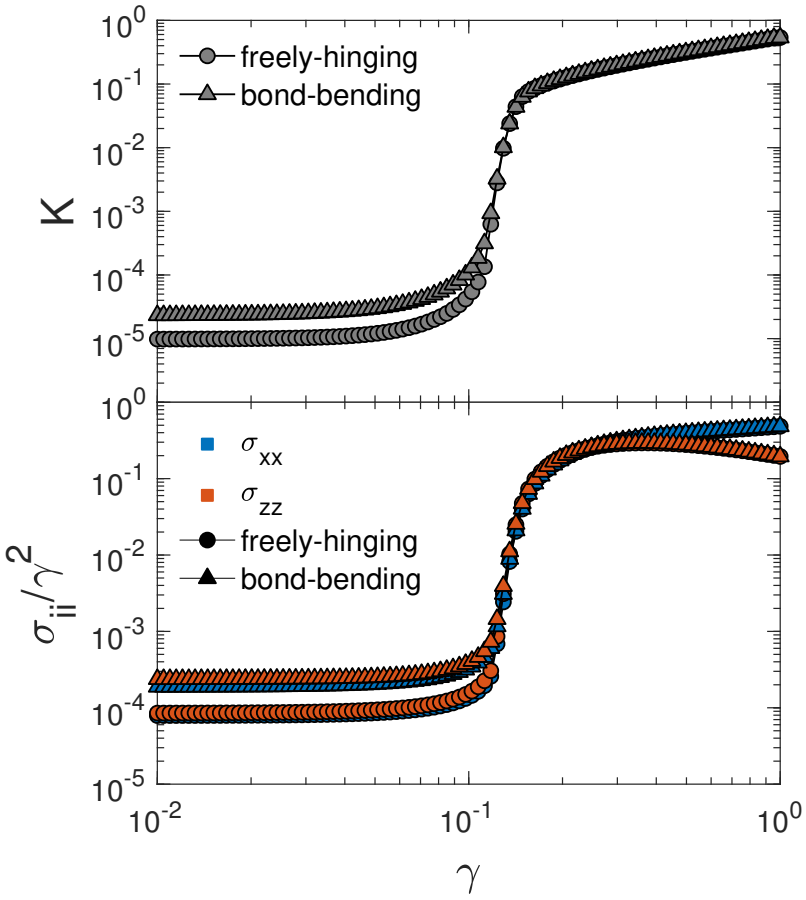

Figure 3.10: Top: Differential shear modulus K vs. shear strain γ for 2D phantomized triangular networks with $z = 3.4$, $\tilde{\kappa} = 10^{-6}$ and $\delta_{\max} = 0.4$, with freely-hinging crosslinks and bending interactions only along fibers (triangles) and with bond-bending interactions between all nearest-neighbor bonds (circles). Bottom: Normal stresses σ_{xx} and σ_{zz}, both normalized by γ^2, as a function of γ for the same systems. Both K and σ_{ii} are higher in networks with bond-bending interactions than in the same networks with freely-hinging crosslinks, due to the additional angle constraints.

3.8.4 Packing-derived networks with varying connectivity

In Fig. 3.11, we show both $N_1/(\sigma_{xz}\gamma)$ and K for 2D packing-derived networks of size $W = 100$ with $\kappa = 10^{-5}$ and varying z. We observe that, for individual samples, peaks in $N_1/(\sigma_{xz}\gamma)$ occur at the z-dependent critical strain. On average, the Lodge-Meissner relation is satisfied.

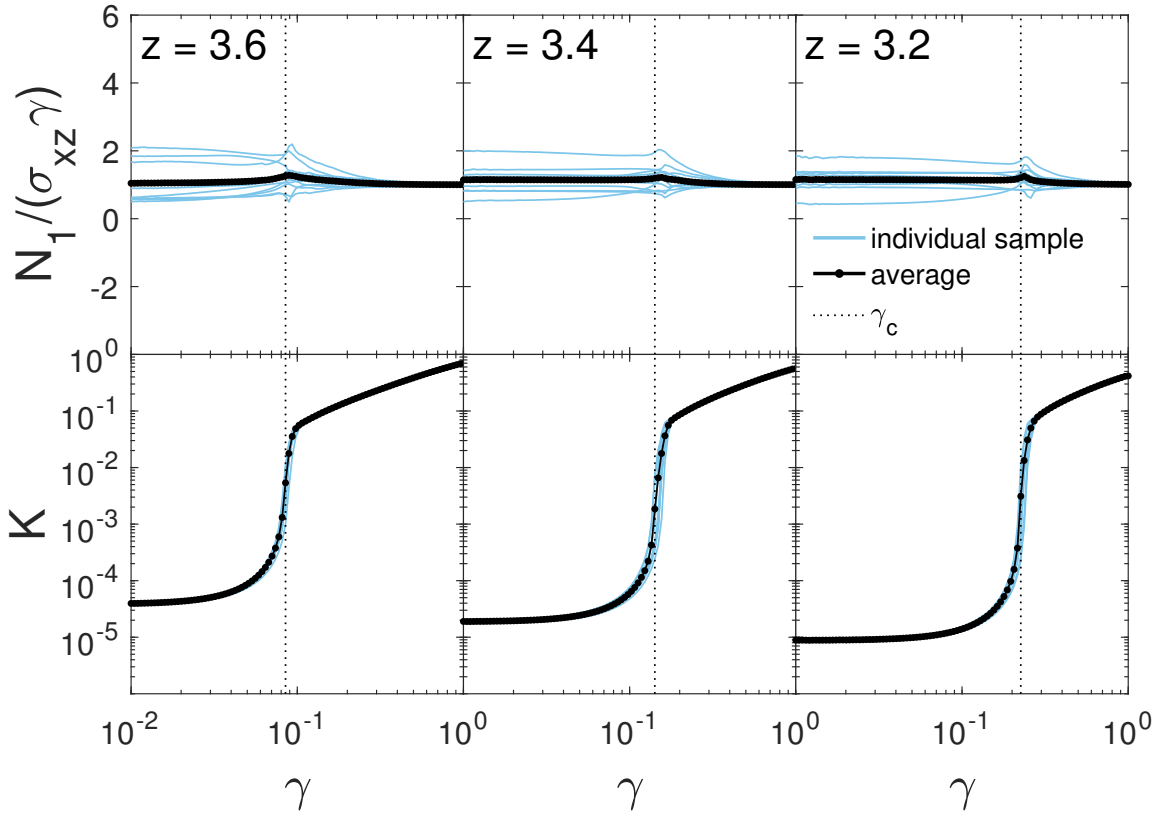

Figure 3.11: In 2D packing-derived networks with $\kappa = 10^{-5}$ and varying z, we observe either upward or downward peaks in $N_1/(\sigma_{xz}\gamma)$ (top) for individual samples at the z-dependent critical strain γ_c, determined as the inflection point of K vs γ (bottom) plotted on a logarithmic scale. When the stress is averaged over all samples, the network ensemble approximately satisfies the Lodge-Meissner relation, such that $N_1/(\sigma_{xz}\gamma) = 1$ over the full strain range.

Chapter 4

Scaling theory for mechanical critical behavior in fiber networks

This chapter is adapted from Ref. [128]:

> **Jordan L. Shivers**, Sadjad Arzash, Abhinav Sharma, and Fred C. MacKintosh. Scaling Theory for Mechanical Critical Behavior in Fiber Networks. ***Physical Review Letters***, 122 (18): 188003, 2019.

4.1 Abstract

As a function of connectivity, spring networks exhibit a critical transition between floppy and rigid phases at an isostatic threshold. For connectivity below this threshold, fiber networks were recently shown theoretically to exhibit a rigidity transition with corresponding critical signatures as a function of strain. Experimental collagen networks were also shown to be consistent with these predictions. We develop a scaling theory for this strain-controlled transition. Using a real-space renormalization approach, we determine relations between the critical exponents governing the transition, which we verify for the strain-controlled transition using numerical simulations of both triangular lattice-based and packing-derived fiber networks.

4.2 Introduction

It has long been recognized that varying connectivity can lead to a rigidity transition in networks such as those formed by springlike, central force (CF) connections between nodes. Maxwell introduced a counting argument for the onset of rigidity for such systems in d dimensions with N nodes, in which the number of degrees of freedom dN is balanced by the number of constraints $Nz/2$, where z is the average coordination number of the network [46]. The transition at this *isostatic* point of marginal stability has been shown to exhibit signatures of criticality. Such a balance of constraints and degrees of freedom is important for understanding rigidity percolation and jamming [41, 65, 81, 129, 130]. Even in networks with additional interactions that lead to stability below the CF isostatic point, the mechanical response can still exhibit strong signatures of criticality in the vicinity of the CF isostatic point [48, 68, 79, 119]. More recently, criticality has been shown in fiber networks as a function of strain for systems well below the isostatic point [50].

While both jammed particle packings and fiber networks exhibit athermal ($T = 0$) mechanical phase transitions and superficially similar critical behavior, these systems have strong qualitative differences. In particular, there is growing evidence that the jamming transition is mean-field [81, 131]. Goodrich et al. recently proposed a scaling theory and performed numerical simulations of jamming which both demonstrate mean-field exponents and support the conclusion that the upper critical dimension $d_u = 2$ for the jamming transition [131]. In contrast, fiber networks to date have shown distinctly non-mean-field behavior [48, 50, 68, 119]. Although many aspects of the critical behavior of fiber networks, including various critical exponents, have been quantified, prior studies have been limited to to simulations and the development of effective medium theories. Importantly, a theory has been lacking to identify critical exponents or even scaling relations among exponents, in order to understand the observed non-mean-field character of the stiffening transition in fiber networks. Here,

we develop a scaling theory for both the sub-isostatic, strain controlled transition, as well as the transition in z near the isostatic point for athermal fiber networks. We derive scaling relations among the various exponents and demonstrate good agreement with numerical simulations. Interestingly, our results imply that the upper critical dimension for fiber networks is $d_u > 2$, in contrast with jamming packings.

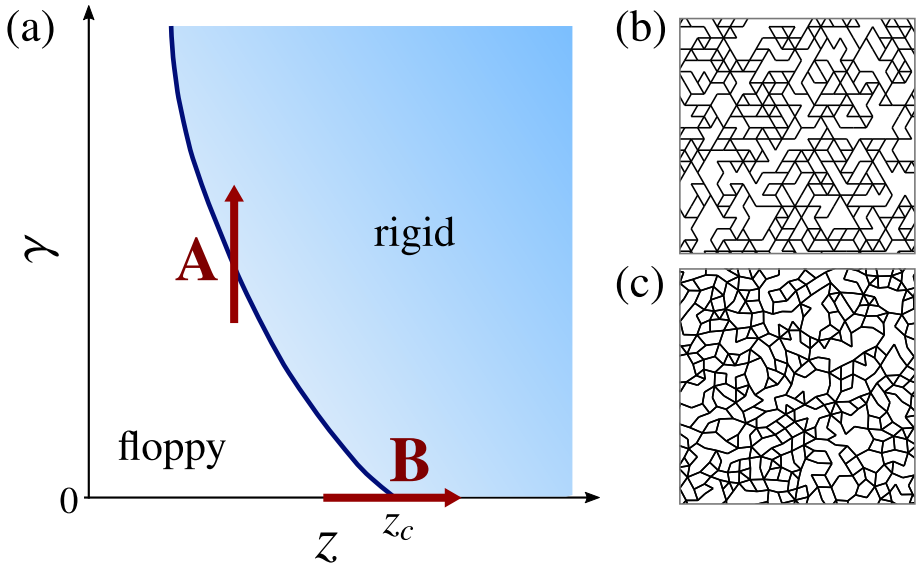

Figure 4.1: (a) Schematic phase diagram depicting the state of mechanical rigidity of a central force network as a function of coordination number z and applied shear strain γ. The arrow A depicts the strain-controlled transition and B depicts the transition at the isostatic point. With the addition of bending interactions, the floppy region becomes instead bending-dominated, but the critical curve $\gamma_c(z)$ vs. z remains the same. (b) Portion of a a triangular network and (c) a 2D packing-derived network, both diluted to $z = 3.3 < z_c$.

Near the isostatic point with average coordination number $z = z_c = 2d$, spring networks exhibit linear shear moduli G that vary as a power of $|z - z_c|$ for $z > z_c$ [79, 81, 132]. In the floppy or sub-isostatic regime with $z < z_c$, such systems can be stabilized by introducing additional interactions [48, 79] or by imposing stress or strain [133, 134]. It was recently shown that sub-isostatic networks undergo a transition from floppy to rigid as a function of shear strain γ [50, 52]. Moreover, this fundamentally nonlinear transition was identified as a line of critical points characterized by a $z-$dependent threshold $\gamma_c(z)$, as sketched in Fig. 4.1a. Above this strain threshold, the differential or tangent shear modulus $K = d\sigma/d\gamma$ scales as

a power law in strain, with $K \sim |\gamma - \gamma_c|^f$. Introducing bending interactions with rigidity κ between nearest neighbor bonds stabilizes sub-isostatic networks below the critical strain, leading to $K \sim \kappa$ for $\gamma < \gamma_c$. Both of these regimes are captured by the scaling form [135]

$$K \approx |\gamma - \gamma_c|^f \, \mathcal{G}_{\pm} \left(\kappa / |\gamma - \gamma_c|^{\phi} \right) \tag{4.1}$$

for $\kappa > 0$, in which the branches of the scaling function $\mathcal{G}_{\pm}$ account for the strain regimes above and below γ_c. This scaling form was also shown to successfully capture the nonlinear strain stiffening behavior observed in experiments on reconstituted networks of collagen, a filamentous protein that provides mechanical rigidity to tissues as the primary structural component of the extracellular matrix [52]. Collagen constitutes an excellent experimental model system on which to study this transition, as it forms elastic networks that are deeply sub-isostatic ($z \approx 3.4$ [136], whereas $z_c = 6$ in 3D) in which individual fibrils have sufficiently high bending moduli to be treated as athermal elastic rods.

4.3 Scaling theory

For the strain-controlled transition at a fixed $z < z_c$ (arrow A in Fig. 4.1a), we define a reduced variable $t = \gamma - \gamma_c$ that vanishes at the transition and let $h(t, \kappa)$ denote the Hamiltonian or elastic energy per unit cell. This energy depends on the bending stiffness κ that also vanishes at the transition. Assuming the system becomes critical as $t, \kappa \to 0$, we consider the real-space renormalization of the system when scaled by a factor L to form a block or effective unit cell composed of L^d original cells, where d is the dimensionality of the system [137]. Under this transformation, the energy per block becomes $h(t', \kappa') = L^d h(t, \kappa)$, where t' and κ' are renormalized values of the respective parameters. We assume that the parameters evolve according to $t \to t' = tL^x$ and $\kappa \to \kappa' = \kappa L^y$, where the exponents x, y can be assumed to be

positive, since the system must evolve away from criticality. Combining these, we find the elastic energy

$$h(t,\kappa) = L^{-d} h(tL^x, \kappa L^y). \tag{4.2}$$

The stress is simply given by the derivative with respect to strain of the elastic energy per volume, which is proportional to $h(t,\kappa)$. Thus, $\sigma \sim \frac{\partial}{\partial\gamma} h \sim \frac{\partial}{\partial t} h(t,\kappa) \sim L^{-d+x} h_{1,0}(tL^x, \kappa L^y)$ and the stiffness

$$K = \frac{\partial}{\partial\gamma}\sigma \sim \frac{\partial^2}{\partial t^2} h(t,\kappa) \sim L^{-d+2x} h_{2,0}(tL^x, \kappa L^y), \tag{4.3}$$

where $h_{n,m}$ refers to the combined n-th partial with respect to t and m-th partial with respect to κ of h. Being derivatives of the energy with respect to the control variable γ, the stress and stiffness are analogous to the entropy and heat capacity for a thermal system with phase transition controlled by temperature. If we let $L = |t|^{-1/x}$, then the correlation length scales according to $\xi \sim L \sim |t|^{-\nu}$, from which we can identify the correlation length exponent $\nu = 1/x$. Thus, the stiffness can be expressed as in Eq. (4.1), where $\mathcal{G}_\pm(s) \sim h_{2,0}(\pm 1, s)$ and

$$f = d\nu - 2 \quad \text{and} \quad \phi = y\nu. \tag{4.4}$$

The first of these is a hyperscaling relation analogous to that for the heat capacity exponent for thermal critical phenomena, but with the opposite sign. Thus, $f > 0$ corresponds to nonlinear stiffness K that is non-divergent. For $\gamma > \gamma_c$, we expect that $h_{2,0}(1,s)$ is approximately constant for $s \ll 1$, so that $K \sim |\gamma - \gamma_c|^f$, while for $\gamma < \gamma_c$ we expect that $h_{2,0}(-1,s) \sim s$ for $s \ll 1$, so that

$$K \sim \kappa |\gamma - \gamma_c|^{-\lambda}, \tag{4.5}$$

consistent with a bending-dominated regime. Moreover, the susceptibility-like exponent

is expected to be $\lambda = \phi - f$.

Near the critical strain, athermal networks exhibit large, nonaffine internal rearrangements in response to small changes in applied strain [50, 52]. These nonaffine strain fluctuations are analogous to divergent fluctuations in other critical systems. In response to an incremental strain strain step $\delta\gamma$, the nonaffine displacement of the nodes is expected to be proportional to $\delta\gamma$. Thus, the nonaffine fluctuations can be captured by $\delta\Gamma \sim \langle \left|\delta\mathbf{u} - \delta\mathbf{u}^A\right|^2 \rangle / \delta\gamma^2$, where $\delta\mathbf{u} - \delta\mathbf{u}^A$ represents the deviation relative to a purely affine displacement $\delta\mathbf{u}^A$. For large systems with small κ, $\delta\Gamma$ diverges as $t \to 0$ [52]. Since the nonaffine displacements δu^2 are determined by the minimization of $h(t, \kappa)$, for small κ, $h \sim \kappa\delta u^2 \sim \kappa\delta\gamma^2\delta\Gamma$. Thus, the nonaffine fluctuations are predicted to diverge as

$$\delta\Gamma \sim \frac{\partial}{\partial\kappa}\frac{\partial^2}{\partial t^2}h(t,\kappa) \sim |t|^{-\lambda}, \tag{4.6}$$

with the same exponent $\lambda = \phi - f$ as in Eq. (4.5).

4.4 Computational model

To test the scaling relations derived above, we study two complementary models of fiber networks: triangular lattice-based networks and jammed packing-derived networks. Our triangular networks consist of fibers of length W arranged on a periodic triangular lattice with lattice spacing $l_0 = 1$, with freely-hinging crosslinks attaching overlapping fibers. To avoid system-spanning straight fibers, we initially cut a single randomly chosen bond on each fiber, yielding an initial network coordination number z approaching 6 from below with increasing W [48, 113]. We prepare packing-derived networks by populating a periodic square unit cell of side length W with $N = W^2$ randomly placed, frictionless bidisperse disks with soft repulsive interactions and with a ratio of radii of 1: 1.4. The disks are uniformly expanded until the point at which the system develops finite bulk and shear moduli, after which a contact network excluding

rattlers is generated [47, 81, 117]. Sufficiently large networks prepared using this protocol have an initial connectivity $z \approx z_c$ [138].

For both network structures, we reduce z to a value below the isostatic threshold by bond dilution and removal of dangling ends (see Appendix, Section 4.8). We use a random dilution process, in contrast with special cutting protocols that have been used previously to suppress variation in local connectivity and promote mean-field behavior [79, 139]. Unless otherwise stated, we use triangular networks of size $W = 140$ and packing-derived networks of size $W = 120$, both with $z = 3.3$, and simulate ensembles of at least 30 network realizations each. Sample network structures are shown in Fig. 4.1b-c.

We treat each bond as a Hookean spring with 1D modulus μ, such that the contribution of stretching to the network energy is

$$\mathcal{H}_S = \frac{\mu}{2} \sum_{\langle ij \rangle} \frac{(l_{ij} - l_{ij,0})^2}{l_{ij,0}} \tag{4.7}$$

in which l_{ij} and $l_{ij,0}$ are the length and rest length, respectively, of the bond connecting nodes i and j. Bending interactions are included between pairs of nearest-neighbor bonds, which are treated as angular springs with bending modulus κ. For triangular networks, bending interactions are only considered between pairs of bonds along each fiber, which are initially collinear, whereas for packing-derived networks we account for all nearest-neighbor bonds. The contribution of bending to the network energy is

$$\mathcal{H}_B = \frac{\kappa}{2} \sum_{\langle ijk \rangle} \frac{(\theta_{ijk} - \theta_{ijk,0})^2}{l_{ijk,0}} \tag{4.8}$$

in which θ_{ijk} and $\theta_{ijk,0}$ are the angle and rest angle, respectively, between bonds ij and jk, and $l_{ijk,0} = (l_{ij,0} + l_{jk,0})/2$. We set $\mu = 1$ and vary the dimensionless bending stiffness κ [1].

[1]Note that κ refers to the dimensionless bending stiffness $\kappa \equiv \kappa_b/(\mu l_c^2)$, in which κ_b is the bending

We apply incremental quasistatic simple shear strain steps using Lees-Edwards periodic boundary conditions [85], minimizing the total network energy $\mathcal{H} = \mathcal{H}_S + \mathcal{H}_B$ at each step using the FIRE algorithm [83]. We compute the stress tensor as

$$\sigma_{\alpha\beta} = -\frac{1}{A}\sum_i f_{i,\alpha} u_{i,\beta}. \tag{4.9}$$

in which $\mathbf{u}_i$ is the position of node i, $\mathbf{f}_i$ is the total force acting on node i, and A is the area of the system [86, 90] (see Appendix, Section 4.8). For the triangular lattice, $A = (\sqrt{3}/2)W^2$, and for packing-derived networks, $A = W^2$. The differential shear modulus K is computed as $K = \partial\sigma_{xy}/\partial\gamma$. To symmetrize K, we shear each network in both the $\gamma > 0$ and $\gamma < 0$ directions. Figure 4.2a shows $K(\gamma)$ for triangular networks with varying bending rigidity.

4.5 Results

4.5.1 Near the critical strain

First, we consider the scaling of K as a function of strain near γ_c. We determine γ_c for individual samples as the strain corresponding to the onset of finite K in the CF ($\kappa = 0$) limit, and utilize the mean of the resulting distribution, $\langle\gamma_c\rangle$, for our scaling analysis. The γ_c distribution for triangular networks of size $W = 140$ is shown in Figure 4.2a. We observe that with increasing system size, the width of the γ_c distribution decreases (see Appendix, Section 4.8). The stiffness K exhibits a small discontinuity at γ_c for $\kappa = 0$, as shown in Fig. 4.2a, consistent with prior reports in similar networks [77, 140]. We note that this discontinuity is, however, consistent with the critical nature of the transition, since K is not an order parameter.

We then determine f from $K \sim |\gamma - \gamma_c|^f$ in the low-κ limit. We obtain a

rigidity used in the simulations and l_c is the average bond length in the unstrained network, $l_c = \langle l_{ij,0}\rangle$, with $l_c = l_0 = 1$ for triangular networks and $l_c \approx 1.03$ for packing-derived networks.

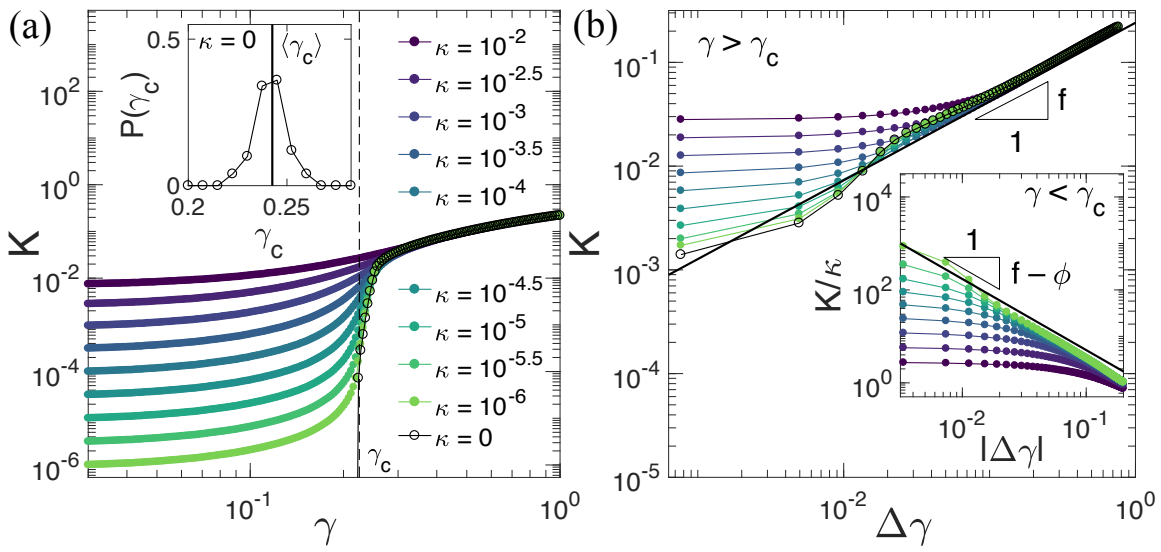

Figure 4.2: (a) Differential shear modulus K vs. shear strain for triangular networks of connectivity $z = 3.3$, with varying reduced bending stiffness κ. The dashed line indicates the observed critical strain γ_c for the ensemble. The inset shows the probability distribution of γ_c for 50 individual network samples with $\kappa = 0$. (b) For $\gamma > \gamma_c$ and with decreasing κ, K converges to the form $K \sim |\gamma - \gamma_c|^f$, with $f = 0.73 \pm 0.04$. These data are for the same networks as in (a). Inset: In the low-κ limit and below γ_c, K/κ converges to a power law in $|\Delta\gamma|$ with exponent $f - \phi \approx -1.5$.

distribution of estimated f values using sample-specific K curves and γ_c values for networks with $\kappa = 0$, yielding an estimate of $f = 0.73 \pm 0.04$ for triangular networks, as shown in Fig. 4.2b with decreasing κ. Similarly, for packing-derived networks we find $f = 0.68 \pm 0.04$ (see Appendix, Section 4.8). We then estimate ϕ by averaging values computed from two separate scaling predictions, as follows. For $\gamma < \gamma_c$, we show the results for Eq. (4.5) in the inset to Fig. 4.2b. We also note that continuity of K as a function of strain near γ_c requires that $\mathcal{G}_{\pm}(s) \sim h_{2,0}(\pm 1, s) \sim s^{f/\phi}$ for large s. Thus, $K(\gamma_c) \sim \kappa^{f/\phi}$, as shown in the insets of Fig. 3a-b. Averaging the ϕ values computed from these corresponding fits, using our previously determined values for f, we estimate $\phi = 2.26 \pm 0.09$ for triangular networks and $\phi = 2.05 \pm 0.08$ for packing-derived networks. These values of f and ϕ are used in Figs. 4.3a-b, which demonstrate the collapse according to Eq. (4.1)[2].

[2]Interestingly, the values of f for these two systems appear to be consistent. It is unclear whether the difference between the corresponding values of ϕ is significant.

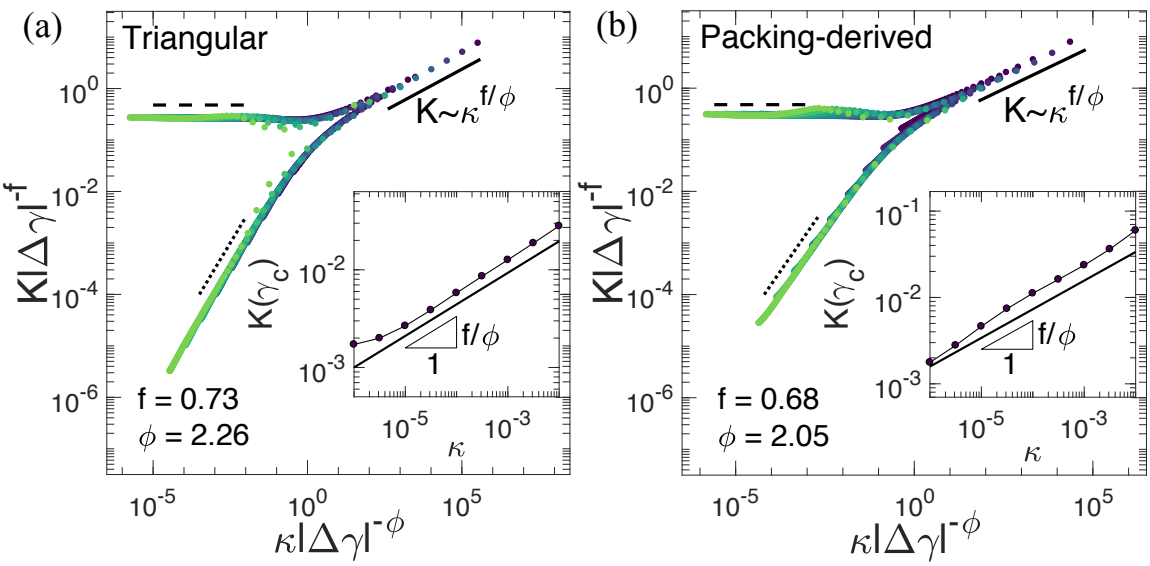

Figure 4.3: Plotting the K vs. $|\Delta\gamma|$ data for both (a) triangular networks and (b) packing-derived networks according to the Widom-like scaling predicted by Eq. 4.1, and using the values of f and ϕ determined previously, yields a successful collapse for both systems. Dashed lines have slope 0 and dotted lines have slope 1. Insets: At the critical strain, $K \sim \kappa^{f/\phi}$.

We compute the nonaffine fluctuations $\delta\Gamma$ as

$$\delta\Gamma = \frac{1}{N l_c^2 \delta\gamma^2} \sum_i \|\delta\mathbf{u}_i^{\mathrm{NA}}\|^2 \tag{4.10}$$

in which N is the number of nodes, l_c is the average bond length, and $\delta\mathbf{u}_i^{\mathrm{NA}} = \delta\mathbf{u}_i - \delta\mathbf{u}_i^{\mathrm{A}}$ is the nonaffine component of the displacement of node i due to the incremental strain $\delta\gamma$. Plotting $\delta\Gamma$ vs. $\gamma - \gamma_c$ in Fig. 4a, we observe agreement with the scaling predicted from Eq. (4.9) using the f and ϕ values determined above. Importantly, as predicted, the corresponding critical exponent $\lambda = \phi - f$ is the same as for Eq. (4.5), with $\lambda \simeq 1.5$ [141]. Further, we observe that near γ_c, the expected scaling $\delta\Gamma(\gamma_c) \sim \kappa^{f/\phi - 1}$ appears to be satisfied (see Appendix, Section 4.8).

It is apparent from Fig. 4a that the divergence of the fluctuations near γ_c is suppressed by finite-size effects. This is consistent with a diverging correlation length $\xi \sim |t|^{-\nu}$. Critical effects such as the divergence of $\delta\Gamma$ are limited as the correlation length becomes comparable to the system size W, corresponding to a value of $t \sim$

$t_W = W^{-1/\nu}$. Thus, the maximum value of $\delta\Gamma$ increases as $\delta\Gamma \sim W^{(\phi-f)/\nu}$ (Fig. 4.4a inset). From least-squares fits to this scaling for both triangular and packing-derived networks with $\kappa = 0$ and $\kappa = 10^{-7}$, combined with our estimates for ϕ and f, we determine that $\nu = 1.3 \pm 0.2$ for both systems. We then verify that this leads to a scaling collapse in a plot of $\delta\Gamma W^{(f-\phi)/\nu}$ vs $tW^{1/\nu}$ for both systems with $\kappa = 0$, as shown in Fig. 4b, and with finite κ (see Appendix, Section 4.8). This finite-size scaling is consistent with the (hyperscaling-like) relation $f = 2\nu - 2$ in 2D from Eq. (4.4).

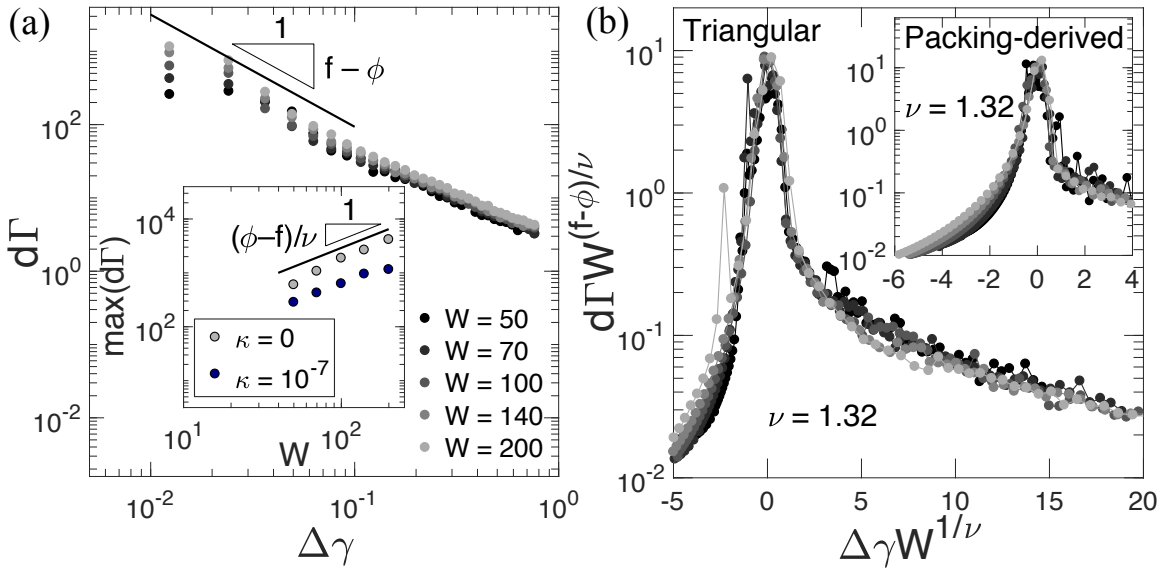

Figure 4.4: (a) Near the critical strain, the nonaffinity scales as $\delta\Gamma \sim |\Delta\gamma|^{f-\phi}$. These data correspond to triangular networks with $\kappa = 10^{-7}$ and $z = 3.3$, with varying system size. Inset: Nonaffine fluctuations are limited by the system size. For small or zero κ, the maximum of $\delta\Gamma$ scales as $\max(\delta\Gamma) \sim W^{(\phi-f)/\nu}$, with $\nu = 1.3 \pm 0.2$. (b) Plots of $\delta\Gamma/W^{(\phi-f)/\nu}$ vs. $(\gamma - \gamma_c)W^{1/\nu}$ for triangular networks and (inset) packing-derived networks with $\kappa = 0$ demonstrate successful scaling collapse using the f and ϕ values determined from K, with ν values determined from the scaling relation.

4.5.2 Near the isostatic point

For networks near the isostatic transition at $z = z_c$, we define a dimensionless distance $\Delta = z - z_c$ from the isostatic point and let $h(\gamma, \kappa, \Delta)$ be the Hamiltonian or elastic energy per unit cell. At the isostatic point, since $\gamma_c = 0$, t above reduces to the strain γ. Assuming the system becomes critical as $\gamma, \kappa, \Delta \to 0$, we can follow a

similar real-space renormalization procedure as above, resulting in

$$h(\gamma, \kappa, \Delta) = L^{-d} h(\gamma L^x, \kappa L^y, \Delta L^w). \tag{4.11}$$

Although the exponents x, y, and w at the isostatic point can be assumed to be positive, we do not necessarily assume the same values of the exponents x and y as determined for the strain-controlled transition. We can again determine the stress σ and stiffness K as in Eq. (4.3). By letting $L = |\Delta|^{-1/w}$, we again identify the correlation length exponent $\nu' = 1/w$ and find

$$K \sim |\Delta|^{f'} h_{2,0,0}(0, \kappa/|t|^{\phi'}, \pm 1), \tag{4.12}$$

where

$$f' = (d - 2x)\nu', \quad \phi' = y\nu'. \tag{4.13}$$

Moreover, following similar arguments as above, it can be shown that $\delta\Gamma \sim |\Delta|^{-\lambda'}$, where $\lambda' = \phi' - f'$ [142] (see Appendix, Section 4.8), consistent with the values $f' \simeq 1.4 \pm 0.1$, $\phi' \simeq 3.0 \pm 0.2$, $\nu' \simeq 1.4 \pm 0.2$, and $\lambda' \simeq 2.2 \pm 0.4$ reported in Ref. [48]. While our approach uses the elastic energy, it is interesting to note that prior work on rigidity percolation has suggested the use of the number of floppy modes as a free energy [44].

4.6 Conclusions

The scaling theory and relations derived here for the strain- and connectivity-controlled rigidity transitions in athermal fiber networks are consistent with our numerical results, as well as prior results near the isostatic point [48, 68, 119]. Interestingly, for the subisostatic, strain-controlled transition, we observe that simulations of both triangular and packing-derived networks exhibit consistent non-mean-field

exponents. This, together with agreement with the hyperscaling relation in Eq. (4.4) suggest that the upper critical dimension for fiber networks is $d_u > 2$, in contrast with jammed packings at the isostatic point [131]. Our observations, combined with prior evidence of similar exponents for alternate subisostatic network structures, including 2D and 3D phantom networks, honeycomb networks, and Mikado networks [50, 51], suggest that non-mean-field behavior might be ubiquitous in randomly-diluted subisostatic networks. Interestingly, the hyperscaling relation in Eq. (4.4), together with the observation that $f > 0$, suggests that fiber networks satisfy the Harris criterion [143], which would imply that such networks should be insensitive to disorder. Further work will be needed to test this hypothesis, as well as the scaling relations derived here in 3D.

4.7 Acknowledgments

This work was supported in part by the National Science Foundation Division of Materials Research (Grant DMR-1826623) and the National Science Foundation Center for Theoretical Biological Physics (Grant PHY-1427654). J.L.S. was supported in part by the Riki Kobayashi Fellowship in Chemical Engineering and the Ken Kennedy Institute for Information Technology Oil & Gas HPC Conference Fellowship. The authors acknowledge helpful discussions with Andrea Liu, Tom Lubensky and Michael Rubinstein, as well as discussions with Edan Lerner and Robbie Rens on central force packing-derived networks.

4.8 Appendix

4.8.1 Removal of disconnected and dangling clusters

Our reported coordination number z corresponds to the average network coordination after the removal of dangling and disconnected bond clusters, which do not contribute to the network's mechanical response in the zero-frequency limit. Dangling clusters, shown in Fig. 4.5a, are defined as clusters of bonds connected to the rest of the network by a single bond, or "bridge". Bridges are identified as biconnected components containing only a single bond and subsequently removed, resulting in disconnected clusters. Disconnected clusters, shown in Fig. 4.5b, are then removed by identifying all connected components in the network and removing all but the largest, corresponding to the bulk network. The Boost graph library [84] is utilized for identification of connected and biconnected components.

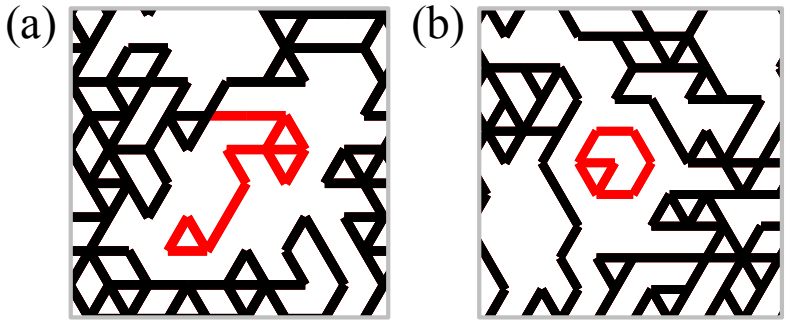

Figure 4.5: (a) A dangling cluster (red) is defined as a cluster of bonds connected to the rest of the network by only one bond. These are detected and removed by removing "bridges," bonds which, if cut, disconnect the graph. Bridges are identified as biconnected components containing only one bond. (b) A disconnected cluster (red) is a cluster of bonds that is disconnected from the bulk network. We remove these by identifying all independent connected components and retaining only the largest one.

4.8.2 System-size dependence of the critical strain distribution

We determine the critical shear strain γ_c for each network sample as the strain corresponding to the onset of finite K in the $\kappa = 0$ limit. Consistent with prior work

[77], we observe a decrease in the width of the γ_c distribution with increasing system size, as shown in Fig. 4.6 for triangular networks.

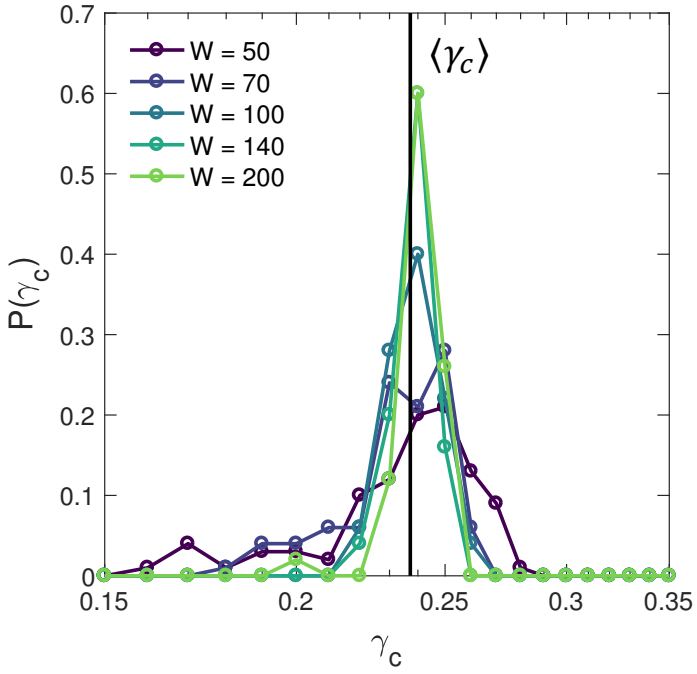

Figure 4.6: The probability distribution of the critical strain γ_c decreases in width with increasing system size. These data correspond to triangular networks with $\kappa = 0$ and $z = 3.3$, with at least 50 networks each for each system size. The vertical black line denotes the average γ_c value for networks of size $W = 200$.

4.8.3 Strain-controlled criticality in packing-derived networks

Fig. 4.7 shows the measured shear stress vs. strain for both triangular and packing-derived networks. A transition from a bending-dominated regime with $\sigma_{xy} \sim \kappa$ to a stretching-dominated regime with $\sigma_{xy} \sim \mu$ occurs at the critical strain γ_c, at which networks with $\kappa = 0$ develop nonzero stress. Figure 4.8 shows the computed K vs. strain curves as well as the scaling of K with $\Delta\gamma$ for packing-derived networks, with $K \sim |\Delta\gamma|^f$ for $\gamma > \gamma_c$ and $K \sim \kappa|\Delta\gamma|^{f-\phi}$ for $\gamma < \gamma_c$.

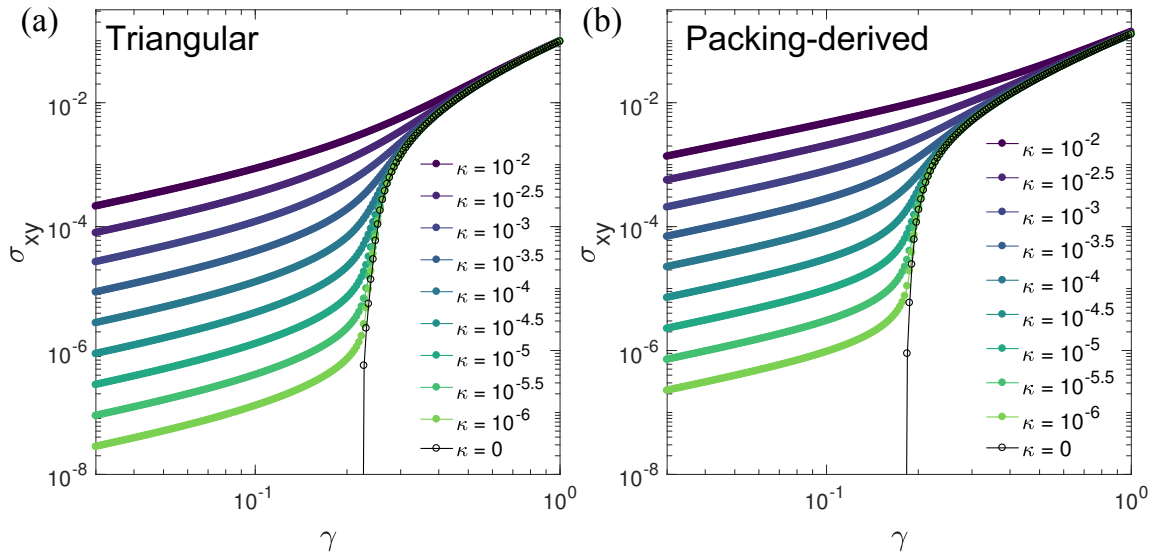

Figure 4.7: Shear stress σ_{xy} vs. shear strain γ for (a) triangular networks of size $W = 140$ and (b) packing-derived networks of size $W = 120$, both diluted to $z = 3.3$, with varying reduced bending stiffness κ.

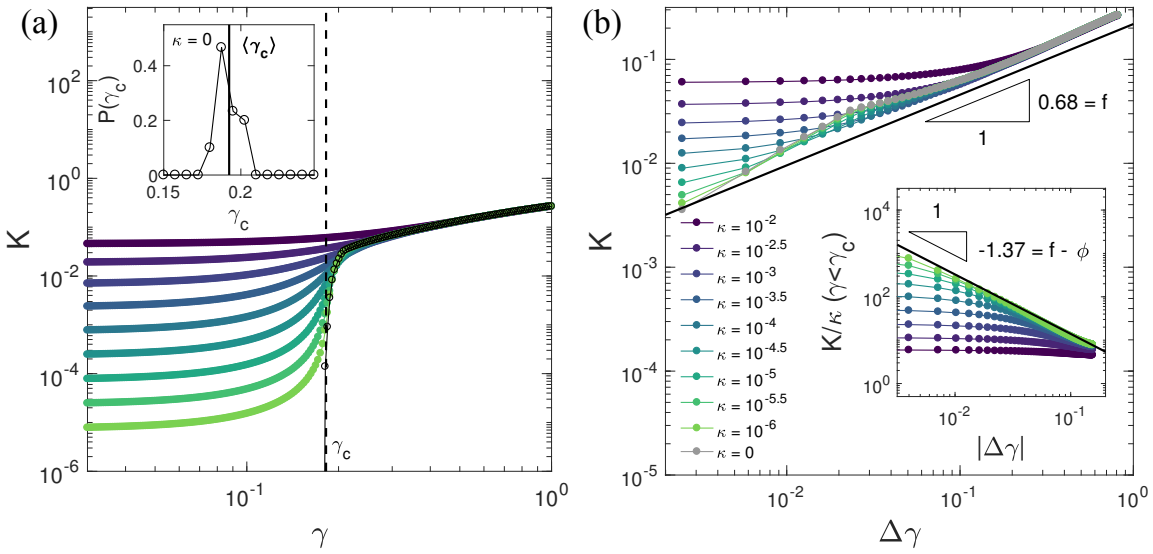

Figure 4.8: (a) Differential shear modulus K vs. shear strain for diluted packing-derived networks of size $W = 120$ and connectivity z = 3.3, with varying reduced bending stiffness κ. The dashed line indicates the observed critical strain γ_c for the ensemble. The inset shows the probability distribution for the measured γ_c values for 30 individual network samples with $\kappa = 0$. (b) For $\gamma > \gamma_c$ and with decreasing κ, K converges to the form $K \sim |\gamma - \gamma_c|^f$, with $f = 0.68 \pm 0.04$. These data are for the same networks as in (a). Inset: In the low-κ limit and below γ_c, K/κ converges to a power law in $|\Delta\gamma|$ with exponent $f - \phi \sim -1.37$.

4.8.4 Bending-rigidity dependence of the nonaffine fluctuations

For both triangular and packing-derived networks, finite bending rigidity suppresses nonaffine fluctuations, as shown in Fig. 4.9a/c. At the critical strain, the nonaffine fluctuations grow with decreasing κ as $\kappa^{(f-\phi)/\phi}$ (see Fig. 4.9b/d), as predicted by the scaling theory in the main text.

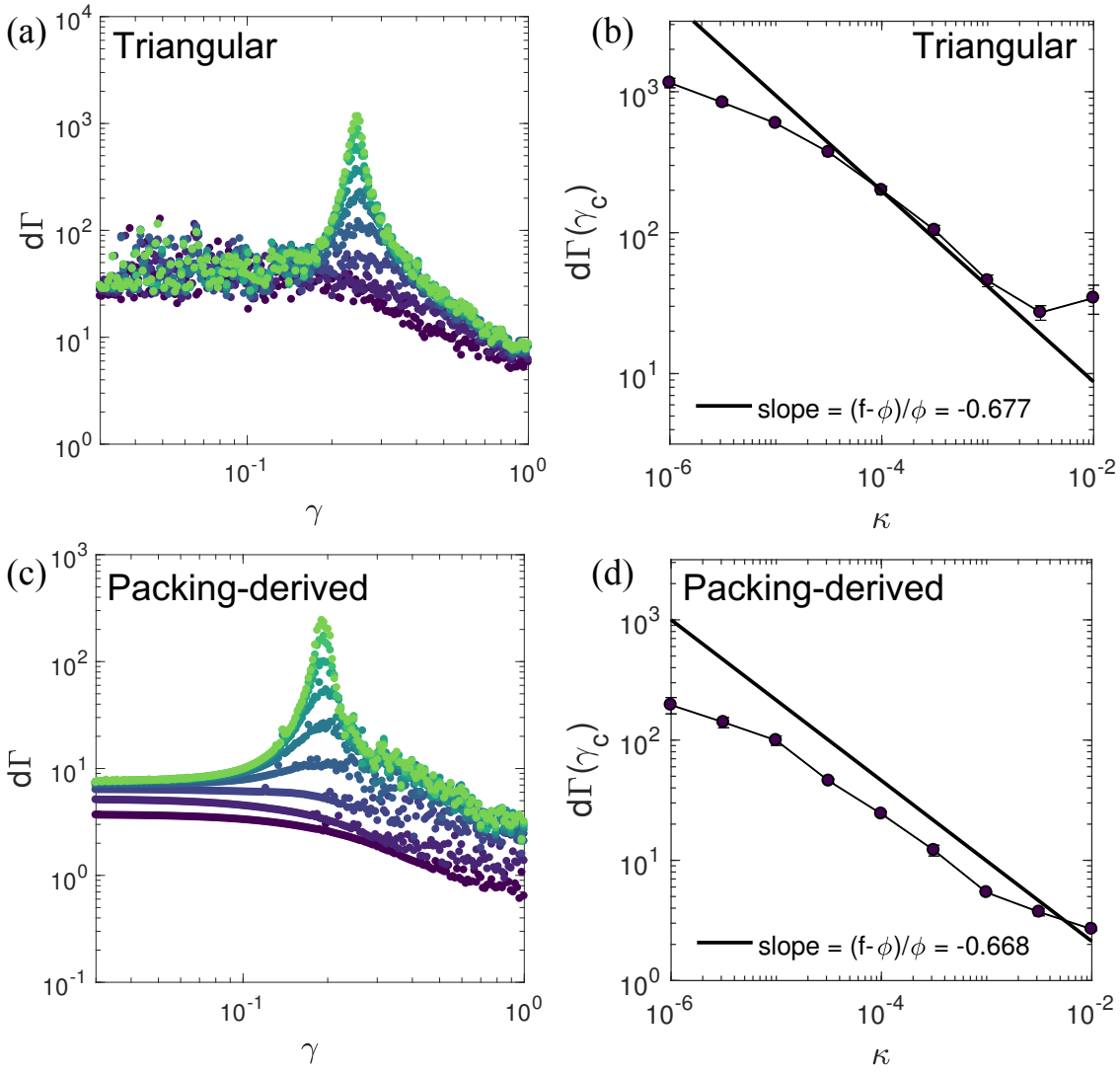

Figure 4.9: Differential nonaffinity $d\Gamma$ vs. strain γ for (a) triangular networks of size $W = 140$ and (c) packing-derived networks of size $W = 120$, both with $z = 3.3$ and varying bending rigidity κ. Colors here correspond to those in Figs. 1-3 of the main text. Plotting the values of $d\Gamma$ at the critical strain as a function of κ, we observe reasonable agreement at the inflection point with the predicted scaling $d\Gamma(\gamma_c) \sim \kappa^{(f-\phi)/\phi}$ for both network models (panels b and d) using the f and ϕ values determined independently based on K. Error bars represent standard error of the mean.

4.8.5 Finite-size scaling of the nonaffine fluctuations in networks with finite bending rigidity

We observe that the same finite size scaling of $d\Gamma$ shown for networks with $\kappa = 0$ in Fig. 4 of the main text is also satisfied for networks with small but finite κ, as shown in Fig. 4.10.

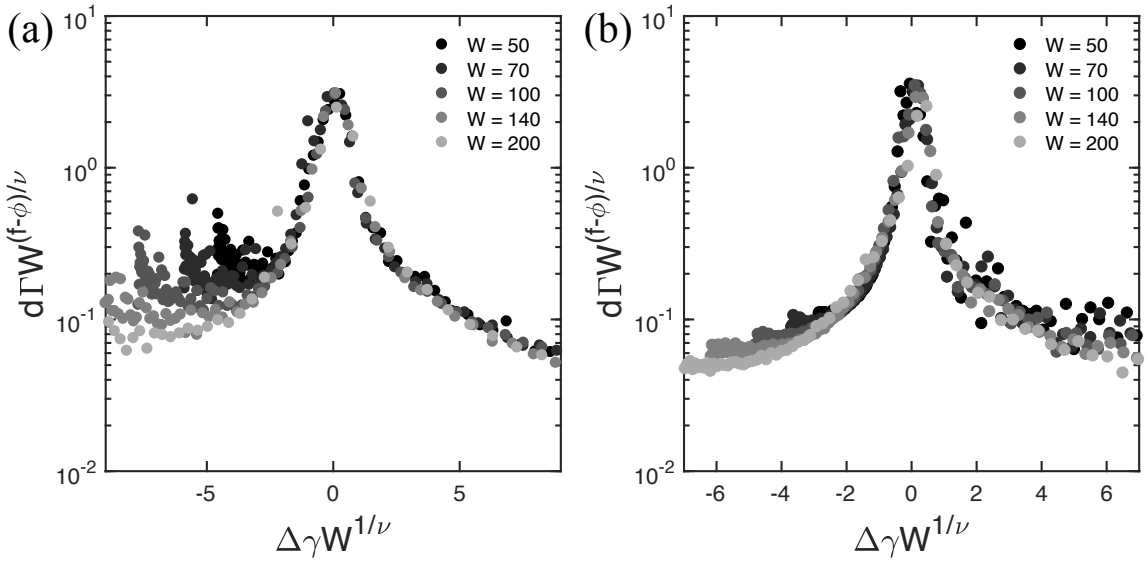

Figure 4.10: Plots of $\delta\Gamma/W^{(\phi-f)/\nu}$ vs. $(\gamma - \gamma_c)W^{1/\nu}$ for (a) triangular networks and (b) packing-derived networks with $z = 3.3$ and $\kappa = 10^{-7}$ and varying system sizes demonstrate successful scaling collapse using the f, ϕ, and ν values determined in the main text.

4.8.6 Finite-size scaling from previous work

We demonstrate that while the exponents of $f = 0.75 \pm 0.05$ and $\nu = 2.0 \pm 0.1$ reported for phantom triangular networks in Ref. [50] disagree with our scaling relation $f = 2\nu - 2$, the data used to determine these exponents can be replotted using the predicted ν value of $\nu = (f + 2)/d = 1.38$ and with an adjusted value of $\gamma_c(\infty)$ to achieve a reasonable scaling collapse (see Fig. 4.11).

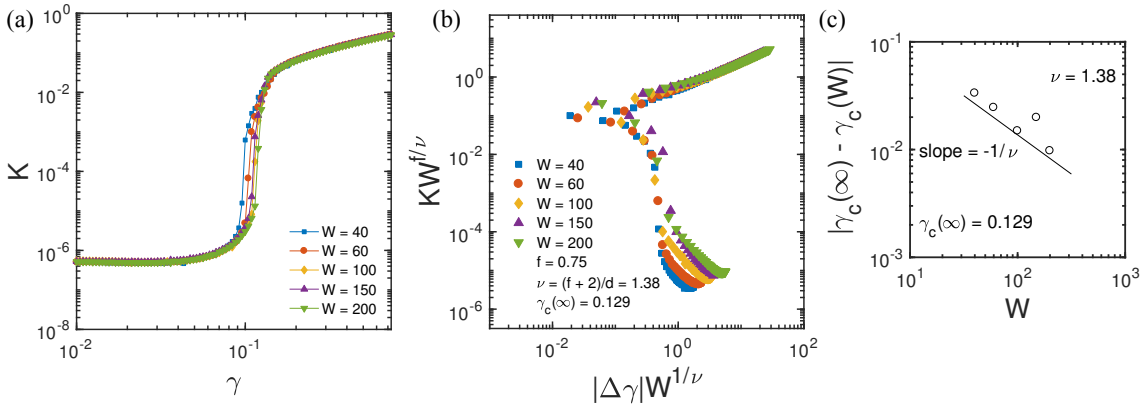

Figure 4.11: Data from Ref. [50], replotted with permission. (a) K vs. γ for phantom triangular networks with $z = 3.2$ and varying system size W. (b) The data from the previous panel plotted according to the finite size scaling relation $K \sim W^{-f/\nu}\mathcal{F}_{\pm}\left(|\Delta\gamma|W^{1/\nu}\right)$, using $f = 0.75$, $\nu = (f+2)/d = 1.38$, and $\gamma_c(\infty) = 0.129$. We observe reasonable collapse, comparable to that shown in Ref. [50]. (c) The scaling of $|\gamma_c(\infty) - \gamma_c(W)|$ vs. W using this modified value of $\gamma_c(\infty)$ shows agreement with the predicted scaling of $|\gamma_c(\infty) - \gamma_c(W)| \sim W^{-1/\nu}$.

4.8.7 Stress tensor calculation

For a system with point-like elements with positions $\mathbf{u}_i$, the stress tensor $\boldsymbol{\sigma}$ can be expressed as follows [86, 90]:

$$\sigma_{\alpha\beta} = -\frac{1}{A}\sum_i f_{i,\alpha}u_{i,\beta} \tag{S1}$$

in which the sum is taken over all nodes i, $\mathbf{f}_i = -\partial\mathcal{H}/\partial\mathbf{u}_i$ is the total force exerted on node i, and A is the system's area (or volume in 3D). Eq. S1 can equivalently be expressed as

$$\sigma_{\alpha\beta} = \frac{1}{2A}\sum_{ij} f_{ij,\alpha}u_{ij,\beta} \tag{S2}$$

in which the sum is taken over all pairs of nodes i and j, $\mathbf{u}_{ij} = \mathbf{u}_j - \mathbf{u}_i$, and the force on node i due to its interactions with node j is

$$\mathbf{f}_{ij} = \frac{\partial\mathcal{H}}{\partial\mathbf{u}_{ij}} = \frac{\partial\mathcal{H}}{\partial u_{ij}}\frac{\partial u_{ij}}{\partial\mathbf{u}_{ij}} = \frac{\partial\mathcal{H}}{\partial u_{ij}}\frac{\mathbf{u}_{ij}}{u_{ij}}, \tag{S3}$$

satisfying $\mathbf{f}_i = \sum_j \mathbf{f}_{ij}$ and $\mathbf{f}_{ij} = -\mathbf{f}_{ji}$. While $\mathcal{H}$ may be composed of many-body potentials, the decomposition of $\mathbf{f}_i$ into (pairwise) central forces $\mathbf{f}_{ij}$ shown in Eq. S3 is possible if $\mathcal{H}$ is continuously differentiable [144, 145]. Several prior studies have demonstrated computation of the stress tensor in systems with many-body potentials using this central force decomposition [146–148].

Additionally, one can compute the components of the stress tensor using the principle of virtual work, by manually taking derivatives of $\mathcal{H}$ with respect to the various shear and normal strains:

$$\sigma_{xz} = \frac{1}{A}\frac{\partial \mathcal{H}}{\partial \gamma} \tag{S3}$$

$$\sigma_{xx} = \frac{1}{A}\frac{\partial \mathcal{H}}{\partial \varepsilon_x} \tag{S4}$$

$$\sigma_{zz} = \frac{1}{A}\frac{\partial \mathcal{H}}{\partial \varepsilon_z} \tag{S5}$$

in which γ is simple shear strain and ε_x and ε_z are uniaxial strains along the x and z axes, respectively. We have verified that these methods yield equivalent $\boldsymbol{\sigma}$ within numerical error.

Chapter 5

Critical slowing down in underconstrained networks

This chapter is adapted from Ref. [149]:

> **Jordan L. Shivers**, Abhinav Sharma, and Fred C. MacKintosh. Nonaffinity controls critical slowing down and rheology near the onset of rigidity. arxiv:2203.04891, 2022.

5.1 Abstract

Fluid-immersed networks and dense suspensions often reside near a boundary between soft (or fluid-like) and rigid (or solid-like) mechanical regimes. This boundary can be crossed either by varying the concentration or by deformation. Near the onset or loss of rigidity, dissipation-limiting nonaffine rearrangements dominate the macroscopic viscoelastic response, giving rise to diverging relaxation times and power-law rheology. Here, we derive a simple relationship between nonaffinity and excess viscosity in fluid-immersed amorphous materials. We then demonstrate this relationship and its rheological consequences in simulations of stress relaxation in strained filament networks and dense suspensions.

5.2 Introduction

Materials such as suspensions, emulsions, foams, and (bio)polymer networks are inherently composite in nature, with both elastic and fluid-like components [53, 90]. In these systems, minor variations in parameters such as volume fraction [43, 150–152], connectivity [46, 48, 129, 133], and applied strain [49, 140] can drive macroscopic transitions between fluid-like and solid-like behavior. These transitions are often heralded by familiar features of critical phenomena [153–155], including power-law scaling of relevant quantities with distance to a critical point [47, 79, 156] and diverging length and time scales [157–160, 160–163]. As a consequence of their disorder, these materials dissipate energy stored by applied stress or strain by deforming in a heterogeneous or *nonaffine* manner, such that the microscopic and macroscopic deformation fields differ significantly [133]. The associated microscopic nonaffine displacements can grow dramatically in magnitude near the onset or loss of rigidity and strongly influence both the static and dynamic mechanical properties of the macroscopic material. However, these displacements are inherently neglected in continuum models and are notoriously difficult to directly measure in experiments [164–166] except in special cases, such as confocal microscopy of colloidal suspensions [167–169].

Indirect evidence of nonaffinity is possible to identify due to the intrinsic connection between nonaffine fluctuations and energy dissipation, although specific rheological models are required to quantify this connection. Prior studies have noted that, for dense suspensions [80, 170–175], foams and emulsions [176, 177], and immersed networks [126, 139, 178], a simple steady-state balance between the power injected by deformation and the power dissipated by nonaffine rearrangement can yield phenomenological scaling relationships between the nonaffinity and the viscoelastic loss modulus, with important consequences for both linear viscoelasticity and steady shear rheology. This has even been used to identify critical exponents, e.g. for networks near isostaticity [126]. Yet, many systems, including biopolymer networks such as the cellular cytoskeleton and

extracellular matrix, are subjected to large and often transient applied stresses and strains; in cells and tissues, this gives rise to highly strain-dependent and typically power-law rheology [179, 180], the origins of which are not yet well understood. As simulated networks under large deformations display enormous nonaffine fluctuations at the onset of tension-dominated rigidity [28, 50, 114, 181, 182], a general understanding of the dynamic effects of nonaffinity in nonlinear viscoelastic regimes is still needed.

Here, we identify a general relationship between the nonaffinity and loss modulus for a fluid-immersed amorphous material and explore the ensuing rheological consequences in simulations of networks and dense suspensions in two and three dimensions. With the strain-dependent rheology of biopolymer networks in mind, we focus primarily on the effects of prestrain on stress relaxation in fluid-immersed elastic networks, although we demonstrate the generality of this approach also for suspensions. Focusing on stress relaxation in underconstrained networks, we show that the longest relaxation time diverges in tandem with the nonaffinity as the system approaches a rigidity threshold. This leads to a scaling ansatz describing the relaxation modulus and nonaffinity near the critical strain, which we validate in simulations. As a consequence of this, we also identify a simple linear relationship between the static nonaffinity and experimentally attainable zero-shear viscosity, which suggests a route for the experimental measurement of nonaffine fluctuations. Finally, we discuss the effects of the nonaffinity-dissipation relationship on the dynamic scaling exponents for strain stiffening networks and demonstrate its utility in describing the rheology of dense suspensions near jamming.

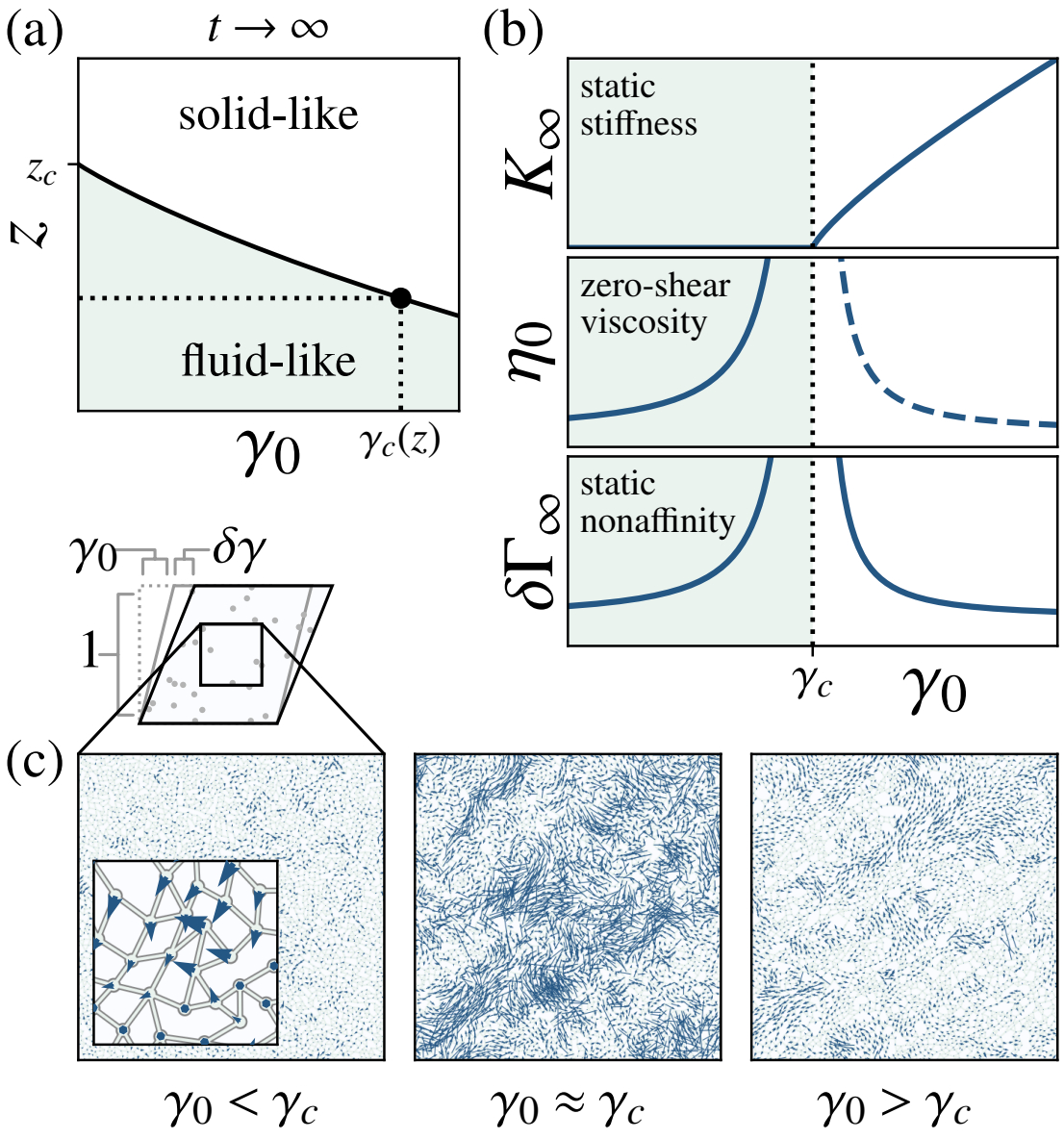

Figure 5.1: (a) A fluid-immersed disordered spring network with connectivity z below Maxwell's isostatic point z_c behaves as a solid, at long times, when subjected to simple shear strain γ_0 that exceeds a z-dependent critical strain γ_c. (b) Near the onset of rigidity, important rheological and kinematic features scale as powers of the distance to the critical point, $|\gamma_0 - \gamma_c|$. At γ_c, the static differential shear modulus K_∞ becomes nonzero, while both the zero-shear viscosity η_0 and static differential nonaffinity $\delta\Gamma_\infty$ diverge in the thermodynamic limit. (c) Energy produced by a small *affine* step strain $\delta\gamma$ is dissipated by microscopic nonaffine displacements $\mathbf{u}_i^{\mathrm{NA}}$, indicated here by arrows with uniformly scaled lengths.

5.3 Methods

We consider the overdamped dynamics of a d-dimensional system composed of N particles with positions $\mathbf{r}_i$ interacting via a potential energy $U = f(\mathbf{r}_1, ..., \mathbf{r}_N)$. These are immersed in a Newtonian fluid with velocity field $\mathbf{v}_f$, which imparts a drag force $\mathbf{f}_{d,i} = -\zeta(\dot{\mathbf{r}}_i - \mathbf{v}_f(\mathbf{r}_i))$ that exactly balances the interaction force $\mathbf{f}_{p,i} = -\partial U/\partial \mathbf{r}_i$, such that each particle's equation of motion is $\mathbf{f}_{d,i} + \mathbf{f}_{p,i} = \mathbf{0}$. This "free draining" description ignores long-range hydrodynamic interactions [183], which in our materials of interest can likely be neglected due to hydrodynamic screening. We apply macroscopic shear strain $\gamma(t)$ via Lees-Edwards periodic boundary conditions [85] and assume that the fluid deforms affinely according to the macroscopically applied strain, such that $\mathbf{v}_f(\mathbf{r}_i) = r_{i,z}\dot{\gamma}(t)\hat{\mathbf{x}}$; this is the widely used "affine solvent model" [43, 80, 126, 157, 171]. For a given strain rate and particle arrangement, the macroscopic shear stress is $\sigma = \eta_f\dot{\gamma} + (2V)^{-1}\sum_{ij} f_{ij,x}r_{ij,z}$, in which η_f is the viscosity of the fluid, V is the system's volume, the sum is taken over all pairs of interacting particles i and j, $\mathbf{f}_{ij}$ is the force on particle i due to its interactions with particle j, $\mathbf{r}_{ij} = \mathbf{r}_j - \mathbf{r}_i$, and x and z denote the flow and gradient directions, respectively.

Nonaffinity quantifies the reorganization required for a system that is initially in mechanical equilibrium (satisfying force balance or, equivalently, sitting at a minimum in $U(\mathbf{r}_i)$) to re-equilibrate after a small affine perturbation [184, 185]. Consider an initially energy-minimized system at some prestrain γ_0, to which we apply an instantaneous affine strain step $\delta\gamma$ yielding transformed particle positions $\mathbf{r}_{i,0}$ with, in general, a net force on each particle. Allowing the equations of motion to evolve until the forces are once again balanced, we find that the particles take on new positions $\mathbf{r}_{i,\infty}$ that define static nonaffine displacements $\mathbf{u}^{\mathrm{NA}}_{i,\infty} = \mathbf{r}_{i,\infty} - \mathbf{r}_{i,0}$, as sketched in Fig. 5.1a. These collectively contribute to the static differential nonaffinity, $\delta\Gamma_\infty = (N\ell_0^2\delta\gamma^2)^{-1}\sum_i \|\mathbf{u}^{\mathrm{NA}}_{i,\infty}\|^2$. As we noted earlier, in response to even very small perturbations, amorphous materials near points of marginal stability tend to undergo

large-scale rearrangement signaled by large $\delta\Gamma_\infty$.

We construct an initial particle configuration $\mathbf{r}_i$ and energy $U(\mathbf{r}_i)$ representing a disordered spring network (or, if bending interactions are included between adjacent bonds, a bond-bending network) as described in Supplemental Material. In disordered networks, the onset of rigidity is controlled by some control variable x, e.g. the connectivity or applied strain. We focus here on subisostatic networks, in which z, the connectivity or average number of springs connected to each network node (particle), is below Maxwell's d-dependent isostatic point $z_c = 2d$ [46]. Note that experimentally observed values of z for three-dimensional biopolymer networks are generally between 3 and 4 [120] and thus below z_c. We choose simple shear prestrain γ_0 as the rigidity control variable; in this case, static ($t \to \infty$) solid-like behavior develops when γ_0 reaches the z-dependent critical strain γ_c [79], as shown in Fig. 5.1a. For $N, V \to \infty$, as γ_0 approaches a critical point γ_c, the system's zero-shear viscosity and nonaffinity diverge, as sketched in Fig. 5.1b.

In Fig. 5.1c, we plot static nonaffine displacement vectors for a representative 2D network with $z = 3.5$ under varying prestrain. The scale and correlation length of the nonaffine displacements are largest at the critical strain γ_c corresponding to the stiffening transition [114], at which the macroscopic static nonaffinity $\delta\Gamma_\infty$ reaches a maximum (see Fig. 5.2b). Although the nonaffinity provides a clear signal of the critical point in simulations, its measurement in experiments, often by tracking the motion of embedded tracer particles [164–166], is challenging and limited in precision. An attractive alternative is to indirectly measure the nonaffinity via its relationship to more experimentally accessible quantities, such as the viscoelastic storage or loss moduli. As we noted earlier, prior studies have shown that such a relationship exists due to energy conservation: at steady state, the power injected into the system by the externally applied stress balances the power dissipated by the system's nonaffine internal reorganization [80, 126, 139, 170–178].

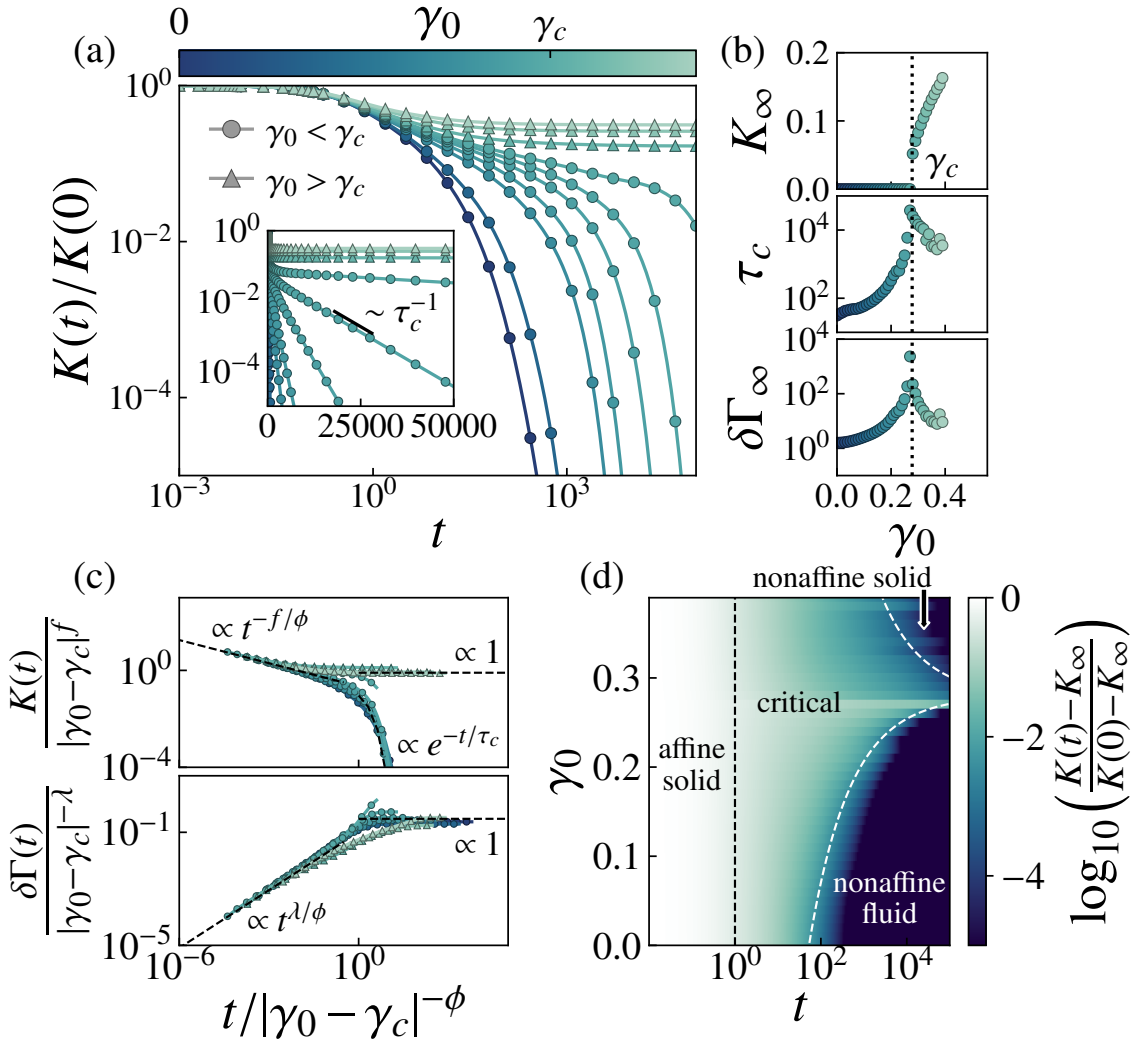

Figure 5.2: Stress relaxation tests reveal a slowest relaxation timescale τ_c that diverges at the critical prestrain. (a) For a network of $N = 6400$ nodes with connectivity $z = 3.5$ and dimensionless bending rigidity $\tilde{\kappa} = 0$ initially relaxed at prestrain γ_0 and subjected to an infinitesimal strain increase $\delta\gamma$, the normalized differential relaxation modulus $K(t)/K(0) = \delta\sigma(t)/\delta\sigma(0)$ decays to an equilibrium value with a γ_0-dependent slowest relaxation time $\tau_c(\gamma_0)$, revealed by the terminal slope on a log-linear scale (inset) and shown in (b) along with the associated static nonaffinity $\delta\Gamma_\infty$, and static differential shear modulus $\delta\sigma_\infty/\delta\gamma$. Here, $\delta\gamma = 10^{-4}$ and dotted lines indicate the critical strain. (c) The time-dependent differential relaxation modulus and differential nonaffinity, measured over a range of prestrains γ_0, collapse according to the Widom-like scaling predicted by Eqs 5.3 and 5.4, with exponents $f = 0.7$, $\phi = 2.2$, and $\lambda = 1.5$. (d) A (γ_0, t) phase diagram summarizes the network's time-dependent mechanical properties. The dashed white curves are proportional to $|\gamma_0 - \gamma_c|^{-\phi}$.

5.4 Results and discussion

We can show that a similar power balance relates the nonaffinity and viscoelasticity in systems within nonlinear viscoelastic regimes. Consider an energy-minimized configuration under prestrain $\gamma(t \leq 0) = \gamma_0$. The system is subjected to a superimposed oscillatory strain of amplitude $\delta\gamma$ and frequency ω, such that $\gamma(t) = \gamma_0 + \delta\gamma \sin(\omega t)$ for $t > 0$. After an initial transient regime, the stress adopts a steadily oscillating profile $\sigma(t) = \sigma_0 + \delta\sigma \sin(\omega t + \theta)$, in which $\delta\sigma$ is the amplitude and θ is the phase shift between the stress and strain. Equivalently, $\sigma(t) = \sigma_0 + \delta\gamma \left(K' \sin(\omega t) + K'' \cos(\omega t)\right)$, in which $K'(\gamma_0, \omega) = (\delta\sigma/\delta\gamma)\cos\theta$ and $K''(\gamma_0, \omega) = (\delta\sigma/\delta\gamma)\sin\theta$ are the frequency-dependent differential storage and loss moduli for systems at prestrain γ_0. For small $\delta\gamma$, each particle orbits a fixed position $\mathbf{r}_{i,0}$ with an elliptical path $\mathbf{p}(t) = \mathbf{r}_i(t) - \mathbf{r}_{i,0}$ combining affine and nonaffine components $\mathbf{p}_i^{\mathrm{A}}(t) = \mathbf{u}_i^{\mathrm{A}}(\omega)\sin(\omega t + \theta^{\mathrm{A}})$ and $\mathbf{p}_i^{\mathrm{NA}}(t) = \mathbf{u}_i^{\mathrm{NA}}(\omega)\sin(\omega t + \theta^{\mathrm{NA}})$, with $\mathbf{p}(t) = \mathbf{p}^{\mathrm{A}}(t) + \mathbf{p}^{\mathrm{NA}}(t)$. Note that for systems without a fixed topology, e.g. suspensions of soft spheres, ensuring that the particles follow closed elliptical trajectories consistent with linearity can require very small $\delta\gamma$ [186]. Collecting the magnitudes of the frequency-dependent nonaffine displacement vectors, we define the frequency-dependent nonaffinity, $\delta\Gamma(\omega) = (N\ell_0^2\delta\gamma^2)^{-1}\sum_i \|\mathbf{u}_i^{\mathrm{NA}}(\omega)\|^2$, in which ℓ_0 is a characteristic length scale, e.g. the typical spring length. The drag acting on each particle is proportional to its nonaffine velocity (its velocity with respect to the fluid), $\partial\mathbf{p}_i^{\mathrm{NA}}/\partial t = \omega\mathbf{u}_i^{\mathrm{NA}}(\omega)\cos(\omega t + \theta^{\mathrm{NA}})$. Averaged over the duration of a cycle, the external power input $P_{\mathrm{in}} = \frac{1}{2}V\omega d\gamma^2\left(K'' - \eta_f\omega\right)$ balances the total power output by nonaffine work, $P_{\mathrm{out}} = \frac{1}{2}N\omega^2\zeta\ell_0^2\delta\gamma^2\delta\Gamma(\omega)$ (see Supplemental Material). Thus we have a quantitative relationship between the differential dynamic viscosity $\eta'(\omega) = K''(\omega)/\omega$ and the frequency-dependent nonaffinity

$$\eta'(\omega) - \eta_f = \rho\zeta\ell_0^2\delta\Gamma(\omega) \tag{5.1}$$

in which $\rho = N/V$ is the number density of particles. In the zero-frequency limit, this relates the zero-shear differential viscosity, $\eta_0 = \lim_{\omega\to 0}\eta'(\omega)$ and the static nonaffinity $\delta\Gamma_\infty = \lim_{\omega\to 0}\delta\Gamma(\omega)$ as

$$\eta_0 - \eta_f = \rho\zeta\ell_0^2\delta\Gamma_\infty. \tag{5.2}$$

It should be emphasized that in Eqs. 5.1 and 5.2 are valid for any prestrain. The latter tells us that the presence of interacting particles (e.g. a spring network) within a fluid with viscosity η_f increases the mixture's effective zero-shear viscosity by a simple multiple of the particles' fluid-independent static nonaffinity. This relationship is valid irrespective of the interaction potential U and thus applies to a wide range of systems including, as we will demonstrate, networks of bending-resistant filaments and soft sphere suspensions near jamming.

To demonstrate the ensuing rheological consequences, we now consider a system's dynamic response to a perturbation in the form of an instantaneous strain step. To an initially relaxed system at prestrain γ_0 with prestress σ_0, we apply an affine strain step of magnitude $\delta\gamma$, such that $\gamma(t) = \gamma_0 + \delta\gamma$ for $t \geq 0$. As the equations of motion are integrated, the particles shift from their initial, affinely-transformed positions with nonaffine displacements $\mathbf{u}_i^{\mathrm{NA}}(t) = \mathbf{r}_i(t) - \mathbf{r}_i(0)$, as sketched in Fig. 5.1a for $t \to \infty$. These collectively define a dimensionless relaxation nonaffinity $\delta\Gamma(t) = (N\ell_0^2\delta\gamma^2)^{-1}\sum_i \|\mathbf{u}_i^{\mathrm{NA}}(t)\|^2$, which eventually settles to the static nonaffinity $\delta\Gamma_\infty = \lim_{t\to\infty}\delta\Gamma(t)$. We measure the corresponding change in shear stress $\delta\sigma(t) = \sigma(t) - \sigma_0$ and compute the differential relaxation modulus $K(t) = \delta\sigma/\delta\gamma$ and differential zero-shear viscosity $\eta_0 - \eta_f = \int_0^\infty (K(t) - K_\infty)dt$, in which the static differential modulus is $K_\infty = \lim_{t\to\infty} K(t)$. Note that, for $\gamma_0 = 0$, K and $\delta\Gamma$ correspond to the usual linear relaxation modulus $G(t) = \lim_{\gamma_0\to 0} K(t)$ and linear nonaffinity $\Gamma(t) = \lim_{\gamma_0\to 0}\delta\Gamma(t)$.

Because the static nonaffinity $\delta\Gamma_\infty$ diverges at the critical strain, Eq. 5.2 implies that we should observe an equivalently diverging zero-shear viscosity and associated diverging slowest relaxation time. In Fig. 5.2a, we plot stress relaxation curves

for a single two-dimensional network with $z = 3.5$, with infinitesimal step strains applied over a range of prestrains γ_0 containing γ_c. The normalized relaxation modulus $K(t)/K(0) = \delta\sigma(t)/\delta\sigma(0)$ decays to its equilibrium value $K_\infty/K(0)$ with a γ_0-dependent slowest relaxation time τ_c (calculated as described in Supplemental Material), which is plotted in Fig. 5.2b as a function of γ_0 along with the corresponding static nonaffinity $\delta\Gamma_\infty$, and static differential modulus $K_\infty = \delta\sigma_\infty/\delta\gamma$. Maxima in τ_c and $\delta\Gamma_\infty$ occur at the critical strain, where K_∞ becomes nonzero. We assign the exponent ϕ to the scaling of τ_c with $|\gamma_0 - \gamma_c|$ and, following previous conventions for the static exponents [50], assign λ to $\delta\Gamma_\infty$ and f to K_∞.

The relaxation modulus decays as a power-law over a range of times spanning from $\tau_0 = \zeta\ell_0/\mu = 1$, corresponding to the relaxation time for a single spring-driven node in the solvent, to a characteristic slow timescale governed by the distance from the critical strain, $\tau_c = |\gamma_0 - \gamma_c|^{-\phi}$. Within this regime, the relaxation modulus is a function of the ratio $t/\tau_c \equiv |\gamma_0 - \gamma_c|^\phi$. Beyond τ_c, we expect to observe the static critical behavior, i.e. $K_\infty \propto |\gamma_0 - \gamma_c|^f$ for $\gamma_0 \geq \gamma_c$. We thus expect the relaxation modulus to obey the scaling form

$$K(t) = |\gamma_0 - \gamma_c|^f \mathcal{F}_\pm \left(t|\gamma_0 - \gamma_c|^\phi\right) \tag{5.3}$$

in which the branches of the scaling function $\mathcal{F}_\pm(x)$ correspond to the regimes above and below the critical strain. When $x \gg 1$, $\mathcal{F}_+(x) \sim$ constant and $\mathcal{F}_-(x) \sim \exp(-x)$, implying $K(t) \sim |\gamma_0 - \gamma_c|^f$ above the critical strain and $K(t) \sim |\gamma_0 - \gamma_c|^f \exp(-t|\gamma_0 - \gamma_c|^\phi)$ below the critical strain. When $x \ll 1$, $K(t)$ remains finite and thus must be independent of $|\gamma_0 - \gamma_c|$, so $\mathcal{F}_\pm(x) \sim x^{-f/\phi}$. Therefore, for systems at the critical point, the relaxation modulus is predicted to decay as $K(t) \propto t^{-f/\phi}$.

Near the critical strain, the differential nonaffinity is controlled by the same diverging timescale τ_c, yet should eventually display the static critical behavior $\delta\Gamma \propto$

$|\gamma_0 - \gamma_c|^{-\lambda}$. We thus expect the scaling form

$$\delta\Gamma(t) = |\gamma_0 - \gamma_c|^{-\lambda}\mathcal{G}_{\pm}\left(t|\gamma_0 - \gamma_c|^{\phi}\right) \tag{5.4}$$

When $x \gg 1$, $\mathcal{G}_+(x) \sim$ constant and $\mathcal{G}_-(x) \sim$ constant. When $x \ll 1$, $\delta\Gamma(t)$ likewise remains finite and therefore must be independent of $|\gamma_0 - \gamma_c|$, so $\mathcal{G}_{\pm}(x) \sim x^{\lambda/\phi}$. This implies that, very close to the critical strain, the differential nonaffinity grows with time as $\delta\Gamma(t) \propto t^{\lambda/\phi}$. We observe excellent collapse of $K(t)$ and $\delta\Gamma(t)$ according to these scaling forms, as shown in Fig. 5.2, for $f = 0.7$, $\phi = 2.2$, and $\lambda = 1.5$.

Before discussing the relationships between these exponents, we verify that the independently measured static differential nonaffinity and differential zero-shear viscosity behave identically. In Fig. 5.3a, we demonstrate that, like $\delta\Gamma_\infty$, the zero-shear viscosity η_0 reaches a maximum at the phase boundary between the statically floppy and rigid regimes, in this case for networks with $\tilde{\kappa} = 0$. In Fig. 5.3b, we plot the differential zero-shear viscosity for networks with varying dimensionless bending rigidity $\tilde{\kappa}$ and observe, in precise agreement with Eq. 5.2, a divergence in $\eta_0 - \eta_f$ at the critical strain that is suppressed by increasing $\tilde{\kappa}$, which acts as a stabilizing field [50]. In Supplemental Material, we verify that the same nonaffinity-viscosity relationship applies in dense suspensions of frictionless soft spheres, in which the viscosity diverges near a critical volume fraction ϕ_c.

The aforementioned power balance leads to a relationship between the static scaling exponents, f and λ, and the dynamic exponent, ϕ. At the critical strain, the relaxation modulus decays as $K(t) \sim t^{-f/\phi}$ and the nonaffinity grows as $\delta\Gamma(t) \sim t^{\lambda/\phi}$, so the corresponding frequency dependence of the complex modulus and nonaffinity must be $K^*(\omega) \sim \omega^{f/\phi}$ and $\delta\Gamma(\omega) \sim \omega^{-\lambda/\phi}$. The former implies that the effective viscosity grows as $\eta'(\omega) \sim \omega^{f/\phi - 1}$, hence Eq. 5.1 implies $\phi = f + \lambda$. Interestingly, this means that the static scaling of the stiffness and nonaffinity controls ϕ and,

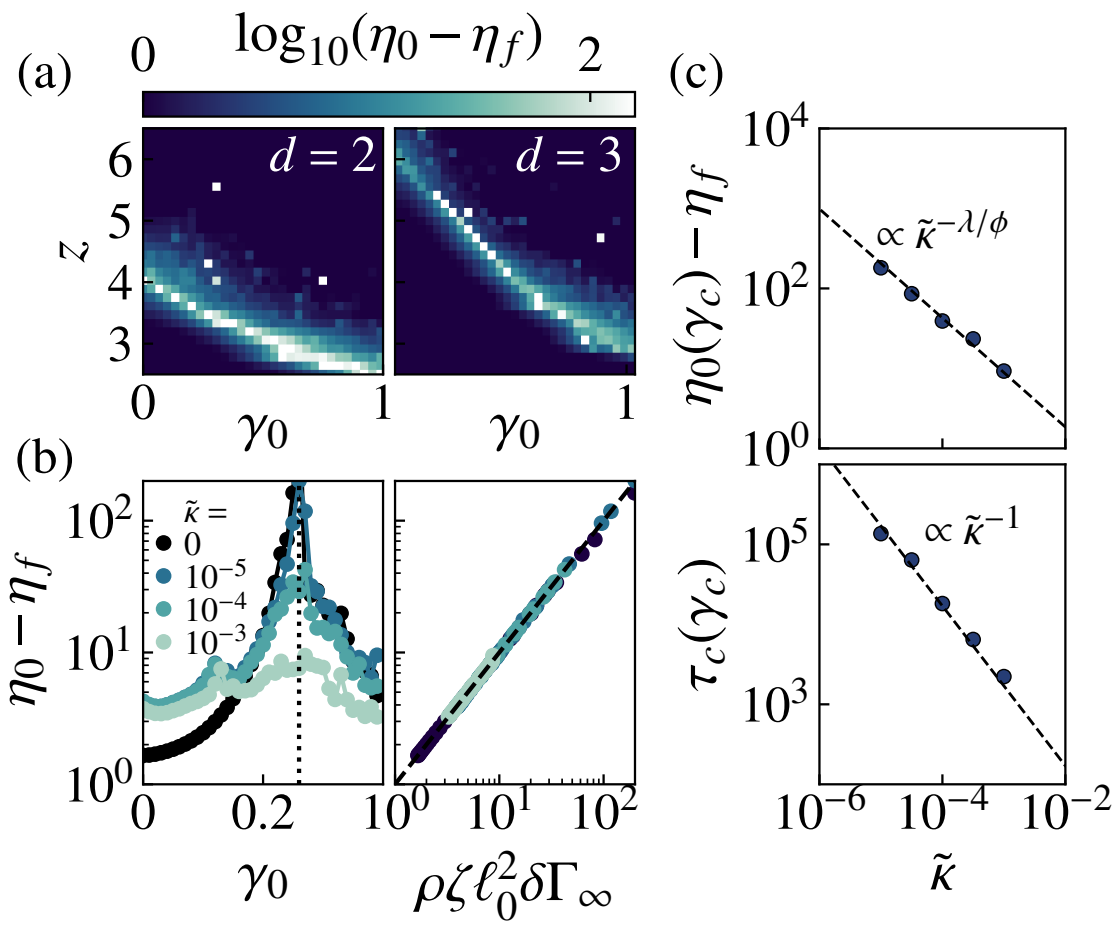

Figure 5.3: The excess zero-shear viscosity $\eta_0 - \eta_f$ precisely tracks the nonaffinity, reproducing (a) its peak at the z-dependent critical strain γ_c. These data correspond to networks in two ($N = 10000$ nodes) and three ($N = 8000$ nodes) dimensions with $\tilde{\kappa} = 0$. (b) For a network ($N = 1600$ nodes) with finite bending rigidity $\tilde{\kappa}$, the divergence of the zero-shear viscosity $\eta_0 - \eta_f$ at γ_c is suppressed by bending, yet Eq. 5.2 (dashed line) is still satisfied for all $\tilde{\kappa}$. (c) The maximum zero-shear viscosity and critical relaxation time, which appear at the critical strain γ_c, scale as negative powers of the dimensionless bending rigidity as predicted by Eqs. 5.5 and 5.6.

by extension, the dynamic exponents f/ϕ and λ/ϕ describing the system's stress relaxation and time-dependent rearrangement, as prior work has noted for the scaling exponents describing connectivity-dependent dynamics in networks near isostaticity [126]. Alternatively, we can rationalize this finding with a more qualitative argument: the relaxation time of large structural rearrangements scales with the "size" of these rearrangements, i.e. $\delta\Gamma_\infty \sim |\Delta\gamma|^{-\lambda}$, divided by the magnitude of their driving force, proportional to $K_\infty \sim |\Delta\gamma|^f$, hence $\tau_c \sim |\Delta\gamma|^{-(\lambda+f)}$, with units set by the fluid

viscosity. This relationship implies that the dynamic exponent ϕ is identical to the exponent describing the critical coupling of a network to the bending rigidity, defined in prior work [50]. Therefore, at the critical strain, the excess zero-shear viscosity should scale with bending rigidity just as the quasistatic nonaffinity does [128],

$$\eta_0(\gamma_c) - \eta_f \propto \tilde{\kappa}^{-\lambda/\phi} \tag{5.5}$$

and the corresponding maximum relaxation time should scale simply as

$$\tau_c(\gamma_c) \propto \tilde{\kappa}^{-1}, \tag{5.6}$$

independently of the critical exponents. In Fig. 5.3c, we show that these relationships are satisfied in our simulations. In experiments, these relationships could be tested by varying a reconstituted gel's protein concentration c (for collagen, past work has suggested $\tilde{\kappa} \propto c$ [50, 98]).

5.5 Conclusions

There is widespread interest in the rational design of materials with tunable viscoelasticity [105, 187, 188]. This generally involves adjusting aspects of a material's preparation, such as the volume fraction of suspended particles or the concentration of a gel-forming polymer. Here, we have shown that a simple connection between nonaffine fluctuations and energy dissipation, which implies proportionality between nonaffinity and viscosity, leads to extreme strain-controlled tunability of stress relaxation in structurally unchanged filament networks. To demonstrate this relationship's generality, we have also shown that it fully captures the diverging zero-shear viscosity in suspensions of soft frictionless spheres near the onset of jamming.

The association of diverging nonaffine fluctuations with the onset of rigidity,

coupled with their microscopic role in slowing stress relaxation, may account for prior observations of slow dynamics in disordered materials such as fractal colloidal gels [189, 190] and crowded, prestressed living cells [20, 191–193]. This also suggests new avenues for tuning the dynamics of stress relaxation; for example, in fibrous networks, microscopic components that generate localized internal stresses can drive macroscopic stiffening transitions and thus precisely control the nonaffinity [134]. Relevant examples include molecular motors in the cellular cytoskeleton [73, 194, 195], contractile cells in the extracellular matrix [33, 109, 196], and embedded particles driven to shrink due to changes in temperature [197] or rearrange under applied magnetic fields [198].

Additional work will be needed to characterize the effects of finite system size on nonaffinity-induced critical slowing down near the onset of rigidity. For networks at the critical strain with correlation length exponent ν, we expect $\tau_c(\gamma_c) \propto L^{\phi/\nu}$ and $\eta_0(\gamma_c) - \eta_f \propto L^{\lambda/\nu}$ (see Supplemental Material), suggesting additional ways to identify ν and test the previously proposed hyperscaling relation, $\nu = (f+2)/d$ [128]. Other areas to investigate include the effects of hydrodynamic interactions near the critical strain, as these both increase nonaffinity near isostaticity [127] and couple with nonaffinity to produce an additional intermediate-frequency viscoelastic regime at small strains [199], and the effects of finite temperature: the Green-Kubo relations tie the stationary stress correlations to the zero-shear viscosity [200, 201] and thus to the athermal static nonaffinity. Finally, it remains to be seen whether connections between nonaffinity and slowing down might provide insight into the glass transition [159, 202–207].

5.6 Acknowledgments

This work was supported in part by the National Science Foundation Division of Materials Research (Grant No. DMR-1826623) and the National Science Foun-

dation Center for Theoretical Biological Physics (Grant No. PHY-2019745). J.L.S. acknowledges additional support from the Lodieska Stockbridge Vaughn Fellowship.

5.7 Appendix

5.7.1 Disordered network model

We consider the behavior of a bond-bending network [118] in a Newtonian solvent, in which drag forces act only on network nodes. We derive network structures with initial connectivity $z_0 \approx 6$ in 2D and $z_0 \approx 10$ in 3D from the contact networks of dense packings of soft spheres, which are generated using protocols described in prior work [79, 128, 139]. We then reduce the connectivity z to the desired value by selectively removing bonds randomly chosen from the set of nodes with the highest coordination number, yielding a network with a relatively homogeneous connectivity distribution [79]. The energy of the network is

$$U = \frac{\mu}{2} \sum_{ij} \frac{\left(\ell_{ij} - \ell_{ij,0}\right)^2}{\ell_{ij,0}} + \frac{\kappa}{2} \sum_{ijk} \frac{\left(\theta_{ijk} - \theta_{ijk,0}\right)^2}{\ell_{ijk,0}}$$

in which μ is the bond stretching stiffness (units of energy / length), κ is the bending rigidity (units of energy $\times$ length) acting between adjacent bonds, the instantaneous and rest lengths of bond ij are $\ell_{ij} = \mathbf{r}_j - \mathbf{r}_i$ and $\ell_{ij,0}$, the instantaneous and rest angle between bonds ij and jk are θ_{ijk} and $\theta_{ijk,0}$, and $\ell_{ijk,0} = (\ell_{ij,0} + \ell_{jk,0})/2$. We define the rest lengths and angles such that $U(\gamma_0 = 0) = 0$.

The node dynamics follow the over-damped, zero-temperature Langevin equation,

$$-\frac{\partial U}{\partial \mathbf{r}_i} - \zeta \left(\frac{d\mathbf{r}_i}{dt} - \mathbf{v}_f(\mathbf{r}_i) \right) = \mathbf{0}$$

in which ζ is the drag coefficient. Here, $\mathbf{v}_f(\mathbf{r}_i)$ denotes the velocity of the solvent at

the position of node i. Note that we are using a free-draining [201] approximation and thus ignoring hydrodynamic interactions between nodes. We integrate this equation using the Euler method with timestep $\Delta t = 10^{-3}$. For convenience, we set $\mu = \zeta = 1$ and vary $\tilde{\kappa} = \kappa/(\mu \ell_0^2)$. Note that for $\tilde{\kappa} = 0$, the characteristic microscopic relaxation time is $\tau_0 = \zeta \ell_0 / \mu$.

5.7.2 Stress relaxation at finite strain

We first obtain the minimum energy configuration of the network at applied shear strain $\gamma = \gamma_0$. Then, we apply a small, instantaneous *affine* shear strain step $\delta\gamma$, such that the strain becomes $\gamma = \gamma_0 + \delta\gamma$. Taking this as the initial state and assuming the solvent is immobile ($\mathbf{v}_f = \mathbf{0}$) in this case, we allow the system to evolve according to the equations of motion. We measure the shear stress $\sigma(t)$ as a function of time as the system evolves and compute the differential relaxation modulus,

$$K(\gamma_0, t) = \lim_{\delta\gamma \to 0} \frac{\sigma(\gamma_0 + \delta\gamma, t) - \sigma(\gamma_0, t \to \infty)}{\delta\gamma}$$

Note that $K_{\text{aff}}(\gamma_0) \equiv K(\gamma_0, t = 0)$ corresponds to the affine differential modulus, and the system eventually settles to the equilibrium (long-time) differential modulus $K_\infty(\gamma_0) \equiv K(\gamma_0, t \to \infty)$, equivalent to that measured under quasistatic shear.

5.7.3 Small-amplitude oscillatory shear at finite strain

For small-amplitude oscillatory shear near the critical strain, the system exhibits power-law scaling of the dynamic moduli over a range of frequencies bounded on the lower end by the critical characteristic frequency $\omega_c = |\gamma_0 - \gamma_c|^\phi$, governed by the proximity to the critical strain, and on the upper end by the characteristic frequency $\omega_0 \approx 1$ above which the network behaves as a solid. We assume that the ratio $\omega/\omega_c = \omega|\gamma_0 - \gamma_c|^{-\phi}$ governs the mechanics for a particular strain, in which case the

differential modulus takes on the scaling form

$$K'(\omega) = |\gamma_0 - \gamma_c|^f \mathcal{H}_\pm \left(\omega |\gamma_0 - \gamma_c|^{-\phi}\right)$$

in which, for $x \gg 1$, $\mathcal{H}_-(c) \sim x^2$ and $\mathcal{H}_+(x) \sim$ constant, while for $x \gg 1$ we must have $\mathcal{H}_\pm(x) \propto x^{f/\phi}$ since $K'(\omega)$ remains finite.

Since at the critical strain we have $\delta\Gamma(\omega) \propto \omega^{-\lambda/\phi}$ and $K^*(\omega) \propto f/\phi$ (i.e. $\eta^*(\omega) \propto^{f/\phi - 1}$), the relation above implies $f/\phi - 1 = -\lambda/\phi$, or

$$f = \phi - \lambda$$

as we find for the stress relaxation case. Note that in Ref. [126], Yucht et al. made essentially the same argument relating the scaling behavior of the linear loss modulus and nonaffinity for networks near the isostatic point.

5.7.4 Power balance

In the steadily oscillating regime (long after initiating the small-amplitude oscillatory shear), the power injected in the external application of strain, averaged over a single cycle, is

$$\begin{aligned} P_{\text{in}} &= V \frac{\omega}{2\pi} \int_{t_0}^{t_0 + 2\pi/\omega} \dot{\gamma} \left(\delta\sigma - \eta_f \dot{\gamma}\right) dt \\ &= V \frac{\omega}{2\pi} \int_{t_0}^{t_0 + 2\pi/\omega} \omega\delta\gamma \cos\omega t \left(\delta\gamma \left[K' \sin\omega t + K'' \cos\omega t\right] - \eta_f \omega \delta\gamma \cos\omega t\right) dt \\ &= \frac{1}{2} V \omega \delta\gamma^2 (K'' - \eta_f \omega) \end{aligned}$$

The nonaffine displacement of node i is $\mathbf{p}_i^{\text{NA}}(t) = \mathbf{u}_i^{\text{NA}}(\omega) \sin\left(\omega t + \theta^{\text{NA}}\right)$, and the nonaffine velocity is $\partial \mathbf{p}_i^{\text{NA}}/\partial t = \omega \mathbf{u}_i^{\text{NA}}(\omega) \cos\left(\omega t + \theta^{\text{NA}}\right)$. The system-wide instantaneous nonaffinity is $\delta\Gamma_i(\omega) = \sum_i \left\|\mathbf{u}_i^{\text{NA}}(\omega)\right\|^2 \sin^2(\omega t + \theta^{\text{NA}})/(\ell_0^2 \delta\gamma^2)$. The power

output, averaged over a single cycle, in dragging the nodes against the solvent is

$$\begin{aligned}
P_{\text{out}} &= \sum_i \frac{\omega}{2\pi} \int_{t_0}^{t_0+2\pi/\omega} \mathbf{f}_{p,i} \cdot \left(\frac{\partial \mathbf{p}_i^{\text{NA}}}{\partial t} \right) dt \\
&= \sum_i \frac{\omega}{2\pi} \int_{t_0}^{t_0+2\pi/\omega} \zeta \left\| \frac{\partial \mathbf{p}_i^{\text{NA}}}{\partial t} \right\|^2 dt \\
&= \sum_i \frac{\omega}{2\pi} \int_{t_0}^{t_0+2\pi/\omega} \zeta \left\| \mathbf{u}_i^{\text{NA}}(\omega) \right\|^2 \omega^2 \cos^2(\omega t + \theta^{\text{NA}}) dt \\
&= \frac{1}{2} \zeta \omega^2 \sum_i \left\| \mathbf{u}_i^{\text{NA}}(\omega) \right\|^2 \\
&= \frac{1}{2} N \omega^2 \zeta \ell_0^2 \delta\gamma^2 \delta\Gamma(\omega)
\end{aligned}$$

Since $P_{\text{in}} = P_{\text{out}}$, we have

$$K''(\omega) - \eta_f \omega = \rho \omega \zeta \ell_0^2 \delta\Gamma(\omega)$$

in which $\rho = N/V$, hence

$$\eta'(\omega) - \eta_f = \rho \zeta \ell_0^2 \delta\Gamma(\omega)$$

For a quasistatic shear strain step $\delta\gamma$, the static nonaffinity, in terms of the individual static nonaffine displacements $\mathbf{u}_{i,\infty}^{\text{NA}}$, is

$$\delta\Gamma_\infty = \frac{1}{N \ell_0^2 \delta\gamma^2} \sum_i \|\mathbf{u}_{i,\infty}^{\text{NA}}\|^2$$

Note that since the static nonaffine displacement vector must be the same as the frequency-dependent nonaffine displacement vector in the zero-frequency limit, i.e. $\mathbf{u}_{i,\infty}^{\text{NA}} = \mathbf{u}_i^{\text{NA}}(\omega \to 0)$, we have $\delta\Gamma_\infty = \delta\Gamma(\omega \to 0)$. Thus, we can write the zero-shear viscosity $\eta_0 = \eta'(\omega \to 0)$ in terms of the static nonaffinity as

$$\eta_0 - \eta_f = \rho \zeta \ell_0^2 \delta\Gamma_\infty$$

5.7.5 Relaxation time

We extract τ_c from the slope, on a log-linear plot, of the terminal exponential decay of $(\delta\sigma(t) - \delta\sigma_\infty)/\delta\sigma(0)$ vs t, as indicated in the inset for $\gamma_0 < \gamma_c$. Specifically, we calculate the slope of the final $n = 5$ points exceeding a sufficiently small threshold of $(\delta\sigma(t) - \delta\sigma_\infty)/\delta\sigma(0) = 10^{-6}$.

Another reasonable way of computing the relaxation time is (see Ref. [163])

$$\tau_c = \lim_{\omega\to 0} \frac{K'(\omega) - K_\infty}{\omega K''(\omega)} \equiv \lim_{\omega\to 0} \frac{\left(K'(\omega) - K_\infty\right)/\omega^2}{\eta'(\omega)}$$

which we can express in terms of $K(t)$. We can compute the dynamic moduli from the relaxation modulus as [208]

$$K'(\omega) = K_\infty + \omega \int_0^\infty \sin(\omega t)\left[K(t) - K_\infty\right] dt$$

and

$$K''(\omega) = \omega \int_0^\infty \cos(\omega t)\left[K(t) - K_\infty\right] dt$$

Thus

$$\lim_{\omega\to 0} \frac{K'(\omega) - K_\infty}{\omega^2} = \int_0^\infty t(K(t) - K_\infty)dt$$

and

$$\lim_{\omega\to 0} K''(\omega)/\omega = \int_0^\infty (K(t) - K_\infty)dt$$

Plugging these in, we find

$$\tau_c = \frac{\int_0^\infty t(K(t) - K_\infty)dt}{\int_0^\infty (K(t) - K_\infty)dt} = \frac{\int_0^\infty t(K(t) - K_\infty)dt}{\rho\zeta\ell_0^2\delta\Gamma_\infty}$$

5.7.6 Finite size effects

We expect to observe the scaling relationships described in the main text when the correlation length is smaller than the system size. If τ_c diverges as $|\gamma_0 - \gamma_c|^{-\phi}$ in the $L \to \infty$ limit, then we expect

$$\tau_c \propto W^{\phi/\nu} \mathcal{A}(L^{1/\nu}(\gamma_0 - \gamma_c))$$

implying that we should observe $\tau_c(\gamma_c) \propto L^{\phi/\nu}$, a plot of $\tau_c L^{-\phi/\nu}$ vs. $L^{1/\nu}(\gamma_0 - \gamma_c)$ for varying L and γ_0 should yield a collapse. For the static differential nonaffinity, prior work has shown [128] $\delta\Gamma \propto L^{\lambda/\nu}\mathcal{B}(L^{1/\nu}(\gamma_0 - \gamma_c))$, so we expect the same finite-size scaling for the zero-shear viscosity,

$$\eta_0 - \eta_f \propto L^{\lambda/\nu}\mathcal{C}(L^{1/\nu}(\gamma_0 - \gamma_c))$$

such that $\eta_0(\gamma_c) - \eta_f \propto L^{\lambda/\nu}$. Likewise, we should see a collapse of $(\eta_0 - \eta_f)L^{-\lambda/\nu}$ vs. $L^{1/\nu}(\gamma_0 - \gamma_c)$ for varying L and γ_0. Here, $\mathcal{A}$, $\mathcal{B}$, and $\mathcal{C}$ are scaling functions.

5.7.7 Nonaffinity and viscosity in soft sphere suspensions

We will now briefly explore the response of dense suspensions of frictionless soft spheres in two and three dimensions near the onset of rigidity (jamming). As noted in the main text, prior work [171] has pointed out a connection between the zero-shear viscosity and quasistatic nonaffine velocity fluctuations in suspensions under steady shear. To highlight the connection between nonaffinity and viscosity we discussed in the main text (Eq. 5.2), we will demonstrate here that the static differential nonaffinity is equivalent to, and diverges as $\phi_0 \to \phi_j$ with the same exponent as, the excess viscosity.

These systems rigidify at a d-dimensional critical sphere volume fraction ϕ_j, with

$\phi_{j,2D} \approx 0.84$ and $\phi_{j,3D} \approx 0.64$. Under steady shear conditions, dense suspensions at volume fractions below ϕ_j these have been shown to exhibit a zero-shear viscosity that scales with the volume (or area) fraction as $\eta_0 \propto (\phi_j - \phi_0)^{-\beta}$, in which β is an exponent generally reported in the range 2–2.8 in both simulations [162, 209–213] and experiments [214, 215].

We consider N spheres with diameters split evenly between $d_i \in (d_0, 1.4d_0)$ to avoid crystallization [82]. The energy of a configuration with positions $\mathbf{r}_i$ is

$$U = \frac{\mu}{2} \sum_i \sum_{j>i} \left(1 - \|\mathbf{r}_j - \mathbf{r}_i\|/d_{ij}\right)^2 \Theta\left(1 - \|\mathbf{r}_j - \mathbf{r}_i\|/d_{ij}\right) \tag{5.7}$$

in which $d_{ij} = (d_i + d_j)/2$ and Φ is the Heaviside step function. To prepare initial configurations, we first randomly place the spheres in a d-dimensional box of side length $3L$ and quasistatically compress the system in small steps to a final side length L, chosen to yield the specified sphere volume fraction ϕ_0. Then, to produce a configuration consistent with slowly applied steady shear strain, we quasistatically apply (again in small steps) an initial simple shear of $\gamma_0 = 5$. Sample configurations are shown in Fig. 5.4.

Using the pre-sheared initial configuration, we follow the same stress relaxation procedure described earlier for networks, with $\delta\gamma = 10^{-5}$, and compute both the excess zero-shear viscosity $\eta_0 - \eta_f$ and static differential nonaffinity $\delta\Gamma_\infty$ as a function of volume fraction. For both $d = 2$ and $d = 3$, we observe values of the scaling exponent β consistent with the range reported in the literature (see Fig. 5.5a) and find that the relationship between zero-shear viscosity and static differential nonaffinity provided in Eq. 5.2, i.e. $\eta_0 - \eta_f = \rho\zeta\ell_0^2\delta\Gamma_\infty$, is consistently satisfied (see Fig. 5.5b). These results suggest that the static differential nonaffinity, which can be inexpensively computed by energy minimization after a single small shear strain step, could provide a complementary route for concretely determining the viscosity divergence exponent β in

this and other related systems (e.g. suspensions of frictional spheres [216]). Note that a different viscosity divergence exponent $\beta \approx 1.5$ is observed for initial configurations generated without pre-shear [163]. Because the static differential nonaffinity necessarily scales with β irrespective of preparation, our results suggest that the distinction in scaling between isotropically compressed and pre-sheared suspensions is due to differences in their nonaffine response.

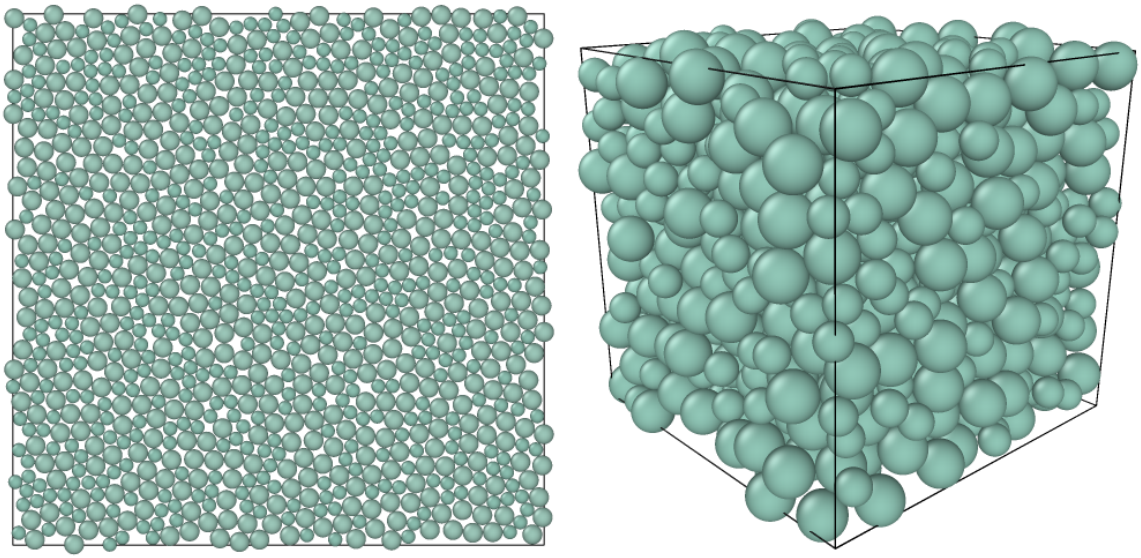

Figure 5.4: (a) Radially bidisperse assemblies of $N = 1000$ spheres in (left) $d = 2$ with area fraction $\phi_0 = 0.84$ and (right) $d = 3$ with volume fraction $\phi_0 = 0.64$. Images prepared using Ovito [217].

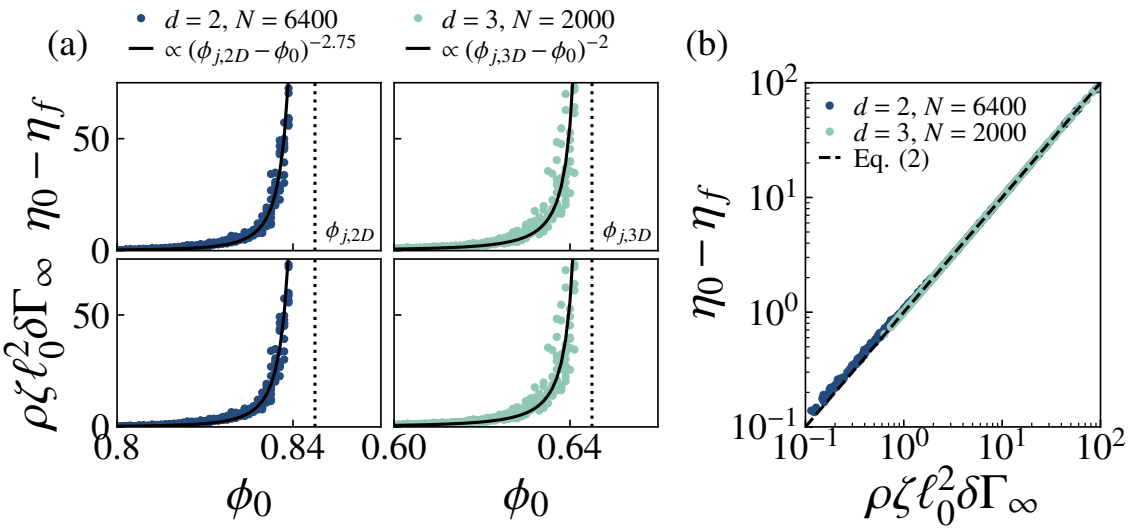

Figure 5.5: (a) Excess zero-shear viscosity $\eta_0 - \eta_f$ and scaled static differential nonaffinity $\delta\Gamma_\infty$ for N spheres in two and three dimensions as a function of volume (or area) fraction ϕ_0, plotted with fits (solid lines) proportional to $(\phi_j - \phi_0)^{-\beta}$ as indicated above each column. Each point represents a measurement for a randomly generated sample, with 10 samples for each ϕ_0. Here, we use $\phi_{j,2D} = 0.845$ and $\phi_{j,3D} = 0.645$. (b) Eq. 5.2 is satisfied for both $d = 2$ and $d = 3$. Data are the same as in (a).

Chapter 6

Nonlinear Poisson effect governed by mechanical critical transition

This chapter is adapted from Ref. [28]:

> **Jordan L. Shivers**, Sadjad Arzash, and Fred C. MacKintosh. Nonlinear Poisson Effect Governed by a Mechanical Critical Transition. ***Physical Review Letters***, 124 (3): 038002, 2020.

6.1 Abstract

Under extensional strain, fiber networks can exhibit an anomalously large and nonlinear Poisson effect accompanied by a dramatic transverse contraction and volume reduction for applied strains as small as a few percent. We demonstrate that this phenomenon is controlled by a collective mechanical phase transition that occurs at a critical uniaxial strain that depends on network connectivity. This transition is punctuated by an anomalous peak in the apparent Poisson's ratio and other critical signatures such as diverging nonaffine strain fluctuations.

6.2 Introduction

When an elastic body is subjected to an infinitesimal strain $\varepsilon_{\parallel}$ along one axis, the corresponding strain $\varepsilon_{\perp}$ in the transverse direction(s) defines Poisson's ratio

$\nu = -\varepsilon_\perp/\varepsilon_\parallel$ [218, 219]. Although this ratio is constrained to the range $\nu \in [-1, 1/2]$ for isotropic materials in 3D, there have been numerous recent reports of anomalously large apparent Poisson's ratios exceeding 1/2 in a variety of fibrous materials at small strain, including felt [25] and networks of collagen [21, 23, 29, 220, 221] and fibrin [24, 221]. This corresponds to an anomalous reduction in volume under extension, in apparent stark contrast to the linear behavior of all isotropic materials, which strictly maintain or increase their volume under infinitesimal extension. This is even true of auxetic materials with $\nu < 0$ [26, 78, 125, 222]. A volume reduction under uniaxial extension can have dramatic effects in living tissue, such as the development of highly aligned, stiffened network regions with reduced porosity between contractile cells in the extracellular matrix [23, 29, 31, 223]. Although it has been argued that this effect is related to stiffening and other nonlinear phenomena in such networks [25, 27, 29], it remains unclear to what extent this anomaly is controlled by network architecture and filament properties.

Here, we show that the anomalous Poisson's ratio of fiber networks is governed by a mechanical phase transition induced by applied axial strain. Using simulations of disordered networks in 2D and 3D, we show that this phenomenon is critical in nature, with diverging strain fluctuations in the vicinity of the transition and a corresponding maximum of the apparent Poisson's ratio. Connecting with recent studies of mechanical criticality in athermal networks [48, 50, 68, 128, 140, 141], we demonstrate that this maximum occurs at a connectivity-controlled strain corresponding to a macroscopic crossover between distinct mechanical regimes, with large-scale, collective network rearrangements as a branched, system-spanning network of tensile force chains develops. Our results highlight the influence of collective properties on the nonlinear mechanics of athermal networks and suggest that controlling connectivity could enable the design of tailored elastic anomalies in engineered fiber networks.

Recent work has demonstrated that the strain-stiffening effect in crosslinked net-

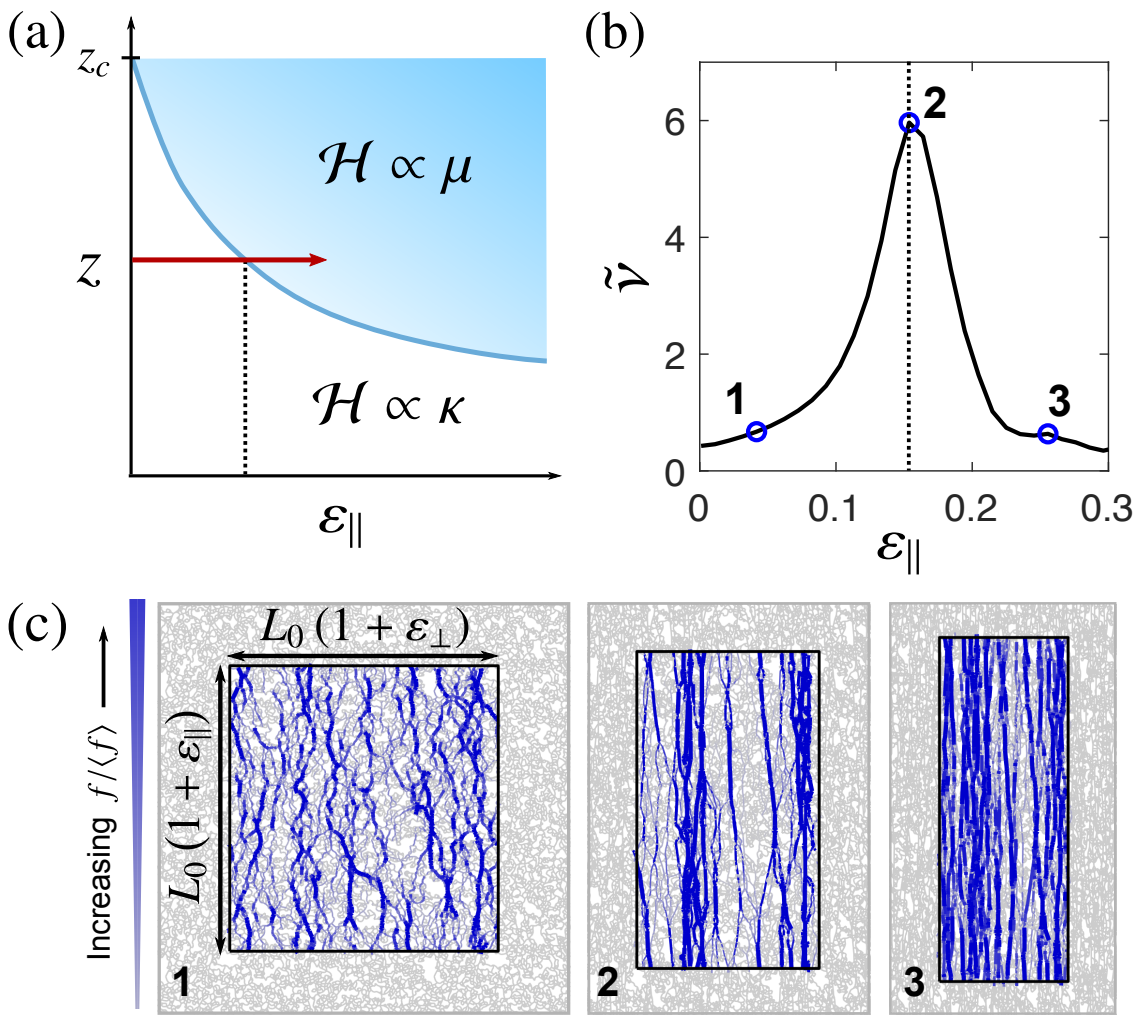

Figure 6.1: (a) Under applied extensional strain $\varepsilon_{\parallel}$ (red arrow) with free transverse strains, subisostatic ($z < z_c$) athermal fiber networks transition from a soft, bending-dominated regime ($\mathcal{H} \propto \kappa$, floppy in the limit of $\kappa \to 0$) to a stiff, stretching-dominated regime ($\mathcal{H} \propto \mu$) at a critical applied strain $\varepsilon_{\parallel,c}$ (dotted line) that increases with decreasing z. As $z \to z_c$, $\varepsilon_{\parallel,c} \to 0$. (b) The incremental Poisson's ratio $\tilde{\nu} = -\partial\varepsilon_\perp/\partial\varepsilon_\parallel$ exhibits a peak at the critical strain, indicated by the dotted line. The black curve corresponds to a 2D packing-derived network with $\tilde{\kappa} = 10^{-5}$ and $z = 3.2$. Network configurations corresponding to the numbered circles are shown in (c). Here, the black box represents the deformation of the initially square periodic boundaries. Bonds under greater tension f than the average, $\langle f \rangle$, are colored blue with thickness proportional to $f/\langle f \rangle$.

works of stiff athermal semiflexible biopolymers, such as collagen, which can be modeled as elastic rods with bending modulus κ and stretching modulus μ, can be understood as a mechanical phase transition between a bending-dominated regime and a stretching-dominated regime at an applied shear or extensional strain governed

by the average network connectivity z [50, 68, 128, 134]. Despite being athermal, such networks exhibit classic signatures of criticality near this transition, including power-law scaling of the elastic moduli with strain and system-size-dependent nonaffine strain fluctuations indicative of a diverging correlation length [50, 128]. In the limit of $\kappa \to 0$, stiffening corresponds to the rearrangement of the network to form a marginally stable, highly heterogenous network of branched force chains [87, 106] similar to the force networks observed in marginal jammed packings under compressive or shear strain [121–123]. Prior work has considered this rigidity transition in networks under applied simple shear [50, 128, 140, 141] or bulk strain [134, 140, 141], with quantitative agreement between shear experiments on collagen and simulations [98].

We find that an analogous collective mechanical phase transition controls the mechanics of networks under uniaxial strain with free orthogonal strains. In athermal semiflexible polymer networks, strain-stiffening and the nonlinear Poisson effect occur at a critical extensional strain controlled by network connectivity, corresponding to a transition from a bending-dominated regime to one dominated by stretching. The expected phase diagram in connectivity-strain space is sketched in Fig. 6.1a. As applied strain drives a network to approach and cross the critical strain boundary, the network's mechanics become stretching-dominated and the resultant nonlinear strain-stiffening induces dramatic transverse contraction coinciding with a peak in the incremental Poisson's ratio $\tilde{\nu}$ (see Fig. 6.1b). Concurrent with this transition, the system exhibits nonaffine strain fluctuations which grow by orders of magnitude as criticality is approached (either by decreasing κ or approaching the critical strain). We demonstrate that this phenomenon occurs irrespective of the details of the underlying network structure, consistent with past observations of networks under simple shear [50, 87]. Our results suggest that the dramatic nonlinear Poisson effect observed in collagen and fibrin gels is macroscopic evidence of this critical rigidity transition.

6.3 Models

We consider 2D and 3D disordered networks comprising interconnected 1D Hookean springs with stretching modulus μ, with additional bending interactions with modulus κ between adjacent bonds. To explore the influence of network structure on the transition, we test a variety of network geometries, including Mikado networks [40], 2D and 3D jammed packing-derived (PD) networks [87], 3D Voronoi networks [27], and 3D random geometric graph (RGG) networks [5] (see Appendix, Section 6.7). The network Hamiltonian $\mathcal{H} = \mathcal{H}_s + \mathcal{H}_b$ consists of a stretching contribution,

$$\mathcal{H}_s = \frac{\mu}{2} \sum_{ij} \frac{(\ell_{ij} - \ell_{ij,0})^2}{\ell_{ij,0}}, \tag{6.1}$$

in which the sum is taken over connected node pairs ij, ℓ_{ij} is the length of the bond connecting nodes i and j, and $\ell_{ij,0}$ is the corresponding rest length, as well as a bending contribution,

$$\mathcal{H}_b = \frac{\kappa}{2} \sum_{ijk} \frac{(\theta_{ijk} - \theta_{ijk,0})^2}{\ell_{ijk,0}}. \tag{6.2}$$

in which the sum is taken over connected node triplets ijk, θ_{ijk} is the angle between bonds ij and jk, $\theta_{ijk,0}$ is the corresponding rest angle, and $\ell_{ijk,0} = (\ell_{ij,0} + \ell_{jk,0})/2$. For Mikado networks, which we designate to have freely hinging crosslinks, the sum in Eq. 6.2 is taken only over consecutive node triplets along initially collinear bonds. Following prior work, we set $\mu = 1$ and vary the dimensionless bending rigidity $\tilde{\kappa} = \kappa/(\mu \ell_c^2)$ [87, 95], where ℓ_c is the average bond length. Since the volume fractions of biopolymer gels are typically 1% or less [98, 224], we do not include excluded volume effects in the results presented below, although we examine their effects in Appendix (see Section 6.7). All network models utilize generalized Lees-Edwards periodic boundary conditions [85, 87], which specify that the displacement vectors between each network node and its periodic images transform according to the deformation gradient tensor

$\mathbf{\Lambda}$. We consider purely extensional strain, with $\Lambda_{ii} = 1 + \varepsilon_i$, where ε_i is the strain along the i-axis relative to the initial configuration. Whereas the primary results of this paper utilize periodic boundaries, we have also performed simulations of non-periodic networks with fixed upper and lower boundaries. We find that fixed boundaries of width equal to or greater than the sample length can suppress the apparent Poisson's ratio (see Appendix, Section 6.7). The normal stress components σ_{ii} are computed as $\sigma_{ii} = (\partial\mathcal{H}/\partial\varepsilon_i)/V$, in which V is the system's volume. Unless otherwise stated, all curves correspond to an average over 15 samples.

To measure the nonlinear Poisson effect, we apply quasi-static longitudinal extensional strain $\varepsilon_\parallel \equiv \varepsilon_1$ in small increments $\delta\varepsilon_\parallel = \varepsilon_{\parallel,n} - \varepsilon_{\parallel,n-1}$ and, at a given strain, first allow the system to reach mechanical equilibrium by minimizing the network's Hamiltonian using the L-BFGS algorithm [225]. After each extensional strain step, we simulate free transverse boundaries by incrementally varying the transverse strain(s) ε_2 (and ε_3 in 3D) in order to reduce the corresponding transverse normal stress component(s) to zero, i.e. $|\partial\mathcal{H}/\partial\varepsilon_i| \approx 0$. In 2D the single transverse strain is $\varepsilon_\perp \equiv \varepsilon_2$, whereas in 3D the stresses along the two transverse axes are relaxed independently and we define the transverse strain, for the purposes of computing the incremental Poisson's ratio, as $\varepsilon_\perp \equiv (\varepsilon_2 + \varepsilon_3)/2$. For orientationally isotropic network models, ε_2 and ε_3 are equivalent in the limit of large system size. The differential Young's modulus $\tilde{E}$ is computed as $\tilde{E} = \partial\sigma_\parallel/\partial\varepsilon_\parallel$.

6.4 Results

Subisostatic athermal networks undergo a transition from a bending-dominated regime to a stiff stretching-dominated regime at a critical applied shear or extensional strain [97, 226]. Recent work showed that athermal networks under extensional strain with free transverse strains, which we consider in this work, undergo a similar transition

from a bending-dominated to stretching-dominated regime corresponding with strain-stiffening [27]. To examine the influence of bending rigidity on this transition, we first consider 2D packing-derived networks with fixed connectivity $z = 3.2 < z_c$ and varying reduced bending rigidity $\tilde{\kappa}$. In Fig. 6.2a, we plot the relaxed transverse strain $\varepsilon_\perp$ as a function of applied longitudinal extensional strain $\varepsilon_\parallel$, with the corresponding incremental Poisson's ratio $\tilde{\nu} = -\partial\varepsilon_\perp/\partial\varepsilon_\parallel$ shown in Fig. 6.2b. The fraction of the total network energy due to bending interactions $\mathcal{H}_b/\mathcal{H}$ as a function of strain is shown in Appendix. Networks with high $\tilde{\kappa}$ deform approximately linearly up to relatively large applied strains, with minimal strain-dependence of $\tilde{\nu}$. In contrast, networks with low $\tilde{\kappa}$ exhibit similar linear deformation (with $\tilde{\nu} < 1$) in the limit of small applied strain, but under increasing applied strain these undergo a transition to a much stiffer stretching-dominated regime, resulting in significant transverse contraction and thus a very large apparent Poisson's ratio. At larger strains, within the stretching-dominated regime, the networks again deform approximately linearly with an incremental Poisson's ratio $\tilde{\nu} < 1$. The transition occurs at a critical applied extension ε_c, which we define as the strain corresponding to the inflection point in the $\varepsilon_\perp$ vs. $\varepsilon_\parallel$ curve as $\kappa \to 0$. By definition, this corresponds to a peak in $\tilde{\nu}$, which grows with decreasing $\tilde{\kappa}$.

This unusual nonlinear Poisson effect results from the asymmetric nonlinear mechanics of these networks, which stiffen dramatically under extensional strain but remain soft under compression [23, 25]. Compressing a semiflexible polymer network induces normal stresses proportional to the bending rigidity κ of the constituent polymers, whereas sufficient extension induces normal stresses proportional to the polymer stretching modulus μ [226]. An athermal network under uniaxial extension with *fixed* transverse strains will exhibit an increase in the magnitude of its normal stresses from $\sigma_{ii} \propto \kappa$ to $\sigma_{ii} \propto \mu$ at the critical strain, both along the strain axis ($\sigma_\parallel$) and the transverse axes ($\sigma_\perp$). Relaxing the transverse boundaries to satisfy $\sigma_\perp = 0$ requires contraction along the transverse axes, which necessarily reduces the stiff

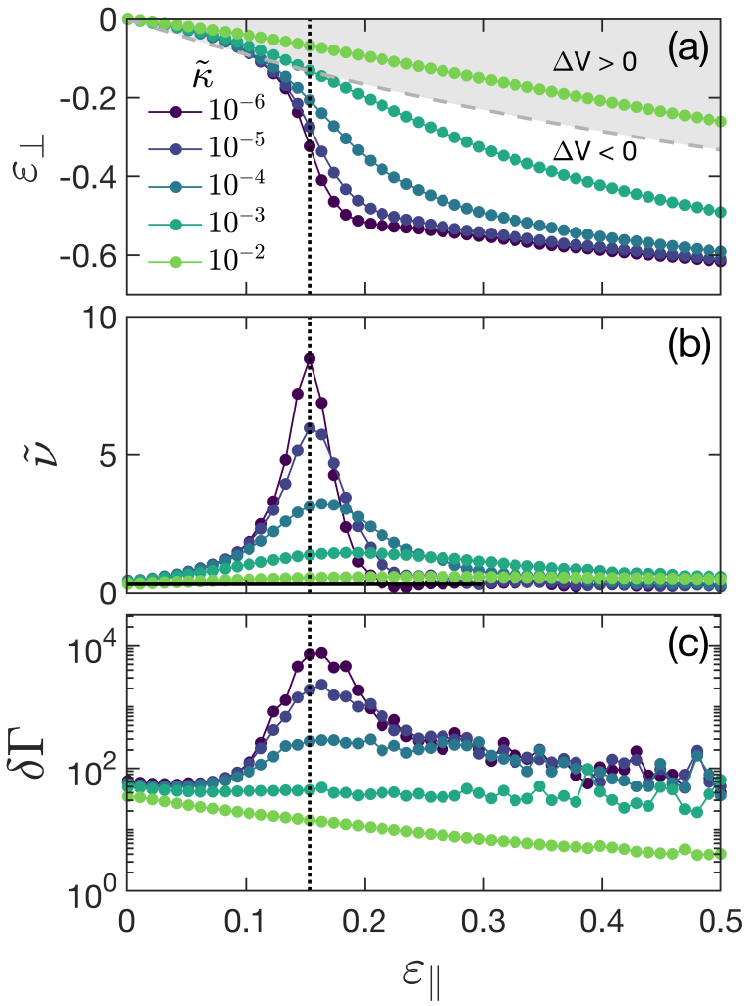

Figure 6.2: (a) Relaxed transverse strain $\varepsilon_\perp$ as a function of applied extensional strain $\varepsilon_\parallel$ for 2D packing-derived networks with $z = 3.2$ and varying $\tilde{\kappa}$. For large $\tilde{\kappa}$, networks deform linearly up to relatively large strains. The gray dashed line corresponds to constant volume, $\Delta V \equiv V - V_0 = 0$. In the limit of low $\tilde{\kappa}$, networks deform linearly at low strains, with a linear Poisson's ratio less than 1, but exhibit a significant increase in transverse contraction at a critical strain $\varepsilon_{\parallel,c}$, indicated by the dotted black line. (b) The magnitude of the incremental Poisson's ratio $\tilde{\nu} = -\partial\varepsilon_\perp/\partial\varepsilon_\parallel$ peaks at the critical strain and increases with decreasing $\tilde{\kappa}$. (c) At the critical strain, we observe a corresponding peak in the nonaffine strain fluctuations $\delta\Gamma$ which increases in magnitude as $\tilde{\kappa}$ is decreased.

stretching-induced contributions ($\propto \mu$) until these are balanced by softer, compression-induced contributions ($\propto \kappa$). The amount of transverse contraction in the vicinity of the critical strain thus increases with μ/κ.

Past work showed that athermal networks under applied shear strain exhibit diverging nonaffine strain fluctuations at the critical strain, in the limit of $\tilde{\kappa} \to 0$,

indicative of a diverging correlation length [50, 52, 128]. Concurrent with the strain-driven transition in this work, we observe similarly large internal strain fluctuations. We use an analogous measure of the strain fluctuations for the deformation gradient tensor $\mathbf{\Lambda}$ defined above. For the nth strain step, the incremental applied extensional strain $\delta\varepsilon_{\parallel} = \varepsilon_{\parallel,n} - \varepsilon_{\parallel,n-1}$ and relaxation of the transverse strain(s) transforms the deformation gradient tensor from $\mathbf{\Lambda}_{n-1}$ to $\mathbf{\Lambda}_n$. We compute the resulting differential nonaffinity $\delta\Gamma$ as

$$\delta\Gamma = \frac{1}{\ell_c^2 \left(\delta\varepsilon_{\parallel}\right)^2} \left\langle \left\| \delta\mathbf{u}_i - \delta\mathbf{u}_i^{\text{aff}} \right\|^2 \right\rangle \tag{6.3}$$

in which the average is taken over all nodes i, ℓ_c is the initial average bond length, $\delta\mathbf{u}_i = \mathbf{u}_{i,n} - \mathbf{u}_{i,n-1}$ is the actual displacement of node i after the extensional strain step and transverse strain relaxation, and $\delta\mathbf{u}_i^{\text{aff}}$ is the displacement of node i corresponding to an affine transformation from the previous configuration at strain state $\mathbf{\Lambda}_{n-1}$ to the new strain state $\mathbf{\Lambda}_n$. Consistent with prior work examining networks under shear strain [128], we find that increasing $\tilde{\kappa}$ results in increasingly affine deformation (decreasing $\delta\Gamma$), whereas in the low-$\tilde{\kappa}$ limit we observe a peak in $\delta\Gamma$ at the critical strain which grows with decreasing $\tilde{\kappa}$ (see Fig. 6.2c).

For athermal subisostatic networks under applied simple shear strain, the critical strain is governed by the average network connectivity z [50, 52, 79], with the critical strain decreasing to zero as z approaches the Maxwell isostatic value $z_c = 2d$, where d is the dimensionality [46]. As sketched in our hypothesized phase diagram (see Fig. 6.1a), we expect z to similarly control the critical strain for networks under extensional strain with free orthogonal strains. In Fig. 6.3, we plot the incremental Poisson ratio $\tilde{\nu}$ as a function of $\varepsilon_{\parallel}$ for several network geometries in 2D and 3D with varying z. While the precise location of the critical strain for a given connectivity is sensitive to the choice of network structure, we find that all networks tested exhibit behavior that is qualitatively consistent with the proposed phase diagram, with a critical strain $\varepsilon_{\parallel,c}$ that decreases as $z \to z_c$.

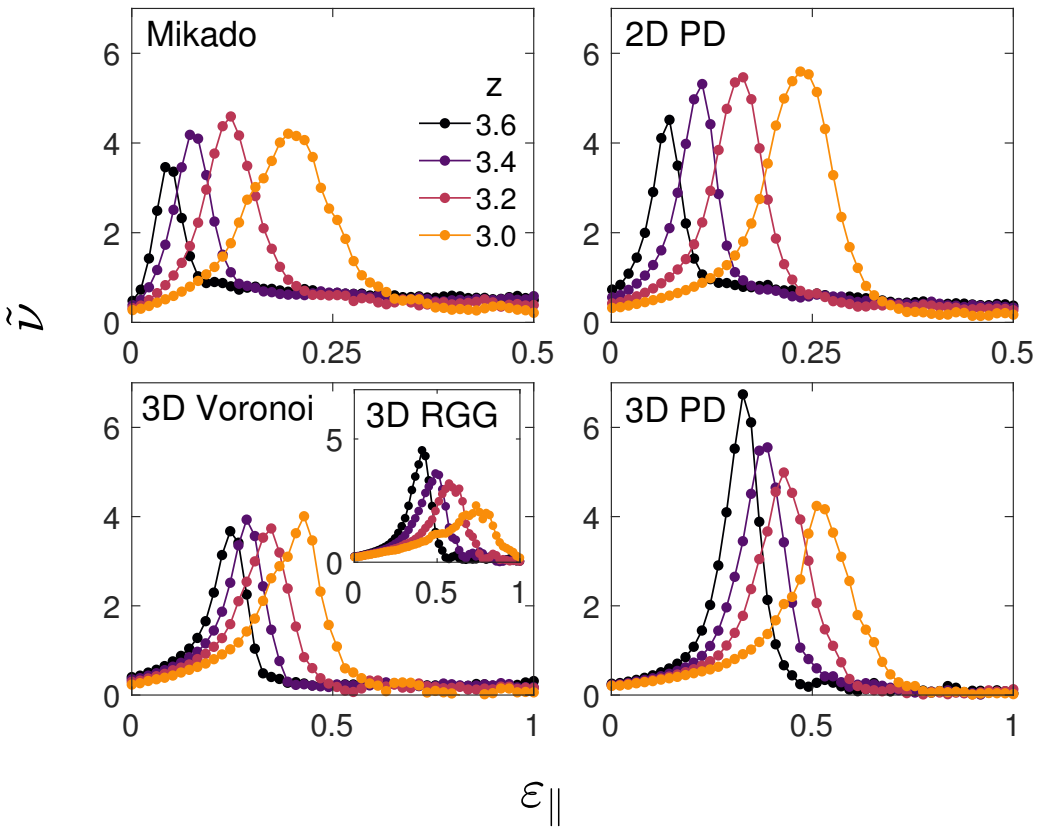

Figure 6.3: Incremental Poisson's ratio $\tilde{\nu} = -\partial\varepsilon_{\perp}/\partial\varepsilon_{\parallel}$ as a function of applied extensional strain $\varepsilon_{\parallel}$ for various 2D and 3D network structures, as labeled in the top right of each panel, with varying connectivity z. In all networks, the critical strain $\varepsilon_{\parallel,c}$, corresponding to the peak in $\tilde{\nu}$, increases with decreasing z.

We also explicitly map out a phase diagram for packing-derived networks in 2D. In Fig. 6.4a, we plot both the incremental Poisson's ratio $\tilde{\nu}$ and differential nonaffinity $\delta\Gamma$ for 2D PD networks as a function of applied strain over a range of z values up to the 2D isostatic point, $z_c = 4$. Both quantities become maximal at a critical strain that approaches 0 as $z \to z_c$. Near z_c, the critical strain grows as $\varepsilon_{\parallel,c} \propto z_c - z$, consistent with prior results [79, 134] (see Appendix, Section 6.7). We plot the corresponding differential Young's modulus $\tilde{E} = \partial\sigma_{\parallel}/\partial\varepsilon_{\parallel}$ as a function of z and $\varepsilon_{\parallel}$ in Fig. 6.4b, demonstrating that the transition of the network from the soft, bending-dominated regime ($\tilde{E} \propto \kappa$) to the stiffer, stretching-dominated regime ($\tilde{E} \propto \mu$) coincides with peaks in both the incremental Poisson's ratio and the differential nonaffinity (Fig. 6.4a). Further, we find that the differential Young's modulus scales as a power law

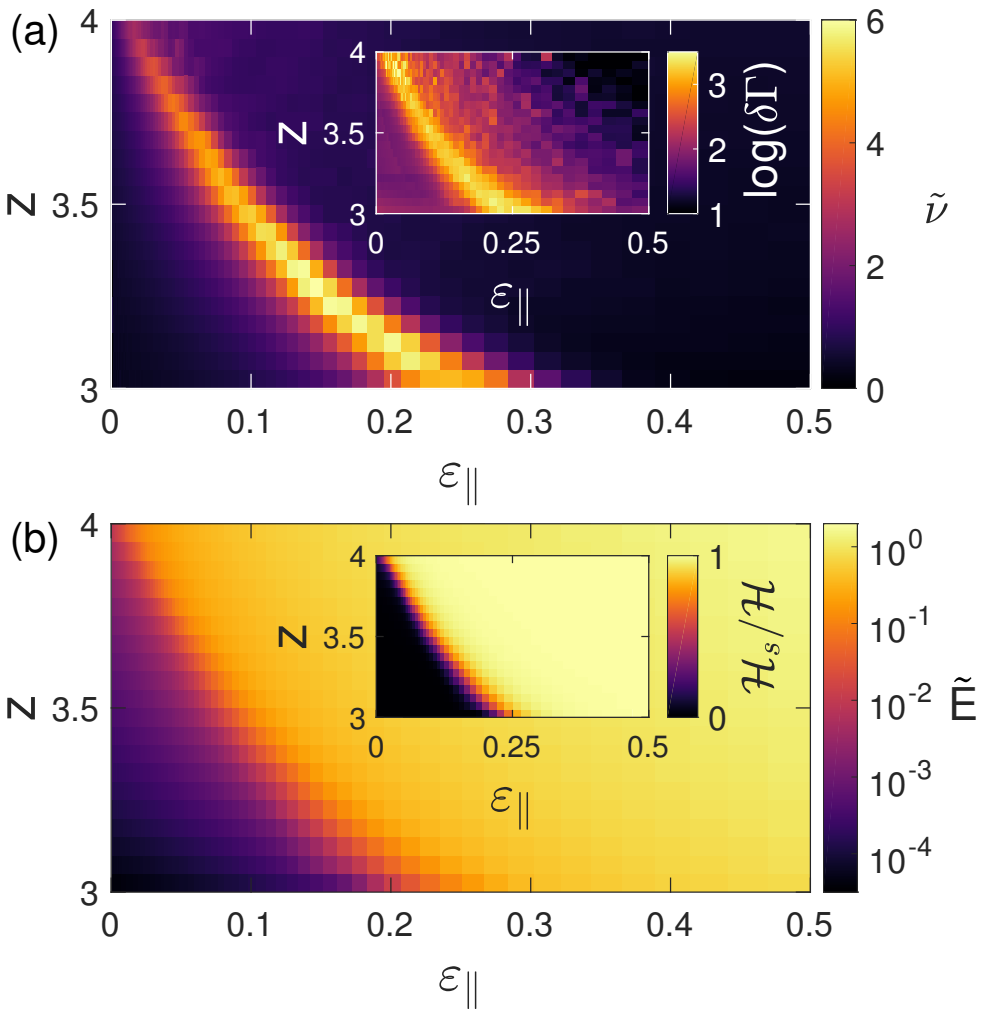

Figure 6.4: (a) Incremental Poisson's ratio $\tilde{\nu} = -\partial\varepsilon_\perp/\partial\varepsilon_\parallel$ as a function of applied extensional strain $\varepsilon_\parallel$ and average connectivity z for 2D packing-derived networks with $W = 100$ and $\tilde{\kappa} = 10^{-5}$. Inset: For a given connectivity z, the differential nonaffinity $\delta\Gamma$ exhibits a peak coinciding with the peak in the incremental Poisson ratio $\tilde{\nu}$. (b) Differential Young's modulus $\tilde{E} = \partial\sigma_\parallel/\partial\varepsilon_\parallel$ for the same networks as in (a). Inset: Corresponding stretching energy fraction $\mathcal{H}_s/\mathcal{H}$.

$\tilde{E} \propto \left|\varepsilon_\parallel - \varepsilon_{\parallel,c}\right|^f$ above the critical strain (see Appendix, Section 6.7).

6.5 Discussion

We have demonstrated that the nonlinear Poisson effect observed in subisostatic networks is a direct consequence of a strain-driven collective mechanical phase transition. Whereas the large apparent Poisson's ratios observed in such networks at finite strains can be qualitatively understood as resulting from their highly asymmetric mechanical properties, i.e. that they stiffen dramatically under finite extension but remain comparatively soft under compression, as discussed conceptually in Refs. [23, 25], we have demonstrated that this asymmetry becomes maximized at a critical phase boundary controlled by strain and connectivity. At this boundary, a network exhibits diverging strain fluctuations as it collectively rearranges to transition from a soft, bending-dominated regime to a stiff, stretching-dominated regime. In the latter, marginally stable state, the mechanics become dominated by an underlying branched network of bonds under tension, which generates tensile transverse normal stresses that drive the lateral contraction of the network against the weaker compression-induced stresses. This results in an apparent Poisson's ratio that exceeds $1/2$ at the phase transition and grows as a function of the relative magnitude the stiff and soft contributions, μ/κ. Whereas we have focused on the $T = 0$ limit with an eye towards networks such as collagen, we note that finite temperature can stabilize otherwise floppy networks [227, 228] and would be expected to reduce the peak in the differential Poisson's ratio in a manner similar to finite κ.

Using simulations of a variety of network architectures in 2D and 3D, we have shown that this effect is robustly controlled by connectivity and occurs independently of the precise underlying network structure. Further, we have demonstrated critical scaling of the differential Young's modulus (see Appendix, Section 6.7) similar to what has been shown for the shear modulus of collagen networks [50]. This suggests that experimental measurements of the differential Young's modulus of collagen gels under uniaxial strain should quantitatively fit the predicted scaling form, with a given

sample exhibiting a peak in the incremental Poisson's ratio at the transition point. Further work could enable prediction of the local stiffness in the extracellular matrix based on the observed local strain asymmetry.

6.6 Acknowledgments

This work was supported in part by the National Science Foundation Division of Materials Research (Grant DMR-1826623) and the National Science Foundation Center for Theoretical Biological Physics (Grant PHY-1427654). J.L.S. acknowledges additional support from the Ken Kennedy Institute Graduate Fellowship and the Riki Kobayashi Fellowship in Chemical Engineering.

6.7 Appendix

Network generation

After generating each initial network structure as described below, we reduce the connectivity z to the desired value by randomly removing bonds and any resulting dangling ends.

Mikado networks [40, 116] are prepared by depositing fibers of length L with random locations and orientations into a 2D periodic square unit cell of side length W and adding freely hinging crosslinks at all fiber intersections. We use $L = 4$ and $W = 30$ and continue depositing fibers until the average coordination number, after the removal of dangling ends, is $z \approx 3.6$. This yields an average crosslink density of $L/\ell_c \approx 11$, where ℓ_c is the average distance between crosslinks. We impose a minimum segment length $\ell_{min} = W/1000$.

2D and 3D packing-derived networks are prepared as in prior work [87]. For 2D PD networks, we randomly place $N = W^2$ radially bidisperse disks with $r \in \{r_0, \phi r_0\}$

in a periodic square unit cell of side length W and incrementally increase r_0 from 0, allowing the system to relax at each step, until the packing becomes isostatic and develops a finite bulk modulus. We use $\phi = 1.4$ to avoid long-range crystalline order [82]. At this point, we generate a contact network between overlapping disks. For 3D PD networks, we follow the same procedure beginning with $N = W^3$ radially bidisperse spheres, also with $r \in \{r_0, \phi r_0\}$ and $\phi = 1.4$, in a periodic cubic unit cell of side length W. We use $W = 20$ in 3D and $W = 100$ in 2D. For sufficiently large systems, this yields a network with initial coordination number $z \approx 2d$ [47, 81, 117], in which d is the dimensionality.

We generate 3D Voronoi networks by randomly distributing N seed points in a periodic cubic unit cell of side length W, from which we generate a Voronoi diagram using the CGAL library [229]. We choose N so that the final network has roughly W^3 nodes, with $W = 15$. These have initial average coordination number $z = 4$.

Three-dimensional random geometric graph (RGG) models have been shown to capture the micromechanics of collagen and fiber networks [5]. Following Ref. [5], we generate RGGs of $N = W^3$ vertices in a periodic box of side length W, where each pair of nodes is connected with probability $P_c \propto e^{-\ell/L}/\ell^2$, where ℓ is the distance between two vertices and $L = 1$ is the length scale of a typical bond. We impose a minimum bond length of $\ell_{min} = 0.5$. We generate RGG networks with $W = 20$ and initial average coordination number $z = 4$.

Midpoints

The amount of contraction induced by the onset of stiffening depends on the resistance of the network to lateral compression. Mikado and 2D PD networks with relatively high values of z exhibit less dramatic contraction upon transitioning to the stretching-dominated regime than those with lower z. This is a consequence of the fact that more dilute (lower z) networks have fewer highly connected regions within

them and are thus less resistant to compression than more highly connected networks. To verify that this is the case, in Fig. 6.5, we consider the same Mikado structures as in Fig. 3, in which we have now added a midpoint hinge to each bond in order to allow the buckling of individual bonds with the same bending energy penalty as is used between adjacent bonds. While the location of the transition in strain is still controlled by connectivity, networks with midpoints contract more dramatically at the critical strain than those without midpoints (for fixed $\tilde{\kappa}$), with larger corresponding peaks in $\tilde{\nu}$. This is because the normal stress induced by transverse compression in networks with midpoints is strictly proportional to the bending rigidity κ, whereas in networks without midpoints there can be additional, stronger contributions ($\propto \mu$) from locally stiff regions at large compression levels.

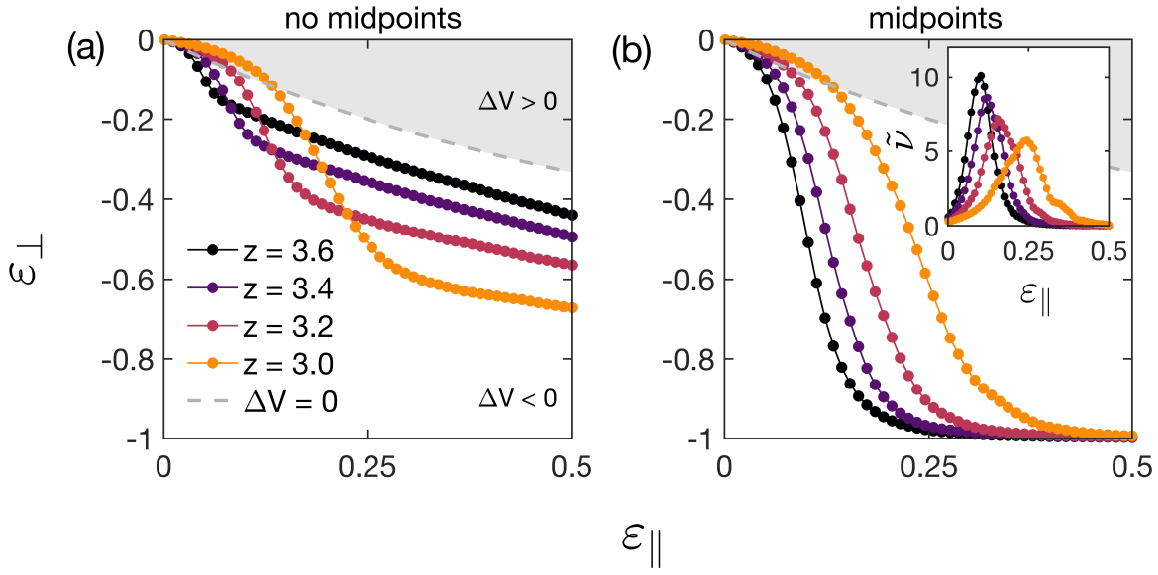

Figure 6.5: Transverse strain $\varepsilon_\perp$ as a function of applied extensional strain $\varepsilon_\parallel$ for Mikado networks with $\tilde{\kappa} = 10^{-5}$ and varying connectivity z (a) without buckling of individual bonds and (b) with buckling of individual bonds, in which an extra node is added at the midpoint of each bond. The dashed line indicates the isochoric transverse strain, with the region above corresponding to an increase in volume ($\Delta V > 0$) and the region below corresponding to a decrease in volume ($\Delta V < 0$). Inset: Incremental Poisson's ratio $\tilde{\nu}$ as a function of $\varepsilon_\parallel$ for networks with midpoints. The corresponding plot for Mikado networks without midpoints is shown in Fig. 3a.

Energy contributions for networks with fixed z and varying $\tilde{\kappa}$

In Fig. 6.6, we plot the fractional contribution of bending to the total network energy, $\mathcal{H}_b/\mathcal{H}$, for a 2D packing-derived network with varying $\tilde{\kappa}$. In the low-$\tilde{\kappa}$ limit, we observe a clear transition from a bending-dominated to stretching-dominated regime at the critical strain, corresponding to the maximum value of the incremental Poisson's ratio $\tilde{\nu}$.

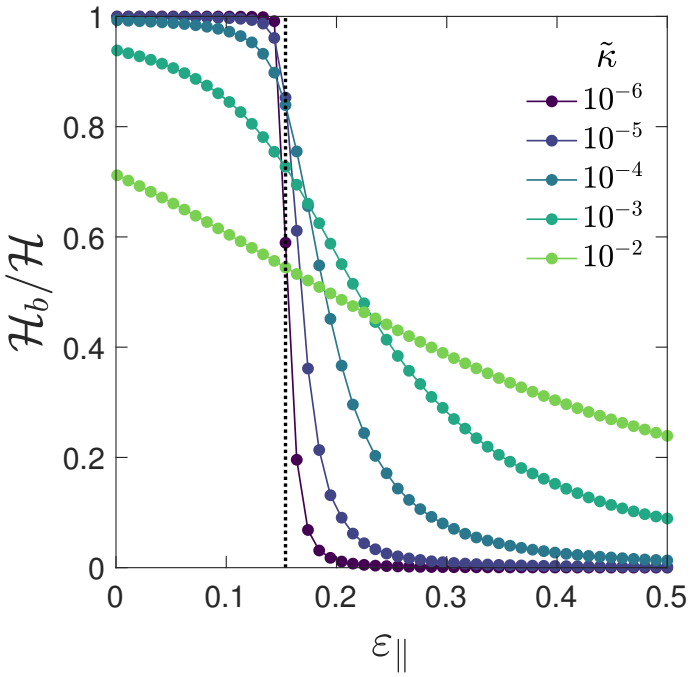

Figure 6.6: Bending energy fraction $\mathcal{H}_b/\mathcal{H}$ for a 2D packing-derived network with $z = 3.2$, $W = 100$ and varying $\tilde{\kappa}$. The dotted line represents the critical strain $\varepsilon_{\parallel,c}$ corresponding to the peak in the incremental Poisson's ratio.

6.7.1 Scaling of the stiffness and nonaffinity

For subisostatic networks in the limit of small applied strain $\varepsilon_\parallel$, the differential Young's modulus $\tilde{E} = \partial\sigma_\parallel/\partial\varepsilon_\parallel$ is proportional to the bending rigidity $\tilde{\kappa}$. Above the critical applied strain $\varepsilon_{\parallel,c}$, $\tilde{E}$ is independent of $\tilde{\kappa}$ and scales as a power law with respect to the distance (along the strain axis) to the critical strain, i.e. $\tilde{E} \propto |\Delta\varepsilon_\parallel|^f$, where $\Delta\varepsilon_\parallel = \varepsilon_\parallel - \varepsilon_{\parallel,c}$. Following prior work [50], we can capture both regimes with the

scaling form

$$\tilde{E}\frac{V}{V_0} \propto |\Delta\varepsilon_\parallel|^f \mathcal{G}_\pm \left(\frac{\tilde{\kappa}}{|\Delta\varepsilon_\parallel|^\phi}\right) \tag{6.4}$$

in which the scaling function $\mathcal{G}_\pm$ has branches corresponding to positive and negative values of $\Delta\varepsilon_\parallel$, and the factor V/V_0 corrects for the change in $\tilde{E}$ due to the change in the system's volume V from the initial volume V_0. In Fig. 6.7a, we show stiffening curves for a large packing-derived network with varying $\tilde{\kappa}$ and demonstrate scaling collapse according to the above scaling form with $f = 0.55$ and $\phi = 2.5$ (see Fig. 6.7b).

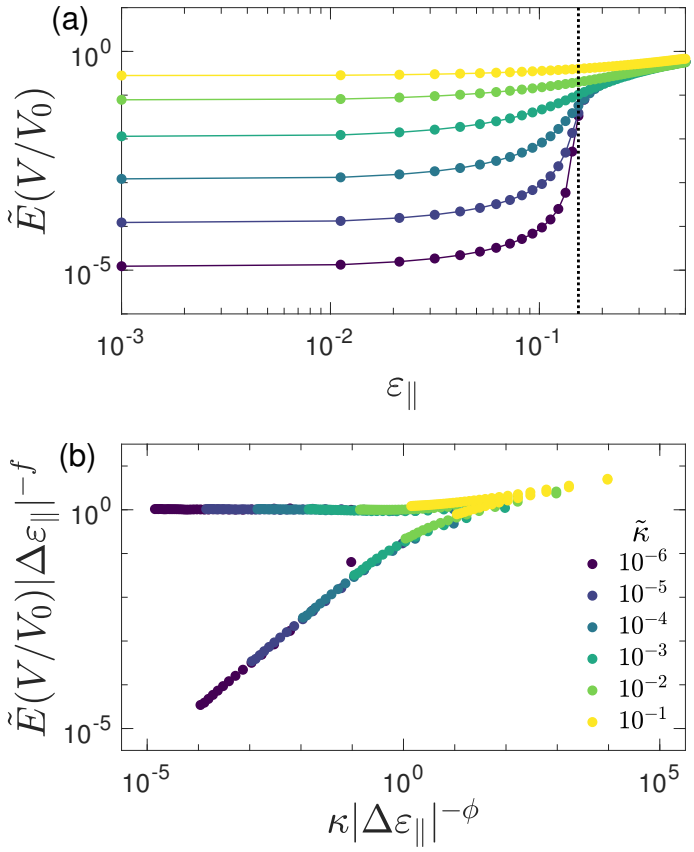

Figure 6.7: (a) Stiffening curves for a 2D packing-derived network with varying κ, $z = 3.2$, $W = 140$. (b) Collapse of the curves in (a) according to Eq. 6.4 with exponents $f = 0.55$ and $\phi = 2.5$.

Recent work has described a hyperscaling relation between the stiffening exponent f, the dimensionality d, and the correlation length exponent ν, [128]

$$f = d\nu - 2, \tag{6.5}$$

and predicts that, at the critical strain, the differential nonaffinity should scale with system size W as

$$\max(\delta\Gamma) \propto W^{(\phi-f)/\nu}. \tag{6.6}$$

Determining ν from Eq. 6.5 using $d = 2$ and $f = 0.55$ (from the prior scaling collapse of $\tilde{E}$), we observe good agreement between measured values of $\max(\delta\Gamma)$ and the predicted scaling of the differential nonaffinity with system size (see Fig. 6.8).

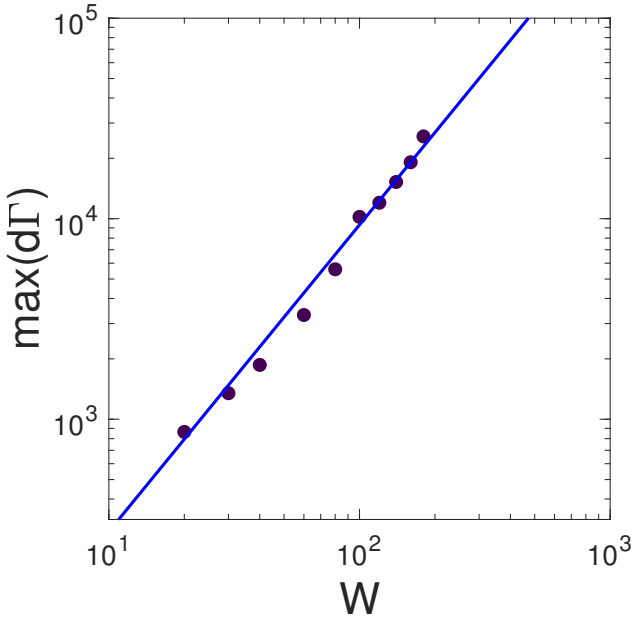

Figure 6.8: In the low-$\tilde{\kappa}$ limit, the magnitude of the differential nonaffinity at the critical strain, $\max(\delta\Gamma)$, grows with increasing system size W as $\max(\delta\Gamma) \propto W^{(\phi-f)/\nu}$ (solid line), with $f = 0.55$ and $\phi = 2.5$ obtained from the scaling collapse of the differential Young's modulus and $\nu = (f + 2)/d$ with dimensionality $d = 2$, as derived in Ref. [128]. These data correspond to averages over 2D packing-derived networks with $z = 3.2$ and $\tilde{\kappa} = 10^{-6}$.

6.7.2 Boundary conditions

Whereas we have exclusively considered periodic systems in this work to avoid boundary effects, we note that real systems are of course non-periodic. In experiments, strain is typically applied via fixed upper and lower boundaries, resulting in necking. Properly measuring transverse strain as a consequence of applied strain in experiments requires a sample with a sufficiently large aspect ratio (ratio of length along the applied

strain axis to width along the transverse axes) to mitigate the influence of boundary effects. Prior experimental work [24] has addressed this issue by considering the strain within the necked region of a stretched cylindrical sample with a large aspect ratio. For a non-periodic simulated network with a sufficiently large aspect ratio, we expect that the strains in the center of the necked region should quantitatively agree with the corresponding strain in a sample with periodic boundary conditions. Smaller aspect ratios, however, are expected to reduce the apparent Poisson's ratio.

To test these assumptions, we generated periodic packing-derived according to the methods described in Section I above, with the initial network structure generated from $N = 10000$ radially bidisperse disks in a periodic box of aspect ratio α with initial dimensions $L_y = \alpha L_x$, where $L_x L_y = N$. After diluting the resulting network to $z = 3$, we cut all boundary-crossing bonds to yield a non-periodic network. We then designated the nodes on the top and bottom boundaries of the network as "fixed," and applied quasistatic strain to the sample by deforming the "fixed" nodes affinely according to the desired applied extension $\varepsilon_{\parallel}$ and minimizing the energy of the network at each applied strain. This results in a "necked" network configuration, as shown in Fig. 6.9, with the amount of apparent necking increasing with the aspect ratio. To obtain a coarse-grained estimate of the transverse strain within the necked region, we first bin the node coordinates according to their y-values into 100 equally spaced bins spanning the height of the network. We then measure the width of the network in each height bin as the difference between the maximum and minimum x-coordinates of the nodes within the bin. and measure the transverse strain $\varepsilon_{\perp} = w/w_0 - 1$ as the fractional change in the average width w of the middle 10% of bins (the center of the necked region) with respect to its initial value w_0. In Fig. S5c, we demonstrate that this effective transverse strain approaches that achieved with periodic boundary conditions as we increase the aspect ratio of the network sample. This indicates that "smearing out" of the phase transition due to necking does indeed occur if the aspect

ratio of the sample is small, resulting in a smaller apparent Poisson's ratio (as shown in Fig. 6.9d), but that the results become equivalent when the aspect ratio is increased sufficiently (as in the experiments of Ref. [24]). We note that this results in a slight downward shift of the apparent critical strain, which can be understood as a result of the higher effective extensional strain near the center of a sample with fixed boundary conditions for a given global extensional strain.

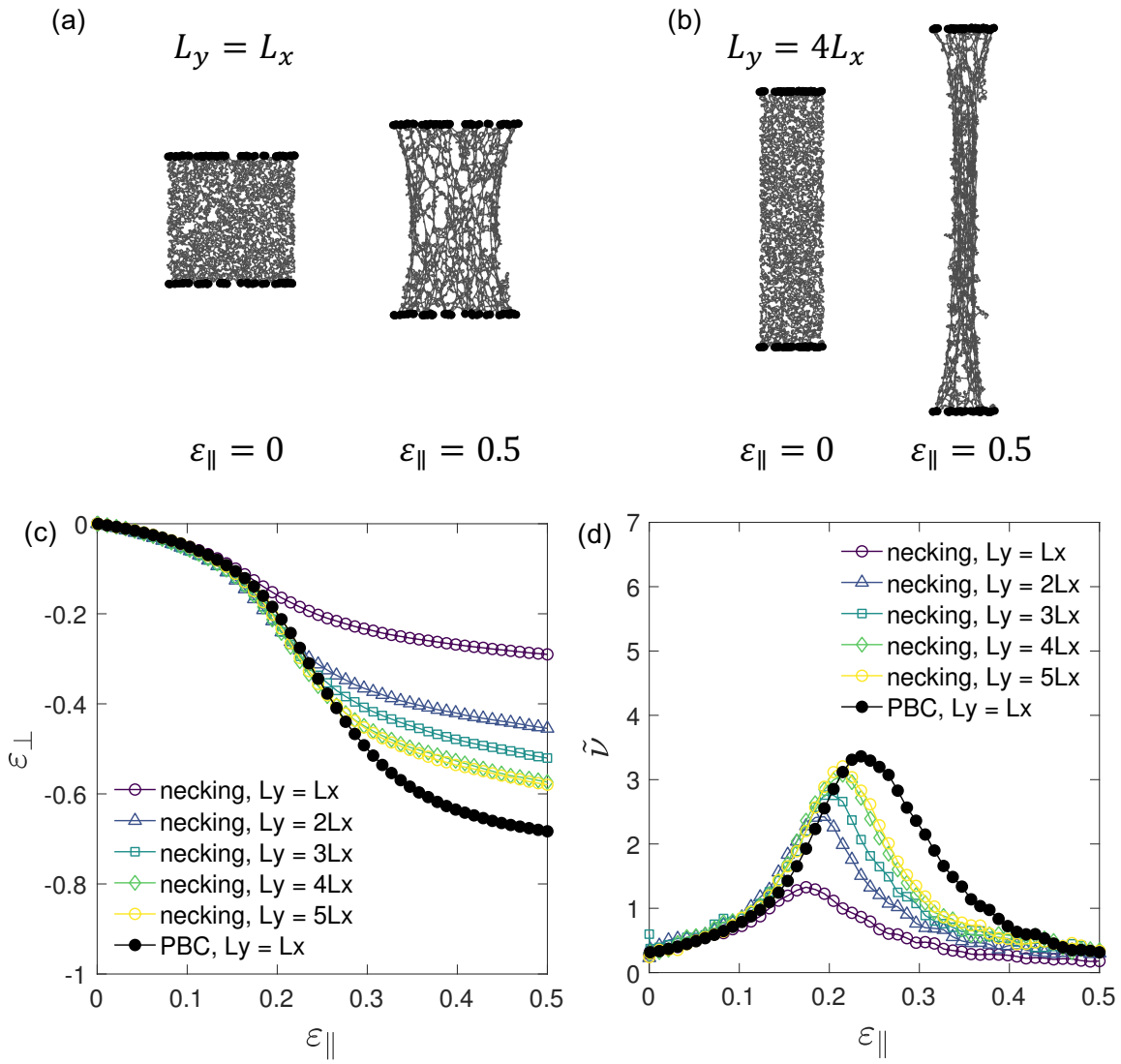

Figure 6.9: (a-b) Non-periodic networks with fixed nodes (solid black circles) at the upper and lower boundaries exhibit necking under applied extensile strain. We consider networks with $\kappa = 10^{-4}$, generated from packings of $N = 10000$ bidisperse disks in periodic boxes of initial width L_x and height L_y, in which $L_x L_y = N$, with varying aspect ratio $\alpha = L_y/L_x$. These networks are then diluted to $z = 3$ and made non-periodic by cutting bonds that cross the boundaries. We affinely deform the "fixed" nodes by extensile strain ε, and the energy of the network is subsequently minimized with the positions of the "fixed" nodes held constant. The transverse strain $\varepsilon_\perp$ is measured as the change in width of the center of the network, as described above, as a function of applied extensile strain $\varepsilon_\parallel$. (c) We find that as the sample aspect ratio is increased, the $\varepsilon_\perp$ vs. $\varepsilon_\parallel$ curves for non-periodic samples approach the corresponding curve for a periodic networks with $L_x = L_y$. (d) Likewise, the incremental Poisson's ratio $\tilde{\nu} = -\partial\varepsilon_\perp/\partial\varepsilon_\parallel$ approaches that of the periodic samples. These data correspond to an average over 15 samples each.

6.7.3 Excluded volume effects

We have thus far ignored excluded volume effects, as these are generally unimportant for networks of filamentous proteins such as collagen and fibrin due to the very low network volume fractions involved (typically less than 1%) and the suppressed bending fluctuations of such fibers. Especially for collagen networks, models such as the present one have been shown to be quantitative and predictive, both in the linear regime and even far into the nonlinear regime.

To explore the influence of excluded volume effects on the nonlinear Poisson effect, we now consider simulations of 2D packing-derived networks with N_m equally spaced midpoint nodes on each bond, with and without including harmonic repulsive interactions between nodes (in this case, each node is treated as a repulsive disk with radius $r = 0.8/(2(N_m + 1))$ and repulsive spring constant $k_r = 1$, which is sufficiently large to prevent any bonds from interpenetrating at the strains we are considering). In Fig. 6.10a-b, we show images of sections of a network with $N_m = 5$ midpoints per bond.

In Fig. 6.10c, we show strain curves for networks of side length $L = 60$ with connectivity $z = 3.2$ and bending rigidity $\kappa = 10^{-5}$, in which we vary the number of midpoints per bond N_m between 1 and 5. For networks without repulsive interactions, the number of midpoints has essentially no effect on the strain curves (Fig 6.10c) or the corresponding incremental Poisson ratio (Fig 6.10d). When repulsive interactions are included, the excluded volume effect is significant for small N_m (i.e. large node radius and large effective bond thickness), but it becomes much less significant as N_m is increased. Further increasing N_m would result in the curves more closely resembling those of networks without repulsive interactions. For node radius r, we can approximate bonds as rods of width $2r$, so we can estimate an effective area fraction ϕ for a network with 2D line density ρ (bond length per area) and node radius r as $\phi = 2\rho r$. For connectivity $z = 3.2$, the 2D line density of our PD networks is

$\rho \approx 1.4$, so we have an effective area fraction of $\phi \approx 0.18$ for $N_m = 5$ and $\phi \approx 0.56$ for $N_m = 1$. We note that these values are significantly larger than the volume fractions of experimentally tested networks ($\phi < 0.005$) [52, 98]. Since the effects of excluded volume in our 2D simulations are already quite small at the relatively large area fraction of $\phi = 0.18$, we conclude that simulations of networks without excluded volume effects are reasonable for this study.

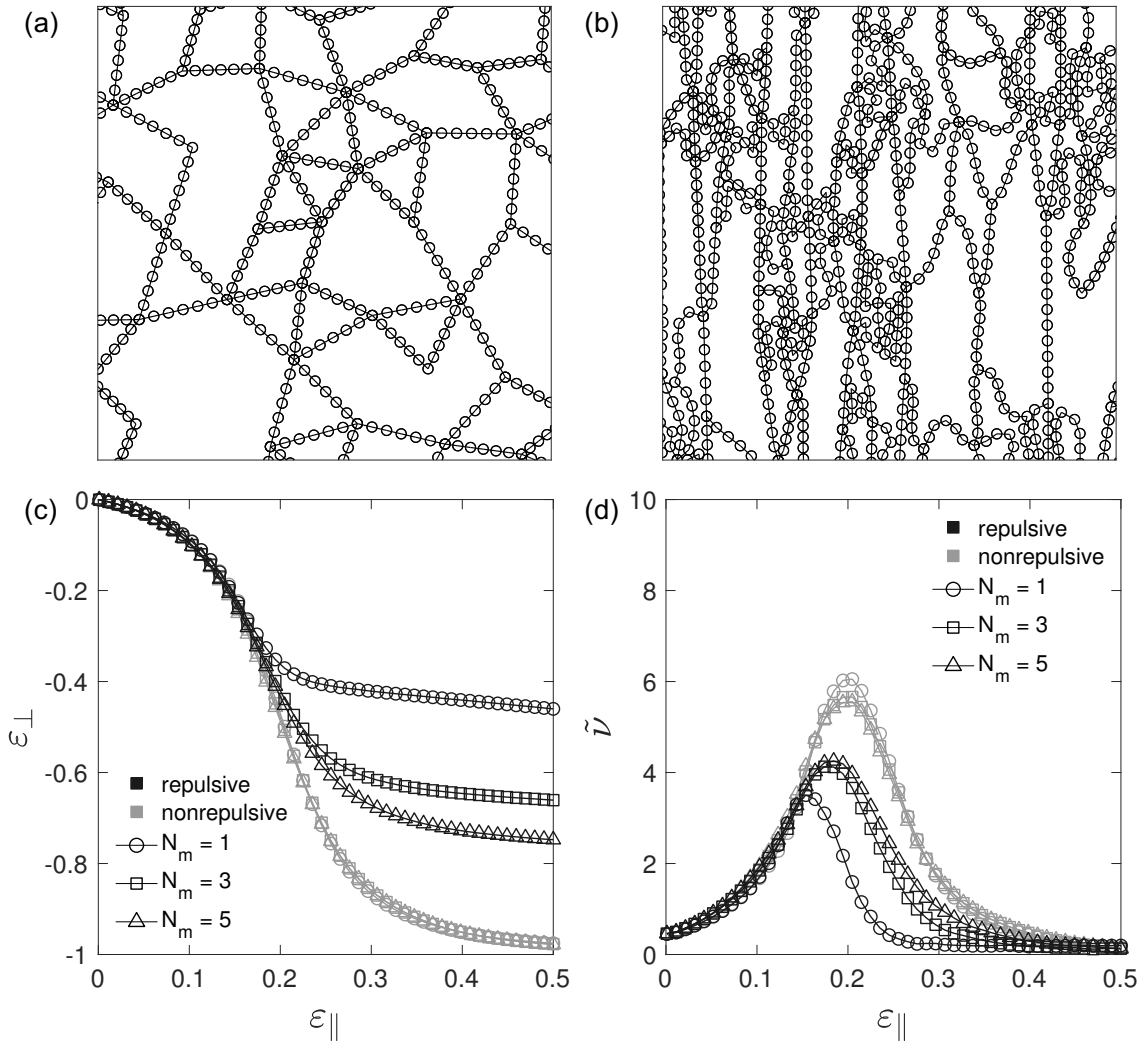

Figure 6.10: Portions of a 2D packing-derived network with $\tilde{\kappa} = 10^{-5}$, $z = 3.2$, and $N_m = 5$ midpoints per bond with individual nodes acting as repulsive disks at (a) $\varepsilon_\parallel = 0$ and (b) $\varepsilon_\parallel = 0.3$. (c) Transverse strain $\varepsilon_\perp$ as a function of applied extensile strain $\varepsilon_\parallel$ for networks with $W = 60$, $z = 3.2$, and $\tilde{\kappa} = 10^{-5}$, in which the number of midpoints N_m is varied, with and without treating individual nodes as repulsive disks with radius $r = 0.8/(2(N_m + 1))$. (d) Incremental Poisson's ratio $\tilde{\nu} = -\partial\varepsilon_\perp/\partial\varepsilon_\parallel$ for the same networks.

6.7.4 Growth of the critical strain with distance from isostaticity

In Fig. S7, we plot the critical strain $\varepsilon_{\parallel,c}$ as a function of the distance to the isostatic point, $z_c - z$, for 15 samples of 2D packing-derived networks with $W = 100$ and $\tilde{\kappa} = 10^{-5}$. Here we determined the critical strain $\varepsilon_{\parallel,c}$ for each sample as the inflection point of the stretching energy fraction $\mathcal{H}_s/\mathcal{H}$ when plotted as a function of $\varepsilon_{\parallel}$. We find that $\varepsilon_{\parallel,c} \propto (z_c - z)$ close to the isostatic point, in agreement with prior observations of the critical strain for packing-derived networks under shear strain [79]. This result may depend on the network structure and/or dilution protocol.

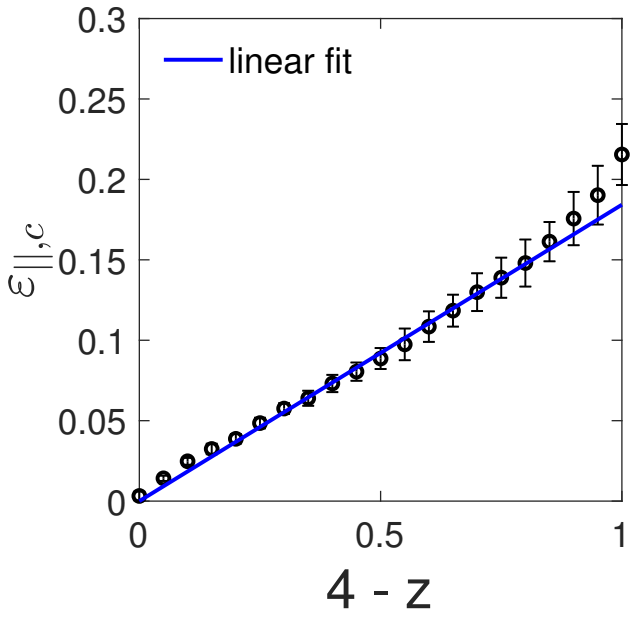

Figure 6.11: The critical strain $\varepsilon_{\parallel,c}$ grows linearly with the distance to the isostatic point, $z_c - z$, for 2D packing-derived networks. These data correspond to 15 samples of 2D packing-derived networks with $W = 100$ and $\tilde{\kappa} = 10^{-5}$. Error bars are ± 1 standard deviation. The blue line corresponds to a linear fit of the 10 points closest to z_c.

Sample configurations

The online Supplemental Material for this article (see Ref. [28]) contains a zipped folder `config.zip` containing sample network configurations for each network type. A description of these files is available in the included text file `config_readme.txt`.

Chapter 7

Compression stiffening of fibrous networks with stiff inclusions

This chapter is adapted from Ref. [230]:

> **Jordan L. Shivers**, Jingchen Feng, Anne S. G. van Oosten, Herbert Levine, Paul A. Janmey, and Fred C. MacKintosh. Compression stiffening of fibrous networks with stiff inclusions. ***Proceedings of the National Academy of Sciences***, 117 (35): 21037–21044, 2020.

7.1 Abstract

Tissues commonly consist of cells embedded within a fibrous biopolymer network. Whereas cell-free reconstituted biopolymer networks typically soften under applied uniaxial compression, various tissues, including liver, brain, and fat, have been observed to instead stiffen when compressed. The mechanism for this compression stiffening effect is not yet clear. Here, we demonstrate that when a material composed of stiff inclusions embedded in a fibrous network is compressed, heterogeneous rearrangement of the inclusions can induce tension within the interstitial network, leading to a macroscopic crossover from an initial bending-dominated softening regime to a stretching-dominated stiffening regime, which occurs before and independently of jamming of the inclusions. Using a coarse-grained particle-network model, we first establish a phase diagram for compression-driven, stretching-dominated stress propagation and jamming in uniaxi-

ally compressed 2- and 3-dimensional systems. Then, we demonstrate that a more detailed computational model of stiff inclusions in a subisostatic semiflexible fiber network exhibits quantitative agreement with the predictions of our coarse-grained model as well as qualitative agreement with experiments.

7.2 Introduction

Semiflexible biopolymer and fiber networks are well known for their unusual tendency to stiffen dramatically under applied shear or extensional strain [19, 25, 29, 36–38, 226, 231–233] and soften under compression [38, 226]. Many biological tissues, however, stiffen under applied compression [234–236], despite the fact that their structural backbone, the extracellular matrix, consists of an otherwise compression softening fiber network. Stiffening of tissues in response to uniaxial compression is ubiquitous in animals large enough to be subjected to gravitational stresses or other large forces. This behavior allows tissues to remain soft to small deformations needed for mechanosensing, while protecting them from damage induced by large compressive strains. In addition, there is increasing evidence that cells sense and respond to compression-driven changes in tissue stiffness [234]. This can have important consequences in, for example, brain tissue, which stiffens in response to increased blood pressure [237] or the pressure gradient generated by a growing tumor [238, 239].

Whereas compression stiffening in tissues can be interpreted as a consequence of incompressibility of either the inclusions (cells) [236] or the entire sample due to poroelastic effects [226, 240], this behavior has also been demonstrated in biopolymer networks containing stiff (i.e. non-deforming) colloidal particles [236], for which the cause of compression stiffening is less clear. Developing a better understanding of the origin of this behavior, and in particular its dependence on the properties of both the inclusions and interstitial network, may improve our knowledge about the nonlinear

mechanics of tissues and support efforts to design functional biomimetic materials.

In recent work, van Oosten and coworkers measured the shear storage modulus, as a function of applied uniaxial strain, of a reconstituted fibrin network containing embedded stiff dextran particles [236]. In Fig. 7.1a, we reproduce their experimental data for samples with an initial inclusion volume fraction of $\phi_0 = 0.5$. Under increasing compression, this material exhibits an initial softening and subsequent stiffening regime. Notably, this unusual compression stiffening effect occurs while the volume fraction of the inclusions remains below the expected jamming threshold (see Appendix, Section 7.6). In contrast to these experiments with strain-stiffening biopolymer networks, the authors observed no compression stiffening effect below jamming in a system containing the same particles embedded within a linear elastic (i.e. non-strain-stiffening) polyacrylamide gel. Thus, this unusual effect in the fibrin experiments appears to originate from some cooperative interaction between the mutual steric repulsion of the particles and strain stiffening properties of the network. In Fig. 7.1c, we sketch a hypothetical mechanism for this behavior, along with a schematic plot of the shear modulus as a function of applied uniaxial strain. In a biopolymer network containing stiff inclusions, we expect that a small amount of applied macroscopic compression will result in homogeneous compression throughout the interstitial network, causing initial macroscopic softening akin to what is typically observed in compressed inclusion-free biopolymer networks [38, 226]. Inevitably, sufficient macroscopic compression of the sample induces contact and rearrangement of the sterically repulsive inclusions [241], driving local shear and extensional strain between neighboring inclusions. Provided that the critical extensional strain for stiffening of the interstitial network is sufficiently low that the magnitude of induced particle rearrangement induces local stiffening, this could lead to macroscopic stiff (tension-dominated) stress propagation before the inclusions become jammed.

In this work, we describe a new mechanism for compression stiffening in fibrous

networks containing inclusions, which we show is related to nonaffine, cooperative particle rearrangement [241, 242] that occurs in random particle dispersions as macroscopic compression increases the particle volume fraction. This rearrangement induces tension within the interstitial network, which in turn causes macroscopic stiffening. To explore the counterintuitive notion of compression-driven tension, we first consider the mechanics of a loosely distributed assembly of stiff, repulsive particles, in which neighboring particles are connected by soft springs that are *rope-like*, meaning that they provide zero mechanical response to compression but behave as harmonic springs when stretched beyond a predefined slack extension. We refer to this as the *rope model*, and treat it as a coarse-grained approximation of the zero-bending rigidity limit of a fibrous network containing inclusions. Across a wide range of initial particle volume fractions, we find that applying sufficient uniaxial compression to this system induces a state of macroscopic stress propagation prior to jamming, in which stretching of the soft springs constitutes the dominant stress contribution. This is distinct from the jamming transition, which occurs at a well-defined particle volume fraction for a given shape and size distribution [81, 82] and is dominated by compressive stress propagation [130]. We find that stretching-dominated stress propagation appears to be related to contact percolation of the particles, which prior work has shown corresponds to the onset of increasing nonaffinity in the particle displacements in a macroscopically compressed particulate assembly [241, 242]. We generate phase diagrams for stretching-dominated stress propagation and jamming in 2D and 3D systems, as a function of both the particle volume fraction and the level of applied extension required for each ropelike spring to bear tension.

We then perform simulations of discrete disordered fiber networks, which have in prior work been shown to reproduce the nonlinear mechanical behavior of reconstituted biopolymer networks [38, 95, 226]. In the absence of inclusions, these remain soft (mechanically bending-dominated) under applied compression and stiffen dramatically

(becoming mechanically dominated by axial stretching of the network fibers) only when stretched beyond a critical extensional strain. We modify these model networks by embedding stiff, sterically repulsive particles that are rigidly connected to the surrounding network bonds. Similar simulations have been performed in recent work by Islam and coworkers [243], who showed that introducing rigid particles increases the linear modulus and reduces the extensional critical strain of strain stiffening networks. However, their work did not consider compression-driven phenomena. Here, we simulate the rheology of such networks under applied uniaxial strain and show that, with a sufficiently large volume fraction of embedded stiff inclusions, these exhibit significant compression stiffening, qualitatively reproducing the rheology of the experimental system. We show that this stiffening coincides with increasing nonaffine (heterogeneous) rearrangement of the inclusion positions. Further, we demonstrate that the volume-fraction dependence of this compression stiffening behavior is quantitatively captured by the predictions of the rope model.

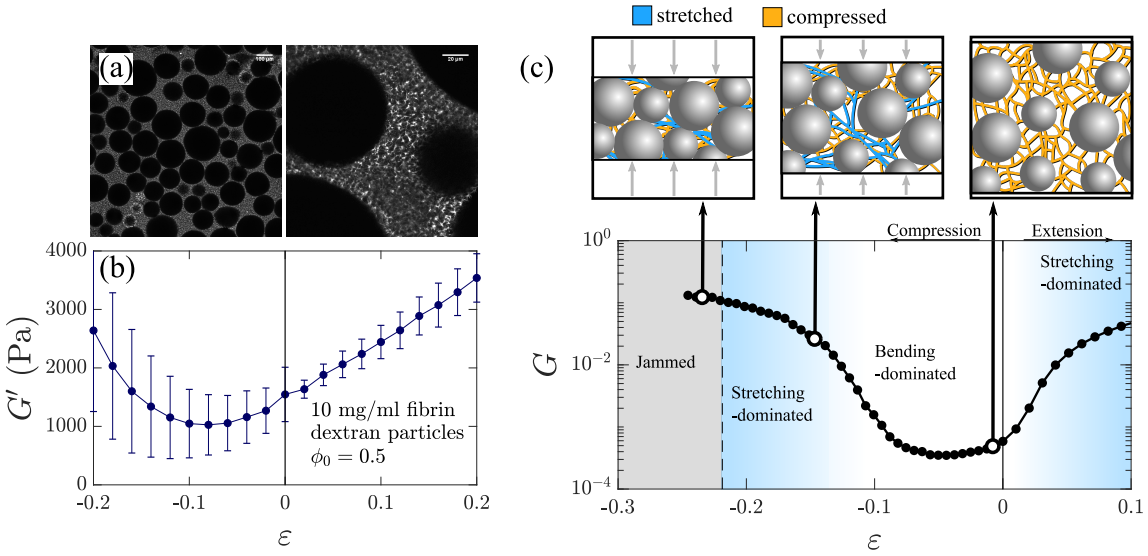

Figure 7.1: (a) Confocal images of a gel of 10 mg/ml fibrin containing stiff spherical dextran particles at a volume fraction of $\phi_0 = 0.5$. (b) Reproduced from Ref. [236]: Shear storage modulus G for the above system as a function of applied uniaxial strain. Under compression, the material initially softens before transitioning to a stiffening regime. (c) Top right: Compression of a biopolymer network containing stiff inclusions initially leads to roughly uniform compression of the interstitial network (compressed fibers are colored orange), which leads to bending of the network fibers and softening of the macroscopic sample. Top middle: Further increasing compression leads to rearrangement of the stiff inclusions, which drives stretching of fibers in network regions between particles that move farther apart (stretched fibers are colored blue), leading to a macroscopic crossover from bending-dominated to stretching-dominated mechanics. Top left: With sufficiently large compression, the inclusions become jammed. Bottom: Schematic plot of the shear modulus G as a function of applied uniaxial strain ε for a simulated system of stiff particles embedded within a strain-stiffening network. The model is discussed in detail in Section III and this data appears in Fig. 7.4.

7.3 Results and discussion

7.3.1 Physical mechanism of compression-driven tension

Biopolymer networks are unique in that they exhibit relatively weak, bending-dominated compressive response but stiffer, stretching-dominated tensile response above a critical applied strain. We hypothesize that the compression stiffening effect observed in particle-network composites is the result of tension within the the interstitial, strain-stiffening network caused by rearrangement of the sterically repulsive particles as the macroscopic sample is uniaxially compressed. This particle rearrange-

ment is driven by the inability of the non-deforming, spherical particles to accomodate a homogeneous deformation field under uniaxial compression due to their mutual steric repulsion. In this section, we consider a coarse-grained model consisting of a random arrangement of stiff repulsive particles, in which neighboring particles are connected by soft, rope-like springs that are harmonic under applied extension but have no resistance to compression. In this zero-bending limit, we demonstrate that compression-driven particle rearrangement can induce stretching-dominated, sample-spanning stress propagation, at a volume-fraction-dependent critical compression prior to jamming.

We consider random arrangements of N radially monodisperse spheres (bidisperse disks in 2D, with a ratio of radii of 1.4 to avoid crystallization [82], in which the two particle size subpopulations are equal in number), in a periodic box of volume L^d, in which L is chosen so that the initial particle volume fraction (area fraction in 2D) is ϕ_0. Further details on sample generation are provided in Methods. We use $N = 1000$ in 3D and $N = 900$ in 2D. Neighboring particles, as identified by the Delauney triangulation of the particle centers, are connected by rope-like springs. The initial lengths of the rope-like springs are set to be equal to the initial distance between each pair of neighboring particles, such that an increase in the distance between two nearest neighbors corresponds to extension of the pair's connecting spring. Because we intend to treat each spring as a coarse-grained approximation of a strain-stiffening network region between each pair of inclusions, we define a "slack extension" λ_c above which each rope-like spring transmits tension. The energy for the rope-like springs is written as follows

$$\mathcal{H}_{\text{rope}} = \frac{\mu}{2} \sum_{ij} \frac{\left(\ell_{ij} - \lambda_c \ell_{ij,0}\right)^2}{\lambda_c \ell_{ij,0}} \Theta\left(\ell_{ij} - \lambda_c \ell_{ij,0}\right) \tag{7.1}$$

in which μ is the spring constant, Θ is the Heaviside step function, ℓ_{ij} is the distance between the centers of particles i and j, and the sum is taken over all springs between

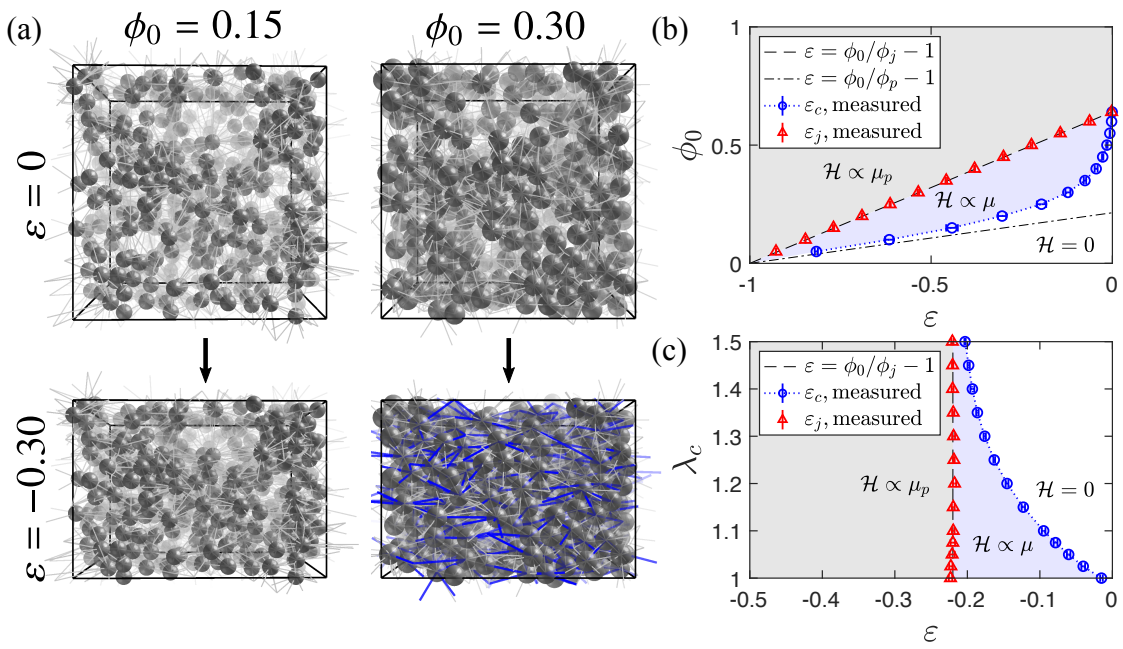

Figure 7.2: (a) We apply uniaxial compression to periodic systems comprised of $N = 1000$ randomly placed, repulsive spherical particles with initial volume fractions $\phi_0 = 0.15$ (left) and $\phi_0 = 0.3$ (right), in which neighboring particles are connected according to the Delaunay triangulation of the particle centers. The springs connecting pairs of particles are rope-like, meaning that they only produce finite tension when stretched beyond a slack extension λ_c. Applying a uniaxial compression of $\varepsilon = -0.3$ to a 3D system with initial volume fraction $\phi_0 = 0.3$ results in sufficient rearrangement of the sterically repulsive particles to induce sample-spanning, tension-dominated stress propagation (blue springs are stretched), whereas the same compression is insufficient to stress propagation for $\phi_0 = 0.15$. (b) Mechanical phase diagram for compressed systems of $N = 1000$ repulsive spheres of modulus $\mu_p = 1$, in which nearest neighbors (by Delaunay triangulation) are connected by rope-like springs of modulus $\mu = 10^{-5}$, as a function of uniaxial strain ε and initial volume fraction ϕ_0. Here, the rope-like springs have critical extension $\lambda_c = 1$. The blue circles correspond to the critical strain for the onset of tension propagation, ε_c, and the red triangles correspond to the onset of jamming, ε_j. The dashed black line corresponds to the predicted applied strain required for jamming of a system with initial volume fraction ϕ_0, $\varepsilon_j = \phi_0/\phi_j - 1$, in which $\phi_j = 0.64$. The white region corresponds to the floppy regime ($\mathcal{H}_{\text{total}} = 0$, blue corresponds to the stretching-dominated regime ($\mathcal{H}_{\text{total}} \propto \mu$), and gray corresponds to the jammed regime ($\mathcal{H}_{\text{total}} \propto \mu_p$). (b) Mechanical phase diagram for volume fraction $\phi_0 = 0.5$ as a function of applied uniaxial strain ε and slack extension of rope-like springs, λ_c. Error bars in both panels correspond to ± 1 standard deviation.

neighboring particles. The repulsive energy between overlapping particles is written as

$$\mathcal{H}_{\text{repulsion}} = \frac{\mu_p}{2} \sum_{mn} \left(1 - \frac{\ell_{mn}}{r_{mn}}\right)^2 \Theta\left(1 - \frac{\ell_{mn}}{r_{mn}}\right) \tag{7.2}$$

in which μ_p is the one-sided repulsive spring constant and the sum is taken over all pairs of particles m and n. As we are interested in the limit in which the particles are much stiffer than the springs, we set $\mu = 10^{-5}$ and $\mu_p = 1$. Again, this system can be thought of as a coarse-grained description of a biopolymer network containing embedded particles, which ignores the relatively weak, bending-dominated linear and compressive mechanical responses of the network and instead considers both repulsion between overlapping stiff particles and the stretching-dominated mechanics of network regions driven above the critical strain.

To this system, we apply quasistatic uniaxial strain ε in small steps ($|d\varepsilon| < 0.01$) using generalized Lees-Edwards periodic boundary conditions [85]. At each step, we minimize the total energy $\mathcal{H}_{\text{total}} = \mathcal{H}_{\text{rope}} + \mathcal{H}_{\text{repulsion}}$ using the L-BFGS method [225]. In Fig. 7.2a, we plot sample configurations for a 3D system with $N = 1000$ particles at initial volume fractions of $\phi_0 = 0.15$ and $\phi_0 = 0.30$, under varying levels of compression, in which the slack extension for the rope-like springs is set to $\lambda_c = 1$, such that any stretching results in a nonzero energy contribution. Under an applied compression of $\varepsilon = -0.3$, no stretching is induced in the system with $\phi_0 = 0.15$, so it remains mechanically floppy, with $\mathcal{H}_{\text{total}} = 0$. When the same amount of compression is applied to the sample with $\phi_0 = 0.3$, however, compression-driven rearrangement of the sterically repulsive particles induces sample-spanning stress propagation in which the mechanics are dominated by stretching, leading to $\mathcal{H}_{\text{total}} \propto \mu$. The stretching of a significant fraction of the bonds is evident in the bottom right panel of Fig. 7.2a, in which stretched bonds are colored blue. Importantly, the stretching-dominated stress propagation shown in Fig. 7.2a occurs at a lower level of applied compression than that required for jamming; thus in the absence of the springs, the system would be a floppy, unjammed particle assembly. Sufficiently increasing the compression applied to a given system eventually leads to jamming, i.e. stress propagation dominated by repulsive forces between particles, such that $\mathcal{H}_{\text{total}} \propto \mu_p$, at $\varepsilon_j = \phi_0/\phi_j - 1$. Here, ϕ_j

is the jamming volume fraction of packings of spheres 3D ($\phi_j \approx 0.64$) and radially bidisperse disks 2D ($\phi_j \approx 0.84$). Note that in our calculation of ε_j, we assume that the particle volume fraction at the onset of jamming is the same for packings under uniaxial compression as for packings under bulk compression, under which ϕ_j is commonly measured. While this assumption may not be strictly true, we find that it works well for our simulations.

To explore the full volume-fraction dependence of this effect, in Fig. 7.2b, we plot a mechanical phase diagram for compressed 3D systems with slack extension $\lambda_c = 1$ and varying initial volume fraction ϕ_0. We show the same phase diagram for 2D systems in Appendix, Section 7.6, Fig. 7.5. We identify the critical compressive strain corresponding to stretching-dominated stress propagation, ε_c, as the first applied strain in which the system's energy becomes finite (we choose a threshold of $\mathcal{H}_{\text{total}}/V = 10^{-11}$). That this initial stress propagation is stretching-dominated is evident from the fraction of the total energy deriving from stretching, $\mathcal{H}_{\text{rope}}/\mathcal{H}_{\text{total}}$, which is approximately 1 at the onset of finite $\mathcal{H}_{\text{total}}$. We identify the critical compressive strain for jamming, ε_j, as the strain at which the fractional contribution of repulsion to the total energy, $\mathcal{H}_{\text{repulsion}}/\mathcal{H}_{\text{total}}$, exceeds 0.5. We find that the measured critical strains for jamming obey the predicted dependence on the initial volume fraction, $\varepsilon_j = \phi_0/\phi_j - 1$, in both 2D and 3D, and we observe that tension propagation occurs prior to jamming over a wide range of initial volume fractions. Near $\phi_0 = 0$, we find that the critical strain for tension propagation with $\lambda_c = 1$ seems to approximately match the expected applied strain for contact percolation of particles with short-range attractive interactions, $\varepsilon_p = \phi_0/\phi_p - 1$, where $\phi_p \approx 0.214$ in 3D and $\phi_p \approx 0.558$ in 2D [241]. Note that this calculation of ε_p has the same caveat as our prediction of ε_j, in that the referenced values of ϕ_p were measured under bulk compression. Perhaps surprisingly, we observe that stress propagation occurs slightly before the contact percolation point for an intermediate range of volume fractions in 2D. We discuss this in Appendix, Section

7.6 (see Fig. 7.6).

Intuitively, for a fixed volume fraction, increasing the slack extension λ_c of the ropelike springs should increase the amount of compression-driven rearrangement required for tension propagation. Consequently, ε_c should become more negative with increasing λ_c. In contrast, the required compression for jamming, ε_j, strictly depends on ϕ_0 and is not expected to show any dependence on λ_c. In Fig. 7.2c, we plot ε_c and ε_j for 3D systems with $\phi_0 = 0.5$ and varying λ_c, and we plot the complementary data for 2D systems in Appendix, Section 7.6, Fig. 7.5. We plot $\varepsilon_c(\lambda_c)$ for a several volume fractions in both 2D and 3D in Appendix, Section 7.6, Fig. 7.7.

This compression-driven, tension-dominated stress propagation is a geometric effect, caused by the inevitably heterogeneous rearrangement of a compressed assembly of sterically repulsive particles as the particle volume fraction increases toward jamming. Thus, the shape of the phase boundaries in Fig. 7.2b-c should not depend on the precise elastic properties of the rope-like springs and particles provided that $\mu_p \gg \mu$. If, in fibrous networks containing embedded stiff particles, the dominant modes of stretching under macroscopic compression correspond to tension between nearest neighbor particles, then the phase boundaries in Fig. 7.2b-c may be useful for predicting the onset of compression stiffening in strain-stiffening networks containing inclusions, such as the example depicted in Fig. 7.1a, provided that the inclusion volume fraction and extensional critical strain of the underlying fiber network are known. In the following section, we test these ideas using simulations of disordered elastic networks containing stiff inclusions.

7.3.2 Model of a strain-stiffening network containing stiff inclusions

This rope model has suggested a new mechanism for compression-driven, stretching-dominated stress propagation in strain-stiffening materials containing sterically repul-

sive particles. To establish the validity of this mechanism, we now perform simulations using a more established fiber network model containing rigid particles, for which we can measure the influence of applied uniaxial strain (compression or extension) on the linear shear modulus.

Prior work has demonstrated that the mechanics of semiflexible polymer networks are strongly influenced by the connectivity z, defined as the average number of bonds connected to a network node [36, 48]. A network of initially unstressed and athermal Hookean springs with 1D modulus μ has a finite shear modulus $G \propto \mu$ only if the average connectivity z is equal to or greater than an *isostatic* threshold $z_c = 2d$, identified by Maxwell, where d is the dimensionality [46]. The addition of soft bending interactions with modulus κ results in a bending-dominated regime with $G \propto \kappa$ for $z < z_c$, with a crossover to a stretching-dominated regime with $G \propto \mu$ for $z > z_c$ [40, 48, 114, 116]. For extracellular matrices of collagen or fibrin, the average connectivity $z \lesssim 4$ is well below the 3D isostatic threshold of 6 [23, 98]. Thus, if such *subisostatic* networks are athermal, it is the former bend-dominated regime that is expected to describe the linear elastic modulus. In this linear, bending-dominated mechanical regime, the introduction of tensile prestress (e.g., by molecular motors [73, 182] or applied extension [38, 226, 244]) drives an increase in the shear modulus. In fact, sufficiently large applied shear or extensional strain [50, 134] can induce a crossover to a stiff, stretching-dominated regime [19, 38, 50, 114, 226], with the magnitude of required strain decreasing to zero as $z \to z_c$ [79]. In contrast, under applied compression, networks typically soften relative to the unstrained state [244], remaining (in the case of biopolymer networks) within the bending-dominated regime [38, 226, 236]. In this section, we demonstrate that embedding repulsive particles within such networks leads to compression stiffening, at a level of compression that is controlled by a combination of the network critical strain and the particle volume fraction. We find that the phase diagram for the rope model discussed in the previous

section quantitatively captures the volume-fraction dependence of the compression stiffening effect in this more realistic model.

We generate periodic, subisostatic fiber networks of average connectivity z derived from dense 3D sphere packings, as described in Methods and Appendix, Section 7.6. Then, we randomly place non-intersecting spherical inclusions of radius r within the simulation box until the desired inclusion volume fraction ϕ_0 is reached. Any network bond that intersects with the boundary of an inclusion is connected to the inclusion surface, at the intersection point, by a freely rotating joint, and all remaining bond segments with the inclusion boundary are removed. Each inclusion transforms as a rigid object with (in 3D) 3 translational and 3 rotational degrees of freedom. Example images of a network containing inclusions, prior to applied deformation, are provided in Appendix, Section 7.6, Fig. 7.9.

For a given configuration, the total energy $\mathcal{H}$ of the system is computed as

$$\mathcal{H} = \mathcal{H}_S + \mathcal{H}_B + \mathcal{H}_R, \tag{7.3}$$

in which $\mathcal{H}_S$, $\mathcal{H}_B$, and $\mathcal{H}_R$ represent stretching, bending, and repulsive contributions, respectively. We treat individual segments as harmonic springs of modulus μ, compute harmonic bending interactions of modulus κ between nearest-neighbor segments, and account for one-sided harmonic repulsive interactions of modulus μ_R between pairs of inclusions and between inclusions and network nodes. Unless stated otherwise, we set $\mu = 1$ and $\kappa = 10^{-4}$ so that the linear elasticity of the interstitial, subisostatic network is bending-dominated. Prior work has shown that networks with κ around this magnitude reasonably capture the mechanical behavior of reconstituted collagen and fibrin networks [38, 95, 98, 226]. We set $\mu_R = 100$ so that the repulsive interactions are significantly stiffer than both the bending and stretching interactions. Further details are provided in Methods. Since we focus on the regime below jamming ($|\varepsilon| < |\varepsilon_j|$)

throughout this work, our results should be qualitatively consistent with $\mu_R \to \infty$ provided that $\mu_R \gg \{\mu, \kappa\}$. Using the procedure described in Methods, we measure the linear shear modulus G as a function of uniaxial strain ε for compressive and extensional strains over a range of inclusion volume fractions.

First, we consider networks with $z = 4$ which, without inclusions, soften under compression but stiffen at a critical extensional strain of $\varepsilon_{c,ext} \approx 0.3$, identified as the inflection point of the G vs. ε curve for $\phi_0 = 0$ in Fig. 7.4a. When inclusions are present with a sufficient ϕ_0, these stiffen under both applied extension and compression. In Fig. 7.4a, we plot the shear modulus for the same networks with varying initial inclusion volume fraction ϕ_0 . We find that networks containing sufficiently large ϕ_0 undergo a compression softening regime at low levels of compression followed by stiffening at higher levels of compression, similar to the behavior observed in the experiments of Ref. [236] shown in Fig. 7.1a. In Fig. 7.3, we provide images of a simulation with $\phi_0 = 0.3$ and $z = 4$ under varying levels of applied compression. Whereas most bonds are compressed (orange) at the relatively low applied macroscopic compression of $\varepsilon = -0.01$, at the more substantial compression of $\varepsilon = -0.35$ we observe significant stretching (blue) of network regions between neighboring inclusions. As in the rope model, this stretching is driven by rearrangement of the sterically repulsive inclusions as the system approaches jamming. We find that increasing ϕ_0 leads to a decrease in the magnitude of applied compression corresponding to the minimum in G, beyond which the networks stiffen with increasing compression. For sufficiently large ϕ_0 and sufficient applied compression, these enter a stretching-dominated stiffening regime with $G \propto \mu$ at a critical compressive strain that decreases with increasing ϕ_0, in qualitative agreement with the phase diagram in Fig. 7.2d. In Fig. 7.4b, we plot the stretching energy fraction $\mathcal{H}_S/\mathcal{H}$ as a function of strain for the same networks, demonstrating that compression stiffening coincides with a crossover from a bending-dominated regime to a stretching-dominated regime. To emphasize this point,

we repeat these measurements for networks with varying the bending modulus κ and fixed $\phi_0 = 0.4$ and $z = 4$ (see Appendix, Section 7.6, Fig. 7.10). These show a clear shift from a softening regime in which $G \propto \kappa$ at small strains, to a crossover stiffening regime at intermediate strains, to a stretch-dominated stiffening regime with $G \propto \mu$ at larger strains. In Fig. 7.4d, we draw a schematic phase diagram for the shear modulus of a strain-stiffening fibrous network containing rigid inclusions as a function of inclusion volume fraction and applied uniaxial strain. In Appendix, Section 7.6, Fig. 7.12, we replot the data from Fig. 7.4, with strain points colored by the magnitude of G, over a plot of ϕ_0 vs. ε, revealing the regimes sketched in Fig. 7.4d.

To explore the influence of strain heterogeneity on the compression stiffening effect, we measure the nonaffinity $\Gamma(\varepsilon)$ of the inclusion deformation field as follows

$$\Gamma = \frac{1}{r^2\varepsilon^2}\left\langle \left|\vec{\boldsymbol{u}}_i(\varepsilon) - \vec{\boldsymbol{u}}_{i,\mathrm{aff}}(\varepsilon)\right|^2 \right\rangle_i \tag{7.4}$$

in which the average is taken over all inclusions, r is the inclusion radius, $\vec{\boldsymbol{u}}_i(\varepsilon)$ is the actual position of inclusion i after relaxation under applied strain ε, and $\vec{\boldsymbol{u}}_{i,\mathrm{aff}}(\varepsilon)$ is the position of inclusion i under affine (homogenous) deformation of the initial network configuration by strain ε. Note that since our simulations are periodic, we shift $\vec{\boldsymbol{u}}_i$ and $\vec{\boldsymbol{u}}_{i,\mathrm{aff}}$ for the purposes of calculating Γ so that the average of each corresponds to the origin. Under an applied compression of ε, particles are displaced by an average distance $d_\Gamma = r|\varepsilon|\sqrt{\Gamma}$ from their expected locations under affine deformation. As Γ is proportional to the typical squared distance of each inclusion from its expected position under macroscopic homogenous compression, increasing rearrangement of the inclusions will be indicated by increasing Γ. In the inset of Fig. 7.4b, we plot Γ for systems with varying ϕ_0. We find that Γ decreases in all systems in the compression softening regime, but it increases throughout the compression stiffening regime, beginning at roughly the same strains in which the shear modulus G begins to increase. As Γ can

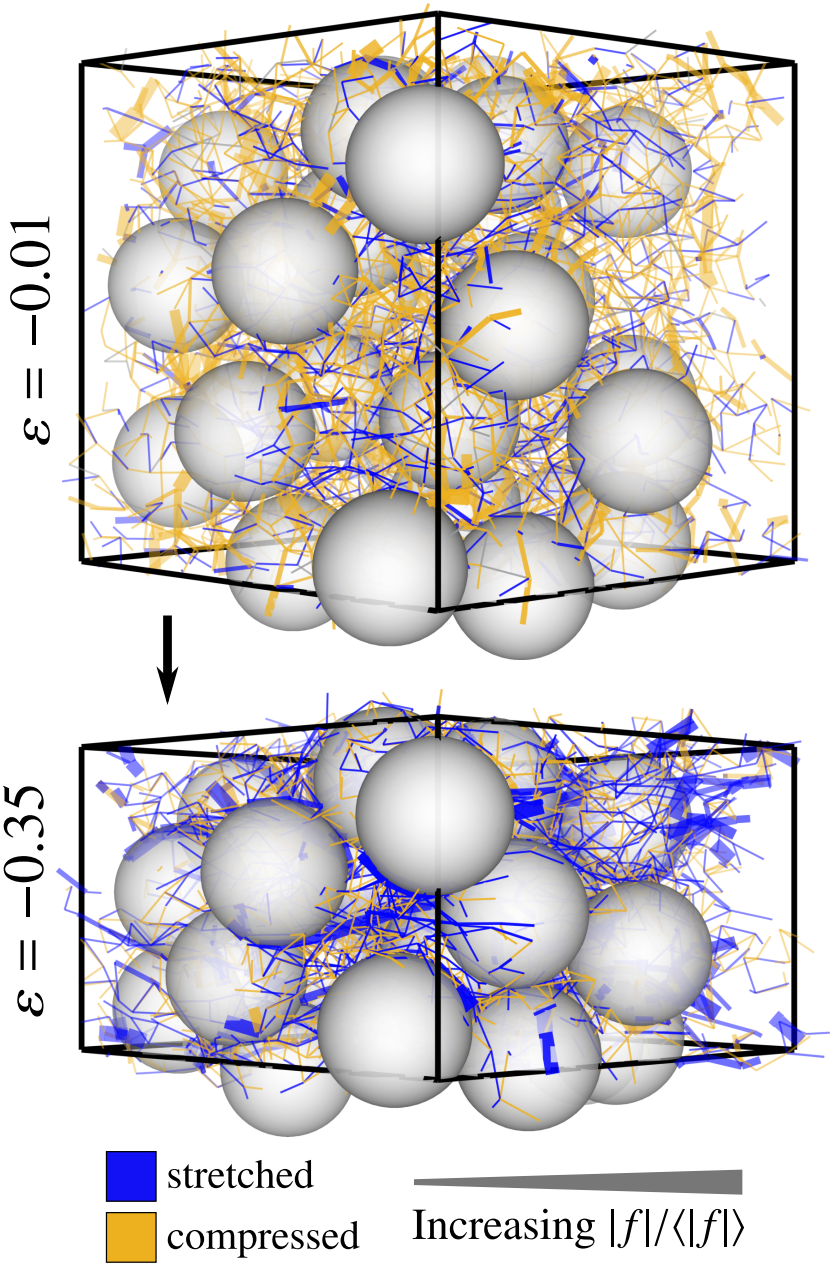

Figure 7.3: Images of a periodic packing-derived network unit cell with $L = 15$, $z = 4$, $\kappa = 10^{-4}$, and spherical inclusions with radius $r = 2$ and volume fraction $\phi_0 = 0.3$ under varying levels of compression. Compressed bonds are colored orange and stretched bonds are blue. Bond thickness is proportional to the magnitude of the tensile/compressive force $|f|$ on the bond normalized by the average force magnitude $\langle|f|\rangle$, with thresholds at $|f|/\langle|f|\rangle = [1, 8]$. The dimensions of the outer box represents the periodic Lees-Edwards boundary conditions.

in principle be measured in experiments via particle-tracking, this quantity could be used to test whether increasing strain heterogeneity drives compression stiffening in

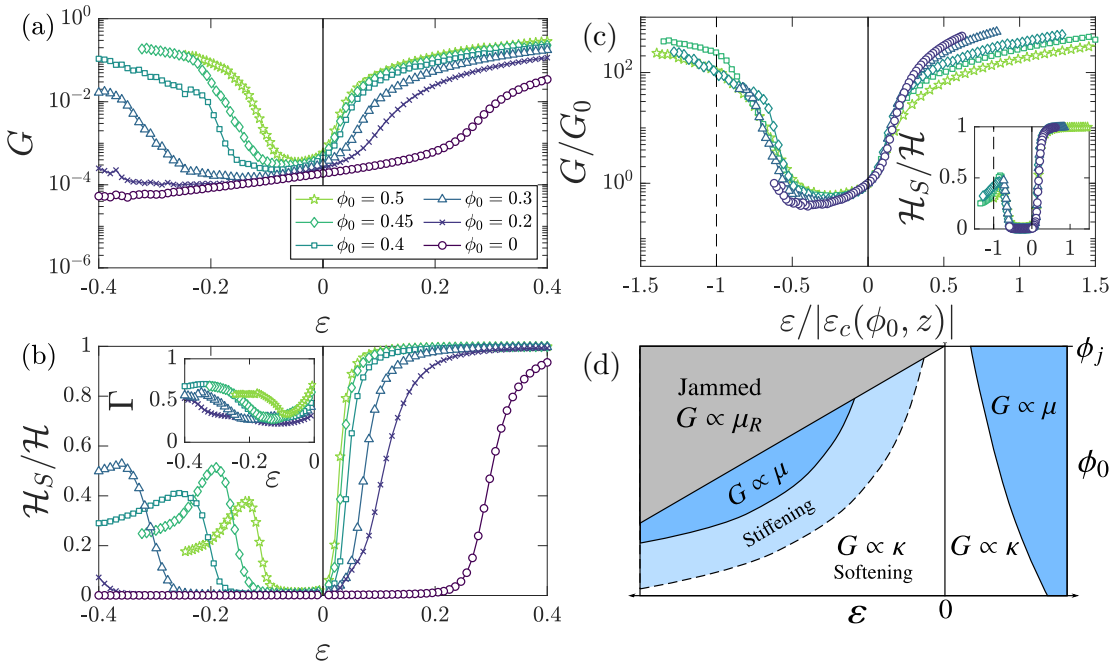

Figure 7.4: (a) Shear modulus G as a function of applied uniaxial strain ε for 3D packing-derived networks with $z = 4$, $\kappa = 10^{-4}$, and varying initial inclusion volume fraction ϕ_0. Networks with large enough ϕ_0 undergo a compression-driven crossover from a bending-dominated softening regime to a stiffening regime and eventually become stretching-dominated, as reflected by the (b) stretching energy fraction $\mathcal{H}_S/\mathcal{H}$. With increasing ϕ_0, the crossover point occurs at lower levels of applied compression. Inset: Nonaffinity Γ of the inclusion deformation as a function of applied compression. (c) Data from (a) normalized by the zero-strain shear modulus $G_0 = G(\varepsilon = 0)$ and plotted as a function of the uniaxial strain ε normalized by the predicted critical strain for compression-driven tension propagation, $\varepsilon_c(\phi_0, z)$, where $\varepsilon_{c,ext} = 0.3$ is the critical *extensional* strain for empty networks with $z = 4$, and $\varepsilon_c(\phi_0, \lambda_c = 1 + \varepsilon_{c,ext})$ is determined from the 3D rope model, as described in Appendix, Section 7.6. (d) Schematic phase diagram for the shear modulus G as a function of applied uniaxial strain ε and initial inclusion volume fraction ϕ_0.

experiments. We note that, given the cooperative nature of inclusion rearrangement, Γ is expected to increase in magnitude with increasing system size (number of inclusions), which is relatively limited for our 3D simulations. In Appendix, Section 7.6, Fig. 7.14, we show that in larger 2D simulations, Γ grows more dramatically than in the smaller 3D systems.

In the previous section, for a random configuration of particles with initial volume fraction ϕ_0, with neighboring particles connected by rope-like springs with slack extension λ_c, we determined the critical compressive strain ε_c for stretching-dominated

stress propagation. Since the rope-like springs act as a coarse-grained approximation of a strain-stiffening network with a known critical extensional strain $\varepsilon_{c,ext}(\phi_0 = 0, z)$, we should compare our simulations to the rope model with slack extension $\lambda_c = 1 + \varepsilon_{c,ext}$. Using $\varepsilon_c(\phi_0, \lambda_c)$ determined for the rope model, as shown in Appendix, Section 7.6, Fig. 7.7, we can thus predict the critical compressive strain $\varepsilon_c(\phi_0, z) \equiv \varepsilon_c(\phi_0, \lambda_c = 1 + \varepsilon_{c,ext}(\phi_0 = 0, z))$ for stretching-dominated stress propagation in our simulations. In Fig. 7.4c, we show that normalizing $G(\varepsilon)$ in Fig. 7.4 by the zero-strain shear modulus $G_0 = G(\varepsilon = 0)$ and normalizing the applied uniaxial strain by the predicted critical compressive strain $\varepsilon_c(\phi_0, z)$ leads to reasonable collapse of the data from Fig. 7.4a under compression. In Fig. 7.4c (inset), we show that the stretching energy fraction $\mathcal{H}_S/\mathcal{H}$ curves also collapse when plotted as a function of $\varepsilon/\varepsilon_c(\phi_0, z)$.

Based on our observation that increasing the slack extension of the springs in the rope model leads to an increase in the magnitude of the critical compression required for stretching-dominated stress propagation, we anticipate that increasing z should decrease the magnitude of compression required for stiffening in our simulated network-inclusion composites. In inclusion-free, subisostatic networks, increasing z results in a decrease in the critical applied extensional strain required for stiffening. In simulations, we find that for systems with a fixed ϕ_0, decreasing the extensional critical strain of the underlying network by increasing z in networks results in a decrease in the magnitude of applied compression at which the system stiffens (see Appendix, Section 7.6, Fig. 7.11a) and becomes stretching-dominated (see Appendix, Section 7.6, Fig. 7.11b), in agreement with our expectations based on the rope model.

For the case of applied extension, we find that our results agree qualitatively with those of Islam and coworkers, who used a similar model of random 3D networks containing inclusions [243]. Under increasing extension, we observe an initial bending-dominated stiffening regime, with $G \propto \kappa$, followed by a crossover to a much stiffer stretching-dominated regime, with $G \propto \mu$, in agreement with their results for bonded

inclusions [243]. This transition occurs at a critical extensional strain that decreases with increasing ϕ_0, in further agreement with their work. Likewise, we find that the volume-fraction-dependence of the critical extensional strain is sensitive to the nature of the connections between the inclusions and network. If the inclusions that are disconnected from the surrounding network, we find that increasing ϕ_0 leads to an increase in the critical extensional strain (see Appendix, Section 7.6, Fig. 7.16), as observed in Ref. [243]. However, we find that these, too, stiffen under compression at a volume-fraction-dependent critical strain, in qualitative agreement with our other results.

In Appendix, Section 7.6, Fig. 7.14, we plot analogous data for Fig. 7.4a for 2D packing-derived networks with $z = 3$ and varying ϕ_0. These exhibit compression stiffening behavior that qualitatively agrees with our 3D simulations.

7.4 Concluding remarks

We have demonstrated that the compression-driven nonaffine rearrangement of stiff particles embedded in a network can generate tension-dominated stress propagation, coinciding with macroscopic compression stiffening, and we have shown how this effect is controlled by both the volume fraction of particles and the strain-stiffening properties of the interstitial network. Using simulations of disordered 3D elastic networks containing stiff inclusions, which qualitatively reproduce the compression stiffening behavior observed in experiments, we have provided evidence that, given both the volume fraction of inclusions and the critical extensional strain of the interstitial strain stiffening network, one can utilize the rope model to predict the critical compressive strain corresponding to stretching-dominated stress propagation. Our results suggest a strategy for rational design of nonlinear mechanics in engineered tissues or synthetic composite materials using controlled volume fractions of inclusions.

Interestingly, a similar rearrangement-driven stiffening effect might occur below the jamming transition for networks containing deformable inclusions, such as cells, provided that these sufficiently resist changes in volume. If so, then the rearrangement-driven stretching effect described in this work may drive the compression stiffening behavior that has been widely observed in living tissues. To study a more direct model of tissues, one could replace the stiff inclusions in our model with deformable particles that resist area/volume change [245, 246] and/or actively exert forces on the network [108, 247]. Contractile cells, for example, might suppress or entirely remove the initial compression softening effect by pre-stretching regions of the interstitial network. Further, large scale force generation induced by contractile cells [109, 196] may enhance the rearrangement-driven stiffening described in our work. Indeed, the authors in Ref. [236] showed that fibrin networks containing particles and cells stiffen more than networks containing particles alone. Prestress may also explain why an initial compression softening regime is not typically observed in tissue samples [234–236].

While our simulations assume that bonds are permanent, real biopolymers rupture under sufficiently large extension. In Appendix, Section 7.6, Fig. 7.15, we plot the maximum bond extension $\max(\ell_{ij}/\ell_{ij,0})$ in a 3D sample with $\phi_0 = 0.5$ and $z = 4$. Even as the sample approaches jamming, the maximum stretch does not exceed 50%. Since this work is motivated by experiments on fibrin, which can be stretched far beyond this value, we do not include effects of rupture. Nevertheless, this effect may be relevant for less extensible biopolymers, such as collagen. In addition, as we focus on the quasistatic limit in this work, we ignore any mechanical influence of the fluid (i.e. poroelastic effects, surface tension, etc.). These may become important in samples with large particle volume fractions. Future work will need to include such effects, particularly if the dynamic properties of the material are to be considered.

Whereas we have considered only the case of zero lateral strain in this study, we

note that different boundary conditions could certainly affect our results. For example, a uniaxially compressed sample with free lateral boundaries would not necessarily jam at ε_j, but rather the inclusions would instead rearrange by spreading outward to accomodate increasing compression. Nevertheless, this effect would lead to increasing shear/extension in the regions between inclusions, so we expect that this would simply increase the duration of the stretching-dominated stiffening regime and delay the onset of jamming. This is possibly relevant to experimental results in Ref. [236] on fibrin networks with dextran inclusions at $\phi_0 = 0.6$. Although $\varepsilon_j \approx -0.06$ for $\phi_0 = 0.6$, these were shown to continue to compression stiffen at even larger compressive strains of up to $\varepsilon = -0.2$.

The rope model, given its simple nature, lends itself easily to further exploration. One could, for example, replace the rope-like springs between neighbors with springs that follow a more complex force-extension curve, e.g. that of extensible thermal worm-like chains [19].

7.5 Methods

7.5.1 Generation of coarse-grained rope model

As described in the main text, we consider N radially monodisperse spheres in a periodic box of volume L^d, in which L is chosen such that the initial particle volume fraction (area fraction in 2D) is ϕ_0. We use $N = 1000$ in 3D and $N = 900$ in 2D. To generate the initial particle configuration, we first randomly choose N initial locations as particle centers and increase the particle radii from 0 in small steps, allowing the system's energy to relax at each step using the L-BFGS method [225] to avoid particle overlap. Upon reaching the desired radii, we generate the Delaunay triangulation of the particle centers [229] to identify pairs of neighboring particles, which we subsequently connect with rope-like springs. The initial lengths of the rope-like springs are set to

be equal to the initial distance between each pair of neighboring particles.

7.5.2 Generation of subisostatic networks containing stiff inclusions

We begin with a packing-derived network composed of N nodes with average connectivity $z_0 \approx 8$ in a 3D periodic unit cell of volume $V = L^3$. We then randomly delete bonds until the desired average network connectivity z is realized. We randomly place inclusions of radius $r = 2$ with total volume fraction ϕ_0 within the periodic box, connecting these to the network at points of intersection by freely rotating joints. Further details are provided in Appendix, Section 7.6. Unless otherwise stated, we use $L = 15$ and $N = 15^3$.

The total energy $\mathcal{H}$ of the network is computed as

$$\mathcal{H} = \mathcal{H}_S + \mathcal{H}_B + \mathcal{H}_R \tag{7.5}$$

in which $\mathcal{H}_S$, $\mathcal{H}_B$, and $\mathcal{H}_R$ represent the stretching, bending, and repulsive contributions, respectively. We treat each network segment as a Hookean spring with spring constant μ, such that

$$\mathcal{H}_S = \frac{\mu}{2} \sum_{ij} \frac{(\ell_{ij} - \ell_{ij,0})^2}{\ell_{ij,0}} \tag{7.6}$$

in which ℓ_{ij} and $\ell_{ij,0}$ are the length and rest length, respectively, of the segment connecting nodes i and j. We add harmonic bond-bending interactions with energy scale κ between connected segments as

$$\mathcal{H}_B = \frac{\kappa}{2} \sum_{ijk} \frac{(\theta_{ijk} - \theta_{ijk,0})^2}{\ell_{ijk,0}} \tag{7.7}$$

in which θ_{ijk} and $\theta_{ijk,0}$ are the angle and rest angle between neighboring segments ij and jk, $\ell_{ijk,0} = (\ell_{ij,0} + \ell_{jk,0})/2$, and the sum is taken over all connected network

node triplets. Rest angles and rest lengths are defined such that the initial network structure corresponds to the zero energy configuration. We also include purely repulsive harmonic interactions with energy scale μ_R as $\mathcal{H}_R = \mathcal{H}_{R,a} + \mathcal{H}_{R,b}$, where $\mathcal{H}_{R,a}$ resists overlap between pairs of inclusions and $\mathcal{H}_{R,b}$ resists overlap between inclusions and network nodes. The first is defined as

$$\mathcal{H}_{R,a} = \frac{\mu_R}{2} \sum_{mn} \left(1 - \frac{u_{mn}}{r_{mn}}\right)^2 \Theta\left(1 - \frac{u_{mn}}{r_{mn}}\right) \tag{7.8}$$

in which $u_{mn} = |\boldsymbol{u}_m - \boldsymbol{u}_n|$ is the distance between the central nodes of inclusions m and n, $r_{mn} = r_m + r_n$ is the sum of their radii, and Θ is the Heaviside step function. The repulsive contribution between inclusions and network nodes is

$$\mathcal{H}_{R,b} = \frac{\mu_R}{2} \sum_{m} \sum_{i} \left(1 - \frac{u_{mi}}{r_m}\right)^2 \Theta\left(1 - \frac{u_{mi}}{r_m}\right) \tag{7.9}$$

in which $u_{mi} = |\boldsymbol{u}_m - \boldsymbol{u}_i|$ is the distance between the center node of inclusion m and network node i and the sums are taken over all inclusions m and network nodes i.

7.5.3 Rheology simulation

We consider quasistatic uniaxial strain ε followed by simple shear strain γ, applied relative to the initial reference configuration using generalized Lees-Edwards boundary conditions [85]. In 3D, the deformation gradient tensor is

$$\boldsymbol{\Lambda}(\gamma, \varepsilon) = \begin{pmatrix} 1 & 0 & \gamma \\ 0 & 1 & 0 \\ 0 & 0 & 1 \end{pmatrix} \begin{pmatrix} 1 & 0 & 0 \\ 0 & 1 & 0 \\ 0 & 0 & 1+\varepsilon \end{pmatrix}. \tag{7.10}$$

At each applied strain step, we numerically minimize $\mathcal{H}$ using the L-BFGS algorithm [225]. About a given relaxed configuration at uniaxial strain ε, we compute the shear

stress $\sigma_{xz}(\varepsilon)$ as

$$\sigma_{xz} = \frac{1}{V}\frac{\partial \mathcal{H}}{\partial \gamma} \tag{7.11}$$

in which V is the volume of the deformed simulation box. We apply small uniaxial strain steps of magnitude $|d\varepsilon| = 0.01$. At a given uniaxial strain, we apply small symmetric positive and negative shear strain steps $d\gamma = 0.01$ to compute the apparent shear modulus

$$G(\varepsilon) = \frac{\partial \sigma_{xz}(\varepsilon)}{\partial \gamma} \tag{7.12}$$

All data reported in this paper correspond to an average over 15 independently generated network samples.

7.6 Appendix

7.6.1 Predicting the required compression for contact percolation and jamming

Consider a parallel-plate rheometer containing a gel sample occupying initial total volume $V = V_0$. The gel consists of a polymer network containing randomly distributed, rigid spherical inclusions with initial volume fraction ϕ_0. The polymer volume fraction is negligible, and an incompressible buffer fluid fills the remaining sample volume. Assuming that the inclusions are rigid and that the network and inclusions are mechanically constrained to remain within the initial sample volume, changes in V amount to fluid flow into or out of the sample. Under uniaxial strain ε with zero lateral strain, the total volume of the sample becomes $V = (1 + \varepsilon)V_0$. Note that compression corresponds to $\varepsilon < 0$. As the volume occupied by the inclusions ($\phi_0 V_0$) remains constant, the strain-dependent inclusion volume fraction is $\phi = \phi_0/(1 + \varepsilon)$. Prior work has shown that contact percolation in radially bidisperse spheres with short-range attractive interactions occurs at a particle volume fraction of $\phi_p \approx 0.214$

in 3D and $\phi_p \approx 0.558$ in 2D [242], under effective bulk compression. Assuming that the volume fraction for contact percolation is protocol independent (which may not be true), then for a system with initial volume fraction ϕ_0, we can estimate the uniaxial strain required for contact percolation as $\varepsilon_p = \phi_0/\phi_p - 1$. Jamming likewise occurs at a specific particle volume fraction ϕ_j (for bidisperse disks in 2D, $\phi_j \approx 0.84$, and for spheres in 3D, $\phi_j \approx 0.64$ [248]). If we again assume that the jamming volume fraction is the same for bulk compression as for uniaxial compression, then for a given ϕ_0, we can estimate the uniaxial strain required for jamming is $\varepsilon_j = \phi_0/\phi_j - 1$. As we show in the main text and in Fig. 7.5, this estimate agrees with our simulations.

7.6.2 Rope model

In Fig. 7.5, we show the complementary figure to Fig. 2 in the main text for the 2D rope model, using radially bidisperse disks. We note that, for an intermediate range of initial particle area fractions, stretching-dominated stress propagation in the $\lambda = 1$ limit occurs at lower levels of applied compression than predicted for contact percolation ($\varepsilon_p = \phi_0/\phi_p - 1$), whereas this is not observed in our 3D results. In Fig. 7.6, we sketch examples of systems in which stretching-dominated stress propagation for $\lambda = 1$ occurs concurrently with contact percolation (Fig. 7.6a) and before contact percolation (Fig. 7.6b). In Fig. 7.7a, we plot the critical compressive strain ε_c for stretching-dominated stress propagation in the 2D rope model as a function of the slack extension of the rope-like springs, $\lambda_c - 1$, for varying ϕ_0. In Fig. 7.7b, we plot the same data for the 3D rope model, as described in the main text. To predict the critical compressive strain for stretching-dominated stress propagation in a system with inclusion volume fraction ϕ_0 and network connectivity z, we interpolate between the measured points to find $\varepsilon_c(\phi_0, \lambda_c = 1 + \varepsilon_c(\phi = 0, z))$, where $\varepsilon_c(\phi = 0, z)$ is the critical extensional strain for an inclusion-free network of connectivity z.

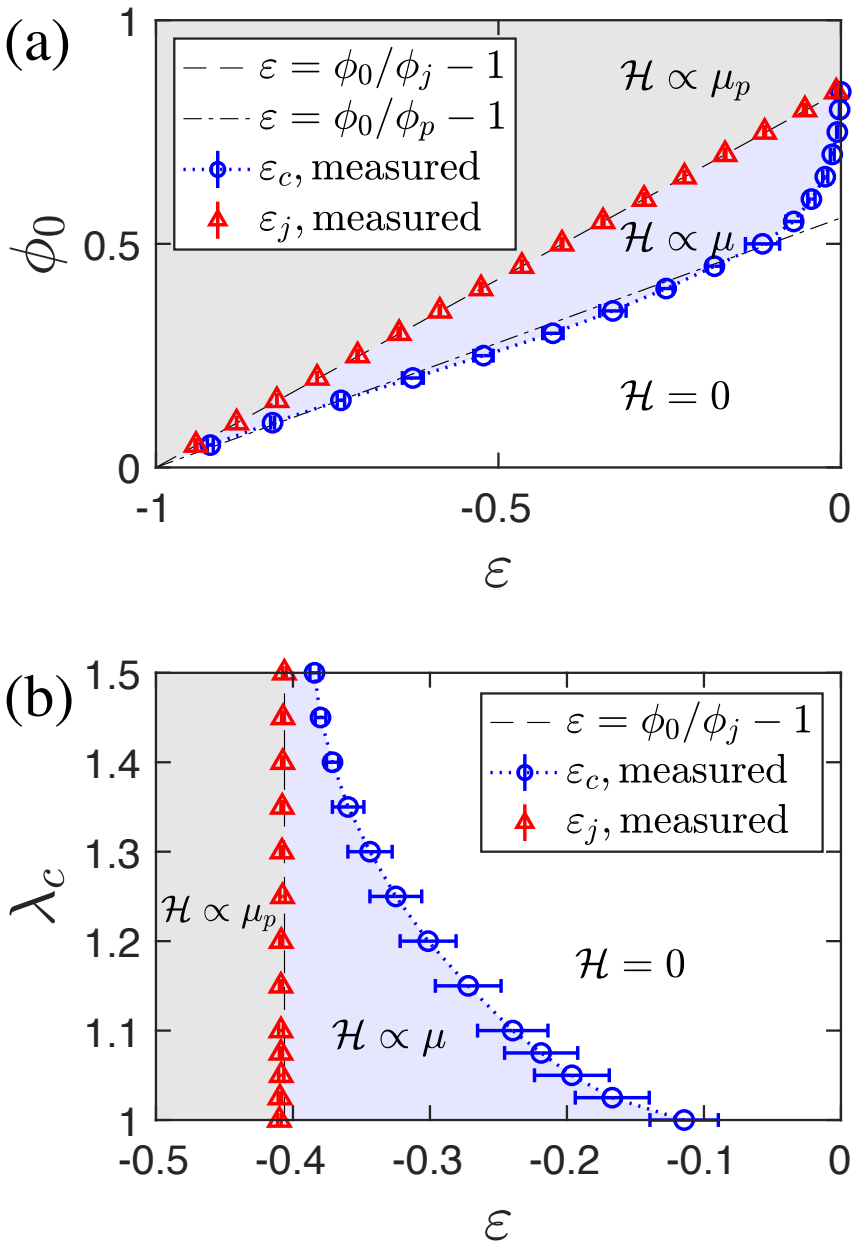

Figure 7.5: (a) Mechanical phase diagram for compressed systems of $N = 900$ radially bidisperse, repulsive disks, in which nearest neighbors (by Delaunay triangulation) are connected by rope-like springs, as a function of uniaxial strain ε and initial volume fraction ϕ_0. Here, $\mu = 10^{-5}$, $\mu_p = 1$, and the rope-like springs have slack extension $\lambda_c = 1$. The blue circles correspond to the critical strain for the onset of stretching-dominated stress propagation, ε_c, and the red triangles correspond to the onset of jamming, ε_j. The dashed black line corresponds to the predicted applied strain required for jamming of a system with initial volume fraction ϕ_0, $\varepsilon_j = \phi_0/\phi_j - 1$, in which $\phi_j = 0.84$. The white region corresponds to the floppy regime ($\mathcal{H} = 0$, blue corresponds to the stretching-dominated regime ($\mathcal{H} \propto \mu$), and gray corresponds to the jammed regime ($\mathcal{H} \propto \mu_p$). (b) Mechanical phase diagram for volume fraction $\phi_0 = 0.5$ as a function of applied uniaxial strain ε and slack extension of rope-like springs, λ_c. Error bars in both panels correspond to ± 1 standard deviation.

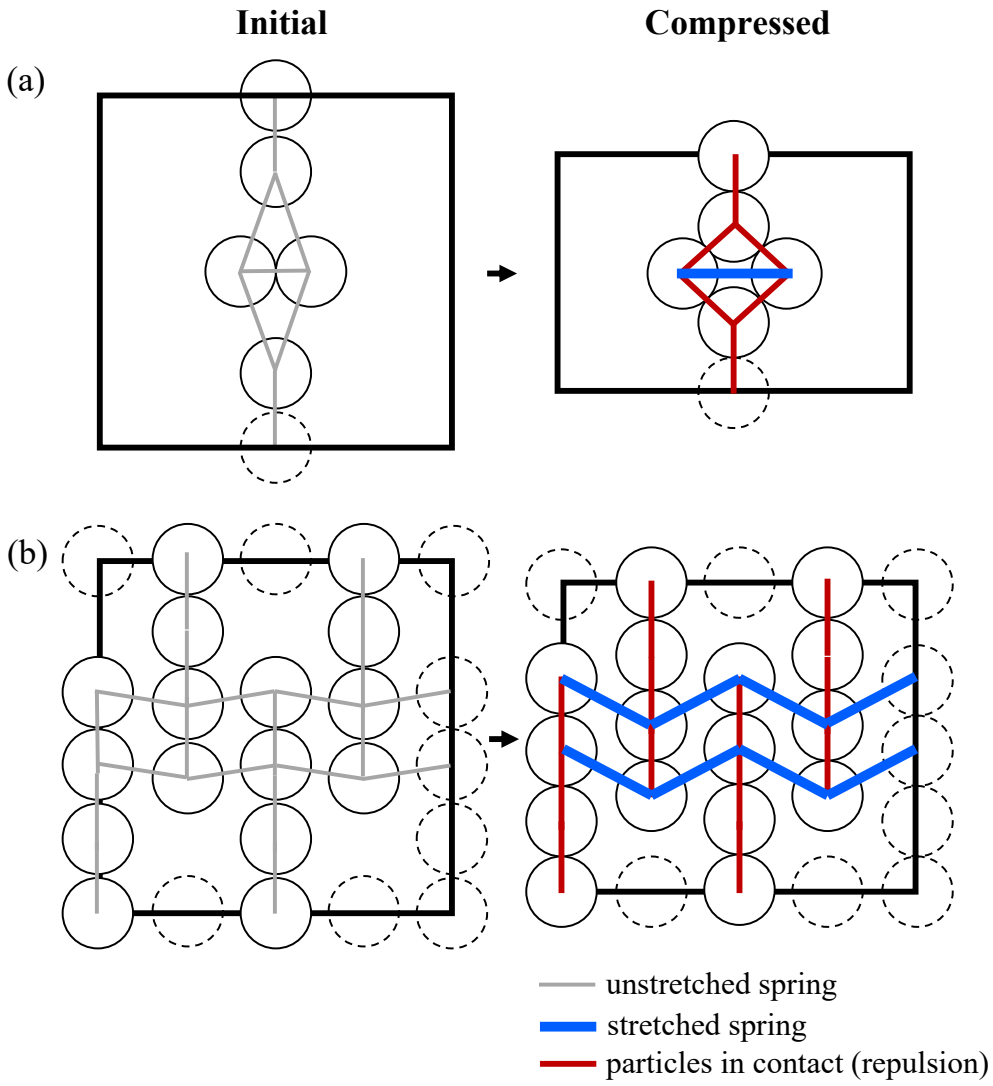

Figure 7.6: Illustrations of periodic assemblies of particles connected by rope-like springs in which, under applied uniaxial compression, stretching-dominated stress propagation occurs (a) concurrent with contact percolation and (b) prior to contact percolation.

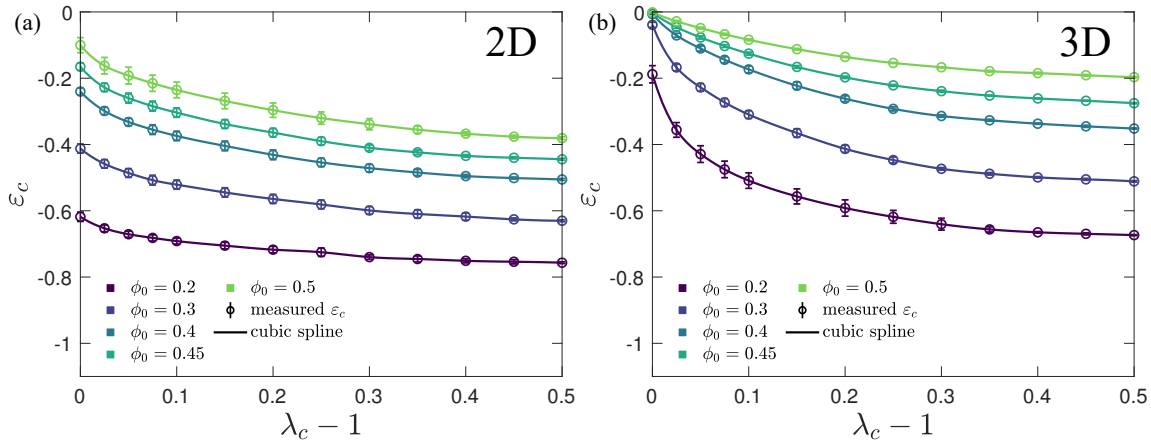

Figure 7.7: Measured critical strain values for compression-driven, stretching-dominated stress propagation in (a) the 2D rope model for systems with $N = 900$ radially bidisperse disks and (b) the 3D rope model for systems with $N = 1000$ radially monodisperse spheres, with varying initial volume fraction ϕ_0, as a function of the slack extension of the rope-like springs, λ_c. Circles represent measured values and solid lines represent cubic spline fits used to interpolate between measured points. We use this plot to empirically predict the critical strain for compression-driven stiffening in simulated particle-network composites in which the interstitial network has a known critical extensile strain.

7.6.3 Fiber network simulations

Underlying random networks

Below we describe the procedures for generating random packing-derived networks in 2D and 3D, to which we eventually insert inclusions.

2D To generate 2D packing-derived networks, we randomly place $N = L^2$ radially bidisperse disks with $r \in (r_0, 1.4r_0)$ in a periodic square unit cell of side length L and incrementally increase r_0 from 0, allowing the system to relax at each step, until the average connectivity of the contact network (joining overlapping disks) exceeds 5.5. We use a ratio of radii of 1.4 to prevent the particles from developing crystalline order [82]. We then selectively remove bonds from the most highly connected pairs of nodes, in order to minimize spatial heterogeneity in the connectivity [79], until the desired average connectivity z is reached. During the dilution procedure, dangling ends are also removed.

3D To generate 3D packing-derived networks, we randomly place $N = L^3$ spheres of radius r_0 in a periodic cubic unit cell of side length L and incrementally increase r_0 from 0, allowing the system to relax at each step, until the average connectivity of the contact network (joining overlapping disks) exceeds 8. We then selectively remove bonds from the most highly connected pairs of nodes, in order to minimize spatial heterogeneity in the connectivity [79], until the desired average connectivity z is reached. During the dilution procedure, dangling ends are also removed. In Fig. 7.8, we show a 3D network with $L = 15$ and $z = 4$ prior to the addition of inclusions.

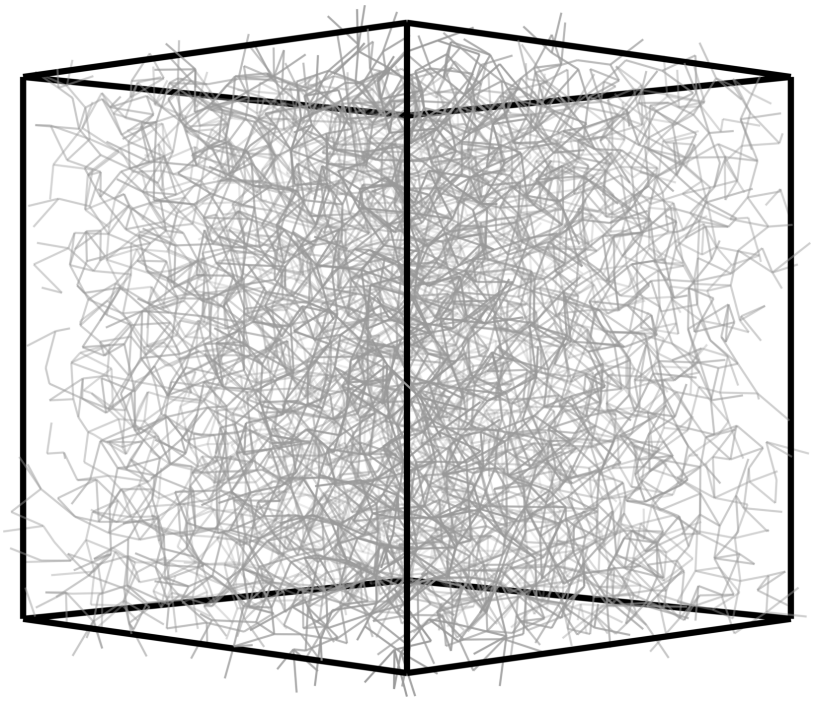

Figure 7.8: Periodic network made up of 15^3 nodes with average connectivity $z = 4$.

Networks with bound inclusions

After the underlying fiber network is generated, non-intersecting inclusions (disks in 2D and spheres in 3D) are randomly placed until the desired inclusion volume fraction is reached. Bonds that intersect with the surface of a placed inclusion are connected to the inclusion surface, at the intersection point, by a freely rotating joint, and all bond segments within the inclusion boundary are removed. Each inclusion behaves as a rigid d-dimensional body with d translational and x rotational degrees of freedom ($x = 1$ for $d = 2$, and $x = 3$ for $d = 3$), such that all of the boundary connections translate and rotate rigidly with the inclusion. In Fig. 7.9, we show images of the resulting networks, containing inclusions, in 2 and 3 dimensions. In 2D, we use radially bidisperse circular inclusions, with a ratio of radii of 1.4, in which half of the inclusions have the larger radius $R = 4$.

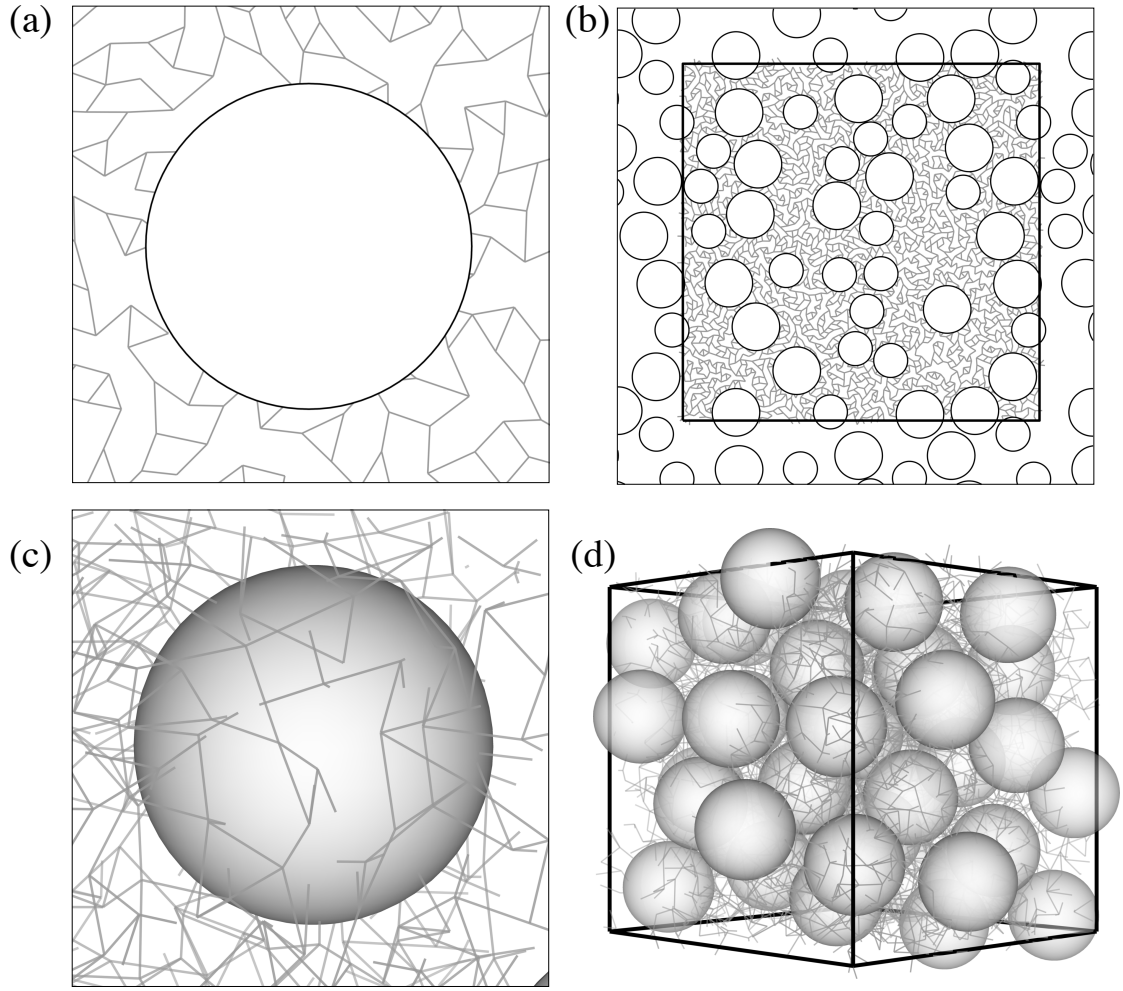

Figure 7.9: (a) Single inclusion of radius $R = 4$ in a 2D packing-derived network with $z = 3$. Bonds that intersect with the inclusion boundary are rigidly connected to the boundary, at the point of intersection, by a freely rotating joint. One-sided repulsive interactions act both between inclusions whose boundaries overlap and between inclusion boundaries and network nodes. (b) Example of an initial configuration of a packing-derived network with $z = 3$ and radially bidisperse inclusions, with area fraction $\phi_0 = 0.4$. (b) Single inclusion of radius $R = 2$ in a 3D packing-derived network with $z = 4$. (b) Example of an initial configuration of a 3D packing-derived network with $z = 4$ and inclusion volume fraction $\phi_0 = 0.4$.

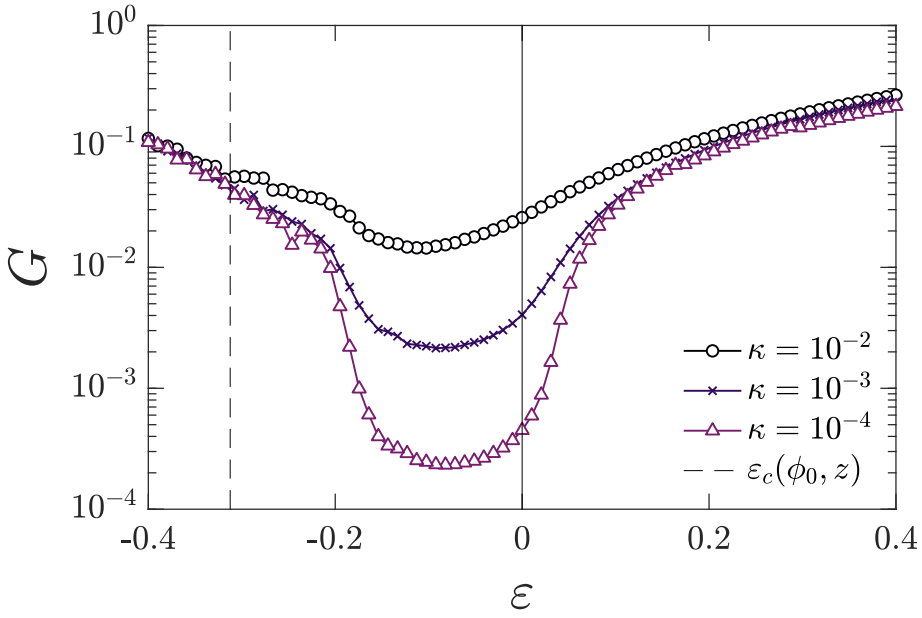

Figure 7.10: Shear modulus G for 3D packing-derived networks with $\phi = 0.4$, $z = 4$, varying bond-bending modulus κ and constant stretching modulus $\mu = 1$. These systems undergo a transition from a regime in which $G \propto \kappa$ at low levels of applied compression to one in which $G \propto \mu$ (independent of κ) at higher compression levels.

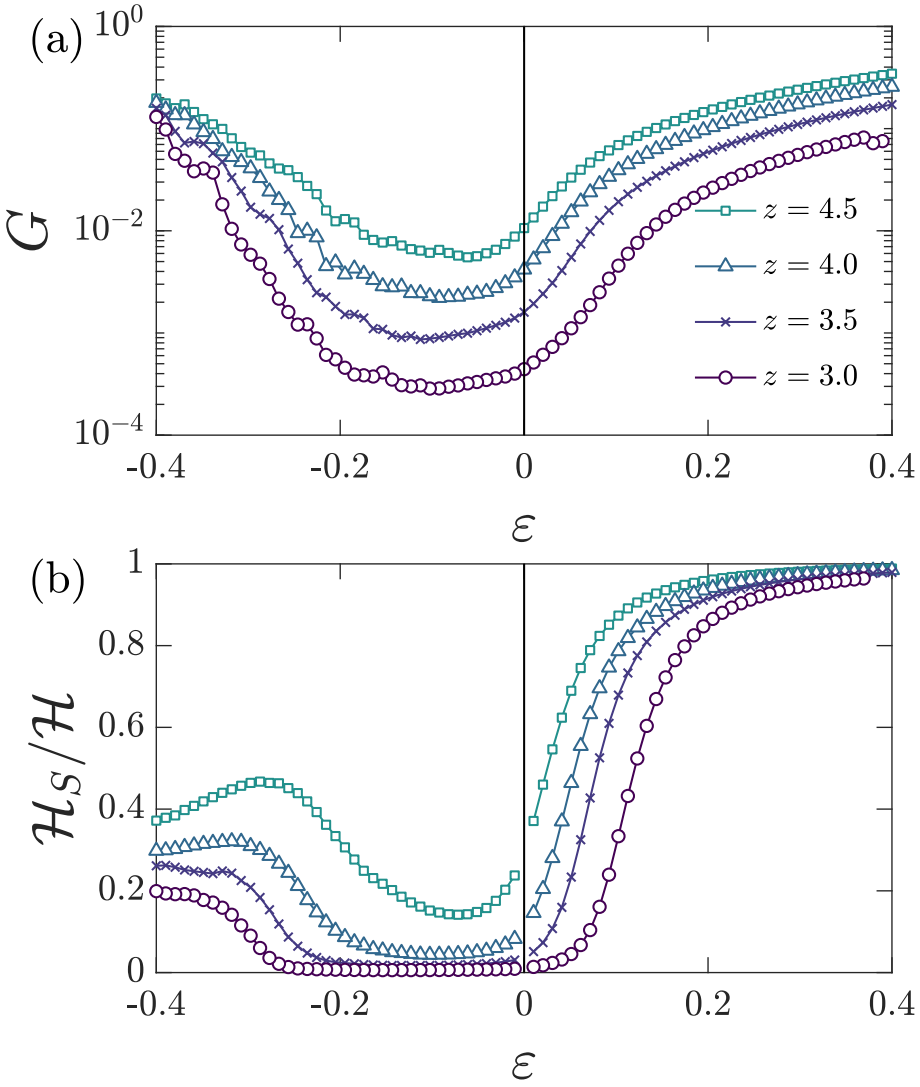

Figure 7.11: (a) Shear modulus G and (b) stretching energy fraction $\mathcal{H}_S/\mathcal{H}$ as a function of applied uniaxial strain ε for 3D packing-derived networks with $\phi_0 = 0.4$, $\kappa = 10^{-3}$, and varying average connectivity z. Under both compression and extension, increasing z leads to a decrease in the magnitude of strain required the onset of the stiff stretching-dominated regime.

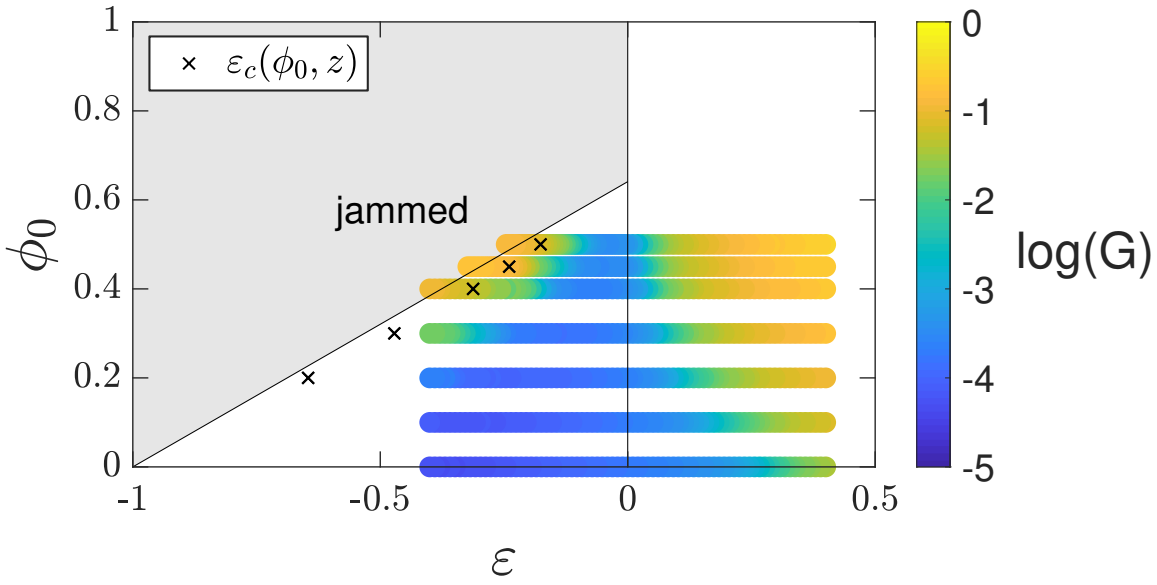

Figure 7.12: Data from Fig. 3a in the main text:. Phase diagram depicting the shear modulus for 3D packing-derived networks with $z = 4$ and $\kappa = 10^{-4}$ as a function of inclusion volume fraction ϕ_0. Each x denotes the predicted critical compressive strain for stretching-dominated stress propagation for the rope model with volume fraction ϕ_0, using an appropriate value of the slack extension λ_c to account for the extensional critical strain $\varepsilon_{c,ext}$ of 3D packing-derived networks with $z = 4$, i.e. $\lambda_c = 1 + \varepsilon_{c,ext}(z = 4) \approx 1.3$.

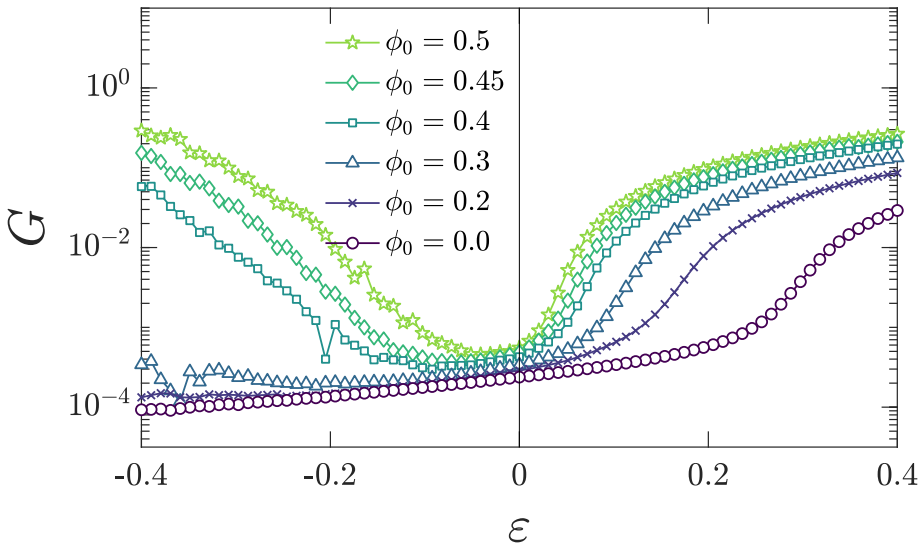

Figure 7.13: (a) Shear modulus G as a function of applied uniaxial compression ε for 2D packing-derived networks with $z = 3$, $\kappa = 10^{-4}$, and varying initial inclusion area fraction ϕ_0.

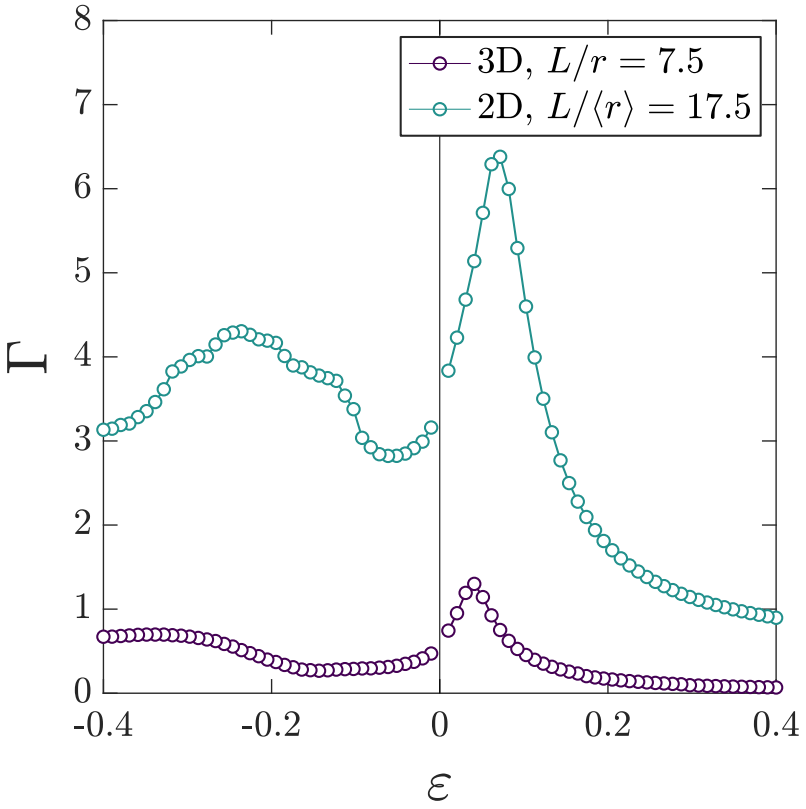

Figure 7.14: Comparison of the strain-dependent inclusion nonaffinity between 2D and 3D packing-derived networks containing inclusions with $\kappa = 10^{-4}$ and volume fraction (area fraction in 2D) ϕ_0. The 3D data correspond to $z = 4$, $L = 15$, and $r = 2$, and the 2D data correspond to $z = 3$, $L = 60$, and average inclusion radius $\langle r \rangle = 3.43$ (we use radially bidisperse inclusions in 2D; half the inclusions are of radius 4 and half $4/1.4$). Given that the ratio of the system size to the inclusion radius is larger in our 2D simulations than in our 3D simulations, it is unsurprising that the 2D systems exhibit more heterogeneous inclusion deformation. Future work will be necessary to explore the system size dependence of Γ in 2D and 3D.

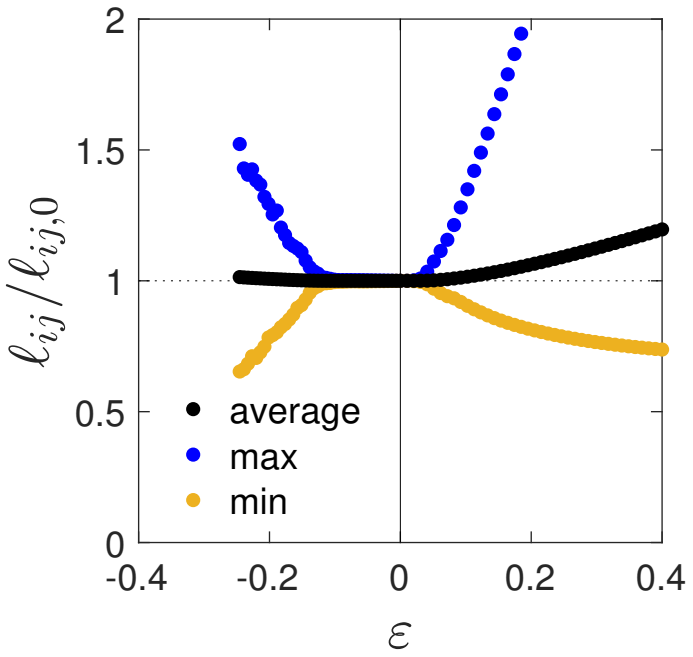

Figure 7.15: Average, minimum, and maximum bond change in bond length for a 3D packing-derived network with $\phi_0 = 0.5$, $z = 4$, and $\kappa = 10^{-4}$. Under compression, we find that the maximum extension of any individual bond does not exceed roughly 50%, even as the system approaches the jamming point. For systems with highly extensible bonds, such as fibrin (which can tolerate extensional strains of over 200% [24]), we can thus expect compression-driven stiffening to occur without stretching-induced bond rupture.

Disconnected inclusions

To test whether bonds between the inclusions and surrounding network are necessary for compression-stiffening, we also consider 2D systems in which the locations of the (radially bidisperse) inclusions are chosen as discussed above, but all bonds are cut within radius $r_{final}/2$ of each inclusion center and then the repulsive inclusion is swollen from radius 0 to r_{final} (in which $r_{final} = R$ or $R/1.4$). In this case, each inclusion interacts with the surrounding network only through repulsive interactions. Parameters are otherwise chosen to be the same as for the 2D data presented in Fig. 7.13. As shown in Fig. 7.16a, the initial inclusion swelling induces prestress within the interstitial network. The corresponding shear moduli, as a function of axial strain, for such systems with varying ϕ_0.

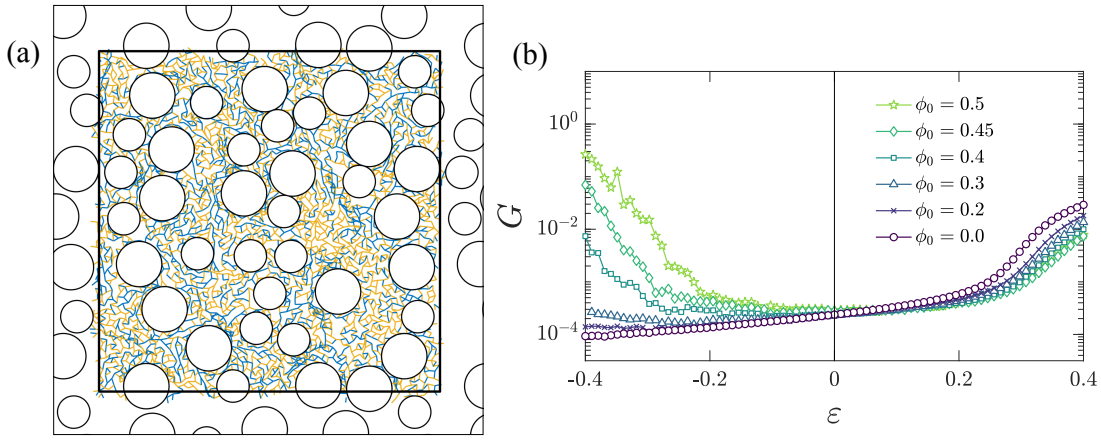

Figure 7.16: (a) 2D packing-derived network with $z = 3$ and radially bidisperse inclusions with $r \in [3, 3/1.4]$ and $\phi_0 = 0.4$ that are not connected to the surrounding network. Blue segments are stretched and orange segments are compressed. (b) Shear modulus G as a function of applied uniaxial compression ε for packing-derived networks with $z = 3$, $\kappa = 10^{-4}$, and varying initial inclusion area fraction ϕ_0

Chapter 8

Conclusion

In this thesis, we made progress in understanding the nonlinear viscoelastic properties of disordered networks. More specifically, we explored how applied deformation drives disordered assemblies of biopolymers, and network-derived materials in general, to collectively transition between dramatically different viscoelastic regimes. These transitions are ubiquitous in biological materials and include strain-driven stiffening of cytoskeletal and extracellular networks, the tension-driven nonlinear Poisson effect in the extracellular matrix and its effects on alignment and densification, and compression-driven, tension-controlled stiffening in network-inclusion composites. Improving our understanding of the factors that control these phenomena, e.g. the elastic properties of filaments or the microstructure of a network, will bolster future efforts to construct synthetic tissues and biomimetic materials with tunable macroscopic mechanical properties.

Chapters 3-5 focused on strain-controlled critical behavior in disordered elastic networks. Recent work has shown that strain stiffening in fiber networks can be modeled quantitatively as a phase transition between distinct soft and rigid mechanical regimes, with applied strain acting as the control variable. Networks traversing the critical point exhibit familiar signatures of continuous phase transitions, including diverging

characteristic length and time scales and power law scaling of various observables with distance to the transition. Our work has focused on understanding the nature of the strain stiffening transition in a minimal model of disordered elastic networks. In Chapter 3, we constructed coarse-grained computational models of disordered elastic networks and demonstrated that, near the onset of rigidity, these display anomalously broad and seemingly scale-invariant force distributions. In Chapter 4, we used real space renormalization to determine relationships between the critical exponents describing the strain-controlled stiffening transition, which we then tested in simulations. We have since expanded upon this work in three-dimensional systems and characterized associated finite size effects [62, 63]. In Chapter 5, we explored the dynamic rheological properties of fluid-immersed networks near the stiffening transition. We found that the application of strain in these systems can drive the growth and even divergence of the time scales controlling stress relaxation, with the remarkable consequence of externally tunable power law rheology.

In Chapter 6, we explored the manifestation in disordered networks of an elastic phenomenon known as the Poisson effect, which describes the tendency of a material that is stretched along one direction to consequently shrink in width. In contrast to common materials such as rubber that shrink only slightly, biopolymer networks tend to exhibit an anomalously large and nonlinear Poisson effect accompanied by an overall reduction in volume, even under relatively small applied strains. In the extracellular matrix, this behavior leads to substantial alignment and increased fiber density in strained regions, which may in turn influence cell-cell communication and durotaxis. Using coarse-grained simulations, we demonstrated that the nonlinear Poisson effect in disordered elastic networks is controlled by a mechanical phase transition, analogous to the shear-driven transition discussed elsewhere in this thesis, that occurs along a line of connectivity-controlled critical points in strain. Near the transition, networks exhibit power-law scaling of the Young's modulus and diverging nonaffine strain fluctuations.

This work could potentially prove useful in learning to design responsive biomimetic materials with tunable stiffness and polarization.

In Chapter 7, we explored how filling biopolymer networks with additional mechanical components, like living cells, can add further complexity to their viscoelastic behavior [249]. Although cell-free networks are easily compressed, experiments have shown that cell-rich living tissues, like liver, brain, and adipose tissue, stiffen significantly under applied compression. Despite an abundance of experimental evidence for this behavior, its physical origin has remained poorly understood. We uncovered a novel physical mechanism for this effect and, using a simple computational model of interconnected repulsive particles, we established a phase diagram for the onset of compression-driven stretching and jamming in particle-network composites, which we used to predict the onset of stiffening in coarse-grained simulations of these composites. This work aims to improve our understanding of disease-driven changes in the response of tissues to compression, in addition to enabling the design of compression-responsive synthetic tissues and biomimetic materials.

References

[1] A. Flamholz, R. Phillips, and R. Milo, Molecular Biology of the Cell **25**, 3497 (2014).

[2] R. L. Satcher and C. F. Dewey, Biophysical Journal **71**, 109 (1996).

[3] D. A. Fletcher and R. D. Mullins, Nature **463**, 485 (2010).

[4] P. A. Janmey, D. A. Fletcher, and C. A. Reinhart-King, Physiological Reviews **100**, 695 (2020).

[5] F. Beroz, L. M. Jawerth, S. Münster, D. A. Weitz, C. P. Broedersz, and N. S. Wingreen, Nature Communications **8**, 16096 (2017).

[6] P. Lu, V. M. Weaver, and Z. Werb, The Journal of Cell Biology **196**, 395 (2012).

[7] S. Özbek, P. G. Balasubramanian, R. Chiquet-Ehrismann, R. P. Tucker, J. C. Adams, and D. Kellogg, Molecular Biology of the Cell **21**, 4300 (2010).

[8] T. Svitkina, Cold Spring Harbor Perspectives in Biology **10**, a018267 (2018).

[9] A. E. Patteson, R. J. Carroll, D. V. Iwamoto, and P. A. Janmey, Physical Biology **18**, 011001 (2020).

[10] G. L. Mullins and W. G. Guntheroth, Nature **206**, 592 (1965).

[11] I. K. Piechocka, A. S. G. van Oosten, R. G. M. Breuls, and G. H. Koenderink, Biomacromolecules **12**, 2797 (2011).

[12] A. Undas and R. A. Ariëns, Arteriosclerosis, Thrombosis, and Vascular Biology **31**, e88 (2011).

[13] R. A. S. Ariëns, T.-S. Lai, J. W. Weisel, C. S. Greenberg, and P. J. Grant, Blood **100**, 743 (2002).

[14] P. A. Janmey, J. P. Winer, and J. W. Weisel, Journal of the Royal Society Interface **6**, 1 (2009).

[15] J.-P. Collet, H. Shuman, R. E. Ledger, S. Lee, and J. W. Weisel, Proceedings of the National Academy of Sciences **102**, 9133 (2005).

[16] R. Altig and R. W. McDiarmid, Herpetological Monographs **21**, 1 (2007).

[17] G. Chaudhary, R. H. Ewoldt, and J.-L. Thiffeault, Journal of The Royal Society Interface **16**, 20180710 (2019).

[18] S. W. Cranford, A. Tarakanova, N. M. Pugno, and M. J. Buehler, Nature **482**, 72 (2012).

[19] C. Storm, J. J. Pastore, F. C. MacKintosh, T. C. Lubensky, and P. A. Janmey, Nature **435**, 191 (2005).

[20] R. H. Pritchard, Y. Y. Shery Huang, and E. M. Terentjev, Soft Matter **10**, 1864 (2014).

[21] B. A. Roeder, K. Kokini, and S. L. Voytik-Harbin, Journal of Biomechanical Engineering **131**, 31004 (2009).

[22] Y. Wang, S. Kumar, A. Nisar, M. Bonn, M. K. Rausch, and S. H. Parekh, Acta

Biomaterialia **121**, 383 (2021).

[23] D. Vader, A. Kabla, D. Weitz, and L. Mahadevan, PLOS ONE **4**, e5902 (2009).

[24] A. E. X. Brown, R. I. Litvinov, D. E. Discher, P. K. Purohit, and J. W. Weisel, Science **325**, 741 (2009).

[25] A. Kabla and L. Mahadevan, Journal of The Royal Society Interface **4**, 99 (2007).

[26] L. A. Mihai and A. Goriely, Proceedings of the Royal Society A **470**, 20140363 (2014).

[27] R. C. Picu, S. Deogekar, and M. R. Islam, Journal of Biomechanical Engineering **140**, 021002 (2018).

[28] J. L. Shivers, S. Arzash, and F. C. MacKintosh, Physical Review Letters **124**, 038002 (2020).

[29] E. Ban, H. Wang, J. M. Franklin, J. T. Liphardt, P. A. Janmey, and V. B. Shenoy, Proceedings of the National Academy of Sciences **116**, 6790 (2019).

[30] A. Mann, R. S. Sopher, S. Goren, O. Shelah, O. Tchaicheeyan, and A. Lesman, Journal of The Royal Society Interface **16**, 20190348 (2019).

[31] H. Wang, A. S. Abhilash, C. S. Chen, R. G. Wells, and V. B. Shenoy, Biophysical Journal **107**, 2592 (2015).

[32] J. Notbohm, A. Lesman, P. Rosakis, D. A. Tirrell, and G. Ravichandran, Journal of The Royal Society Interface **12**, 20150320 (2015).

[33] K. A. Jansen, R. G. Bacabac, I. K. Piechocka, and G. H. Koenderink, Biophysical Journal **105**, 2240 (2013).

[34] T. Odijk, Macromolecules **28**, 7016 (1995).

[35] F. C. MacKintosh, J. Kas, and P. A. Janmey, Physical Review Letters **75**, 4425 (1995).

[36] C. P. Broedersz and F. C. MacKintosh, Reviews of Modern Physics **86**, 995 (2014).

[37] M. L. Gardel, J. H. Shin, F. C. MacKintosh, L. Mahadevan, P. Matsudaira, and D. A. Weitz, Science **304**, 1301 (2004).

[38] A. S. G. van Oosten, M. Vahabi, A. J. Licup, A. Sharma, P. A. Galie, F. C. MacKintosh, and P. A. Janmey, Scientific Reports **6**, 19270 (2016).

[39] P. A. Janmey, M. E. McCormick, S. Rammensee, J. L. Leight, P. C. Georges, and F. C. MacKintosh, Nature Materials **6**, 48 (2007).

[40] D. A. Head, A. J. Levine, and F. C. MacKintosh, Physical Review Letters **91**, 108102 (2003).

[41] A. J. Liu and S. R. Nagel, Nature **396**, 21 (1998).

[42] M. Wyart, Annales de Physique **30**, 1 (2005).

[43] D. J. Durian, Physical Review Letters **75**, 4780 (1995).

[44] D. J. Jacobs and M. F. Thorpe, Physical Review E **53**, 3682 (1996).

[45] W. G. Ellenbroek, V. F. Hagh, A. Kumar, M. Thorpe, and M. van Hecke, Physical Review Letters **114**, 135501 (2015).

[46] J. C. Maxwell, The London, Edinburgh, and Dublin Philosophical Magazine and Journal of Science **27**, 294 (1864).

[47] C. O'Hern, L. Silbert, and S. Nagel, Physical Review E **68**, 011306 (2003).

[48] C. P. Broedersz, X. Mao, T. C. Lubensky, and F. C. MacKintosh, Nature Physics **7**, 983 (2011).

[49] Biot, Maurice A., *Mechanics of Incremental Deformations* (John Wiley & Sons, 1965).

[50] A. Sharma, A. J. Licup, K. A. Jansen, R. Rens, M. Sheinman, G. H. Koenderink, and F. C. MacKintosh, Nature Physics **12**, 584 (2016).

[51] R. Rens, M. Vahabi, A. J. Licup, F. C. MacKintosh, and A. Sharma, Journal of Physical Chemistry B **120**, 5831 (2016).

[52] A. Sharma, A. J. Licup, R. Rens, M. Vahabi, K. A. Jansen, G. H. Koenderink, and F. C. MacKintosh, Physical Review E **94**, 042407 (2016).

[53] D. T. Chen, Q. Wen, P. A. Janmey, J. C. Crocker, and A. G. Yodh, Annual Review of Condensed Matter Physics **1**, 301 (2010).

[54] F. C. MacKintosh and C. F. Schmidt, Current Opinion in Colloid & Interface Science **4**, 300 (1999).

[55] M. L. Gardel, M. T. Valentine, J. C. Crocker, A. R. Bausch, and D. A. Weitz, Physical Review Letters **91**, 158302 (2003).

[56] A. J. Levine and T. C. Lubensky, Physical Review Letters **85**, 1774 (2000).

[57] R. M. Robertson-Anderson, ACS Macro Letters **7**, 968 (2018).

[58] M. Feric, C. P. Broedersz, and C. P. Brangwynne, Scientific Reports **5**, 16607 (2015).

[59] M. L. Gardel, K. E. Kasza, C. P. Brangwynne, J. Liu, and D. A. Weitz, in *Methods in Cell Biology* (Academic Press, 2008), vol. 89, pp. 487–519.

[60] C. W. Macosko and R. G. Larson, *Rheology: Principles, Measurements, and Applications* (Wiley, 1994).

[61] H. C. de Cagny, B. E. Vos, M. Vahabi, N. A. Kurniawan, M. Doi, G. H. Koenderink, F. MacKintosh, and D. Bonn, Physical Review Letters **117**, 217802 (2016).

[62] S. Arzash, J. L. Shivers, and F. C. MacKintosh, Soft Matter **16**, 6784 (2020).

[63] S. Arzash, J. L. Shivers, and F. C. MacKintosh, Physical Review E **104**, L022402 (2021).

[64] C. P. Broedersz, C. Storm, and F. C. MacKintosh, Physical Review E **79**, 061914 (2009).

[65] S. Feng and P. N. Sen, Physical Review Letters **52**, 216 (1984).

[66] M. F. Thorpe, Journal of Non-Crystalline Solids **76**, 109 (1985).

[67] X. Mao, N. Xu, and T. C. Lubensky, Physical Review Letters **104**, 85504 (2010).

[68] J. Feng, H. Levine, X. Mao, and L. M. Sander, Soft Matter **12**, 1419 (2016).

[69] X. Mao, Q. Chen, and S. Granick, Nature Materials **12**, 217 (2013).

[70] A. V. Dobrynin and J. M. Y. Carrillo, Macromolecules **44**, 140 (2011).

[71] D. B. Liarte, O. Stenull, X. Mao, and T. C. Lubensky, Journal of Physics: Condensed Matter **28**, 165402 (2016).

[72] O. Stenull and T. C. Lubensky, arXiv:1108.4328 (2011).

[73] C. P. Broedersz and F. C. MacKintosh, Soft Matter **7**, 3186 (2011).

[74] A. J. Licup, Ph.D. thesis, Vrije Universiteit Amsterdam (2016).

[75] D. A. Head, A. J. Levine, and F. C. MacKintosh, Physical Review E **68**, 061907 (2003).

[76] A. R. Cioroianu and C. Storm, Physical Review E **88**, 052601 (2013).

[77] M. F. Vermeulen, A. Bose, C. Storm, and W. G. Ellenbroek, Physical Review E **96**, 053003 (2017).

[78] R. Rens and E. Lerner, The European Physical Journal E **42**, 114 (2019).

[79] M. Wyart, H. Liang, A. Kabla, and L. Mahadevan, Physical Review Letters **101**, 215501 (2008).

[80] E. Lerner, G. Düring, and M. Wyart, Proceedings of the National Academy of Sciences **109**, 4798 (2012).

[81] M. van Hecke, Journal of Physics Condensed Matter **22**, 033101 (2010).

[82] D. J. Koeze, D. Vågberg, B. B. Tjoa, and B. P. Tighe, Europhysics Letters **113**, 54001 (2016).

[83] E. Bitzek, P. Koskinen, F. Gähler, M. Moseler, and P. Gumbsch, Physical Review Letters **97**, 170201 (2006).

[84] *The Boost Graph Library: User Guide and Reference Manual* (Addison-Wesley Longman Publishing Co., Inc., 2002).

[85] A. W. Lees and S. F. Edwards, Journal of Physics C: Solid State Physics **5**, 1921 (1972).

[86] M. Doi and S. F. Edwards, *The Theory of Polymer Dynamics* (Oxford University Press, 1988).

[87] J. L. Shivers, J. Feng, A. Sharma, and F. C. MacKintosh, Soft Matter **15**, 1666 (2019).

[88] J. H. Poynting, Proceedings of the Royal Society of London. Series A **82**, 546 (1909).

[89] J. H. Poynting, The India-Rubber Journal p. 6 (1913).

[90] R. G. Larson, *The Structure and Rheology of Complex Fluids* (Oxford University Press, 1999).

[91] A. S. Lodge and J. Meissner, Rheologica Acta **11**, 351 (1972).

[92] H. Kang, Q. Wen, P. A. Janmey, J. X. Tang, E. Conti, and F. C. MacKintosh, Journal of Physical Chemistry B **113**, 3799 (2009).

[93] C. Heussinger, B. Schaefer, and E. Frey, Physical Review E **76**, 031906 (2007).

[94] E. Conti and F. C. MacKintosh, Physical Review Letters **102**, 88102 (2009).

[95] A. J. Licup, S. Münster, A. Sharma, M. Sheinman, L. M. Jawerth, B. Fabry, D. A. Weitz, and F. C. MacKintosh, Proceedings of the National Academy of Sciences **112**, 9573 (2015).

[96] F. Meng and E. M. Terentjev, Soft Matter **12**, 6749 (2016).

[97] A. J. Licup, A. Sharma, and F. C. MacKintosh, Physical Review E **93**, 012407 (2016).

[98] K. A. Jansen, A. J. Licup, A. Sharma, R. Rens, F. C. MacKintosh, and G. H.

Koenderink, Biophysical Journal **114**, 2665 (2018).

[99] M. Vahabi, B. E. Vos, H. C. G. de Cagny, D. Bonn, G. H. Koenderink, and F. C. MacKintosh, Physical Review E **97**, 032418 (2018).

[100] R. S. Rivlin, Philosophical Transactions of the Royal Society A: Mathematical, Physical and Engineering Sciences **241**, 379 (1948).

[101] R. G. Larson and H. Brenner, *Constitutive Equations for Polymer Melts and Solutions: Butterworths Series in Chemical Engineering*, Butterworths Series in Chemical Engineering (Elsevier Science, 1988).

[102] T. S. Majmudar, M. Sperl, S. Luding, and R. P. Behringer, Physical Review Letters **98**, 058001 (2007).

[103] C. Voivret, F. Radjaï, J. Y. Delenne, and M. S. El Youssoufi, Physical Review Letters **102**, 178001 (2009).

[104] J. R. Melrose and R. C. Ball, Journal of Rheology **48**, 961 (2004).

[105] N. Y. C. Lin, C. Ness, M. E. Cates, J. Sun, and I. Cohen, Proceedings of the National Academy of Sciences **113**, 10774 (2016).

[106] C. Heussinger and E. Frey, The European Physical Journal E **24**, 47 (2007).

[107] H. E. Amuasi, C. Heussinger, R. L. Vink, and A. Zippelius, New Journal of Physics **17**, 083035 (2015).

[108] L. Liang, C. Jones, S. Chen, B. Sun, and Y. Jiao, Physical Biology **13**, 066001 (2016).

[109] P. Ronceray, C. P. Broedersz, and M. Lenz, Proceedings of the National Academy of Sciences **113**, 2827 (2016).

[110] R. Mari, R. Seto, J. F. Morris, and M. M. Denn, Journal of Rheology **58**, 1693 (2014).

[111] C. D. Cwalina and N. J. Wagner, Journal of Rheology **58**, 949 (2014).

[112] R. Seto and G. G. Giusteri, Journal of Fluid Mechanics **857**, 200 (2018).

[113] M. Das, F. C. MacKintosh, and A. J. Levine, Physical Review Letters **99**, 038101 (2007).

[114] P. R. Onck, T. Koeman, T. van Dillen, and E. van der Giessen, Physical Review Letters **95**, 178102 (2005).

[115] C. P. Broedersz, M. Sheinman, and F. C. MacKintosh, Physical Review Letters **108**, 078102 (2012).

[116] J. Wilhelm and E. Frey, Physical Review Letters **91**, 108103 (2003).

[117] S. Dagois-Bohy, B. P. Tighe, J. Simon, S. Henkes, and M. van Hecke, Physical Review Letters **109**, 095703 (2012).

[118] S. Arbabi and M. Sahimi, Physical Review B **38**, 7173 (1988).

[119] M. Das, D. A. Quint, and J. M. Schwarz, PLOS ONE **7**, e35939 (2012).

[120] S. B. Lindström, D. A. Vader, A. Kulachenko, and D. A. Weitz, Physical Review E **82**, 051905 (2010).

[121] F. Radjai, M. Jean, J. J. Moreau, and S. Roux, Physical Review Letters **77**, 274 (1996).

[122] C. S. O'Hern, S. A. Langer, A. J. Liu, and S. R. Nagel, Physical Review Letters **86**, 111 (2001).

[123] T. S. Majmudar and R. P. Behringer, Nature **435**, 1079 (2005).

[124] J. Rottler and M. O. Robbins, Physical Review Letters **89**, 195501 (2002).

[125] D. R. Reid, N. Pashine, J. M. Wozniak, H. M. Jaeger, A. J. Liu, S. R. Nagel, and J. J. de Pablo, Proceedings of the National Academy of Sciences **115**, E1384 (2018).

[126] M. G. Yucht, M. Sheinman, and C. P. Broedersz, Soft Matter **9**, 7000 (2013).

[127] M. Dennison and H. Stark, Physical Review E **93**, 022605 (2016).

[128] J. L. Shivers, S. Arzash, A. Sharma, and F. C. MacKintosh, Physical Review Letters **122**, 188003 (2019).

[129] M. F. Thorpe, Journal of Non-Crystalline Solids **57**, 355 (1983).

[130] M. E. Cates, J. P. Wittmer, J.-P. Bouchaud, and P. Claudin, Physical Review Letters **81**, 1841 (1998).

[131] C. P. Goodrich, A. J. Liu, and J. P. Sethna, Proceedings of the National Academy of Sciences **113**, 9745 (2016).

[132] W. G. Ellenbroek, E. Somfai, M. van Hecke, and W. van Saarloos, Physical Review Letters **97**, 258001 (2006).

[133] S. Alexander, Physics Reports **296**, 65 (1998).

[134] M. Sheinman, C. P. Broedersz, and F. C. MacKintosh, Physical Review Letters **109**, 238101 (2012).

[135] B. Widom, The Journal of Chemical Physics **43**, 3898 (1965).

[136] S. B. Lindström, A. Kulachenko, L. M. Jawerth, and D. A. Vader, Soft Matter

9, 7302 (2013).

[137] H. J. Maris and L. P. Kadanoff, American Journal of Physics **46**, 652 (1978).

[138] C. P. Goodrich, A. J. Liu, and S. R. Nagel, Physical Review Letters **109**, 095704 (2012).

[139] B. P. Tighe, Physical Review Letters **109**, 168303 (2012).

[140] M. Merkel, K. Baumgarten, B. P. Tighe, and M. L. Manning, Proceedings of the National Academy of Sciences **116**, 6560 (2019).

[141] R. Rens, C. Villarroel, G. Düring, and E. Lerner, Physical Review E **98**, 62411 (2018).

[142] C. P. Broedersz, Ph.D. thesis, Vrije Universiteit Amsterdam (2011).

[143] A. B. Harris, Journal of Physics C: Solid State Physics **7**, 1671 (1974).

[144] N. C. Admal and E. B. Tadmor, Journal of Elasticity **100**, 63 (2010).

[145] T. J. Delph, Modelling and Simulation in Materials Science and Engineering **13**, 585 (2005).

[146] T. Ishikura, T. Hatano, and T. Yamato, Chemical Physics Letters **539-540**, 144 (2012).

[147] Y. Fu and J.-H. Song, The Journal of Chemical Physics **141**, 54108 (2014).

[148] A. T. Fenley, H. S. Muddana, and M. K. Gilson, PLOS ONE **9**, e113119 (2014).

[149] J. L. Shivers, A. Sharma, and F. C. MacKintosh, arXiv:2203.04891 (2022).

[150] M. Mooney, Journal of Colloid Science **6**, 162 (1951).

[151] R. A. Bagnold, Proceedings of the Royal Society of London. Series A. Mathematical and Physical Sciences **225**, 49 (1954).

[152] J. Paredes, M. A. J. Michels, and D. Bonn, Physical Review Letters **111**, 015701 (2013).

[153] K. G. Wilson, Scientific American **241**, 158 (1979).

[154] M. E. Fisher, Reports on Progress in Physics **30**, 615 (1967).

[155] L. P. Kadanoff, W. Götze, D. Hamblen, R. Hecht, E. A. S. Lewis, V. V. Palciauskas, M. Rayl, J. Swift, D. Aspnes, and J. Kane, Reviews of Modern Physics **39**, 395 (1967).

[156] J. A. Drocco, M. B. Hastings, C. J. O. Reichhardt, and C. Reichhardt, Physical Review Letters **95**, 088001 (2005).

[157] T. Hatano, Physical Review E **79**, 50301 (2009).

[158] P. Olsson, Physical Review E **91**, 062209 (2015).

[159] D. Bonn, M. M. Denn, L. Berthier, T. Divoux, and S. Manneville, Reviews of Modern Physics **89**, 035005 (2017).

[160] H. A. Vinutha, K. Ramola, B. Chakraborty, and S. Sastry, Granular Matter **22**, 16 (2019).

[161] K. N. Nordstrom, E. Verneuil, P. E. Arratia, A. Basu, Z. Zhang, A. G. Yodh, J. P. Gollub, and D. J. Durian, Physical Review Letters **105**, 175701 (2010).

[162] A. Ikeda, T. Kawasaki, L. Berthier, K. Saitoh, and T. Hatano, Physical Review Letters **124**, 058001 (2020).

[163] K. Saitoh, T. Hatano, A. Ikeda, and B. P. Tighe, Physical Review Letters **124**, 118001 (2020).

[164] Q. Wen, A. Basu, J. P. Winer, A. Yodh, and P. A. Janmey, New Journal of Physics **9**, 428 (2007).

[165] J. Liu, G. H. Koenderink, K. E. Kasza, F. C. MacKintosh, and D. A. Weitz, Physical Review Letters **98**, 198304 (2007).

[166] A. Basu, Q. Wen, X. Mao, T. C. Lubensky, P. A. Janmey, and A. G. Yodh, Macromolecules **44**, 1671 (2011).

[167] P. Schall, D. A. Weitz, and F. Spaepen, Science **318**, 1895 (2007).

[168] V. Chikkadi, G. Wegdam, D. Bonn, B. Nienhuis, and P. Schall, Physical Review Letters **107**, 198303 (2011).

[169] V. Chikkadi and P. Schall, Physical Review E **85**, 031402 (2012).

[170] B. P. Tighe, E. Woldhuis, J. J. C. Remmers, W. van Saarloos, and M. van Hecke, Physical Review Letters **105**, 088303 (2010).

[171] B. Andreotti, J.-L. Barrat, and C. Heussinger, Physical Review Letters **109**, 105901 (2012).

[172] E. Woldhuis, V. Chikkadi, M. S. v. Deen, P. Schall, and M. v. Hecke, Soft Matter **11**, 7024 (2015).

[173] E. DeGiuli, G. Düring, E. Lerner, and M. Wyart, Physical Review E **91**, 062206 (2015).

[174] H. Ikeda, The Journal of Chemical Physics **153**, 126102 (2020).

[175] H. Ikeda and K. Hukushima, Physical Review E **103**, 032902 (2021).

[176] G. Katgert, B. P. Tighe, and M. Van Hecke, Soft Matter **9**, 9739 (2013).

[177] J. Boschan, S. A. Vasudevan, P. E. Boukany, E. Somfai, and B. P. Tighe, Soft Matter **13**, 6870 (2017).

[178] G. Düring, E. Lerner, and M. Wyart, Physical Review E **89**, 022305 (2014).

[179] X. Trepat, L. Deng, S. S. An, D. Navajas, D. J. Tschumperlin, W. T. Gerthoffer, J. P. Butler, and J. J. Fredberg, Nature **447**, 592 (2007).

[180] Y. Mulla, F. C. MacKintosh, and G. H. Koenderink, Physical Review Letters **122**, 218102 (2019).

[181] E. M. Huisman, C. Storm, and G. T. Barkema, Physical Review E **78**, 051801 (2008).

[182] M. Sheinman, C. P. Broedersz, and F. C. MacKintosh, Physical Review E **85**, 021801 (2012).

[183] V. Shankar, M. Pasquali, and D. C. Morse, Journal of Rheology **46**, 1111 (2002).

[184] A. Tanguy, J. P. Wittmer, F. Leonforte, and J.-L. Barrat, Physical Review B **66**, 174205 (2002).

[185] B. A. DiDonna and T. C. Lubensky, Physical Review E **72**, 066619 (2005).

[186] S. Dagois-Bohy, E. Somfai, B. P. Tighe, and M. v. Hecke, Soft Matter **13**, 9036 (2017).

[187] C. Raffaelli and W. G. Ellenbroek, Soft Matter **17**, 10254 (2021).

[188] O. Chaudhuri, L. Gu, D. Klumpers, M. Darnell, S. A. Bencherif, J. C. Weaver,

N. Huebsch, H.-p. Lee, E. Lippens, G. N. Duda, et al., Nature Materials **15**, 326 (2016).

[189] T. H. Larsen and E. M. Furst, Physical Review Letters **100**, 146001 (2008).

[190] S. Aime, L. Cipelletti, and L. Ramos, Journal of Rheology **62**, 1429 (2018).

[191] B. Fabry, G. N. Maksym, J. P. Butler, M. Glogauer, D. Navajas, and J. J. Fredberg, Physical Review Letters **87**, 148102 (2001).

[192] P. Bursac, G. Lenormand, B. Fabry, M. Oliver, D. A. Weitz, V. Viasnoff, J. P. Butler, and J. J. Fredberg, Nature Materials **4**, 557 (2005).

[193] X. Trepat, G. Lenormand, and J. J. Fredberg, Soft Matter **4**, 1750 (2008).

[194] G. H. Koenderink, Z. Dogic, F. Nakamura, P. M. Bendix, F. C. MacKintosh, J. H. Hartwig, T. P. Stossel, and D. A. Weitz, Proceedings of the National Academy of Sciences **106**, 15192 (2009).

[195] S. Wang and P. G. Wolynes, Proceedings of the National Academy of Sciences **109**, 6446 (2012).

[196] Y. L. Han, P. Ronceray, G. Xu, A. Malandrino, R. D. Kamm, M. Lenz, C. P. Broedersz, and M. Guo, Proceedings of the National Academy of Sciences **115**, 4075 (2018).

[197] G. Chaudhary, A. Ghosh, N. A. Bharadwaj, J. G. Kang, P. V. Braun, K. S. Schweizer, and R. H. Ewoldt, Macromolecules **52**, 3029 (2019).

[198] G. Chaudhary, N. A. Bharadwaj, P. V. Braun, and R. H. Ewoldt, ACS Macro Letters **9**, 1632 (2020).

[199] D. Head and C. Storm, Physical Review Letters **123**, 238005 (2019).

[200] D. Levesque, L. Verlet, and J. Kürkijarvi, Physical Review A **7**, 1690 (1973).

[201] P. B. Visscher, P. Mitchell, and D. Heyes, Journal of Rheology **38**, 465 (1994).

[202] J. D. Stevenson, J. Schmalian, and P. G. Wolynes, Nature Physics **2**, 268 (2006).

[203] F. Léonforte, A. Tanguy, J. P. Wittmer, and J.-L. Barrat, Physical Review Letters **97**, 055501 (2006).

[204] V. Lubchenko and P. G. Wolynes, Annual Review of Physical Chemistry **58**, 235 (2007).

[205] G. Brambilla, D. El Masri, M. Pierno, L. Berthier, L. Cipelletti, G. Petekidis, and A. B. Schofield, Physical Review Letters **102**, 085703 (2009).

[206] M. Ballauff, J. M. Brader, S. U. Egelhaaf, M. Fuchs, J. Horbach, N. Koumakis, M. Krüger, M. Laurati, K. J. Mutch, G. Petekidis, et al., Physical Review Letters **110**, 215701 (2013).

[207] A. Ikeda, L. Berthier, and P. Sollich, Physical Review Letters **109**, 018301 (2012).

[208] J. D. Ferry, *Viscoelastic Properties of Polymers* (John Wiley & Sons, 1961).

[209] A. Ikeda, L. Berthier, and P. Sollich, Soft Matter **9**, 7669 (2013).

[210] T. Kawasaki, D. Coslovich, A. Ikeda, and L. Berthier, Physical Review E **91**, 012203 (2015).

[211] P. Olsson, Physical Review Letters **122**, 108003 (2019).

[212] Y. Nishikawa, A. Ikeda, and L. Berthier, Journal of Statistical Physics **182**, 37

(2021).

[213] M. Wang and J. F. Brady, Physical Review Letters **115**, 158301 (2015).

[214] F. Boyer, E. Guazzelli, and O. Pouliquen, Physical Review Letters **107**, 188301 (2011).

[215] W. B. Russel, N. J. Wagner, and J. Mewis, Journal of Rheology **57**, 1555 (2013).

[216] A. Singh, C. Ness, R. Seto, J. J. de Pablo, and H. M. Jaeger, Physical Review Letters **124**, 248005 (2020).

[217] A. Stukowski, Modelling and Simulation in Materials Science and Engineering **18**, 015012 (2009).

[218] S. D. Poisson, in *Annales de Chimie et de Physique* (1827), vol. 36, pp. 384–387.

[219] L. D. Landau and E. M. Lifshitz, *Theory of Elasticity*, Course of Theoretical Physics (Elsevier Science, 1959).

[220] S. P. Lake and V. H. Barocas, Annals of Biomedical Engineering **39**, 1891 (2011).

[221] J. Steinwachs, C. Metzner, K. Skodzek, N. Lang, I. Thievessen, C. Mark, S. Münster, K. E. Aifantis, and B. Fabry, Nature Methods **13**, 171 (2015).

[222] G. N. Greaves, A. L. Greer, R. S. Lakes, and T. Rouxel, Nature Materials **10**, 823 (2011).

[223] A. S. Abhilash, B. M. Baker, B. Trappmann, C. S. Chen, and V. B. Shenoy, Biophysical Journal **107**, 1829 (2014).

[224] S. Motte and L. J. Kaufman, Biopolymers **99**, 35 (2013).

[225] J. Nocedal and S. J. Wright, *Numerical Optimization* (Springer Science & Business Media, 2006).

[226] M. Vahabi, A. Sharma, A. J. Licup, A. S. G. van Oosten, P. A. Galie, P. A. Janmey, and F. C. MacKintosh, Soft Matter **12**, 5050 (2016).

[227] M. Dennison, M. Sheinman, C. Storm, and F. C. MacKintosh, Physical Review Letters **111**, 095503 (2013).

[228] L. Zhang and X. Mao, Physical Review E **93**, 22110 (2016).

[229] The CGAL Project, *CGAL User and Reference Manual* (CGAL Editorial Board, 2013).

[230] J. L. Shivers, J. Feng, A. S. G. v. Oosten, H. Levine, P. A. Janmey, and F. C. MacKintosh, Proceedings of the National Academy of Sciences **117**, 21037 (2020).

[231] Y. Fung, American Journal of Physiology **213**, 1532 (1967).

[232] R. Tharmann, M. M. A. E. Claessens, and A. R. Bausch, Physical Review Letters **98**, 88103 (2007).

[233] R. C. Picu, Soft Matter **7**, 6768 (2011).

[234] K. Pogoda, L. Chin, P. C. Georges, F. J. Byfield, R. Bucki, R. Kim, M. Weaver, R. G. Wells, C. Marcinkiewicz, and P. A. Janmey, New Journal of Physics **16**, 75002 (2014).

[235] M. Perepelyuk, L. Chin, X. Cao, and A. V. Oosten, PLOS ONE **11**, e0146588 (2016).

[236] A. S. G. van Oosten, X. Chen, L. Chin, K. Cruz, A. E. Patteson, K. Pogoda, V. B. Shenoy, and P. A. Janmey, Nature **573**, 96 (2019).

[237] A. Arani, H.-K. Min, N. Fattahi, N. M. Wetjen, J. D. Trzasko, A. Manduca, C. R. Jack Jr., K. H. Lee, R. L. Ehman, and J. Huston III, Magnetic Resonance in Medicine **79**, 1043 (2018).

[238] G. Seano, H. T. Nia, K. E. Emblem, M. Datta, J. Ren, S. Krishnan, J. Kloepper, M. C. Pinho, W. W. Ho, M. Ghosh, et al., Nature Biomedical Engineering **3**, 230 (2019).

[239] P. A. Janmey and K. Pogoda, Nature Biomedical Engineering **3**, 171 (2019).

[240] T. A. Engstrom, K. Pogoda, K. Cruz, P. A. Janmey, and J. M. Schwarz, Physical Review E **99**, 52413 (2019).

[241] T. Shen, C. S. O'Hern, and M. D. Shattuck, Physical Review E **85**, 011308 (2012).

[242] G. Lois, J. Blawzdziewicz, and C. S. O'Hern, Physical Review Letters **100**, 028001 (2008).

[243] M. R. Islam and R. C. Picu, Physical Review E **99**, 63001 (2019).

[244] B. Cui, G. Ruocco, and A. Zaccone, Granular Matter **21**, 69 (2019).

[245] M. Delarue, J. Hartung, C. Schreck, P. Gniewek, L. Hu, S. Herminghaus, and O. Hallatschek, Nature Physics **12**, 762 (2016).

[246] A. Boromand, A. Signoriello, F. Ye, C. S. O'Hern, and M. D. Shattuck, Physical Review Letters **121**, 248003 (2018).

[247] Y. Zhang, J. Feng, S. I. Heizler, and H. Levine, Physical Biology **15**, 26001

(2018).

[248] C. S. O'Hern, S. A. Langer, A. J. Liu, and S. R. Nagel, Physical Review Letters **88**, 75507 (2002).

[249] D. Song, J. L. Shivers, F. C. MacKintosh, A. E. Patteson, and P. A. Janmey, Journal of Applied Physics **129**, 140901 (2021).